SIZE-SELECTIVE SEDIMENT TRANSPORT AND CROSS-SHORE PROFILE EVOLUTION IN THE NEARSHORE ZONE

A Thesis
Presented to
The Academic Faculty

by

Chatchawin Srisuwan

In Partial Fulfillment
of the Requirements for the Degree
Doctor of Philosophy in the
School of Civil and Environmental Engineering

Georgia Institute of Technology
December 2012

SIZE-SELECTIVE SEDIMENT TRANSPORT AND CROSS-SHORE PROFILE EVOLUTION IN THE NEARSHORE ZONE

Approved by:

Dr. Paul A. Work, Advisor
School of Civil and Environmental Engineering
Georgia Institute of Technology

Dr. Kevin A. Haas
School of Civil and Environmental Engineering
Georgia Institute of Technology

Dr. Hermann M. Fritz
School of Civil and Environmental Engineering
Georgia Institute of Technology

Dr. J. David Frost
School of Civil and Environmental Engineering
Georgia Institute of Technology

Dr. Emanuele Di Lorenzo
School of Earth and Atmospheric Sciences
Georgia Institute of Technology

Date Approved: October 29, 2012

To my beloved father

Mr. Chaisak Srisuwan

April 15, 1953 - August 15, 1994

ACKNOWLEDGEMENTS

I would like to thank my advisor Dr. Paul Work for opportunities, precious research ideas and guidance, motivation and encouragement, patience and understanding, examples of professionalism and supreme work standards, and for sharing his flawless living philosophy and personal interests, and many more- I certainly cannot thank him enough. I would also like to thank his wife Dr. Catherine Rendon for many special occasions that made me feel at home, though I never visited my real home once during my study.

I sincerely thank Drs. Kevin Haas and Hermann Fritz for educating me in some of the rarest topics in coastal engineering, and for serving on my PhD thesis committee. I also wish to thank the other two committee members Dr. David Frost and Dr. Emanuele Di Lorenzo for their support and invaluable comments on my research.

My deepest appreciation goes to literally the hardest working gentlemen in the world who assisted me during my laboratory study at Karadeniz Technical University in Turkey. Drs. Murat İhsan Kömürcü, Servet Karasu, İsmail Hakkı Özölçer, and Murat Kankal not only tirelessly helped me but also treated me like a VIP. The excellent wavemaker programmers and my good friends Tuncay Değermenci and Cenk Albayrak are also thanked.

I thank Kemal Cambazoğlu for helping me get started with some of the numerical models. I thank friends who worked hard and played little with me: Heidi Hammerstein, Chad Spurlock, Mesut Türel, Brian McFall, Xiufeng Yang, Brittany Bruder, Fahad Mohammed, Adam Sapp, Thomas Gay, Justin Hawthorne, and Zafer Defne.

I definitely owe most to my mother Dr. Galaya Srisuwan who never believes hard time or bad luck even exists. She is just simply incredible in helping me get my head right. She is also the hardest working woman in the world. I thank you Mama.

I am honored to be the first recipient of the “Strategic Scholarships for Frontier Research Network” in ocean engineering (CHE-PhD-SFR). For 4+ years in the USA, I had been taken care of very excellently by the Office of Educational Affairs at the Royal Thai Embassy in Washington DC.

TABLE OF CONTENTS

LIST OF TABLES

LIST OF FIGURES

LIST OF SYMBOLS AND ABBREVIATIONS

$\bar{f}$	mean wave frequency	Hz
$\bar{\zeta}$	mean water level including wave setup or setdown	m
β	profile slope, positive for shoreward decreasing depth	[-]
β_ϵ	proportionality factor relating sediment diffusivity to eddy viscosity	[-]
δ	elevation of the reference concentration from the sediment bed	m
δ_{sw}	total depth of the water column at the swash edge	m
ϵ_s	sediment diffusivity factor	m^2/s
η	instantaneous water surface	m
γ	wave breaking index in relation to local water depth	[-]
γ_s	sediment specific gravity	[-]
κ_s	sediment grain roughness	mm, μm
λ_i	hiding/exposure factor on instantaneous shear stress term	[-]
$\mathbb{V}$	instantaneous water volume between a location and the swash front	m^3
μ	water dynamic viscosity	$N.s/m^2$
∇_h	horizontal gradient operator	m^{-1}
ν	water kinematic viscosity	m^2/s
ν_t	total eddy viscosity	m^2/s
$\overline{c_{\text{crest},i}}$	phase-averaged sediment concentration in the wave crest	%
$\overline{H_{xx\%}}$	average height of the largest $xx\%$ of the waves	m

ϕ	wave asymmetry parameter	rad
ϕ_s	sediment angle of repose	deg
ρ	water density	kg/m^3
ρ_s	sediment density	kg/m^3
σ	wave angular frequency	rad/s
σ_g	standard deviation of the sediment size composition	mm, μm
σ_r	angle of wave breaking roller front slope	deg
τ_x^B	bottom shear stress in cross-shore direction (SHORECIRC)	N/m^2
$\tau_x^{B,str}$	bottom shear stress due to steady streaming	N/m^2
τ_{b,eff,d_i}	instantaneous effective shear stress of the i^{th} size class	N/m^2
τ_{b,eff,d_m}	instantaneous effective shear stress of the mean diameter	N/m^2
$\tau_{b,cr}$	critical bed shear stress for incipient motion	N/m^2
τ_b, $\tau_{b,ins}$	instantaneous bed shear stress	N/m^2
Θ'	normalized effective shear stress	[-]
θ_{cr}	critical Shield's parameter	[-]
φ	surf similarity parameter	[-]
ϱ	sediment porosity	[-]
ξ_i	hiding/exposure factor on the critical shear stress term	[-]
ζ	instantaneous elevation of water surface, measured from SWL	m
ζ_t	elevation of water surface at wave trough	m

A	complex amplitude of the wave	m
A'	estimated wave roller area	m^2
a_b	amplitude of breaking wave	m
A_u	amplitude of linear-wave horizontal orbital velocity	m/s
A_w	amplitude of linear-wave vertical orbital velocity	m/s
A_{br}	coefficient in the wave breaking factor	[-]
B	coefficient representing intensity of wave breaking	[-]
B_o	wave surface shape parameter	[-]
B_{st}	bed-slope adjustment factor	[-]
C	wave celerity	m/s
C_b	bedload transport efficacy factor	[-]
C_d	drag coefficient	[-]
C_g	wave group celerity	m/s
c_i	individual concentration of the i^{th} sediment size class	%
C_s	suspended-load transport efficacy factor	[-]
C_τ	bed-shear stress coefficient	[-]
$c_{b,br}$	reference concentration induced by wave-breaking turbulence	%
$c_{b,sh}$	reference concentration induced by bottom-shear stress	%
C_{sp}	relative width of wave energy spectrum	[-]
C_{wm}	calibration factor in the wavemaker program	[-]

$C_{x,k}$	celerity of the evolving bedform	m/s
D	wave energy dissipation	N/m
D_*	non-dimensional sediment particle size	[-]
d_i	grain diameter of an individual size class	mm, μm
$D_{k,i}^{dep}$	abundance of the i^{th} size class in the deposited layer at the k^{th} cell	%
$D_{k,i}^{ero}$	abundance of the i^{th} size class in the eroded layer at the k^{th} cell	%
$D_{k,i}^{ini}$	abundance of the i^{th} size class in the initial sediment at the k^{th} cell	%
$D_{k,i}^{mix}$	abundance of the i^{th} size class in the mixing layer at the k^{th} cell	%
$D_{k,i}^{rem}$	abundance of the i^{th} size class in the remaining layer at the k^{th} cell	%
d_m	mean sediment diameter- weighted average	mm, μm
d_{rep}	representative diameter of a sediment mixture	mm, μm
d_{xx}	sediment size at which xx percents of the mixture is finer	mm, μm
E	wave energy per unit width	N/m
E_{fx}	cross-shore wave energy flux	W/m
eef	profile-equilibrium modeling performance index	[-]
f	wave frequency	Hz
f_w	wave friction factor in hydrodynamic model	[-]
f_{cw}	combined wave-current bottom friction factor (SHORECIRC)	[-]
f'_{cw}	wave-current related friction coefficient (sediment transport)	[-]
F_{ecg}	wave breaking factor for turbulence-induced sediment pickup	[-]

$f_{s,\text{crest},i}$	phase-averaged, mean sediment flux in the wave crest	m^2/s
$f_{s,i}$	phase-averaged, depth-integrated, sediment flux in the water column	m^2/s
f_{sw}	bottom friction coefficient in the swash zone	[-]
G_k^{dep}	thickness of deposition layer at the k^{th} cross-shore cell	m
G_k^{ero}	thickness of erosion layer at the k^{th} cross-shore cell	m
G_k^{mix}	thickness of mixing layer at the k^{th} cross-shore cell	m
G_k^{rem}	thickness of remaining layer at the k^{th} cross-shore cell	m
h	mean water depth (including wave setup)	m
H_b	wave height at breaking	m
h_b	water depth at wave breaking	m
h_o	still water depth	m
H_s	significant wave height	m
H_{mo}	spectral wave height	m
H_{orms}	offshore root-mean-square wave height	m
h_{sw}	instantaneous thickness of swash lens	m
k	wavenumber	m^{-1}
k_p	wavenumber at peak wave frequency	m^{-1}
K_r^m	wave reflection coefficient from measurement	[-]
K_r^p	wave reflection coefficient from prediction	[-]
L	wave length	m

L_o	deep water wave length	m
L_{swm}	maximum wave run-up distance, from still-water shoreline	m
N	geometric distortion in the physical model	[-]
n_x	horizontal scale of the physical model	[-]
n_z	vertical scale of the physical model	[-]
P_b	probability distribution of breaking wave	[-]
p_i	percent occurrence of the ith size fraction	%
p_n	percent occurrence of the n^{th} statistical wave	%
ppf	profile-evolution modeling performance index	[-]
Q_b	fraction of breaking waves	[-]
Q_x	total volume flux in the cross-shore direction	m^2/s
$q_{b,i}$	fractional bedload sediment transport rate of the i^{th} size class	m^2/s
$Q_{b,lag}$	fraction of breaking waves considering roller lag	[-]
$Q_{b,tot}$	total fraction of breaking waves	[-]
$q_{b,t}$	total bedload sediment transport rate summing all size classes	m^2/s
$q^L_{k,i}$	offshore transport rate of i^{th} size fraction at the k^{th} cell	m^2/s
$q^R_{k,i}$	onshore transport rate of i^{th} size fraction at the k^{th} cell	m^2/s
$q_{s,i}$	fractional suspended-load transport rate of the i^{th} size class	m^2/s
$q_{s,t}$	total suspended-load transport rate summing all size classes	m^2/s
q_{tot}	total, combined net bedload and suspended load, transport rate	m^2/s

Q_{wx}	cross-shore wave induced volume flux	m^2/s
r	nominal parameter for skewed-wave form	[-]
$R_{2\%}$	wave run-up distance induced by $\overline{H_{2\%}}$	m
SF	grain sorting efficacy factor	[-]
T	wave period	s
T_m	mean wave period	s
T_p	peak wave period	s
T_s	total swash oscillatory period	s
T_{gm}	duration over which the grain sorting model is called	s
$u,\ v,\ w$	instantaneous total water particle velocities in three directions	m/s
U_s	initial waterline speed according to terminal breaking bore	m/s
$u_w,\ w_w$	wave orbital velocities, horizontal and vertical components	m/s
u_x	instantaneous horizontal wave orbital velocity	m/s
$u_{b,tot}$	total near-bed fluid velocity (wave+undertow)	m/s
$u_{o,b}$	near-bed wave orbital velocity amplitude	m/s
$u_{sed,i}$	instantaneous horizontal velocity of the i^{th} sediment size class	m/s
u_{sw}	instantaneous velocity in the swash zone	m/s
v_s	Smagorinsky eddy viscosity	m^2/s
V_x	wave-averaged cross-shore current velocity	m/s
v_*	shear velocity	m/s

V_{dx}	depth-varying mean cross-shore current	m/s
V_{mx}	depth-uniform mean cross-shore current	m/s
V_{sw}	depth-uniform mean cross-shore velocity in the swash zone	m/s
$v_{t,0}$	background constant eddy viscosity	m^2/s
W	wave-averaged vertical velocity	m/s
W_f	sediment fall velocity	m/s
X	instantaneous position of the waterline (swash front)	m
X_L	cross-shore distance shoreward from the mean water shoreline	m
X_{sw}	location where the swash zone and the surf zone are connected	m
z_{wm}	wave run-up elevation measured from SWL	m
S_I	wave spectral energy of incident wave	m^2/Hz
S_k	wave skewness parameter	[-]
S_R	wave spectral energy of reflected wave	m^2/Hz
S_η	wave energy density in a spectrum	m^2/Hz
S_{xx}	cross-shore wave radiation stress	N/m
ADV	acoustic Doppler velocimeter	–
MWL	mean water level, including wave setup and setdown	m
RMSD	root-mean-square deviation	given unit
SWL	still water level	m

SUMMARY

Cross-shore profile evolution is a dynamic phenomenon that often leads to threatening consequences such as beach profile erosion and shoreline retreat in the coastal zone. This study introduces a new comprehensive morphodynamic model that can be used to describe and predict related processes in the phenomenon. The concept of size-selective sediment transport and grain sorting was regarded as the key for the model development. Physical modeling of the problem was also performed to obtain new data sets that aided the numerical study.

Various physical models of beach profile evolution were studied in a random wave flume laboratory. Each model was carried out until the profile evolution tended to discontinue, referred to as "an equilibrium state". The novel aspects in the design of the experiment include:

- Three profile types constructed of coarse, fine, and bimodal mixed sands;
- Consecutive tests that imitated beach erosion, storm event, and beach recovery;
- Measurement and analysis of sediment size characteristic changes on the profile.

Erosive-, storm-, and accretive-type profiles were all observed in the experiment with the mean sediment size changing up to 20%. Important beach profile features such as sandbar structure and foreshore slope were found sensitive to the sediment characteristics. Consistent coarsening and fining of the surface sediment suggested that size-graded sediment fractions tended to relocate to various energetic zones along a beach profile.

The numerical morphodynamic model employs existing wave and circulation models (REF/DIF S and SHORECIRC) with several additional components for a more complete description of the complex nearshore flow, including

- Parametric models for wave skewness and wave orbital velocities;

- Ballistic swash zone model including wave runup prediction;
- New analysis technique and predictive formula for filtering out wave reflection.

Based on available data from the measurement, important wave parameters and undertow currents on the profiles were predicted with mean absolute differences less than 10% and 41%, respectively. A novel, multi-size sediment transport model was utilized to resolve individual transport rates of size-graded sediment fractions, following two important size-selectivity mechanisms. One is the "hiding/exposure" effect which promotes the transport of coarser sediment fractions in a mixture; the other is the non-linear "grain size dependency" which leads to an opposite fractional transport behavior. Some of the state-of-the-art components in this sediment transport model include:

- Prediction of intra-wave, fractional transport rates in both sediment transport modes;
- Velocity skewness and acceleration included in the determination of bed shear stress;
- Wave breaking effect on sediment mobility and reference concentration;
- Estimation of extra onshore sediment transport through the wave crest flux;
- Effects of bed slope and differences between fluid and particle velocities;

The multi-size sediment transport model is coupled with a new grain sorting model that resolves cross-shore grain sorting and vertical grain lamination. The model was shown to be capable of simulating the cross-shore bathymetric changes observed in the laboratory for both erosive- and accretive-type profiles, including the events of sandbar formation, migration, and deformation. The model also successfully resolved the consistent grain sorting trends observed in the experiment.

The new model proved to be most advantageous for a condition with prominent and highly-varying sediment grain sorting, which is always the case of sand-size material in nature. Beach profile equilibrium was also better simulated since size-graded fractions are predicted to relocate to different zones where they could withstand local hydrodynamic intensities. The resulting grain sorting and its history in the domain are also a useful set of information provided by the new model.

CHAPTER I

INTRODUCTION

The coastal zone is unquestionably important to human welfare. Most of the countries in the world have a coastline which is home to 80% of their population (Martinez et al., 2007). Adverse natural phenomena in the coastal zone such as sea level rise and storm weather have also increased dramatically in the past few decades (Hecht, 2007; Cazenave et al., 2008). Advanced numerical models for simulating coastal morphodynamics have been advocated in order to study these threatening phenomena. This type of tool serves to predict nearshore profile evolution, shoreline setback, and impacts of coastal engineering projects such as beach nourishment and coastal protection structures.

Ocean waves, currents, and their interactions create the primary forces that drive sediment transport in the coastal zone. Propagating towards the shoreline, the waves transform and their heights, skewness, and asymmetry increase. The waves also refract and their incident angles tend to approach shore-normal. When the waves break, the available ordered wave energy is converted into turbulence. The onshore volume flux from the breaking waves leads to an undertow current and a longshore current. Inside the wave boundary layer at the bottom, the wave orbital velocities also interact and result in a steady streaming in the wave propagation direction. These complex mechanisms are among the most influential processes that need to be considered in modeling the coastal morphodynamics.

Most existing sediment transport models only consider the mean (d_m) or median diameter (d_{50}) of the sediment mixture to represent the effect of grain size. This typical approach leads to one counter-intuitive consequence that the mobile sediment and the sediment bed are of the same permanent size characteristics. In reality, different size fractions in a sediment mixture are not always transported proportionally to their percent occurrences. This fact can be confirmed by many observations of grain sorting phenomena and seasonal variations in sediment size characteristics along natural beach profiles. In many cases,

sediment mixtures may even feature multi-modal size distributions which contribute to higher non-uniformities in both the sediment bed and the mobile sediment.

The approach that computes multi-fractional sediment transport rates is referred to as size-selective or multi-size sediment transport modeling. This approach also allows a computation of horizontal and vertical grain sorting in the sediment bed. With the sediment transport, grain sorting, and beach profile evolution being highly interactive, the approach provides a more realistic description of the morphodynamics. Despite this promising feature, very few of the existing coastal sediment transport models adopt this approach and none of them have ever before been applied to a full coastal morphodynamic problem where waves, currents, sediment transport, grain sorting and their temporal/spatial variations are considered.

A complete morphodynamic modeling system usually includes wave, circulation, sediment transport, and morphology models. The present research is a comprehensive study of the modeling system which utilizes newly-developed, numerical process-based models for computing size-selective sediment transport and cross-shore grain sorting. The particular domain of interest is the 2-D cross-shore profile, spanning from the location of maximum wave runup to a depth of 10-12 m, within which the sediment transport is active. The study exclusively focuses on the predominant transport induced by short waves and wave-driven circulation. Existing wave and circulation models that have been extensively verified with measured data are utilized with some extensions for the prediction of wave orbital velocity and wave swash velocity.

The new sediment transport model resolves both bed- and suspended- transport loads by incorporating the hiding/exposure concept and non-linear grain size dependencies that correct for resulting forces on particular sediment size fractions. The model also takes into account the effect of wave breaking that acts to enhance the sediment transport rates. Using a multi-layer, size-composition tracking algorithm, the new morphology model is designed to resolve grain-sorting processes over vertical layers along the cross-shore domain. The application of the new modeling system is exclusively focused on, but not limited to, the evolution of a profile to an equilibrium state, after which the profile only changes very little with time (Dean and Dalrymple, 2002).

In conjunction to the numerical modeling effort, a uniquely-designed laboratory experiment was also part of the study. The experiment was performed in the random-wave flume at Karadeniz Technical University, Trabzon, Turkey. Various types of beach profiles were physically modeled including those constructed from fine (0.18 mm), coarse (0.37 mm), and bimodal sands (a 50:50 mix of the fine and coarse sands). Three conditions of random waves were applied to both initially-plane slopes and beach nourishment scenario that featured a fill and a native slope with different grain sizes. Hydrodynamic and bathymetry data were collected in the experiment for investigating the significance of the related processes and for testing the numerical model.

In the experiment, an equilibrium state of every test under constant wave forcing was observed after carefully tracking and surveying the profile. Sediment samples showed measurable changes in grain size as the profile evolved, with d_m varying by 20% along the cross-shore domain. Influences of grain size were also noticeably clear between the coarse and the mixed sand experiments as the two resulting profiles were distinct despite being tested with identical wave conditions. Both erosive and accretive profile changes were achieved and the grain sorting trends observed in all experiments were consistent.

Chapter 2 provides a literature review on relevant topics, focusing mainly on previous research efforts on the size-selective sediment transport problem. Chapter 3 illustrates the design, implementation, measurement, and data analysis of the laboratory experiment. Chapter 4 provides detailed descriptions of the numerical hydrodynamic models, as well as a validation of the simulation results against the laboratory data. Chapter 5 illustrates the development of the new sediment transport and grain sorting models, including sensitivity analyses. Chapter 6 demonstrates the use of the integrated modeling system for simulating cross-shore morphodynamics. The model performance is tested against various profile evolution and grain sorting data collected from the experiment. The conclusion of the study is provided in Chapter 7, summarizing both the physical and the numerical model results, as well as the capability and the applicability of the new comprehensive morphodynamic model.

CHAPTER II

LITERATURE REVIEW

This chapter provides a comprehensive review on the study of cross-shore morphodynamics. Section 2.1 gives an overview of the problem. Some common modeling options for the nearshore hydrodynamics are discussed in Section 2.2. Section 2.3 covers some examples of conventional, single-grain-size approaches for modeling the sediment transport. Section 2.4 discusses the dynamic grain sorting phenomena found in nature, leading to a confirmation on the existence of size-selective sediment transport and its significance in the morphodynamic problem. Section 2.5 provides a thorough review of the modeling of cross-shore profile evolution with existing size-selective sediment transport and grain sorting models.

2.1 Morphodynamics overview

Coastal morphodynamics is involved with many complex mechanisms. The problem is often simplified by focusing only on the cross-shore or the longshore process that features different length and time scales (e.g. De Vriend et al. 1993; Soulsby 2001; Van Rijn et al. 2003). Cross-shore morphodynamics is usually the more dynamic component closer to the shoreline, especially in the surf zone. This dominance is primarily due to the fact that the refracting waves approach the shoreline in a near-normal incident angle. Many nearshore processes also feature spatial gradients, which essentially drive the circulation and bathymetric change, that are much greater in the cross-shore direction than the longshore direction.

Validity of this simplification is also generally supported by the fact that most coastal engineering scenarios are dominated by either the cross-shore or the longshore process alone. The cross-shore morphodynamics greatly influences profile changes of relatively straight beaches far away from structures and inlets, including the cases of rising water levels, storms and beach nourishment (Zheng and Dean, 1997). Usually a cross-shore and

a longshore morphodynamic model can be coupled for simulating the interactive processes between the two components.

2.1.1 Beach profile behavior

Waves, currents and their interactions in the coastal zone create the major forces that drive cross-shore profile evolution. Dean and Dalrymple (2002) suggested that a beach profile in an absence of such forces would have a linear shape corresponding to the sediment angle of repose. Bruun (1954) proposed that a profile with a specific grain size exposed to a constant forcing will evolve to and remains in an equilibrium shape. This concept is widely known as "equilibrium beach profile theory" and has been extensively studied using both field and laboratory data, as well as analytical studies (e.g. Dean 1977, 1987; Kraus 1994; Peters et al. 1996). The original equilibrium profile theory, however, cannot be used to describe non-monotonic beach profiles that usually occur in nature; needless to say the theory does not explain any time-dependent process during the profile evolution.

Both erosive and accretive profile behaviors are observed in nature. An erosive profile usually occurs under energetic wave conditions, when a strong undertow acts to carry the sediment seaward, resulting in the formation and offshore migration of sandbars. Under milder wave conditions, the effect of onshore-skewed waves dominates over the undertow, leading to an accretive profile associated with the onshore migration and partial deformation of sandbars (e.g. Stive 1988; Cambazoglu et al. 2006; Hsu et al. 2006). Besides these major contributors, other phenomena such as wave breaking and infragravity waves are also hypothesized as the causes of the cross-shore profile evolution (e.g. Dally 1987; Roelvink and Stive 1989; Thornton et al. 1996).

Seasonal changes of natural beach profiles reflect the two common types of cross-shore profile evolution (Figure 1). Larger waves and frequent storms in winter are found associated with steeper cross-shore slopes and sandbars. Subsequent accretion on the profile, sometimes referred to as beach recovery, usually occurs in the subsequent seasons. The erosive and the accretive seasonal timescales range from hours to days and months to years, respectively. Seasonal variations in the dry part of a beach are also a result of these profile behaviors. Mean annual shoreline relocations are usually on the order of 1 m for

straight coasts and up to 10 m for irregular planforms and inlet areas; fluctuating shoreline changes such as those due to seasonal variations could be up to ten times greater than these two mean numbers (Van Rijn et al., 2003; Dean and Dalrymple, 2002).

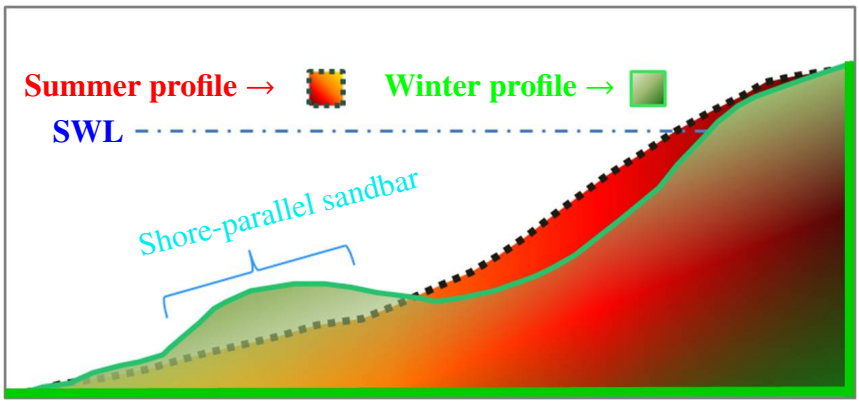

Figure 1: Example of typical beach profiles that vary by seasons. Summer and winter beach profiles may also be referred to as accretive- and erosive-type profiles, respectively.

2.1.2 Cross-shore profile modeling

Early beach profile models were mostly developed using behavior-oriented approaches, based on empirical studies, experiences, or physical models (Schoonees and Theron, 1995). This type of model may assume that the profile evolution is a function of the deviation from an equilibrium profile (e.g. Kriebel and Dean 1985; Kriebel et al. 1991), or follows an empirical shape function (e.g. Swart 1976; Russell and Huntley 1999; Masselink 2004). Process-based models that simulate the actual physics of the problem are preferred over this approach. Conceptually, a process-based model is designed so that a satisfactory prediction would be achieved if all of the relevant processes are described accurately. A successful process-based model would also help explain the underlying physics and offers a wider applicability for other similar scenarios of interest. However, due to limited understanding of the physics still, recent process-based modeling efforts have been aimed towards including the most important processes under optimal modeling options.

A process-based beach profile model typically consists of four major modules that simulate waves, circulation, sediment transport, and bathymetric change. These individual models are normally configured to interact as a single integrated unit. The major inputs for the model may include directional wave information and initial bathymetry data with other

possible inputs such as wind and ambient current depending on the model capability. The three-dimensional coastal processes are usually described using either a two-dimensional horizontal model (2DH depth-averaged) or a three-dimensional (3D) model, noting that one dimension is removed when neglecting the longshore component. A quasi-3D model is a hybrid of the two typical approaches. This type of model resolves the vertical structure of the circulation by incorporating a set of analytical solutions as an extension to a 2DH model (e.g. De Vriend and Stive 1987; Svendsen et al. 2002).

The approach in resolving the time dependency in the model is either to compute the wave-averaged or intra-wave quantities of the related dynamic parameters. Most quasi-3D morphodynamic models are of the wave-averaging type except for some that may utilize 2DH Boussinesq wave equations (e.g. Rakha 1998; Li et al. 2007). The wave-resolving approach allows a direct inclusion of many non-linear processes with a trade-off of much greater computational expense. While this factor is often argued in the modeling effort, another debatable issue is that many dynamic processes, especially those relevant to sediment transport, have not yet been described well enough for a utilization in the fully intra-wave approach.

As the description of the related processes improves and the computational expense decreases, a fully 3D, wave-resolving model would become the most promising option. For the present time, many researchers have shown that a well-developed, quasi-3D model is efficient for simulating both of the waves and the circulation (e.g. De Vriend and Stive 1987; Haas et al. 2003; Haas and Warner 2009) as well as the sediment transport and profile evolution (e.g. Ding et al. 2006; Cambazoglu 2009; Luijendijk et al. 2010). It should be noted that these research efforts usually also include an extra model for resolving wave orbital velocities of random waves or a representative wave (e.g. Demir 2007; Cambazoglu 2009).

2.2 *Cross-shore hydrodynamics*

Accurate prediction of the hydrodynamics is one of the keys to a successful morphodynamic modeling. Some commonly-used approaches for modeling essential processes in three distinct zones on a cross-shore profile are discussed below. An overview for the boundaries and typical processes in these zones are illustrated in Table 1.

Table 1: Example of major dynamic zones on a beach profile. Typical forms of waves, wave-induced currents, and sediment mobilization in each zone are listed in the tabular.

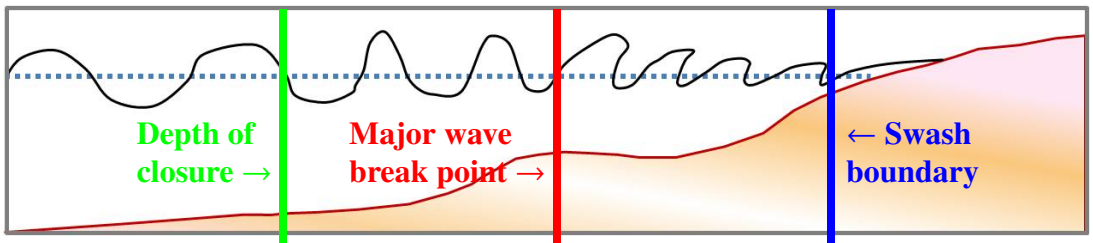

Outer nearshore	Inner nearshore	Surf zone	Swash zone
linear/skewed waves	skewed/asymmetric waves	breaking waves	uprushing breaking bores
negligible currents	small currents	strong currents	offshore-directed mean flow
no incipient motion	shear-induced motion	shear/breaking-induced motion	shear/swash-induced motion

2.2.1 Nearshore zone

The nearshore zone is defined here as the region between the location that the waves start to feel the bottom and the location that they begin to break. At the depth of closure, where the sediment transport begins to occur, the zone can be split again into the inner and the outer nearshore zones.

The outer nearshore zone may be irrelevant to the bathymetric change but usually the wave information for a morphodynamic model is obtained or prescribed in this zone. Certainly, accurate wave information is vital for the modeling system. Recent technologies have shown improvement and consistency in estimating the wave information, for example, surface-following wave buoys, acoustic Doppler current profilers, and more advanced remote systems (e.g. Work 2008; Terray et al. 1999; Haus et al. 2010). One common issue found in the nearshore wave measurement is that the data observed by an

instrument sometimes do not represent the actual wave field. Apart from measurement errors, this issue frequently occurs when the waves are modified by local effects such as strong ambient current or density stratification. With the use of an acoustic Doppler current profiler, Srisuwan and Work (in review) outlined and discussed alternative data analyzing methods for compensating for these effects.

In the inner nearshore zone, the shoaling waves become skewed about the mean water level, resulting in water surface and orbital velocity time series with narrower and sharper crests but wider and flatter troughs. Closer to the shoreline, these wave profiles are also asymmetric as the wave crests incline forward. Many sediment transport studies have shown that the presence of these nonlinear waves leads to a net onshore sediment transport (e.g. Hoefel and Elgar 2003; Cambazoglu et al. 2006). An advanced, non-linear, wave-resolving model may be utilized to resolve these wave forms. More practical, less computationally intensive, models are introduced as semi-empirical formulas requiring local wave parameters and bathymetry as the model inputs (e.g. Isobe and Horikawa 1982; Elfrink et al. 2006). Alternatively, a parameterized wave equation may be used directly to reproduce the wave profiles with a user-defined wave skewness and asymmetry (e.g. Hsu and Hanes 2004; Abreu et al. 2010).

Onshore-directed steady streaming inside the wave boundary layer is more prominent under a laminar condition, which could be the case in the nearshore zone (Trowbridge and Madsen, 1984; Davies and Villaret, 1999). This problem has long been studied and the wave boundary layer equation can be solved for the streaming velocity (e.g. Fredsoe and Deigaard 1992). To consider the streaming effect on the flow outside the boundary layer, a simpler method by Longuet-Higgins (1956) can be an alternative. This method estimates the shear stress due to the steady streaming, which can be utilized for adjusting the bottom shear stress computed on top of the boundary layer.

2.2.2 Surf zone

The surf zone is defined here as the area between the initial wave breaking and the shoreline. Not only does the wave breaking drive substantial circulation in this zone, it also leads to strong turbulence over the water column that may drive the sediment transport

directly. The concept of radiation stress by Longuet-Higgins and Stewart (1964) allows a prediction of the wave-driven circulation using a wave-averaged approach. Besides the radiation stress, the wave volume flux and the energy dissipation are the major parameters required for the prediction of the circulation. While the wave period, celerity, and group celerity are reasonably assumed to follow linear wave theory, these parameters can be estimated based on the wave height information (e.g. Svendsen et al. 2002).

A wave transformation model serves to describe the spatial variation in wave heights along a beach profile, commonly achieved by solving an energy balance equation (Battjes and Janssen, 1978; Thornton and Guza, 1983). Inside the surf zone, the energy dissipation due to the wave breaking is paramount to other damping terms and a dedicated dissipation model is usually employed. Under random waves, this type of model computes the average dissipation by considering the probabilities of breaking and dissipation rates of random waves, represented by breaking bores of corresponding heights. The probabilities of breaking are usually estimated on the basis of Rayleigh distribution function (e.g. Battjes and Stive 1985; Ruessink et al. 2003).

The undertow current is particularly strong inside the surf zone, partly because of the additional mass flux induced by the wave breaking rollers. The undertow may be assumed to be depth-uniform and estimated directly based on the onshore volume flux (e.g. Van Rijn 1993). However, the actual undertow profile is well known to vary significantly over the depth with a stronger flow in the lower part of the water column. Putrevu and Svendsen (1999) showed that the depth-averaged momentum equation can be solved using a perturbation expansion technique, thus allowing a set of analytical solutions resolving for the undertow profile.

Very few studies have focused on the direct effect of wave breaking on sediment transport. One such effect is the evident sediment pickup and dispersal as the wave roller tumbles down on the sediment bed. Dally and Dean (1984) attempted to capture this effect via a term that directly relates the sediment concentration to the rate of turbulent energy dissipation. The method was found to overestimate the dissipation effect as the predicted troughs shoreward of evolving sandbars were much deeper than observed. Contradictorily, this outcome was attributed to an improper modeling of a cushioning effect of the water

column that acts to absorb or dissipate the turbulence.

2.2.3 Swash zone

Most phase-averaged wave models predict the wave heights at breaking that are proportional to the water depths. Thus, for boundedness of the solution, the wave height at the shoreline must vanish as the water depth there is effectively zero. In nature, the bore-like breaking wave propagates beyond the mean water level, leading to wave uprush and backwash, sometimes referred to as runup and rundown. Albeit several other definitions, it is between the uprush and the backwash limits that the swash zone is commonly defined (e.g. Butt and Russell 2000).

The swash area is arguably the most poorly understood zone on a beach profile, largely due to the complexities of wave-wave interaction, reversing flows, and infiltration through the sediment bed (Elfrink and Baldock, 2002; Bakhtyar et al., 2009a). To resolve for the swash hydrodynamics, several nonlinear approaches have been attempted and proved fairly satisfactory, e.g. nonlinear shallow water equation (Kobayashi et al., 1989) and Boussinesq equation (Sorensen et al., 2004). A more classical approach is to treat the swash motion as a ballistic problem. Despite not generally including the infiltration effect, this simpler approach is shown to predict the surface profile and the velocity during the swash period very well based on many comparisons to experimental data (e.g. Baldock and Holmes 1999; Hughes and Baldock 2004; Erikson et al. 2005).

A ballistic swash model predicts the swash velocity based on a semi-empirical equation that describes the time-dependent swash lens. In order to utilize this type of equation, the instantaneous position of the bore front (waterline) and the total swash period need to be known. For this purpose, the ballistic-type governing equation can then be solved numerically for an arbitrary slope, or analytically for a plane slope. More advanced ballistic-type models may include swash-swash interaction where colliding and overriding of multiple bore fronts are also considered.

2.3 Conventional single-size sediment transport models

Sediment transport in the coastal zone is commonly classified as bedload or suspended load. The bedload represents the transport through sliding, rolling and saltation of the particles on the sediment bed. The suspended load refers to the transport in suspension over the water column, primarily initiated by the flow turbulence. While both transport modes usually occur simultaneously along a beach profile, the suspended load may become dominant around the most energetic areas such as the wave breaking location.

This section is meant for discussing typical sediment transport models that compute transport rates based on a representative grain size, categorized by different process-based approaches. These models have been utilized in many full morphodynamic modeling systems (e.g. Nairn and Southgate 1993; Schoonees and Theron 1995; Van Rijn et al. 2003). A detailed review on size-selective sediment transport models and related morphodynamic modeling systems is given separately later in the chapter.

2.3.1 Energetics models

The energetics approach is based on the hypothesis that a portion of available power in the flow can be related to the sediment transport rate. Bagnold (1956) developed a pioneering bedload formula for steady flow that computes the transport rate as a function of turbulent diffusion. The formula was validated with numerous hydraulic flume and river data sets (Bagnold, 1966), as well as windblown sand transport data from wind tunnels (Bagnold, 1937).

Bagnold's original formula had been developed extensively before its first application in the coastal zone. First, it was modified for oscillatory flow with superposed mean flow where the symmetrical oscillatory motion also acts to pick up the sediment that is being convected in the mean flow direction (Bagnold, 1963). Bailard (1981) improved the formula by accounting for the bed-slope effect, meanwhile Bailard and Inman (1981) extended the model to include the suspended load. The transport formula by Bailard and Inman (1981) was shown to predict a beach profile with some certain behaviors observed in nature, including the slope that decreases with the depth, sediment fall velocity, and wave period.

The formulas introduced by Bagnold (1956) and Bailard and Inman (1981) employ the flow velocities to compute the transport rates directly. This method implies that the sediment transport is active at any non-zero flow speed, which is not always the case when considering the sediment incipient motion. To overcome this deficiency, the transport rate may be computed in terms of the effective bed shear stress, defined as the shear stress in excess of the critical level to mobilize the sediment. This alternative is sometimes referred to as a force/momentum balance approach (Van Wellen et al., 2000).

Watanabe (1987, 1992) introduced a total sediment transport formula for a combined wave-current flow where the effective shear stress is computed as the difference between the maximum and the critical bed-shear stresses, and the depth-averaged mean flow is employed for the sediment convection term. Ribberink (1998) applied the bed-shear concept of Meyer-Peter and Muller (1948) to develop a bedload transport formula that estimates the transport rate as a function of the Shields mobility number. The inclusion of the threshold shear stress sometimes poses a question regarding the lack of sediment transport when the effective shear stress term is equal to or marginally less than zero. Camenen and Larson (2005) investigated this inaccuracy and introduced a new formula that includes an exponential term to adjust for the effect of the critical Shields parameter under a minimal transport condition.

2.3.2 Concentration-based models

The energetics approach allows an estimation of the transport rate only in a depth-averaged fashion. Sediment transport in nature, however, always features vertical variation which is better described by the use of a concentration-based approach. Considering the sediment suspension as a diffusive process, the vertical concentration profile is commonly modeled using the advection-diffusion type equation (e.g. Deigaard et al. 1999). This method involves the need for the bottom boundary condition, which is typically defined either as a reference sediment concentration (e.g. Zyserman and Fredsoe 1994; Van Rijn 1997b), or as a reference sediment flux (e.g. Van Rijn 1984; Nielsen 1992; Davies et al. 1997).

Dally (1980) and Dally and Dean (1984) introduced a concentration-based formula that computes the suspended sediment flux in the lower part of the water column due to

both mean flow and orbital velocity, but in the upper part due to the mean flow only. The interface between the two parts is defined at the maximum height to which the sediment can reach and fall back to the bed within one wave period. The concentration profile is estimated using a diffusion-type equation for unidirectional flow (Rouse, 1937). Steetzel (1987, 1990) introduced a model similar to Dally and Dean's model except for extending the surface boundary to the wave crest level and dividing the two vertical sections as below and above the wave trough. Both models were proven capable of simulating erosive profile evolution with offshore bar migration. Only Dally and Dean's model could describe accretive profile evolution successfully. Neither models allows a prediction of an equilibrium state due to the lack of incipient motion description (Schoonees and Theron, 1995).

Most concentration-based models represent the suspended load as the only transport portion but some are also aimed at computing sediment transport in the entire vertical section. This extension is normally achieved by considering several transport mechanisms, and sediment fluxes in multiple vertical layers altogether (e.g. Ribberink and Al Salem 1995; Kaczmarek and Ostrowski 2002; Demir 2007).

2.3.3 Sheet-flow models

When the bed-shear stress increases to a certain level, bed ripples are washed out and an intensive transport layer forms close to the sediment bed, commonly referred to as a sheet-flow layer. Due to fluid-particle and particle-particle interactions under high shear stress, phase lags between the flow and the sediment transport are often found to be significant inside this sheet-flow layer. General criteria for the threshold of sheet flow and phase-lag effects are given by Camenen and Larson (2006), in terms of the Shields parameter and grain size Reynolds number.

Semi-unsteady, sheet-flow models have been introduced to adjust for the phase-lag effect via deterministic factors in their transport rate formulas. Dibajnia and Watanabe (1992) introduced a formula for a total transport rate with alternating offshore/onshore transport directions. Offshore transport occurs when the ratio between the sediment settling time and half of the wave period is greater than unity. Dohmen-Janssen (1999) suggested a phase-lag correction factor considering delayed entrainment and settlement

of the sediment via an analytical diffusion model (e.g. Nielsen 1986). Dohmen-Janssen et al. (2002) compared this semi-unsteady model to the quasi-steady model by Ribberink (1998) and showed that up to 50% overestimation of the net transport rate could be avoided by utilizing the phase-lag correction factor.

Unsteady sheet-flow models solve for time-dependent (intra-wave) sheet-flow concentration and velocity within a wave cycle, for example, following empirical profiles based on experimental data (e.g. Malarkey et al. 2003), or using the 1DV advection-diffusion equation (e.g. Ribberink and Al Salem 1995). More sophisticated sheet-flow models may also resolve the effects of fluid-particle or particle-particle interactions. This type of model solves the mass and the momentum equations between the fluid and the solid phases separately (e.g. Dong and Zhang 1999; Bakhtyar et al. 2009b). Besides an improvement for the computational time and numerical stability, this two-phase modeling approach still awaits better descriptions in several mechanisms such as the multiple-phase interactions and the thresholds among the different transport stages (Liu and Sato, 2006; Li et al., 2008).

2.4 Cross-shore grain sorting

Sediment grain sorting is referred to here as a mixing of size-graded sediment fractions that results in both spatial and temporal variations of sediment size characteristics. Cross-shore grain sorting always occurs along a natural beach profile as well as vertical grain lamination in the sediment bed. This section discusses these grain sorting phenomena which confirm the fact that size-selective sediment transport occurs extensively on a beach profile. In general, the sorting process may depend on many factors, including sources of sediment supply, winds, waves and tidal variations. The main focus here is on the wave-induced grain-sorting process in non- or micro-tidal environment, reflecting the cases simulated in the physical and the numerical models in this study.

2.4.1 Field studies

Most previous studies of sediment grain-sorting processes in the nearshore zone were conducted in the field. Beach profiles are normally found to feature sediment grain sizes

fining non-monotonically in the offshore direction. Based on the median grain size (d_{50}), the local maxima of the sediment are commonly found in the swash zone, at the wave plunge point, and around the bar structure. Terwindt (1962) illustrated that a median grain size variation of up to 30% was not uncommon on a beach profile, and a local median grain-size change of up to 20% could easily occur after a storm event.

Sonu (1972) found that poorly-sorted sediment in the swash zone, consisting of both sands and gravels, was present after a storm event. These materials were subsequently removed or sorted during the beach recovery stage, after which the zone appeared to feature dominant fine sand. Richmond and Sallenger (1984) reported a similar finding and suggested that the opposite transport directions of size-graded sediment fractions, regardless of the seasons, also contribute to the grain sorting in the swash zone.

Wave plunge points, though obscured under random waves, are usually associated with coarser sediments due to the high amount of energy that carries away fine sediments to less energetic zones. On a bar structure, two different features of the grain size variation have been reported. Sediment on the bar crest may be found to be coarser than that in the bar trough (e.g. Moutzouris 1988; Katoh and Yanagishima 1995), but the opposite trend is also possible (e.g. Terwindt 1962; Stauble and Cialone 1996). These contrary findings could possibly be a result of different observation and initial sediment conditions, neither of which can be identified easily in the field. A storm period usually leads to coarsening of the sediment bed throughout the profile, especially over the sandbar structure where the major wave breaker locates. The beach recovery stage that occurs later on leads to wave breaking closer to the shoreline and the consequent onshore sediment transport may carry the material previously deposited on the bar crest into the bar trough area.

Locations of the highest and the lowest grain-sorting indexes (d_{90}/d_{10}) of sediment mixtures along a beach profile are still largely unknown. Fox et al. (1966) and Inman (1953) found the poorest sorting in the breaker location while Zeigler et al. (1959) found the highest degree of sorting in this dynamic zone. Edwards (2001) suggested that the sorting degree tends to be size-dependent rather than location-dependent, though these two interpretations are closely related. The study showed that many of the fine mixtures were better sorted which is consistent with the finding by Moutzouris (1988). Medina

et al. (1994) addressed the discrepancy in identifying this grain-sorting degree as a result of various sediment types and inadequacy in using the standard deviation for multi-modal sediments.

2.4.2 Laboratory experiments

Very few laboratory studies have been performed to investigate the grain sorting phenomena on a beach profile. Many experiments were conducted in oscillatory water tunnels to study the transport process of size-graded sands (e.g. Dibajnia and Watanabe 1996; O'Donoghue and Wright 2004a; Hassan and Ribberink 2005b). This type of experiment, however, does not generally provide the grain sorting information since the entire domain is simulated under only one pseudo wave motion.

Sistermans (2002) performed a flat-bed experiment under irregular non-breaking waves and currents. Despite lacking a clear sign of horizontal grain sorting, many tests consistently showed that the grain-sorting index (d_{90}/d_{10}) increased as a function of the depth into the sediment bed. Together with the reduction of d_{50} of the sediment in suspension, this finding affirmed that the finer grains in the sediment bed were size-selectively picked up and transported in the suspended mode.

Celikoglu et al. (2006) conducted a cross-shore grain sorting experiment on a 1:5 plane slope using monochromatic waves and two types of sand, both nonuniform but clearly unimodal. It was shown that the finer and coarser sediment size classes were always dominant on the crest and the trough of the bar, respectively. Accumulations of the coarser materials on the bar shoulders were also observed and hypothesized to affect the dynamic equilibrium conditions of the profiles due to armoring effects. The tendency of the finer size fractions being better sorted than the coarser fractions was also illustrated. The study also included a dimensional analysis to relate the sorting phenomena to the wave conditions. Three parameters were found to influence the grain sorting: the relative grain diameter (d_{50}/h), wave period ($T/\sqrt{h/g}$), and breaking wave height (H_b/h).

The authors concluded that the grain-sorting process was only present when the above three parameters fell below 0.004, 15, and 1.5, respectively. Although insisted by the

experimental findings, these suggested parameters and their thresholds seem to be questionable for a general prediction of the phenomena. For example, increasing the amount of coarser sand fractions will lead to larger d_{50}/h and the mixture uniformity likewise, which should clearly encourage the sorting process (e.g. Dibajnia and Watanabe 1996; O'Donoghue and Wright 2004b). The parameters H_b/h and $T/\sqrt{h/g}$ may also not be representative since various hydrodynamic regimes on a beach profile may always exist independently of these two numbers. Such variations would lead to a grain-sorting process since each particular size fraction would seek for its equilibrium zone (e.g. Ingle 1966; Bowen 1980; Van Rijn 1997a).

2.4.3 Numerical modeling efforts

Early efforts to numerically model the cross-shore grain sorting were focused on directly relating the hydrodynamics to the grain sorting phenomena using empirical or statistical descriptions (e.g. Bagnold 1940; Inman and Chamberlain 1959; Liu and Zarillo 1993). Bowen (1980) suggested a theoretical concept that a particular size fraction will sustain in its equilibrium at a specific location on a beach profile. Likewise, the coarser and the finer materials at the same location, that are not in their equilibriums, will tend to move onshore and offshore, respectively. This equilibrium theory provides the transport directions identical to those predicted using the classic null-point hypothesis by Ippen and Eagleson (1955), and the asymmetrical threshold hypothesis by Bagnold (1940).

For a more process-based description, the grain sorting can be resolved by considering the median grain size (d_{50}) on a beach profile while still "excluding" size-selective transport processes. To achieve this, the mobile sediment and the local sediment bed are assumed to feature an identical size composition which, however, is not necessarily the same as that at the deposition location. A new local value of d_{50} is then recomputed considering mixing between the deposited fraction and the local bed mixture. Usually a mixing depth is required for this computation. This approach has been applied for longshore sediment transport in the beach nourishment scenario (Dean, 2002; Work et al., 2010), and in large-scale 3D sediment transport and morphology models (Warner et al., 2008).

Certainly the most appropriate approach to resolve the grain sorting phenomena should involve the use of a size-selective sediment transport model coupled with a sediment-tracking algorithm for resolving the sediment composition change. Van Rijn (1997a,b) applied this approach to his cross-shore profile model CROSMOR (Van Rijn, 1993). The grain-sorting algorithm in the model is designed for the surface layer only, neglecting possible vertical lamination of the sediment bed. The model was shown to be able to predict sediment coarsening around the most energetic area, i.e. wave-breaker and strong-velocity zones, and fining in both offshore and onshore directions. Only one simulation was compared to measured data to illustrate a fairly successful prediction for locations onshore to the major wave-break point.

2.5 Size-selective sediment transport models

Many researchers have emphasized the fact that sediment transport is essentially size-selective, as also supported by the evident grain sorting phenomena. Due to their interdependencies, the size-selective transport and sediment grain sorting should be considered as interactive processes. Medina et al. (1994) insisted that a beach profile model cannot be fully successful without this consideration. The state of the art in this modeling approach is reviewed below including both relevant basic principles and previous modeling efforts in three different flow conditions in increasing order of complexity.

2.5.1 Physics of the problem

The mechanisms of size-selective sediment transport are unique because of two major effects. One is the nonlinear dependency of the sediment transport on particle sizes, and the other is the interaction among the size-graded sediment fractions or a "hiding and exposure" effect. Accounting only for the nonlinear dependency, Van Rijn (2007b) found that a size-selective approach may yield up to 25% greater net transport rates than the values computed based only on d_{50} of the mixture. The difference also tends to increase as the size distribution widens. Despite showing reasonable results for the case of dominant fine sand, the method lacks general applicability for the size-selective sediment transport prediction. For example, it does not produce a fractional transport trend that agrees with

the measurement of incipient motion of size-graded sediments (e.g Komar 1987; Wilcock 1993). This particular example shows that, while it is certainly important, the inclusion of the nonlinear size dependency alone is not sufficient to describe the size-selective sediment transport process.

The hiding/exposure effect is often accounted for via a factor that adjusts for the critical bed-shear stress of each individual size fraction in a mixture. Fenton and Abbott (1977) illustrated this shear-stress alteration by considering the protrusion of a grain placed between or above other grains glued to the bottom. For a maximum protrusion of 0.8, i.e. a grain sitting above an interstice formed by other two identical grains, the result showed that the grain only required around 10% of the critical shear stress found for the zero protrusion case, where the three grains were all laid on the same bed level. Although not explicitly demonstrated in the study, the case of natural size-graded particles can be expected to yield a greater variation in the protrusion degree, and likewise in the critical shear stresses, due to a higher nonuniformity in the mixture.

Egiazaroff (1965) suggested a definition for the hiding/exposure factor as a ratio between the dimensionless critical bed-shear stress of an individual fraction and that of the mean grain size (d_m) of the mixture. The early version of Egiazaroff's expression was modified by several others, generally due to discrepancies in determining the two shear-stress terms based on data sets from different experiments (e.g. Hayashi et al. 1980; Parker et al. 1982). These different formulas, however, predict a consistent tendency that a size fraction finer than the mean ($d_i < d_m$) will feature a correction factor greater than one. Similar to the protrusion concept, the primary argument is that these finer sands are sheltered and thus less exposed to the flow. Komar (1996) suggested another formula for the factor as a function of the pivoting angle of a grain sitting on two other grains. This angle is equal to 60^o for spherical grains with the same size, i.e. equivalent to the relative protrusion of 0.8 defined by Fenton and Abbott (1977). Both Egiazaroff's and Komar's factors lead to similar results but the latter yields larger numbers for the finer fractions.

Van Rijn (1997a) compared the capabilities of several suggested exposure factors against many experimental data sets (e.g. Kuhnle 1993; Wilcock 1993; Petit 1994). It was found that Komar's formula provide unreasonably large values for very fine fractions

($d_i/d_{50} \leq 0.5$). Van Rijn (2007b) argued that even the factor by Egiazaroff is somewhat too large for very fine ($d_i/d_{50} \leq 0.2$) and very coarse size classes ($d_i/d_{50} \geq 3$). For this reason, an alternative form for the factor was suggested as a ratio between the critical stresses of each fraction in a size-graded mixture and that of a nominally uniform sediment of the same size. The distinction between Egiazaroff's and Van Rijn's formulas is discussed later in Chapter 5 (see Figure 48).

The hiding/exposure factors mentioned above are only meant for adjusting the incipient motion terms due to the size gradation effect. A similar correction parameter can also be applied to adjust the effect on the instantaneous shear stress term (e.g. Day 1980; Komar 1996). This factor is usually expressed as a power function of the relative grain diameter, e.g. given as $A(d_i/d_m)^n$, where A and n are positive constants implying that larger grains are more exposed to fluid drag compared to smaller grains. Unlike the one for the critical shear stress, this type of exposure factor is much less developed, most likely due to a limited capability in measuring instantaneous bed shear stress. Typically, the constants in the formula are user-defined numbers and often treated as calibration parameters. It is worthwhile to note that this factor is sometimes applied to adjust the "effective" shear stress or the net sediment transport rate directly (e.g. Hassan 2001; Van Rijn 2007b).

2.5.2 Transport in steady flows

Like most sediment transport problems, size-selective sediment transport was first studied in steady flows in rivers and open channels. Under these conditions, horizontal grain sorting always results in a sediment bed fining in the downstream direction. Einstein (1950) was a pioneer to explain and develop a formula for estimating size-selective sediment transport rates in nonuniform sediments. Widely applied in river problems, Einstein's bedload and suspended load functions compute fractional sediment transport rates by relating fluid mechanics and stochastic principles. Several key mechanisms in the processes were attributed to the non-uniformity of the sediment bed that leads to the hiding/exposure effects, and the alterations in the grain roughness and lifting forces.

Several other fractional transport formulas have been introduced since, mostly as improved versions of Einstein's original method (e.g. Parker et al. 1982; Misri and Raju

1984; Bridge and Bennett 1992). Wu et al. (2003) classified the available formulas into four categories. Each group of the formulas, however, takes into account the same non-uniformity effects just by using different approaches. Arguing that many formulas failed to estimate the total sediment transport rates, Wu et al. (2003) introduced a new formula based on the transport capacity concept. This concept allows the fractional transport estimation to match the total transport rate yielded by a coupled single-size transport formula based on d_{50} of the mixture. The prediction accuracy was improved under this constraint, partly due to the fact that, compared to a multi-size formula, most single-size sediment transport formulas have been more extensively developed and verified against measured data.

2.5.3 Transport in oscillatory flows

Most of the laboratory studies of size-selective sediment transport under this flow environment have been performed in oscillating water tunnels. Dibajnia and Watanabe (1996) investigated the transport mechanism of a bimodal mixture consisting of a fine and a coarse sand with d_{50} of 0.2 mm and 0.87 mm. For many ratios of the two sands, the experiment showed that the transport rates of the fine sand were significantly reduced with the presence of the coarse sand in the mixture. This selective transport process can reasonably be attributed to the effects of hiding/exposure where coarser sands shelter finer sands meanwhile being more exposed to the flow.

Hassan and Ribberink (2005b) conducted a full-scale experiment in an oscillatory water tunnel. Several of the tests showed that the size gradation had almost no effect on the "net" sediment transport rates provided that all sands in the mixtures were greater than 0.2 mm. However, the "individual" transport rate of each fraction was found to be affected by the presence of the other size fractions, with the coarser sands being more prone to transport than the finer sands. These size-selective effects are not only consistent with the results in Dibajnia and Watanabe (1996) mentioned above, but also some other results from similar oscillatory-flow studies (e.g. Dohmen-Janssen et al. 2002; Ahmed and Sato 2003; Malarkey et al. 2003).

The effects of size-graded sediments on the sheet-flow sediment concentration and the

transport fluxes were extensively studied by O'Donoghue and Wright (2004a) and (2004b). For the coarsest sand in the experiment (0.51 mm), the time-averaged fluxes were found to be onshore-directed and confined to a layer immediately above the bed. On the contrary, the fluxes of the finest sand (0.15 mm) were directed offshore in the sheet-flow layer but onshore in the upper suspended layer. These phenomena were attributed to an unsteady effect that caused the fine sands to be carried high off the bed and failed to deposit before the flow reversal. The bimodal mixture of 50:50% of 0.15 mm and 0.51 mm sands featured almost the same magnitudes of the onshore suspended flux and the offshore sheet-flow flux, resulting in a very small net transport rate. With the fine-sand percentage raised to 60%, the offshore flux became dominant and the net flux was finally directed offshore.

Most of the numerical models for oscillatory-flow fractional sediment transport have been attempted with the aid of experimental data. Dibajnia and Watanabe (1996) developed a semi-empirical, two-fraction formula assuming that the amount of energy consumed to transport each fraction is a power function of its abundance. The phase lag effect is considered in the formula by relating the fall velocity to the wave period. Dibajnia and Watanabe's formula was tested with a strictly two-size mixture and shown to provide accurate results including the possible opposite transport directions between the fine and the coarse sands.

On the basis of Ribberink (1998)'s single-size formula, Hassan (2001) attempted to develop a new formula for multi-fractional transport rates with the use of the exposure factor by Day (1980). The model does not include the possible phase-lag effect and was only verified using limited data sets from an oscillatory water tunnel experiment. Ahmed and Sato (2003) introduced a model that employs a newly-defined exposure effect referred to as an armoring coefficient. The model was shown to perform much better than Hassan's, which generally can be debated since the armoring coefficient was self-estimated from the validation data sets.

Hassan and Ribberink (2005a) suggested another two transport models, still with the use of the exposure factor by Day (1980). The first model allowed the net transport rates to be estimated within a factor of two compared to several sets of measured data. Generally the coarser fractions could be estimated much more accurately than the finer fractions. The

other model also included a correction factor for the entrainment height of each fraction in the mixture. This model also showed a similar capability to the first model for the prediction of fractional and net transport rates. Admittedly, the size-selective transport of the finer fractions still could not be modeled accurately, in terms of the transport rates and even for the transport directions in some cases.

2.5.4 Transport in waves and currents

Size-selective sediment transport involving waves and currents in a cross-shore environment is much more complex than the scenario under oscillatory flows. While some results under the two conditions are consistent (e.g. Nielsen 1992), oscillatory-flow experiments do not feature a free surface or any gradient of the flow or the bathymetry; needless to mention they do not represent any unique nearshore processes such as wave breaking, depth-varying current, and steady streaming.

A number of previous studies were focused on beach profiles that consist of sands (≤ 2 mm) and gravels (≥ 2 mm), or shingle beaches (e.g. Misri and Raju 1984; Lawrance et al. 2002; Lopez de San Roman-Blanco et al. 2006). Compared to the case of a sandy beach, the inclusion of gravels is shown to make the transport processes unique in many aspects. Very coarse grains will almost never be eroded and likely form a permanent armoring layer that impedes finer grains in lower layers (Van Rijn, 2007b). A sand-gravel mixture also features much higher permeability, bed roughness, and angle of repose. Given these reasons, the size-selective transport of a sand-gravel mixture is typically considered as a separate case to the with sand-size material.

Most existing size-selective sediment transport models for the coastal zone adopt some basic principles observed in steady and oscillatory flows. The attempt to compute the selective transport rates is generally achieved by modifying available, conventional single-size models. Through the use of a hiding/exposure factor, Van Rijn (1997a) modified his earlier single-size sediment transport formula to compute multi-fractional transport rates for both bedload and suspended load. This new model was compared to its original version and found to yield a net bedload that is slightly greater for $d_{50} \leq 0.2$ mm but significantly lower for larger d_{50}. For the suspended load, the model always predicts a smaller transport

rate especially for a low-energy condition.

Compared to that of the sediment bed, the size composition associated with the bedload in the model always contains more coarser fractions (d_i/d_{50}>1) due to their increased exposures. The difference can be very obvious under a very low-energy condition since some of the finer fractions may not be predicted to transport at all. On the other hand, more of the finer fractions in the suspended load may be found since their concentrations are predicted to be higher up in the water column. Van Rijn (1997a) included these multi-fractional transport formulas into the CROSMOR cross-shore profile model. A coupled wave-current model is utilized to solve for the undertow with an assumed logarithmic velocity profile. The near-bed orbital velocity in the model is described by an empirical form based on Stokes second-order and linear wave theories (see also Van Rijn 1997b).

The capability of the CROSMOR model was illustrated by simulating two field scenarios including both accretive and erosive profile evolutions. In the accretive test, the use of the multi-fractional transport model significantly influenced the profile simulation with the onshore bar migration being better represented but the erosion in the bar trough was overemphasized. In the erosive case, the model underpredicted the offshore bar migration as well as the erosion near the shoreline. These modeling inaccuracies possibly originated from the fact that the model computed very low suspended sediment transport rates near the shoreline. Even though the model could predict both erosive and accretive profile changes correctly, the success was largely based on adjusting the empirical factor of the wave-related transport term which primarily controlled the sediment transport directions.

Later, Van Rijn (2007b) introduced four different approaches to formulate a size-selective sediment transport model. Each of the approaches follows either Egiazaroff's or his own expression for adjusting the critical shear stress, and with or without the correction factor for the effective shear stress suggested by Day (1980). These new transport formulas were tested using measured data from both steady flows (Kleinhans and van Rijn, 2002), oscillatory flows (Hassan et al., 1999), and non-breaking waves on a horizontal bed (Sistermans, 2002). Arguably, the method that employs the hiding factors for the critical shear stress by Egiazaroff (1965) and for the effective shear stress by Day (1980) showed the best performance.

For a unimodal mixture with d_{50} of 0.24 mm in the oscillatory flows, the best Van Rijn (2007b)'s transport formula was shown to yield around 20% overestimation of the net transport rate, compared to 40% with the use of the original single-size model. For the case with non-breaking waves, the use of the single-size model was found to severely underpredict the concentration by a factor of 5-10 for a size-graded mixture of 0.26 mm. Meanwhile, the size-selective formula was found to improve the prediction significantly due to the increased concentrations of the finer fractions. As a final conclusion, Van Rijn (2007b) suggested that the single-size approach should not be used for any size-graded sediments with a grain-sorting index (d_{90}/d_{10}) greater than four. Despite their potentials, these size-selective formulas have never been applied to a situation on an actual beach profile that includes a bathymetric variation and a surf zone.

Kaczmarek et al. (2004) introduced a unique size-selective sediment transport model that resolves for a two-phase process. This model does not take into account any hiding/exposure factor but includes an effect of grain-grain interaction described by Coulomb friction theory. The model resolves the transports in three layers with different transport mechanisms under an intensive flow condition (Kaczmarek and Ostrowski, 2002). The model's capabilities to compute fractional sediment transport rates and grain sorting were verified using field and oscillatory water tunnel data. The field validation showed that the model could provide accurate grain sorting information at few locations around the sandbar after a storm event. Neither the size-selective sediment transport that led to the grain sorting nor the morphology change along the cross-shore profile evolution was illustrated in the study.

It is clear that size-selective sediment transport, grain sorting, and cross-shore profile evolution are highly interactive. Prior to the present research, the state of the art in modeling these processes was very limited to steady or purely 1-D oscillatory flow condition. The models that were developed in this study extend the body of the knowledge in the processes to the scenario of an actual cross-shore profile with a surf zone, which includes many hydrodynamic and sediment transport regimes. The physical and numerical modeling efforts that led to this accomplishment are described in the following chapters.

CHAPTER III

PHYSICAL MODELING AND DATA ANALYSIS

The physical modeling effort in this study was performed at the wave flume facility of Karadeniz Technical University, Trabzon, Turkey. The main objectives were to obtain various types of data required for calibrating and validating the numerical models. The physical modeling effort also provided many insights into grain size effects on sediment transport, beach profile evolution, and associated grain-sorting processes.

Several physical models of beach profiles, including a beach nourishment scenario, were simulated using non-uniform sands of both unimodal and bimodal size distributions. With the main focus on the grain size effects, these novel experimental settings had never been attempted in any previous physical models before. This chapter provides detailed descriptions of the experimental design, related data analyses, and important results of the cross-shore profile evolution, hydrodynamics, and grain sorting observed in the experiment.

3.1 Wave flume facility and wavemaker

The wave flume features dimensions of $30 \times 1.4 \times 1.2$ m with a paddle-type random wavemaker at its offshore end, and a glass window section at the other end (Figure 2). The flume width is 1.8 m near the wavemaker ($x \leq 5$ m) and 1.4 m elsewhere (Figure 2(c)). This design increases the incident wave height generated from a given paddle stroke to allow larger waves. The data analysis and the numerical modeling efforts here only consider the section of the flume onshore of the incident wave gauge placed at $x = 13$ m. The water depth in the flume (D) was kept constant at 0.8 m during all of the tests.

The random wavemaker in the flume was custom-built and tested prior to the experiment. A schematic of its operation is shown in Figure 3. The operation is designed to follow the first-order wavemaker solution (e.g. Hughes 1993). Random waves are introduced by estimating the instantaneous water surface $\eta(t)$, likewise the paddle position

$S_p(t)$, contributed from all individual wave components using a random-phase method (Massel, 1996). Based on the calibration between the voltage and the paddle excursion, a voltage time series is output to the control unit that responds to the requested paddle motion.

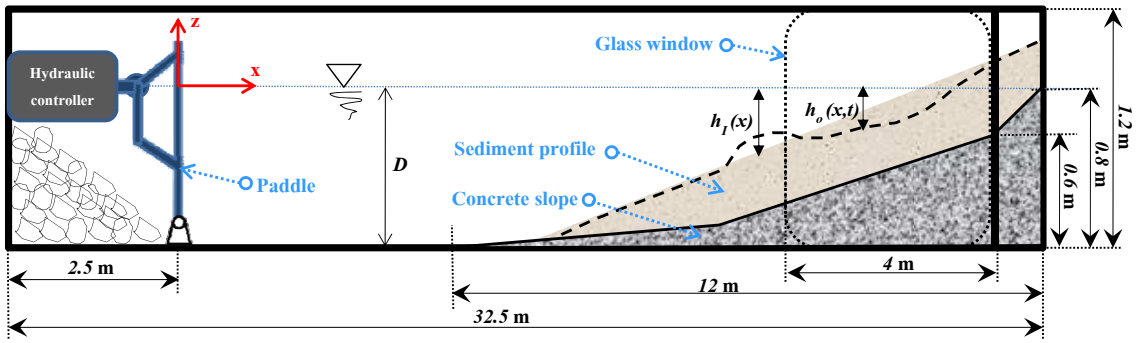

(a) Elevation view of the flume.

(b) Shoreline side of the flume with the glass-window section on the left.

(c) Offshore side of the flume with the random wavemaker.

Figure 2: Wave flume utilized for the experimental study: (a) h_I is the profile depth at the initial condition; h_o is the instantaneous depth measured from the still water level.

The feedback and adjustment steps in Figure 3 might be achieved based on a real-time wave measurement; however, they were only considered via monitoring the paddle motion in this experiment. The factor C_{wm} was therefore treated as a constant for both calibrating the paddle motion and relating it to the voltage input. The wavemaker was utilized successfully in the experiment despite two intermittent operational issues: (1) undesired paddle position due to mechanical uncertainty, and (2) overheating hydraulic controller due to excessive acceleration during the paddle reversals. The adjustment based on monitoring the paddle motion helped attenuate these problems, but also traded off

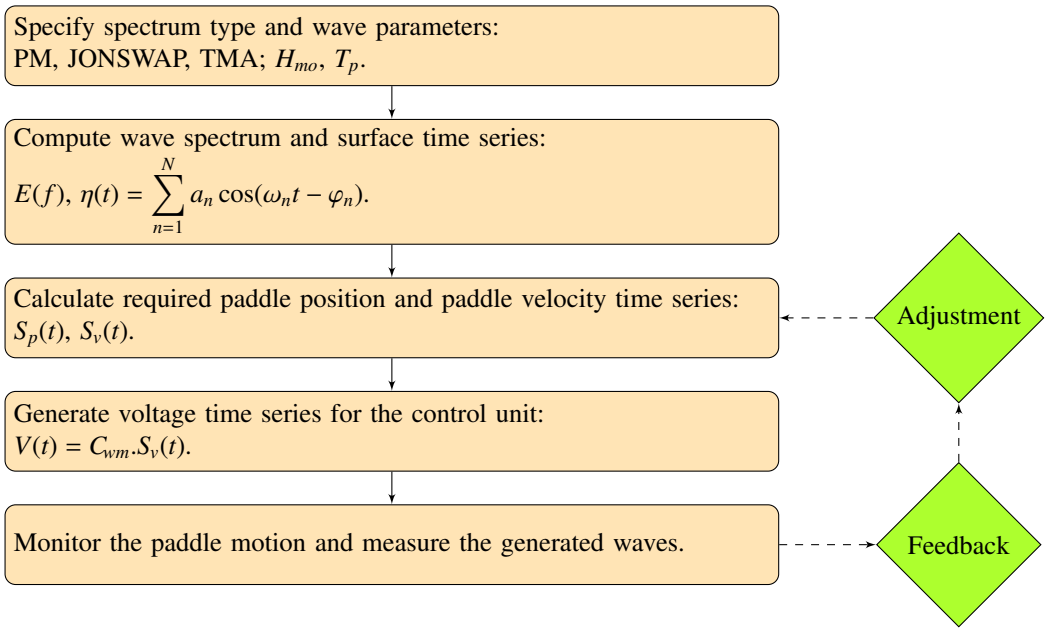

Figure 3: Schematic of the wavemaker operation: a_n, ω_n and φ_n are the amplitude, angular frequency and random phase of the n^{th} wave-frequency component, respectively; C_{wm} is the calibration parameter relating the paddle velocity $S_v(t)$ to the voltage input $V(t)$.

in an additional inaccuracy in the generated spectra. Certainly a more rigorous control algorithm, preferably by means of real-time feedback, will be required for improving the wave generation accuracy (e.g. Cimaglia and Thosteson 2002; Miskovic et al. 2008). The uncertainty in the wave-making process did not lead to any obstruction in this study as all of the desired wave conditions were still successfully generated. To avoid possible error in the input wave information, the measured wave spectra were utilized in the numerical modeling effort as opposed to the target wave spectra.

3.2 Experimental design

3.2.1 Materials

Three sediment mixtures were utilized in the experiment, referred to as fine, coarse and mixed sands. The latter was produced by mixing the fine and the coarse sands in the same proportion under the criterion to obtain a bimodal sediment mixture. Grain size distributions of the sands are shown in Figure 4(a); specific gravities and porosities of the fine and the coarse sands and some of their dominant size fractions are shown in Figure 4(c). Table 2 summarizes the physical properties of the sands.

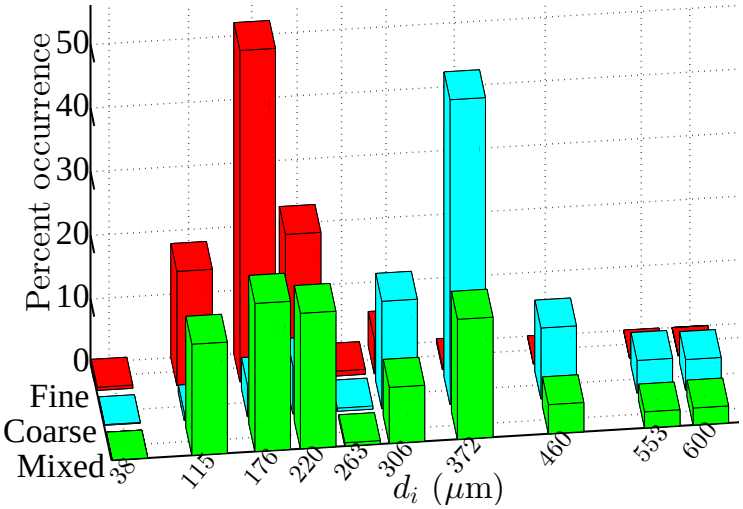

(a) Grain size distributions of the sands.

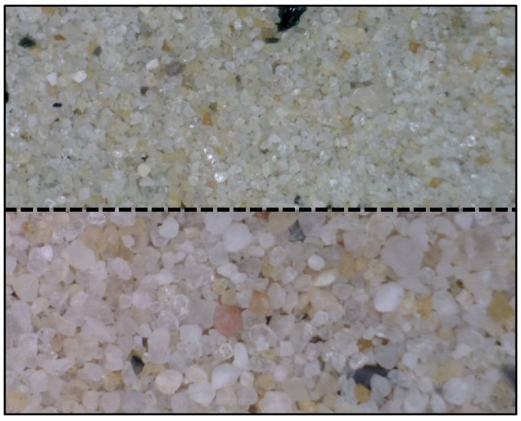

(b) Fine sand compared to coarse sand (with the same focal length).

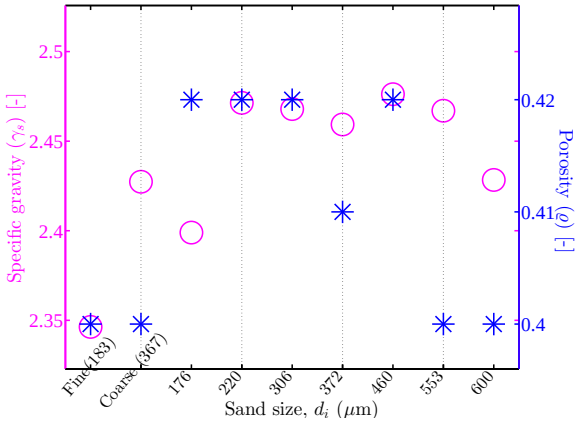

(c) Specific gravities and porosities of the sands and some individual size fractions.

Figure 4: Characteristics of the sands utilized in the experiment.

Table 2: Physical properties of the sands utilized in the experiment.

Property	**Sand type**		
	Fine	**Coarse**	**Mixed**
Median grain size (d_{50})	180 μm	363 μm	217 μm
Mean grain size (d_m)	183 μm	367 μm	257 μm
Standard deviation ($\sigma_g = (d_{84} - d_{16})/2$)	40 μm	84 μm	119 μm
Sorting index (d_{90}/d_{10})	2.3	2.0	3.5
Sediment porosity (ϱ)	≈ 0.40		
Specific gravity (γ_s)	2.34	2.42	2.38†

†Estimated- actual mixture was not processed.

The size distributions of the coarse and the fine sands were essentially unimodal as shown in Figure 4. The mixed sand showed a clear bimodality in its size composition that suited the requirement for simulating a bimodal-mixture case. Because of their variations are only around 5%, the specific gravities and the porosities of the sands and their individual size fractions, were taken to be 2.35 and 0.40 constant, respectively.

3.2.2 Physical model profiles

Three types of beach profiles constructed and tested in the experiment are considered here. These include two plane slopes with the coarse or the mixed sand, and a beach nourishment scenario with the coarse sand placed on top of the fine sand (Table 3 and Figure 5).

Table 3: Three physical models considered in the study and their geometric scales. Illustration of the profiles is shown in Figure 5.

Profile Type	**Sand Type**	**Scaling**		**Geometric distortion (N)**	**Slope** ($z : x$)	
		Vertical (n_z)	**Horizontal** (n_x)		**Prototype**	**Model**
1	Coarse	12.5	44.2	3.5	1:60	1:6
2	Mixed			5.2	1:90	
3	Coarse (upper)			3.1	1:20	
	Fine (lower)				1:110	1:11

Generally, a physical model will truly represent the prototype if all of the geometric, kinematic and dynamic criteria of similitude are satisfied (Work and Rogers, 1998). Like cases in any rescaled experiments, this ideal aspect was not possible for the design here due to a restriction in the flume size. Appropriate geometric scaling in the design was introduced following beach equilibrium profile theory. Subsequently, the Froude model criterion that is suitable for a surface gravity wave experiment was applied to determine desired wave conditions.

Since the equilibrium profile theory does not describe a plane beach profile, an initial profile slope was approximated based on the cross-shore distance in the prototype X_L measured seaward from the waterline to a depth of 10 m, computed following

$$X_L^{\text{prototype}} = \left[\frac{h_{\text{off}}}{A(d_{50})}\right]^{(3/2)} \tag{1}$$

where h_{off} is the depth at the profile toe taken to be 10 m here, and A is the empirical equilibrium-shape parameter given as 0.094 for the fine sand, 0.138 for the coarse sand, and 0.106 for the mixed sand, respectively (CEM, 2006). Following the prototype dimensions, the physical model slopes were estimated by selecting geometric scales that allowed appropriate beach profiles according to the size of the wave flume, given as

$$n_z = n \tag{2}$$

$$n_x = n_z^{3/2} \tag{3}$$

$$n_x^{\text{distorted}} = n_x.N \tag{4}$$

where n is the geometric scale; n_z is the vertical scale; n_x is the horizontal scale; and N is the geometric distortion. Scaling of parameter A in Equation (1) was not performed since the same sands were assumed in both the physical models and the prototypes. The geometric scale n was chosen to be 12.5, considering a suitable water depth in the flume of 0.8 m. This value yields the horizontal scale n_x of 44.2. If these two scaling numbers were preserved, the physical models would be geometrically undistorted but the required lengths of the profiles would have been very large or even greater than the flume length. The actual horizontal scale for each profile type was thus determined including an appropriate geometric distortion (N) as shown in Table 3.

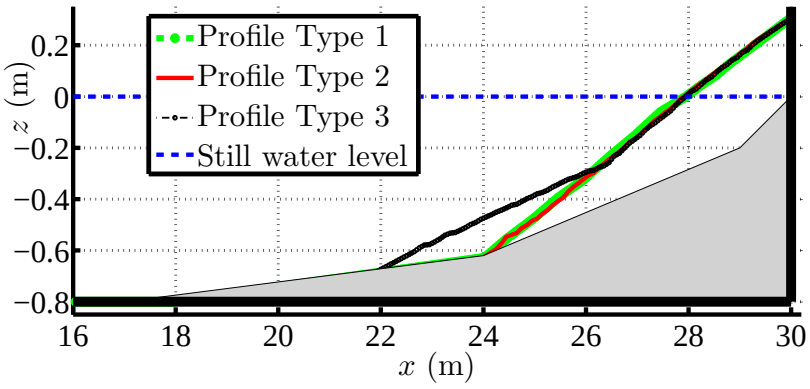

Figure 5: Three profile types considered in the study. See Table 3 for scaling details and type of material on each profile.

It is of primary importance to note that the scaling numbers and distortion of Profile Type 3 were identical for the upper and the lower slopes as required. The upper slope

Table 4: Important dimensionless parameters based on the scaling consideration. The parameters are applied to all of the three profile types. R_N is the ratio between the prototype and the model values and all other variables are defined in the list of symbols and abbreviations (page xiv).

Parameter	Expression	R_N	Parameter	Expression	R_N
Wave steepness	H/L	1	Dean number	$H_b/(wT)$	3.5
Relative water depth	h/L	1	Relative sediment density	ρ_s/ρ	1
Relative roughness	k_s/L	0.08	Relative time	$t(g/H_b)^{1/2}$	1
Viscosity parameter	$\rho g^{1/2}L^{3/2}/\mu$	45	Relative wave height	H_b/h_b	1
Grain size *Re* number	$v_* d_m/\nu$	3.5	Mobility number	$\rho v_*^2/(\gamma_s d_m)$	12.5
Relative grain size	a_b/d_m	12.5	Fall velocity ratio	$W_f/(gH_b)^{1/2}$	0.3

was assumed to be a man-made fill slope of which the prototype and the model are related linearly based on the geometric distortion. The prototype fill slope (1:20) was selected to be within a typical range of beach-fill slopes of 1:10 to 1:30 (Van Rijn et al., 2011). Based on the chosen scales, kinematic and dynamic similitudes between the prototypes and the physical models can be determined using a dimensional analysis (e.g. Hughes 1993). The similitudes of some important dimensionless parameters are listed in Table 4.

Most of the ratios (R_N) in Table 4 that deviate from unity originated from the fact that the sands were not scaled down in the experiment. The only exception is the viscosity parameter ($\rho g^{1/2}L^{3/2}/\mu$) in which only the wave length L was scaled down while the other parameters, ρ, g and μ, were unchanged. Unfortunately, the similitudes could not reasonably be preserved in the experiment due to several constraints. If scaled down, the required sediments would have to feature d_{50} of 10-30 μm. Such silt-size materials could possibly be provided but the cohesion between particles would lead to a different problem of cohesive sediment transport. Water properties could slightly be modified, e.g. via temperature and salinity, but certainly not to the extent where the viscosity parameter is conserved.

Regardless of their similitudes, some of the parameters in Table 4 might be very small and insignificant, or could be large but lead to similar fundamental processes in both domains. For example, despite the bias in the viscosity parameter, highly-turbulent

hydrodynamics may be anticipated in most parts of both the prototypes and the physical models. Generally, the scaling and geometric distortions are hypothesized to result in an increased effect of gravity due to the steeper slopes. The preserved sand sizes will result in reduced sediment transport rates, i.e. based on the mobility number $\rho v_*^2/(\gamma_s d_m)$. The deviation in the Dean number $H_b/(wT)$ also indicates that the trajectory of a sediment particle will not be equivalent to that in the prototype since the sediment fall times in the two scales are not proportional. In this case, suspended sediment transport may be underemphasized due to a reduction in the relative suspension duration of the sediment.

3.2.3 Wave spectra and experiment implementation

Table 5 illustrates three JONSWAP-type wave spectra that were utilized in the experiment. The peak wave periods were determined based on typical wave periods of 7 s and 10 s at prototype scale (Kamphuis, 2009). The spectral wave heights were subsequently estimated in order to include an erosive, a storm, and an accretive condition in the simulation of every profile type. The threshold between the erosive and the accretive conditions was predicted following the semi-empirical equation (Dalrymple, 1992; Kraus and Mason, 1993)

$$\frac{H_{mo}^2\, g}{T W_f^3} = 26,500 \tag{5}$$

where W_f is the fall velocity based on the mean sediment size (d_m). Equation (5) may be regarded as a modified version of the Dean Number in Table 4 that serves to predict the net sediment transport direction as a function of the sediment entrainment height, the fall velocity, and the wave period. An approximation was involved in the determination of the spectral wave heights so that the chosen wave conditions could be applied to all of the profiles with the different sand mixtures. The storm wave condition was assumed to be the situation where the wave height doubled from the regular erosive condition.

Logistics of the experiment implementation is illustrated in Figure 6. The three wave spectra were applied sequentially on each designed profile without reconstructing the initial condition. This design was intended to encourage a simulation of seasonal beach profile evolution starting from erosive and storm conditions, and then followed by an

Table 5: Three JONSWAP-type wave spectra implemented in the experiment. The model values are referred to as "nominal" since the actual values might be slightly different due to wave reflection effect and wave generation uncertainty.

Wave condition →	**A: Erosive**	**B: Storm**	**C: Accretive**
Prototype H_{mo} (m)	1.25	2.5	1.25
Model (nominal) H_{mo} (m)	0.10	0.20	0.10
Prototype T_p (s)	7		10
Model (nominal) T_p (s)	1.5		2.0

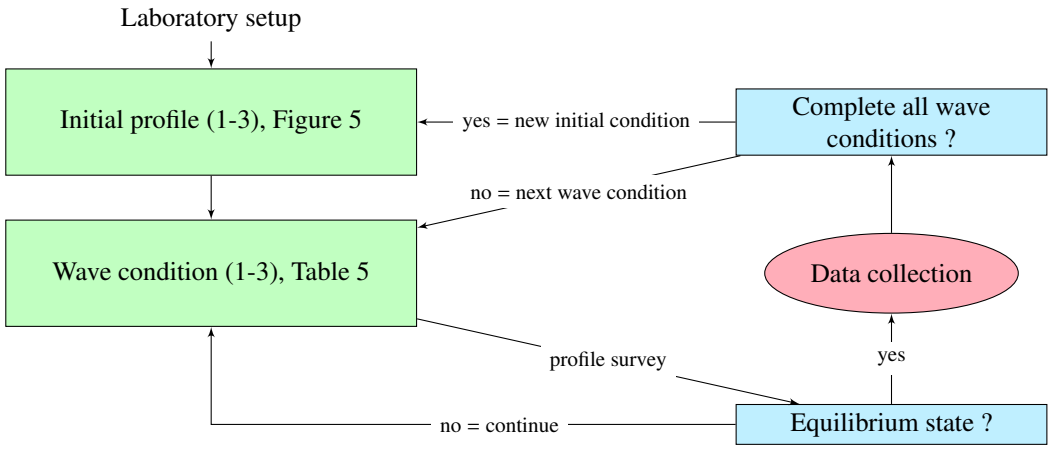

Figure 6: Logistics of the experiment implementation. Note that profile survey was also performed after the data collection to ascertain the equilibrium state.

accretive beach recovery. Each experiment, with a particular initial profile and wave condition, was continued until the profile reached an equilibrium state. Waves and mean flows were subsequently measured on the steady profile. The equilibrium state was ascertained by surveying the profile both before and after the data collection. If any significant profile evolution still occurred, the experiment was continued and the data collection was repeated later on. Typically, an equilibrium state was found after around 100-140 mins for an erosive-type profile and up to 180-210 mins for an accretive-type profile. For convenience, all of the experiments are labeled and summarized in Table 6.

3.3 Data collection and analysis

3.3.1 Equipment

Several tools were utilized for collecting important data in the experiment. Two capacitance wave gauges were employed to record instantaneous water surface displacement

Table 6: Summary of the experiments considered in this study and related designed parameters. Note that the label numbers (1-3) indicate the starting profile types (Figure 5), and the label characters (A-C) indicate the wave conditions (Table 5). The actual wave parameters measured in each experiment can be found in Figure 11.

Exp.	**Initial profile**	**Sand type**	**Nominal wave spectrum**	
			Peak period, T_p	**Wave height,** H_{mo}
1A	Type 1	Coarse	1.5 s	10 cm
1B	From 1A			20 cm
1C	From 1B		2.0 s	10 cm
2A	Type 2	Mixed	1.5 s	10 cm
2B	From 2A			20 cm
2C	From 2B		2.0 s	10 cm
2B2[†]	From 2C		1.5 s	20 cm
3A	Type 3	Coarse on fine	1.5 s	10 cm
3B	From 3A			20 cm
3C	From 3B		2.0 s	10 cm

[†]Repeated storm-wave test starting on the equilibrium profile of the preceding accretive test.

$\eta(t)$ for analyzing wave spectra and mean water level. One gauge, referred to as WG1, was mounted at an offshore location 13 m away from the wavemaker. The other gauge (WG2) was fixed at a particular position during a profile evolution and relocated to many locations once the equilibrium state was reached, to collect the data along the profile.

A down-looking acoustic Doppler velocimeter (ADV) was employed to record instantaneous water particle velocities ($u(t)$, $v(t)$, and $w(t)$). The ADV and the wave gauge WG2 were equipped on two dial gauges mounted on two separate carriages that allowed them to be relocated freely in both the horizontal and the vertical (Figure 7). A mechanical profiler was utilized for measuring the bathymetry in each experiment.

Sand samples were collected from the profile surface at the waterline, bar trough, bar crest, and offshore part of the sandbar structure, as well as a subsurface sample at the bar-crest area. These five locations were expected to be associated with significant local grain-size changes and their influences on the profile evolution. The samples were collected using a scooper that provided a sample unit of 10×15 cm over a thickness of 1-2 cm. This sample size satisfies the ASTM standard for the minimum bulk volume of 120 cm^3, or around 320 grams dry weight (Pope and Ward, 1998).

(a) Wave gauge (left) and ADV probe (right).

(b) Carriage that moved along the flume with sensors.

Figure 7: Capacitance wave gauge and acoustic Doppler velocimeter (ADV) utilized for data collection in the experiment.

3.3.2 Measurement uncertainty and data filtering

All parameters measured in any experiment include measurement uncertainty, typically expressed as a percentage of the measured values. Uncertainties in the data from the wave gauges and the ADV should be very minimal according to the instrument specifications (Table 7). These numbers, however, are expected to be slightly greater ($\approx$ 5-10%) under breaking waves, primarily due to the presence of air bubbles (Van Rijn, 2000).

One problem for the wave gauge WG2 and the ADV arose as the instruments were sometimes above the instantaneous water level during the passages of very deep wave troughs. For screening purpose, ADV data points were marked bad if the signal-to-noise ratios reduced by more than two standard deviations. The bad data, typically less than 3%, were then replaced with new values obtained from a spline fitted through the time series (Figure 8). Erroneous data points in the wave time series were found to be a negligible portion in any entire wave record (0.5% or lower). The wave time series were thus left unfiltered since such very rare occurrence would not bias the wave parameters beyond the measurement uncertainty.

Uncertainty in the bathymetric profiling was expected to arise primarily from bed ripples with a typical height of around 1 cm. Bathymetric measurement were repeated on two profiles to quantify the uncertainty. One was achieved by re-profiling the depth on

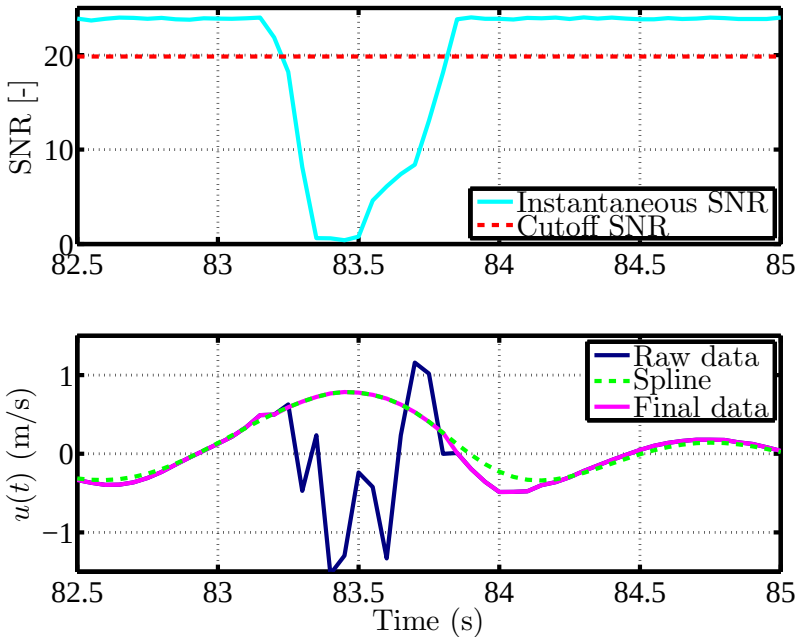

Figure 8: Example for screening and replacing bad raw ADV data. Data replacement is performed to the section where the signal-to-noise ratios (SNR) fall below the cutoff level.

the same centered line along the profile. The other was achieved by profiling the depths at three locations across the flume and taking an average value for every position along the profile. The two redundant data sets were then compared to the original profiling data set. Figure 9 shows the two comparisons based on the root-mean-square deviations in the profiling data. The maximum deviation was found to be around 0.8 cm, leading to an approximation of the uncertainty of ± 0.5 cm for the bathymetric profiling in general.

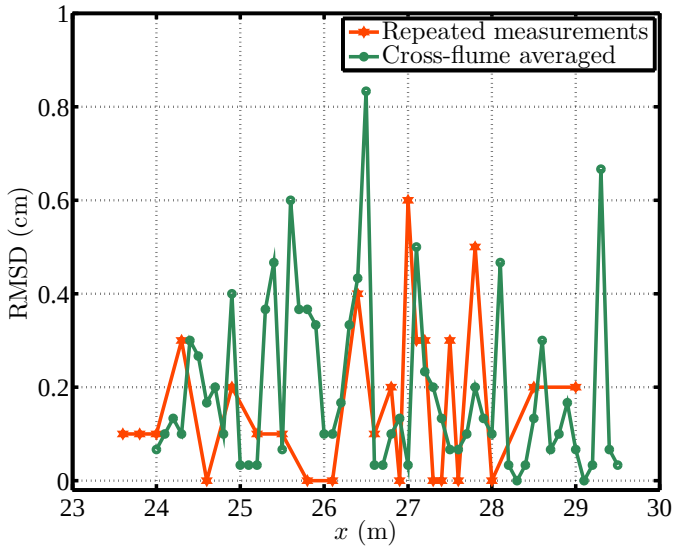

Figure 9: Root-mean-square deviations between originally measured data and repeated profiling data. Values were shown separately for each of the two redundant data sets available.

The sieve analysis in the experiment was conducted with the best care according to the ASTM standard. Since insufficient sieve motion was likely to be the biggest source of the uncertainty, the sieve shaker was initially operated for 25 mins but continued for another 10-15 mins each time after checking sediment passages in the sieves. In general, the uncertainty in the analysis is estimated to be around 5% in terms of the mean and the median grain sizes (e.g. Van Rijn et al. 2003), or around ±5 μm assuming the most probable maximum in the case of the fine sand (183 μm).

Table 7: Measurement resolutions and uncertainties in the data collected in the experiment. †Cea et al. (2004); ††Nortek (2004).

Instrument(s)	Type of data	Resolution	Uncertainty	Major sources of uncertainty
Wave gauges†	Water level time series	1 mm	≤ 1% of measured data	Signal conversion, inaccurate capacitance
ADV††	Instantaneous velocities	1 mm/s	≈ 1% of range (± 1 mm/s)	Doppler noise, echo intensity
Depth profiler	Bathymetry	1 mm	± 0.5 cm	Reading error, bed ripples
Sieves	Sediment size composition	1 μm	± 5 μm	Material loss, undersized retention

3.3.3 Wave reflection

Wave reflection affected the wave field in the flume and needed to be addressed prior to the data analysis stage. The aim here is to be able to separate the reflected waves from the incident waves for any given wave records. A dedicated setup for continuously measuring the reflection would be a solution but this was limited by equipment availability.

Alternatively, a predictive formula is utilized for the purpose, which is obtained by modifying and recalibrating an existing formula for regular waves on a plane beach (Sunamura and Okazaki, 1996). The new definition of the reflection coefficient for each i^{th} wave frequency component and the general form of the formula are given as

$$K^p_{r(i)} = \frac{S_R(i)}{S_I(i)} = A[1 - \exp(B \tan M)] \tanh\left[C\varphi(i)^D\right] \tag{6}$$

in which $K^p_{r(i)}$ is the predicted reflection coefficient as the ratio between the reflected and

the incident wave energies $S_R(i)$ and $S_I(i)$, respectively; A, B, C and D are the calibration factors; and M is the profile slope assumed to be plane from the profile toe to the still-water shoreline. The surf similarity parameter $\varphi(i)$ is defined as

$$\varphi(i) = \frac{M}{\sqrt{H_b(i)/L_o(i)}} \tag{7}$$

The offshore wave length $L_o(i)$ is known from the wave period and the offshore water depth. The breaking wave height $H_b(i)$ is solved by a simple iterative equation that computes wave shoaling on a beach profile constrained by $H_b = \gamma h$, with the breaking index γ equal to 0.6. The offshore wave heights are assumed to follow a Rayleigh distribution described on the basis of the spectral wave parameters. The formula was calibrated using data from nine dedicated test cases where the ADV was located offshore and the recorded velocity time series were analyzed for the reflection coefficients. The Iterative Maximum Likelihood Method (IMLM) by Pawka (1983), originally developed for directional wave spectra, was utilized for the analysis. With the flume application, the method resolved bidirectional-like energy contents that were taken as the incident and the reflected wave spectra. The calibration provides the best fit with the empirical coefficients A, B, C and D equal to 0.92, 19.8, 0.35, and 1.2 respectively.

Figure 10(a) shows the comparison between the reflection coefficients predicted using Equation (6) and those analyzed from the recorded wave data, yielding an r-squared value of 0.84. The linear line fit through the data reveals that the formula slightly underpredicts the coefficients. In Figure 10(b), typical wave spectra and reflection coefficients are shown together as a function of wave frequency. The observed reflection coefficients are found to be very high (up to 0.95) for less-energetic components at both ends of the spectrum and the performance of the formula is rather low for such wave frequencies. Nevertheless, the formula is shown to have the most important capability to resolve accurate reflection coefficients for the most energetic components, yielding the ratio of spectral wave height (reflected/incident) of 0.12 for this particular test.

After filtering out the wave reflection, the incident wave spectrum for each experiment at its equilibrium state was determined. For both H_{mo} and T_p (Figure 11), the influence

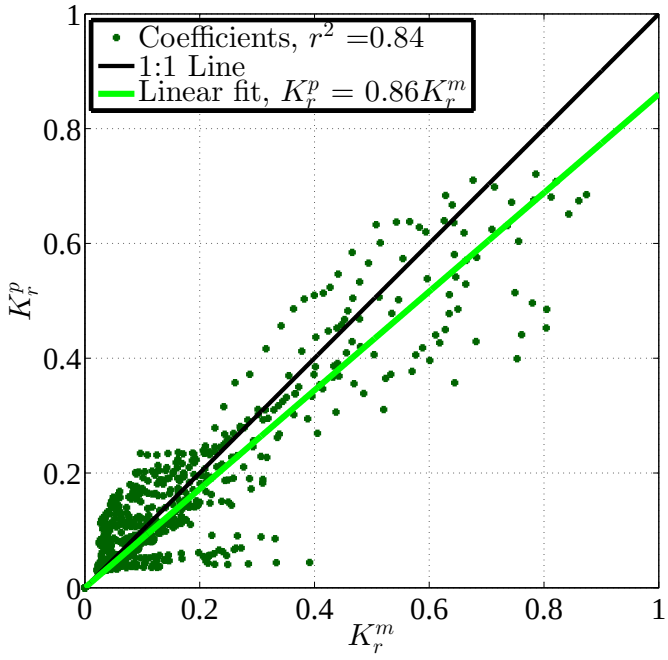

(a) Comparison between the observed (K_r^m) and the predicted (K_r^p) reflection coefficients (dimensionless) based on data from nine test cases.

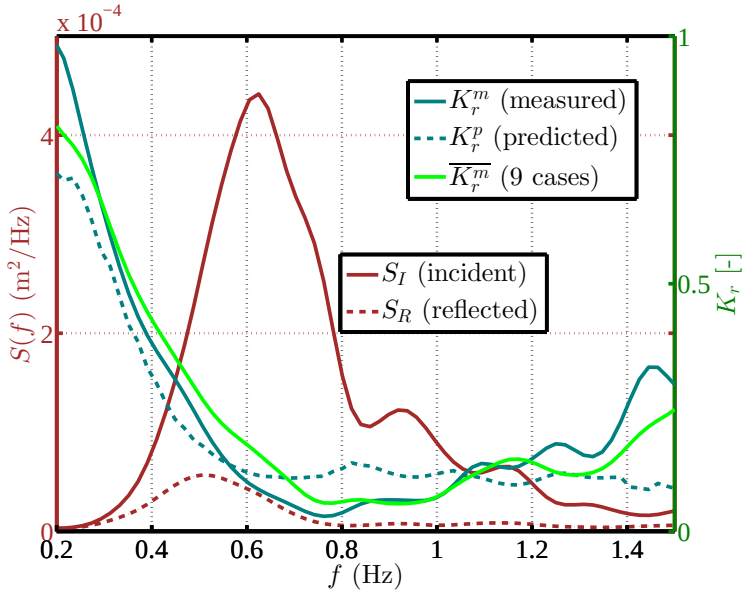

(b) Example of typical incident (S_I) and reflected (S_R) wave spectra and the reflection coefficients; the ratio of H_{mo} (reflected/incident) is 0.12 in this particular test.

Figure 10: Illustration of the wave reflection analysis showing (a) performance of the predictive formula for analyzing the wave reflection and (b) typical incident and reflected wave spectra found in the test cases.

of the wave reflection were found to be smaller than 5%, though this number could be somewhat greater in an earlier state with a steeper profile slope. The deviations of the measured wave parameters from the nominal values mostly originated from the uncertainty in the wave-generation process as mentioned earlier. It should be emphasized that these deviations did not bias any experimental objectives. The three wave spectra still represented reasonable values in the corresponding prototypes as well as the capabilities to provide the desired erosive, storm and accretive wave conditions.

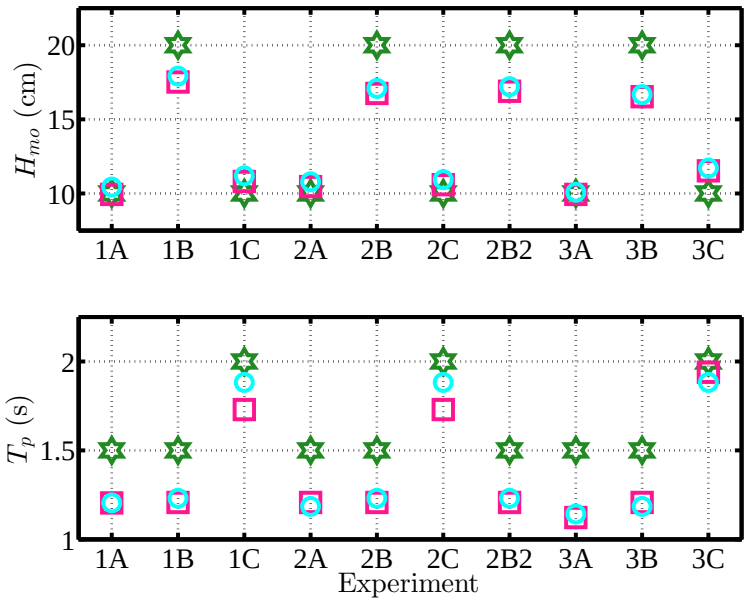

Figure 11: Spectral wave heights and peak periods measured in all of the experiments: green hexagons are the originally-designed values; cyan circles are the values before filtering out wave reflection; and magenta squares are the final values for the actual incident waves with wave reflection filtered out.

3.4 Profile evolution results

Cross-shore profile changes observed in selected experiments are illustrated in this section with the main emphasis on the resulting equilibrium profiles. To reassure the equilibrium state, the mean absolute bathymetric changes between the two surveyed equilibrium profiles in every test, conducted prior to and after the data collection, are compared to the mean absolute changes during the entire experiments in Figure 12. The mean changes at equilibrium were found to be up to 2-3 times smaller than the mean from the entire

durations; the maximum mean change at equilibrium is, in fact, equivalent to 7 mm which is below the profiling uncertainty (≈ 1 cm).

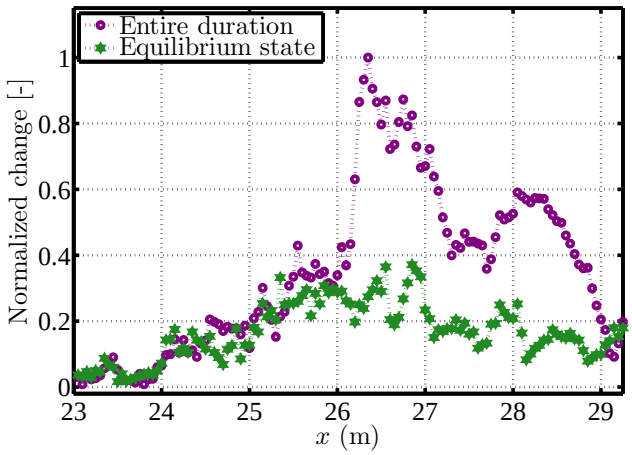

Figure 12: Comparison between the mean absolute profile changes during the experiments and at the equilibrium states. The values were computed based on all experiments and normalized against the maximum.

Figure 13 shows the profile evolution observed in the mixed-sand tests in Exp. Set 2. In Exp. 2A, with the erosive wave condition, the initially-plane slope evolved significantly during the first 70 mins leading to the maximum erosion around the shoreline and the formation of a bar structure. As the experiment continued for another 50 mins, the bar structure tended to migrate offshore and the profile continued to evolve, however, at a much smaller rate. The storm wave condition in Exp. 2B led to a much more severe erosion and likewise the bar structure became increasingly large before the equilibrium state was observed after 135 mins. Significant erosion was found at the highly-concave bar trough as a result of wave breaking where most collapsing wave fronts were tumbling down on the sediment bed.

The accretive wave condition in Exp. 2C resulted in a very obvious accretive-type profile. An onshore migration and deformation of the sandbar was observed as a result of the erosion at the initial bar crest. The accretion was mostly limited to the region around the existing bar structure; only slight deposition was observed offshore of the bar and almost no visible change occurred near the shoreline or in the swash zone. Non-breaking waves propagating over the initial bar structure are believed to be the major agent to this significant onshore sediment transport event. The longer wave period should also be associated with a reduced phase-lag effect that would otherwise allow a possibility of net offshore sediment transport over a wave cycle.

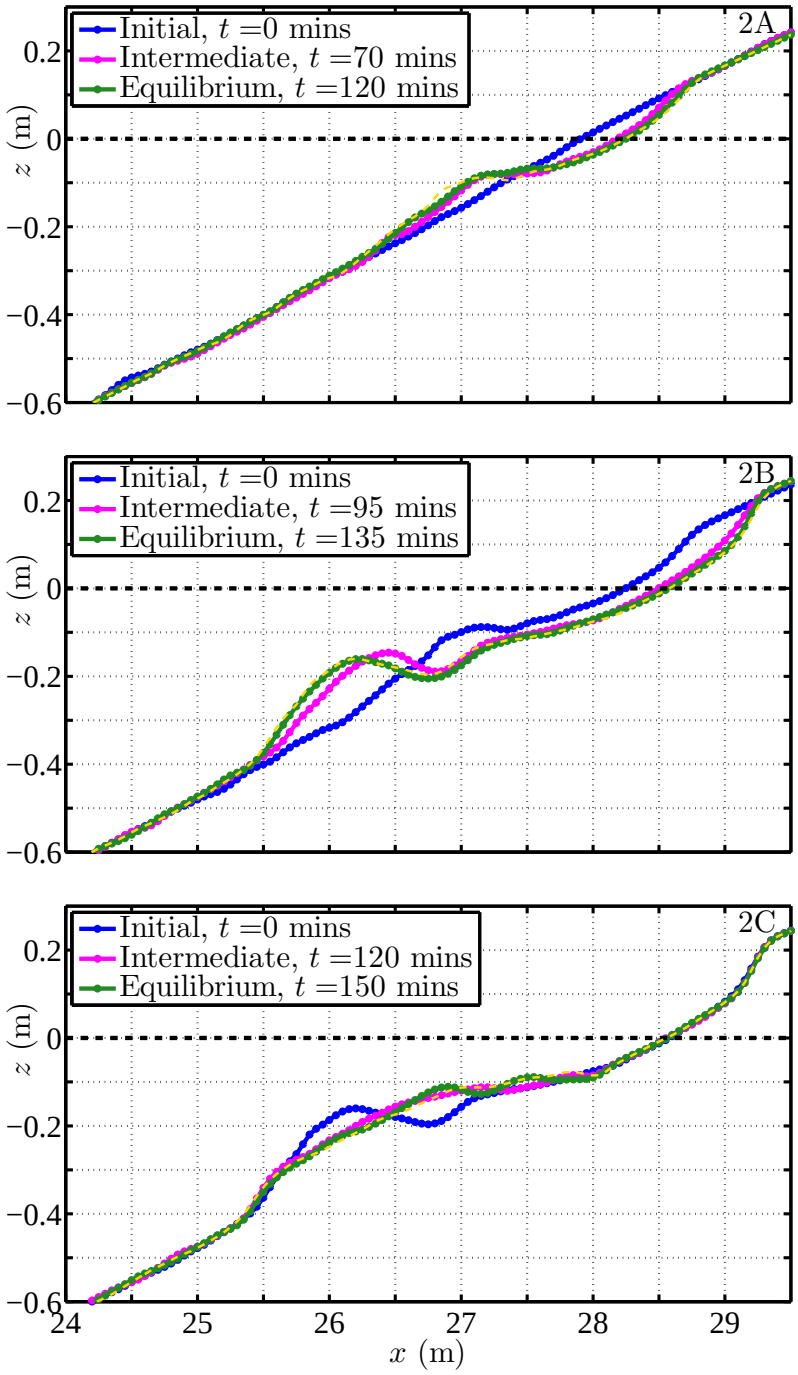

(a) Exp. 2A: H_{mo} = 10.5 cm, T_p = 1.21 s.

(b) Exp. 2B: H_{mo} = 16.8 cm, T_p = 1.21 s.

(c) Exp. 2C: H_{mo} = 10.5 cm, T_p = 1.73 s.

Figure 13: Sequential profile changes observed in Experiments 2A-2C. Yellow-dashed lines show the profiles re-surveyed after the hydrodynamic measurements, which confirm the equilibrium states.

The storm wave condition was repeated in Exp. 2B2 after the accretive test. Figure 14 shows that the resulting profiles from Exp. 2B and 2B2 appear to be very similar, considering the formation and the offshore migration of the sandbar. Nonetheless, additional erosion in the swash zone and a much flatter bar trough could be observed in Exp. 2B2. Such erosion is very likely a result of stronger backwashing in the swash zone, initiated by a larger wave runup because of the deeper initial water depth near the shoreline. Likewise, the flatter bar trough occurred due to an additional deposition contributed by the additional sand supplied from the swash zone. Based on this evidence, the shape of an equilibrium profile should also depend at least weakly on the initial profile in addition to the wave condition and the characteristics of the sediment bed.

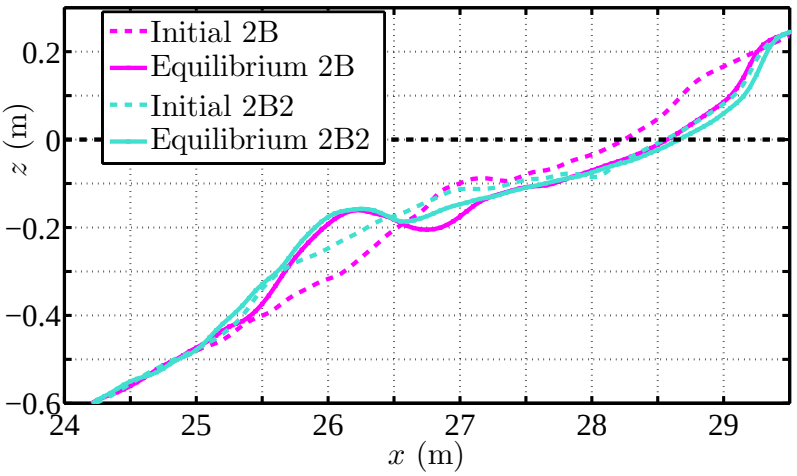

(a)

Exp.	**2B**	**2B2**
H_{mo} (cm)	16.8	16.9
T_p (s)	1.73	

Figure 14: Comparison between the two mixed-sand experiments under the storm wave condition: Exp. 2B with the initial condition from the erosive test (2A); Exp. 2B2 with the initial condition from the accretive test (2C).

Exp. 1A-1C, with the coarse sand, showed general trends of the profile evolution that are very similar to the above observed for the mixed-sand profiles. The resulting profiles from these two sets of experiments are compared in Figure 15. For the erosive and the storm wave conditions in Figure 15(a) and (b), the mixed-sand experiments show considerably greater erosion on the profiles extending from the bar troughs to the maximum wave run-up locations. The excess amounts of sand eroded from such areas therefore led to the formation of larger sandbars compared to those observed in the coarse-sand tests. Essentially, the differences between these two experiment sets can be attributed to a simple fact that the mixed sand featured a higher mobility due to the influence of the

fine sand that accounted for 50% of the mixture. This argument can also be supported by the resulting profiles under the accretive wave condition in Figure 15(c) where the more apparent onshore migration of the bar is observed in the mixed-sand test.

Figure 16 shows the sequential profile changes observed in Exp. 3A to 3C, the beach nourishment scenario that focused on the possible mixing between the coarse and the fine sands and its effects on the sediment transport. All of the experiments under this setting still resulted in profile changes that resemble the observations in the previous cases of the single-material profiles. The profile evolution under the erosive wave condition was observed only on the upper slope with the offshore end of the bar structure lying right at the toe of the fill slope. The subsequent storm wave condition led to a significant growth and offshore migration of the bar with the crest that located at the previous toe position. The bar structure is expected to be composed of a significant fraction of fine sand that would affect the sediment transport process in the succeeding simulation under the accretive condition (Figure 16(c)). Important findings in grain sorting in these tests are given together with those from the other experiments in Section 3.6.

3.5 Hydrodynamic results

Wave heights and mean currents measured in selected experiments are illustrated here as they are related to the resulting profile evolution and grain sorting. Information on mean water level is excluded since the typical range of wave setup and setdown at the measurement locations were found to be smaller than the estimated measurement uncertainty. More information and other hydrodynamic parameters are illustrated, discussed, and compared to the numerical model results in Chapter 4.

In each experiment, the wave gauge WG2 and the ADV were relocated to collect data at various locations along the profile. A particular problem arose for the ADV since the sensor probe has to be around 5 cm above its recording location but below the minimum water level under large wave troughs ($z \approx$-10 cm). This requirement restricted the ADV to be deployed only in the zone where the local water depth was greater than 15 cm. The total measurement duration on a profile was usually around 25 to 35 mins depending on the wave period, constrained by the need for recording at least around 100 waves at each

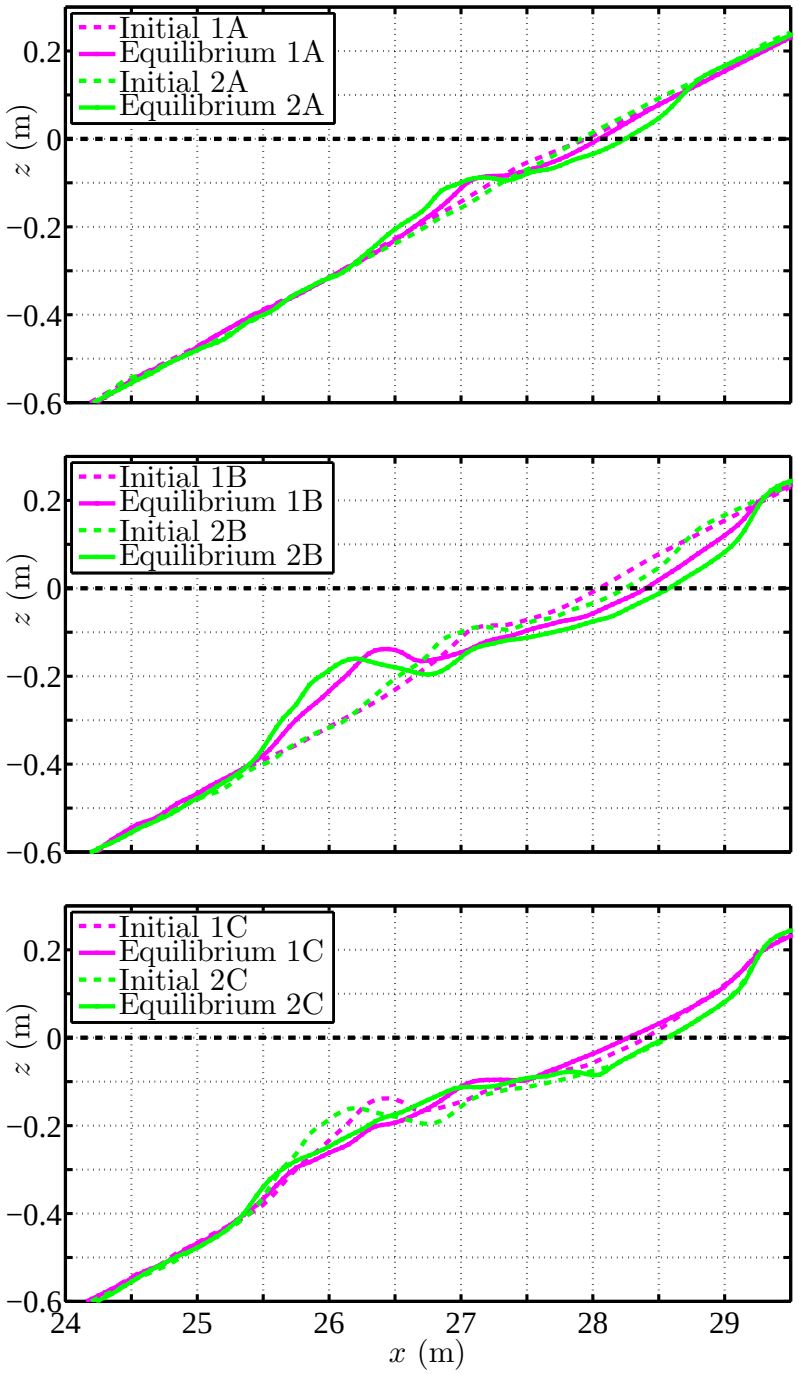

(a)

Exp.	**1A**	**2A**
H_{mo} (cm)	10.0	10.5
T_p (s)	1.21	

(b)

Exp.	**1B**	**2B**
H_{mo} (cm)	17.5	16.8
T_p (s)	1.21	

(c)

Exp.	**1C**	**2C**
H_{mo} (cm)	10.8	10.6
T_p (s)	1.73	

Figure 15: Comparisons on the resulting equilibrium profiles between the coarse-sand (Exp. 1) and the mixed-sand (Exp. 2) tests under identical wave conditions. A: Erosive wave, B: Storm wave, and C: Accretive wave.

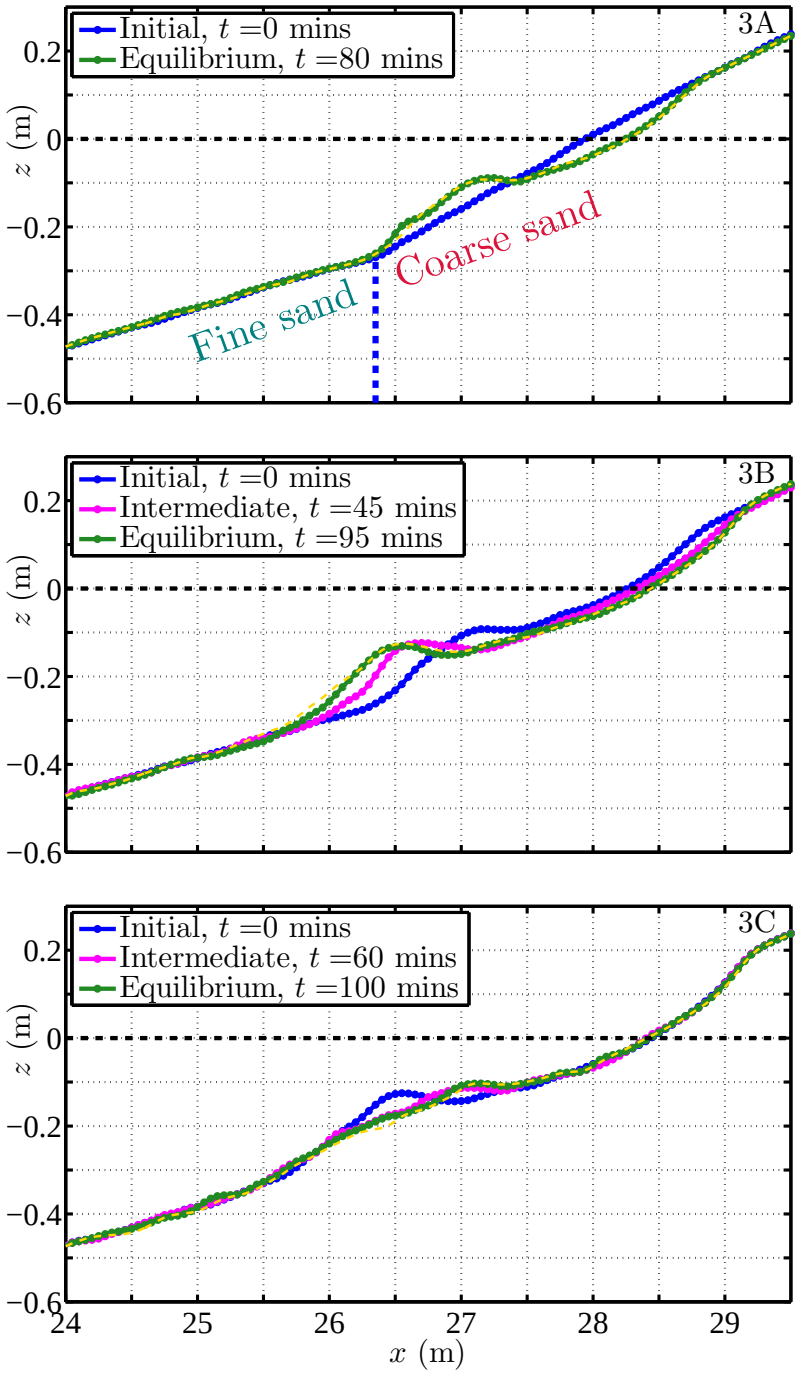

(a) Exp. 3A: H_{mo} = 10.0 cm, T_p = 1.13 s.

(b) Exp. 3B: H_{mo} = 16.5 cm, T_p = 1.21 s.

(c) Exp. 3C: H_{mo} = 11.5 cm, T_p = 1.93 s.

Figure 16: Sequential profile changes observed in Experiments 3A-3C. See Figure 13 for details.

individual location. The maximum wave run-up location is defined as the most shoreward position where the change on the bed profile could be observed.

Wave heights and mean velocities measured in Exp. Sets 2 and 3 are shown in Figure 17 and Figure 18, respectively. In Exp. 2A, the wave heights measured at the four locations ($25.7 \leq x \leq 27.0$ m) on the profile were all found to be very close to the incident wave height of 10.5 cm. Primarily, these consistent values are believed to be a result of equal effects from the frictional damping and the shoaling on the profile slope. The decrease of wave heights towards the shoreline could not be observed in such positions since they were offshore of the major wave break point on the sandbar, located around $x = 27.5$ m.

The pronounced bar structure in Exp. 2B led to much variation of the wave heights on the profile. The steep slope at the offshore side of the bar caused the waves to shoal, thus their heights increased. The decrease in the wave heights observed shoreward from the bar crest implies that some of the very large waves already broke on the sandbar. This decrease is however observed to be rather small since some of the waves might also shoal and began to break on the onshore side of the bar trough, where the slope started to be positive again. Beyond the trough area, most of the large waves had already broken leading to a much smaller value of the measured wave height. Exp. 2B and Exp. 2B2, both conducted under the storm wave condition, show a very consistent trend of the wave heights along the profiles.

Experiments 2A and 2C were carried out under the same spectral wave height but different wave periods according to the erosive and the accretive wave conditions, respectively. In Exp. 2C, the wave heights approaching the small bar crest shows a slightly greater effect of wave shoaling than observed in Exp. 2A. This difference between the two experiments occurred essentially as a result of the steeper slope and the longer wave period in Exp. 2C. The wave heights in Exp. 2C then tended to decrease beyond the bar crest location as would also be expected in Exp. 2A. Because of the more gradual wave breaking, the decrease of the wave heights in this case occurred much more slowly towards the shoreline than observed under the storm wave conditions in Exp. 2B and 2B2.

Under the erosive wave condition (2A), the maximum wave run-up location was found to be around x=28.7 m, yielding a horizontal wave run-up distance of approximately 0.5

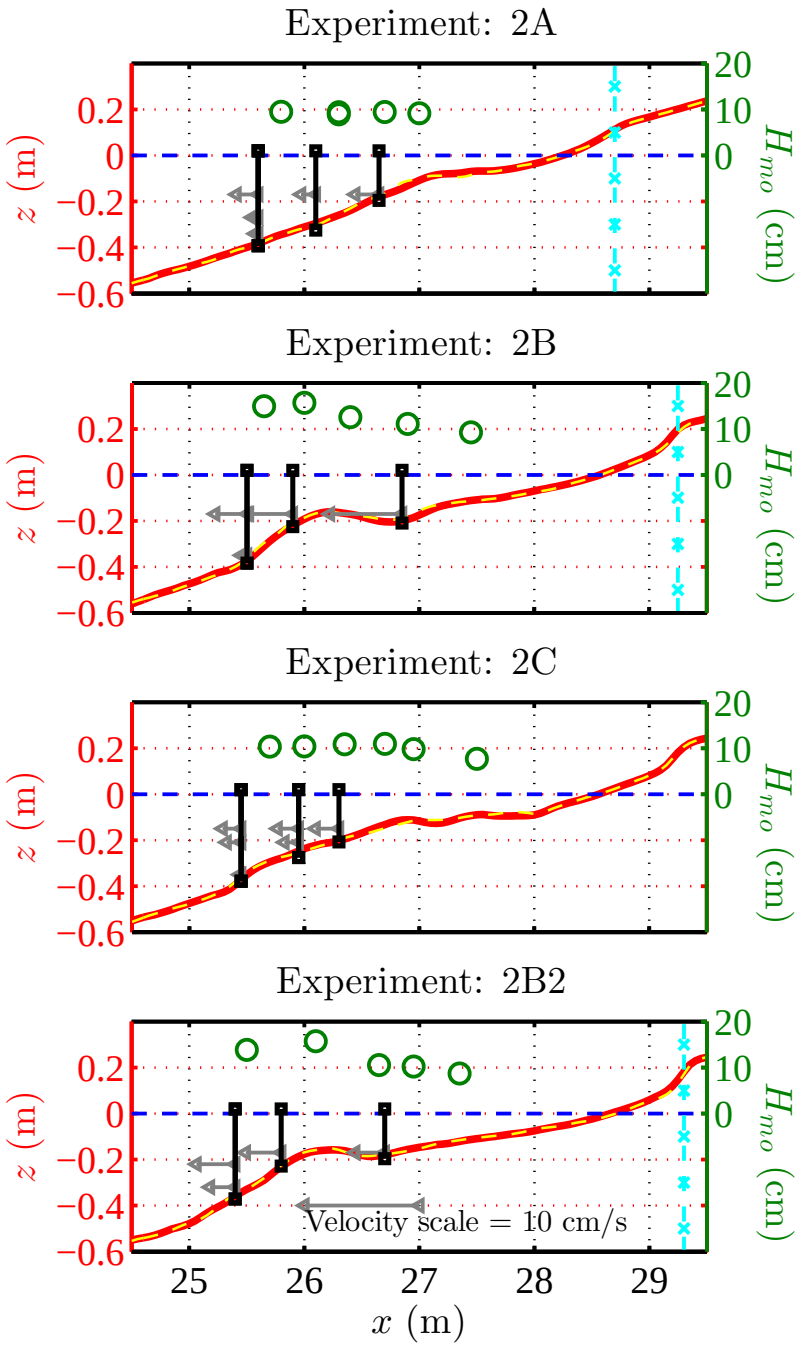

Figure 17: Wave heights and mean flow velocities measured in Exp. 2A-2B2. Solid-red and dashed-yellow lines plotted against the left axis show the profiles surveyed prior to and after the data collection. Circles plotted against the right axis show the wave heights. Arrows show the velocities following the scale shown in the bottom panel. Vertical cyan lines show the maximum wave run-up locations.

m. For the storm wave condition in Exp. 2B, these two numbers shifted to 29.2 m and 0.7 m, respectively. Note that the run-up distance increased less since the shoreline also retreated for an additional 0.3 m. The maximum wave runup for the accretive test in Exp. 2C could not be defined due to the lack of evident change in the dry part of the resulting profile. The repeated storm wave condition in Exp. 2B2 showed a very small onshore shift of the maximum run-up location ($\approx$ 5 cm) compared to that in Exp. 2B. Both of these experiments, however, showed the same numbers of horizontal and vertical run-up distances since a slight additional erosion around the shoreline also occurred in Exp. 2B2.

The mean velocities measured under the storm wave condition were generally larger than those observed under the smaller wave conditions, according to the relationship between the wave mass flux and the undertow magnitudes, among others. Most of the measurement locations were offshore of the major wave breaking positions due to the operational limitation of the ADV mentioned earlier. The velocities in this particular zone, measured around 20 cm below the water surface, showed quite consistent magnitudes even for some locations that were horizontally apart by up to one meter. These velocities were in the range of -4 to -5 cm/s for the storm condition and around -1 to -3 cm/s under the smaller wave heights, with negative indicating offshore-directed. The velocities measured at the same horizontal locations but closer to the bed always featured significantly smaller magnitudes that could be very close to zero, as expected. Under the storm wave tests, the ADV could be deployed in the bar trough locations. The near-bed velocities in these particular areas were found to be around -7 cm/s, considerably larger than the velocities observed at the locations further offshore.

The limited number of measurement positions may not be sufficient for resolving complete velocity profiles in the experiments. Even so, most available velocity data have shown the tendencies that follow the common theoretical description for undertow (e.g. Svendsen 2006). The magnitudes of the velocities inside the surf zone were all found to be significantly greater than those observed outside the surf zone. In this latter region, the consistent decreases of the velocities measured closer to the bed agree with a typical offshore undertow profile which is associated with stronger flows up high in the water column (Putrevu and Svendsen, 1993). A thorough discussion regarding undertow is given

in Chapter 4 where the velocity data are compared to the numerical modeling results.

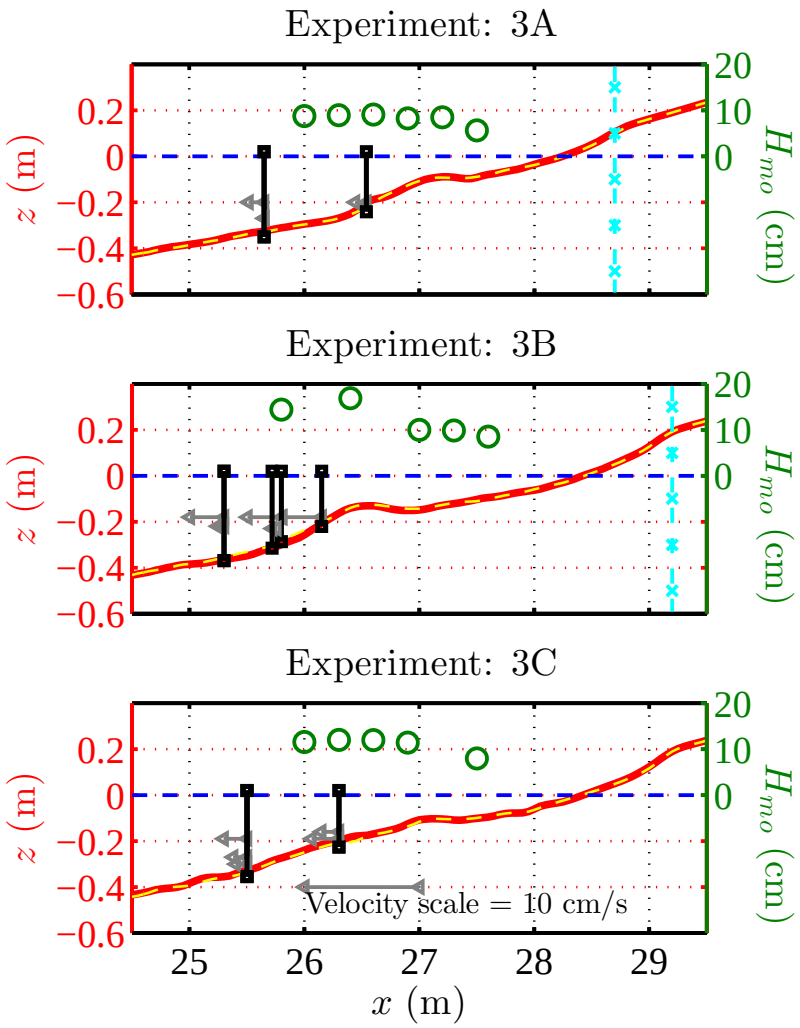

Figure 18: Wave heights and mean flow velocities measured in Exp. 3A-3C. See Figure 17 for details.

3.6 Grain sorting results

Sand grain sorting observed in each experiment is illustrated and discussed in this section based on the sieve analysis results of the sand samples collected at five particular locations along each beach profile (Table 8). The results were interpreted primarily in terms of the mean grain size (d_m) and the weighted-average standard deviation (σ_m). For all of the experiments, the characteristics between the bar-crest surface and subsurface samples were found to differ less than the estimated uncertainty (≈ 10 μm). Therefore, only the surface samples will be emphasized at the bar-crest locations.

Table 8: Sand sampling locations along each beach profile and their descriptions.

Location	Description
A: Still-water shoreline	The intersection between the still-water line and the profile.
B: Bar trough	The deepest location in the bar trough.
C: Bar crest surface	The shallowest location on the bar structure.
D: Bar crest subsurface	Beneath Sample C.
E: Offshore	The furthest location with an observed profile change.

3.6.1 Initially plane slopes: Experiment Sets 1 and 2

In Exp. 2 with the mixed sand, sand samples were collected and analyzed for all of the tests including the erosive (2A), storm (2B), accretive (2C), and repeated storm (2B2) wave conditions. For Exp. 1 with the coarse sand, the samples were collected only after the storm (1B) and the accretive (1C) wave conditions.

Figure 19(a) shows the changes of the mean grain sizes along the profiles after Exp. 2A and 2B. Starting from the plane slope with nominally-uniform mixed sand, the profile evolution after Exp. 2A led to a slightly decreased mean grain size at the still-water shoreline. The mean grain sizes at the bar trough and the bar crest locations were both found to increase with the latter showing a value of around 20 μm larger than the initial mean grain size (257 μm). The offshore sample featured a mean grain size that decreased around 35 μm from the bar-crest location despite being only about 1 m apart.

In Exp. 2B the shoreline sampling location was shifted onshore due to the shoreline retreat and the sample was shown to have been coarsened slightly. The sample at the bar trough was collected at a location very close to the previous bar crest location in Exp. 2A and the grain size change in such location was minimal. As the bar continued to grow and migrated offshore, the mean grain size at the bar crest increased by up to 25 μm compared to that of the previous bar-crest sample. A sharp decrease of the mean grain sizes between the bar-crest and the offshore locations was still observed in this case with the difference rising to around 40 μm.

Figure 19(b) shows the resulting grain size changes in the experiments conducted subsequently after the experiments shown in Figure 19(a). Note that the results from Exp.

2B are included in both illustrations for reference. After the accretive wave condition in Exp 2C, the variation of the mean grain sizes along the profile decreased noticeably from a 45-μm to a 25-μm range. The largest mean size was found switching to the bar-trough location. Meanwhile, the samples at the bar-crest location decreased from the previous test by up to 35 μm. The mean grain sizes at the shoreline and the offshore locations showed very small decreases that are less than the measurement uncertainty (± 5 μm).

In Exp. 2B2, the storm wave condition was repeated after the accretive test with the greatest interest in comparing its resulting profile and grain sorting to those in Exp. 2B. Like the final equilibrium profiles, the grain sorting trends between the two experiments were closely comparable despite having different initial conditions. The largest mean grain size was found to switch back to the bar-crest location and was within 10 μm of the value observed in Exp. 2B. The bar-trough and the bar-crest locations in Exp. 2B2 were identified to be twice closer to each other than they were in Exp. 2B. With this reason, the mean size of the bar-trough sample in Exp. 2B2 was only slightly smaller to the bar-crest sample, and much larger than that of Exp. 2B. Both the shoreline and the offshore mean grain sizes also changed, although very marginally, so that they approached the values observed in Exp. 2B.

The mean grain size changes in Exp. Set 1 with the coarse sand, not shown here, were observed to closely follow the tendencies found in Exp. Set 2. Figure 20 (a) and (b) compare the grain sorting characteristics along the profiles under the erosive and storm wave conditions in both Exp. Sets 1 and 2. The comparisons are based on the ratios between the mean grain sizes at the equilibrium and the initial conditions (d_m^E/d_m^I), and a similar ratio for the weighted standard deviations (σ_m^E/σ_m^I). This standard deviation ratio greater than unity indicates an increase in the size gradation in the mixture.

Regardless of different control conditions among the experiments, Figure 20(a) shows a clear agreement of the mean grain size changes over the five sampling locations. The grain size ratios start to increase from the shoreline location where the values are about unity, reach the maximum at the bar crest and decrease sharply to below unity again at the offshore location. Unsurprisingly, the ratios for Exp. 1B deviate very little from unity due to the narrow grain size distribution of the coarse sand. The standard deviation ratios

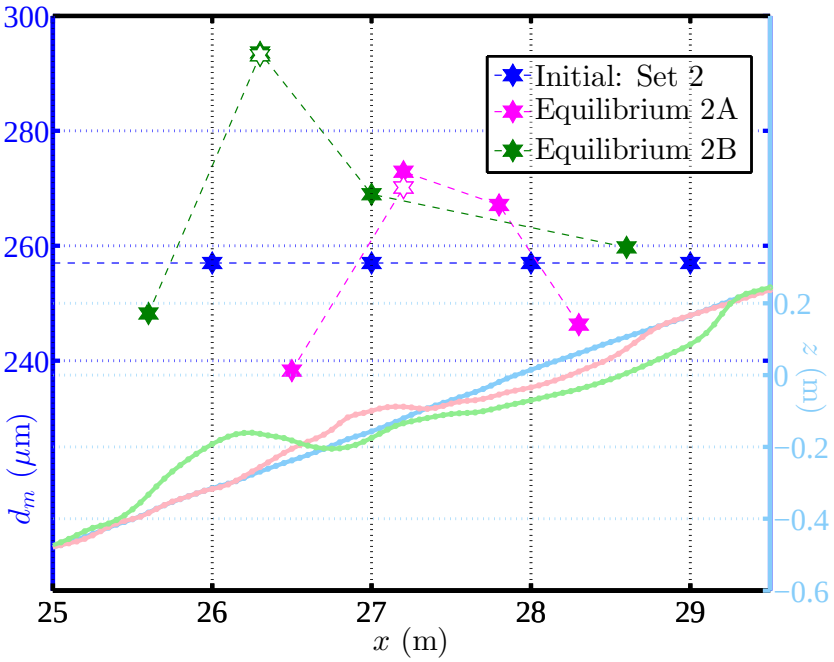

(a) Initial condition, erosive test (2A), and storm test (2B).

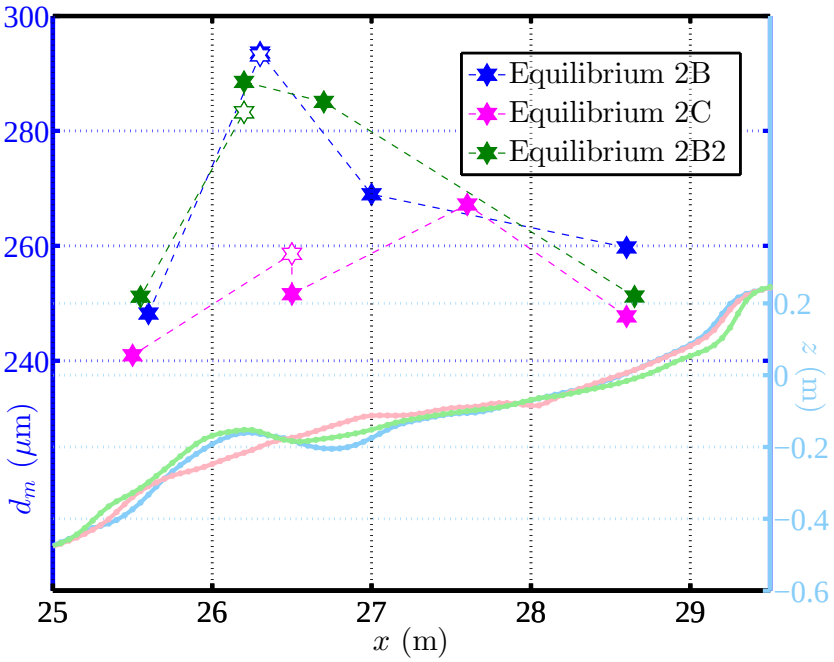

(b) Storm test (2B), accretive test (2C), and repeated storm test (2B2).

Figure 19: Mean grain size changes observed on the mixed-sand profiles in Exp. Set 2. The corresponding profile changes are shown against the right axis in the lighter colors. Hollow markers indicate the values found in subsurface samples.

shown in Figure 20(b) are found to be correlated to the mean size ratios with a correlation coefficient of 0.8. This tendency implies that the degree of size gradation of a mixture would be proportional to the coarsening degree in the grain-sorting process. Therefore, a finer mixture on the profiles under these wave and sediment conditions is more likely to be better sorted than a coarser mixture.

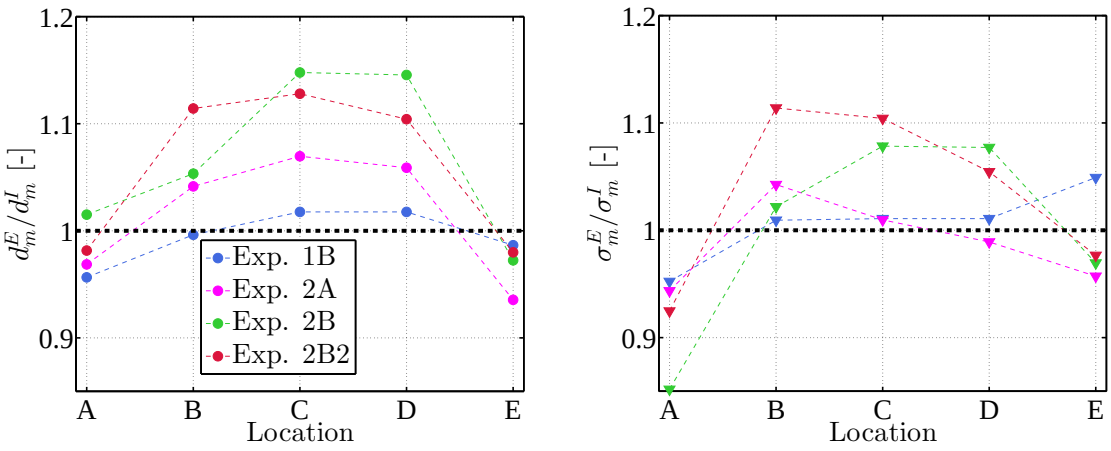

(a) Mean grain size ratios. **(b)** Standard deviation ratios.

Figure 20: Ratios of the mean grain sizes and the standard deviations between the sand samples collected on the equilibrium profiles and the initial mixtures in the erosive and the storm-wave tests of Exp. Sets 1 and 2.

The same ratios are shown in Figure 21 for Exp. 1C and 2C, the accretive tests in the coarse- and the mixed-sand experiments. In these cases, the mean grain size ratios of the shoreline samples lie closely below unity and only the values at the bar-trough locations are clearly greater than unity. The ratios at the bar-crest and the offshore locations were decreased in both experiments, with about 6 to 8% lower for the coarse-sand condition. In Figure 21(b), the ratios of the standard deviations between the two experiments are shown to be almost the same at the shoreline and the offshore locations. For the other three locations, while those for Exp. 2C remain below unity, the ratios for Exp. 1C are found to be up to 8% greater than unity. Among many possibilities, a greater reduction in the dominant size fraction (372 μm) in the coarse sand, which would widen the size distribution, is expected to be the primary cause of such difference.

In Figure 22, sediment size distribution changes as a result of profile evolution are shown for the erosive and the storm tests of Exp. 2, for samples collected at the four

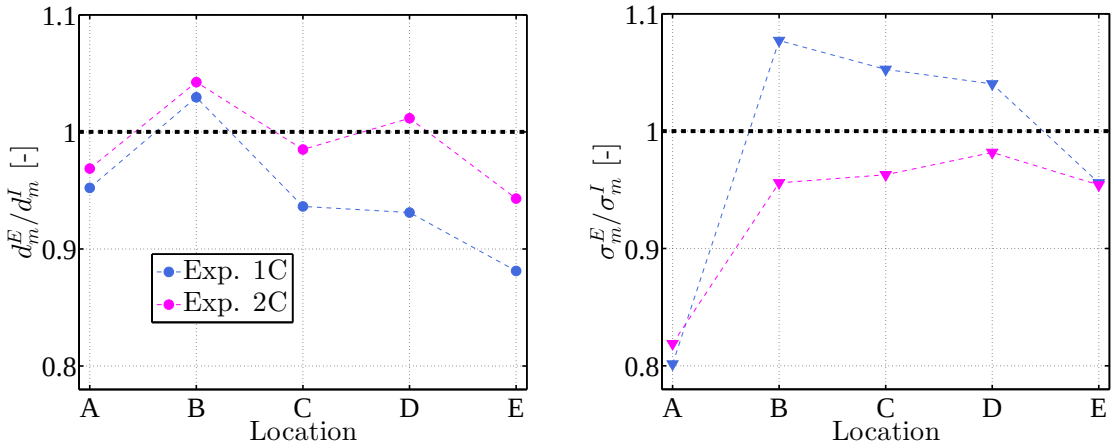

(a) Mean grain size ratios.

(b) Standard deviation ratios.

Figure 21: Ratios of the mean grain sizes and the standard deviations between the sand samples collected on the equilibrium profiles and the initial mixtures in the accretive tests of Exp. Sets 1 and 2.

surface locations A, B, C and E. The changes found in all of the shoreline samples were found to be small among the experiments except for Exp. 2B. In this case, a substantial reduction of the finer modal size fraction (176 μm) was found, likewise an increase of the coarser modal fraction (372 μm). This process might occur since it was the first storm-wave condition with the mixed sand at the shoreline that had not seen any change before.

For all of the experiments, the size distribution changes for both the bar-trough and the bar-crest samples were found to be qualitatively comparable. The three coarsest size fractions were found to increase slightly while the three finest fractions were observed to decrease by up to 5%. The major difference between the changes at the two locations is the greater increase of the 372-μm fraction in the bar-crest samples (up to 5%). Clearly, these opposite changes between the finer and the coarser size fractions led to the increases in the mean grain sizes shown earlier in Figure 20. The change at the offshore location in Exp. 2A, starting from an undisturbed mixed-sand slope, was found to be larger than those of the other two experiments.

3.6.2 Beach nourishment scenario: Experiment Set 3

In the beach nourishment scenario, sand samples were collected and analyzed after the storm wave condition (Exp. 3B) and the accretive wave condition (Exp. 3C), (Figure 23).

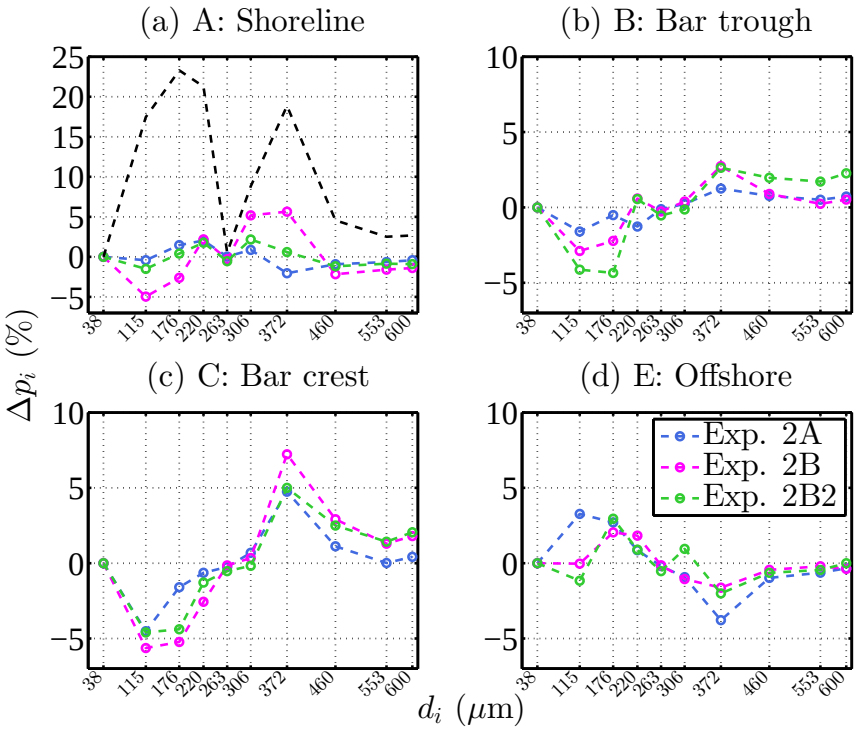

Figure 22: Size composition changes in the sand samples as a result of profile evolution in the mixed-sand tests. The numbers are simply the differences between the percent occurrences found at the equilibrium state and those of the initial mixed sand (black-dashed line in (a)).

The bathymetric profile changes in this experiment were observed to be very similar to the other cases of the single-mixture, initially plane slopes. An obvious bar-type profile was created after the storm-wave condition in Exp. 3B and the bar subsequently migrated onshore and partially deformed in Exp 3C. At first glance, these profile changes could possibly be perceived as a result of the sole transport of the coarse sand on the upper slope. If this is true, the grain sorting would only exist for the size fractions in the coarse sand alone. However, it will be shown according to the observation that the two types of sands were mixed and resulted in substantial changes in sediment size compositions on the beach profile.

The bar-trough and the bar-crest samples in Figure 23 are associated with smaller mean grain sizes than that of the initial coarse sand. This difference indicates that the fine sand in the outer region actually transported onshore and caused grain fining on this upper profile slope. A local degree of this fining process is likely to depend on the distance from the fine-sand slope, without which the bar-crest sample would almost certainly have been

substantially coarser than the bar-trough sample. This influence is also very obvious based on the offshore sample that appeared to feature a much large portion of the fine sand.

The mean grain size changes after the accretive test in Exp. 3C were found to be very similar to observed earlier for the coarse and mixed sand experiments. The largest mean grain size among the five locations was found to change from the bar-crest to the bar-trough locations. The bar crest samples became around 5% finer while the shoreline sample only showed a negligible change. The offshore sample was collected only about 0.5 m shoreward from the sample in Exp. 3B, which in fact could be identified as another bar-crest sample due to the length of the bar. Therefore, the mean grain size at this location appears to be almost the same as that of the bar-crest sample.

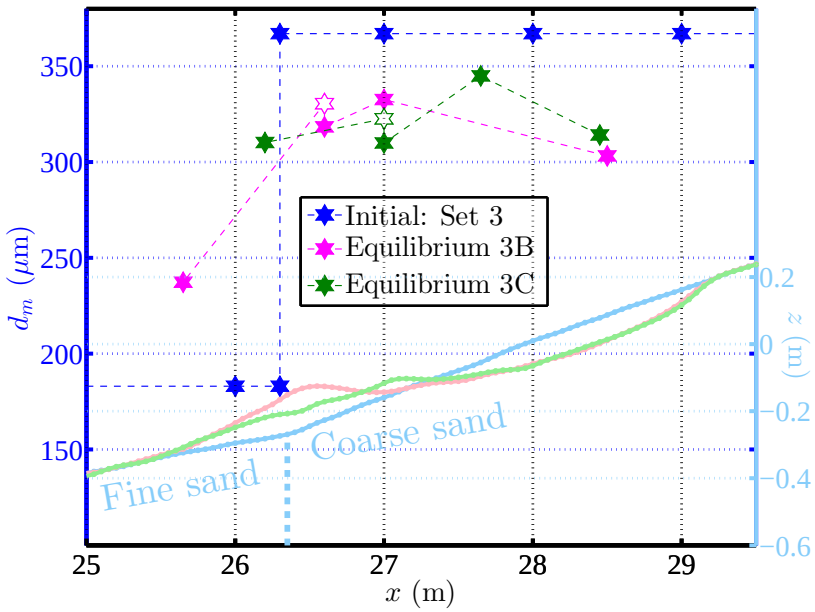

Figure 23: Mean grain size changes observed in the beach nourishment scenario. The profiles evolution corresponding to the sand samples are shown against the right axis with the lighter colors.

Figure 24 illustrates percent occurrence changes of all size fractions for four locations in Exp. 3B and 3C. At the shoreline location, the numbers for almost all size fractions are comparable between the two experiments with those in Exp. 3C having slightly lower changes. Note that the "mean" grain sizes in the two cases are almost identical despite these differences. The changes in the bar-trough and the bar-crest samples in both experiments were similar except for a lower reduction in the modal fraction (372 μm) in the bar-trough sample of the accretive case (Exp. 3C). These tendencies imply that this modal

fraction increased in the accretive case after it had been reduced previously under the storm wave condition. Unsurprisingly, the offshore samples in Exp. 3B featured very significant changes as the samples were collected very close to the intersection of the coarse and the mixed sand slopes.

The consistent reduction of the mean grain sizes on the upper profile might originate from either a loss of the coarse sand or an accumulation of the fine sand supplied from the lower native slope. Certainly a simultaneous occurrence of these two processes is the most likely scenario because the fact that the lower profile did not change implies that the materials on the two slopes were exchanging. The intensity in this grain mixing process appears to be proportional to the distance from the native slope. For example, the bar-crest samples on the erosive-type profile, typically the coarsest, were found to be generally finer than the bar trough sample that was further shoreward from the fine sand source.

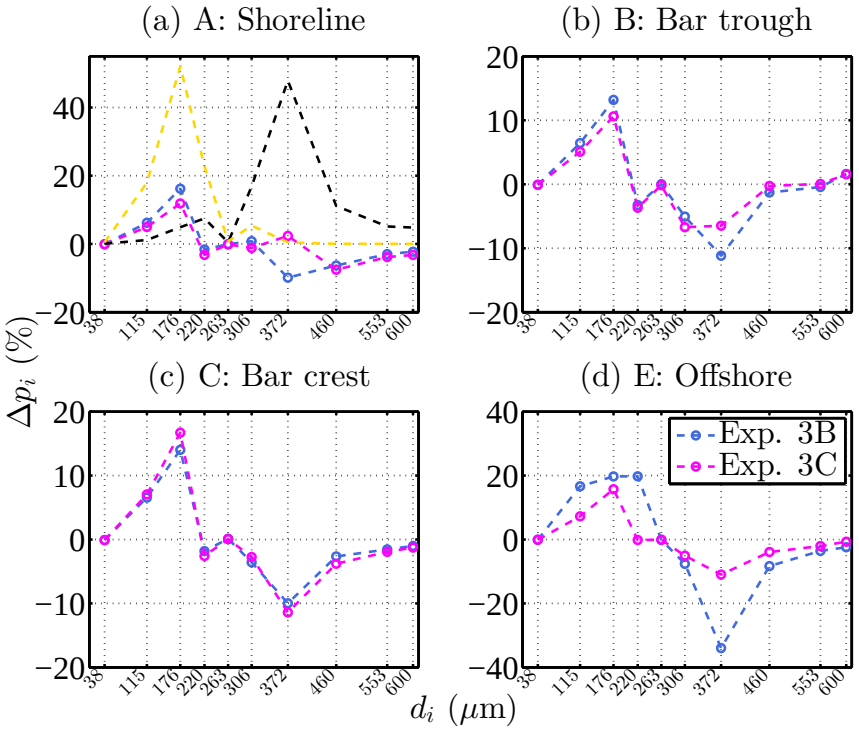

Figure 24: Size composition changes in the sand samples as a result of profile evolution in the beach nourishment tests. The numbers are simply the differences between the percent occurrences found at the equilibrium state and those of the initial sands, i.e. coarse sand: black-dashed line in (a); fine sand: yellow-dashed line in (a).

To prove the presence of the fine sand on the seemingly coarse-sand surface, one indisputable means is to investigate the sand samples for a size fraction that did not exist in the original coarse sand. In this case, the best choice would be the 115-μm fraction which accounted for 20% of the original fine sand. The percent occurrences of this size fraction in all of the collected sand samples are shown in Figure 25. The numbers in the figure show around 5-7% in most of the cases but as high as 17% for the offshore sample in Exp. 3B. These numbers should be interpreted with care since they do not inform any specific percentage of the fine sand or any certain degree of grain sorting between the two types of mixtures.

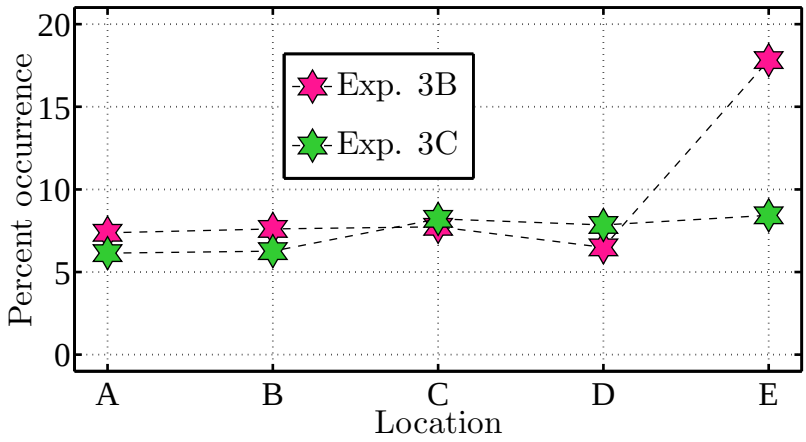

Figure 25: Percent occurrences of the 115-μm fraction in the sand samples collected at five locations along the beach profiles in Exp. 3B and 3C. These numbers indicate a contribution from the fine sand in the mixtures.

CHAPTER IV

NUMERICAL MODELING OF CROSS-SHORE HYDRODYNAMICS

The morphodynamic modeling system developed in this study was based partly on the Nearshore Community Model, funded thru the National Oceanographic Partnership Program. An overview of the system is shown in Figure 26. This chapter provides descriptions of the existing wave and current models and two new modeling components developed for the prediction of wave orbital velocities and swash zone hydrodynamics. Under the laboratory condition described in the previous chapter, important wave and hydrodynamic parameters are modeled and compared to the available data sets. Performance of the models after calibration are illustrated and the most optimal results are concluded for the utilization in modeling size-selective sediment transport in the next chapter.

4.1 Existing numerical models

4.1.1 Wave model: REF/DIF S

REF/DIF S (Kirby et al., 2005) is a phase-averaged spectral wave transformation model that accounts for combined refraction and diffraction, shoaling, and energy dissipation. The spectral wave field is simulated by means of a wave-by-wave approach superposing all individual random waves. Besides configuration options and bathymetry, a wave spectrum is the only wave input required in the model. The model is weakly nonlinear due to optional wave dispersion relations that consider wave-current interactions and waves in shallow water (Hedges, 1976). A forward scattered wave field is obtained in the model by solving the mild slope equation of Berkhoff (1972)

$$\nabla_h \cdot (CC_g \nabla_h A) + \sigma^2 \frac{C_g}{C} A = 0 \tag{8}$$

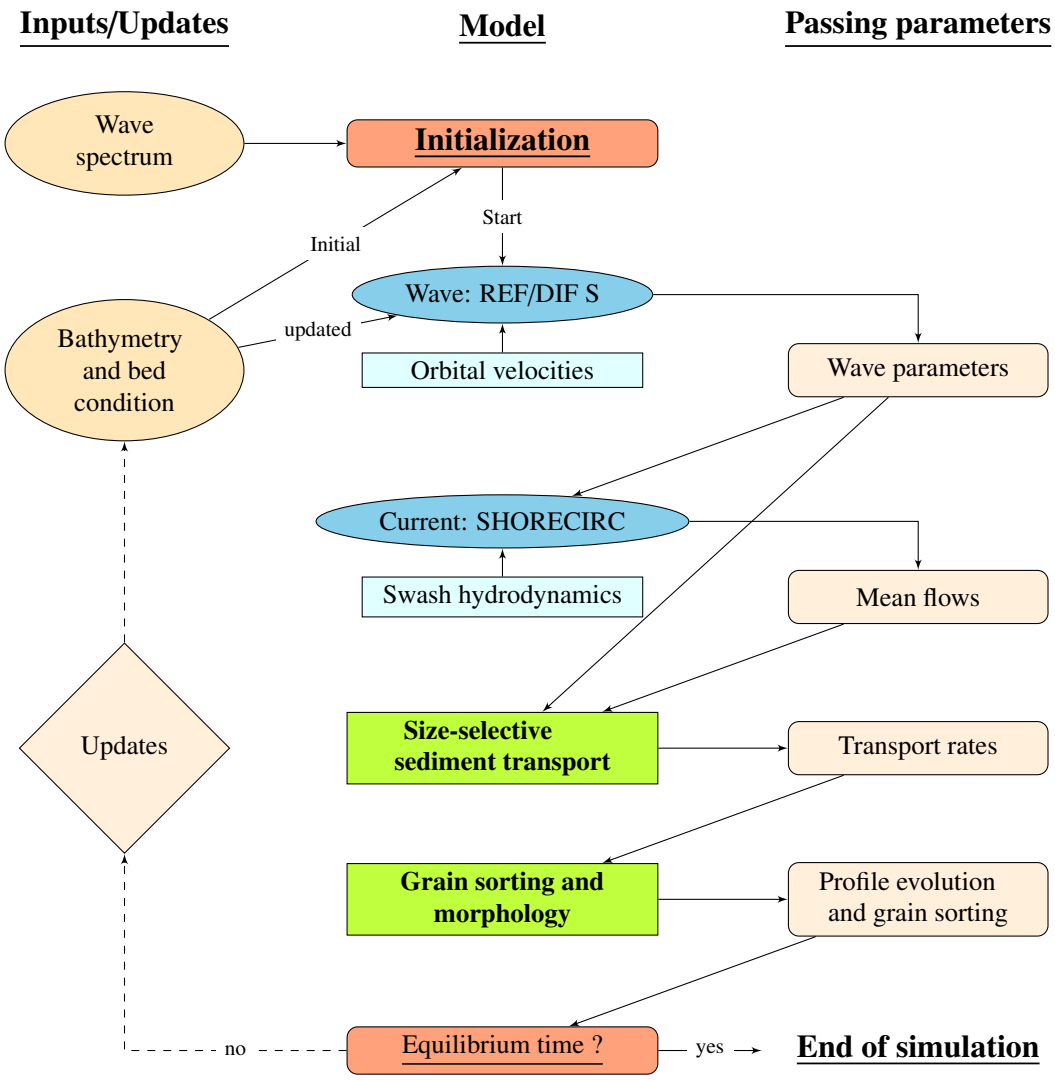

Figure 26: Overview of the numerical models that are integrated into the morphodynamic modeling system in this study. Rectangles indicate the components that are newly developed. The equilibrium time is based on the observation of an equilibrium state in the laboratory experiment.

where A is the complex wave amplitude; ∇_h is the horizontal gradient operator; σ is the angular wave frequency; C and C_g are the wave celerity and group celerity, respectively. The parabolic approximation by Kirby and Dalrymple (1983) is applied to solve Equation (8) using a finite-difference method with an implicit Crank-Nicholson scheme. For the cross-shore domain of interest in this study, wave shoaling and energy dissipation are the only influencing processes in the transformation of the wave field. Effects of surface wind, wave reflection, and wave-wave interaction are not considered in the model. For non-breaking waves, damping and shoaling of the waves are the counteracting mechanisms that

result in changing wave spectra. The damping is computed in terms of energy dissipation written in a linear form of the mild slope equation as

$$\frac{\partial A}{\partial x} = \Omega A \tag{9}$$

where Ω is the energy dissipation accounted for via the contributions of turbulent bottom boundary layer and the influence of sand bed permeability, given respectively in the following terms

$$\Omega = \frac{2\sigma k f_w |A| (1 - i)}{3\pi \sinh 2kh \sinh kh} + \frac{gkC_p(1 - i)}{\cosh^2 kh} \tag{10}$$

in which f_w is the wave friction factor and C_p is the coefficient of permeability. These two dissipation terms are active throughout the domain but the energy dissipation due to wave breaking becomes the dominant dissipation process inside the surf zone. An energy decay mechanism is included in the model for breaking waves following the energy balance equation

$$\frac{\partial EC_g}{\partial x} = -D \tag{11}$$

where E is the wave energy per unit width and D is the energy dissipation rate per unit area. This wave-breaking dissipation rate is calculated by averaging the dissipation of each broken wave, weighted by its breaking probability at the given wave height $P_b(H)$, which follows

$$D = \frac{\rho g B^3 \bar{f}}{4h} \int_0^\infty H^3 P_b(H)\, dH \tag{12}$$

where B is the breaking intensity with unity representing bore-like breaking and $\bar{f}$ is the mean wave frequency. Thornton and Guza (1983) applied the Rayleigh distribution function for estimating the wave breaking probability $P_b(H)$ which allows the fraction of

local wave breaking (Q_b) to be written as

$$Q_b = \frac{H_{rms}^2}{\gamma^4 h^4} \tag{13}$$

where γ is the breaking wave coefficient. To account for wave breaking history, Cambazoglu and Haas (2011) introduced a new method for the prediction of Q_b that includes "persistence length" of breaking waves over a certain distance where the waves still continue to break and dissipate energy. With the method, the energy dissipation equation is rewritten as

$$D = \frac{3\sqrt{\pi}}{16}\rho g B^3 \bar{f} \frac{H_{rms}^3}{h} Q_{b,tot} \tag{14}$$

where $Q_{b,tot}$ is the total fraction of wave breaking at a location that may exceed the local fraction due to the persistent breakers. It is recommended to refer to Cambazoglu and Haas (2011) for the derivation of this factor and further details of this method which is shown to predict the energy dissipation more accurately especially for bar-type beach profiles.

The mild slope equation is then solved with the above energy dissipation terms for the complex amplitudes of the waves. With the inclusion of the wave breaking roller, the cross-shore wave radiation stress S_{xx} and mass flux Q_{wx} in the model are computed including two separate components following

$$S_{xx} = \rho g \sum_{n=1}^{N} |A_n|^2 \left[\frac{C_{g,n}}{C_n} - \frac{1}{4} \right] + \rho \sum_{n=1}^{N} \frac{A_n' C_n^2}{L_n} \tag{15}$$

$$Q_{wx} = \frac{g}{2} \sum_{n=1}^{N} \frac{|A_n|^2}{C_n} + \sum_{n=1}^{N} \frac{A_n'}{T_n} \tag{16}$$

in which the subscript n denotes the wave frequency component; L_n is the wave length; T_n is the wave period; A_n is the complex amplitude; and A_n' is the surface roller area in the breaking wave. Each of the two terms on the right in these equations represents the contribution from non-broken waves and breaking wave rollers, respectively. Wave energy

flux E_{fx} was not originally computed in the model but can be determined using a similar form of equation according to Svendsen (2006), given as

$$E_{fx} = \rho g \sum_{n=1}^{N} |A_n|^2 C_{g,n} + \frac{\rho}{2} \sum_{n=1}^{N} \frac{A'_n C_n^2}{L_n} C_{g,n} \tag{17}$$

The roller area A'_n in the above equations is defined according to Lippmann et al. (1996) following

$$A'_n = \frac{D_n T_n}{\tan \sigma_r} \tag{18}$$

where D_n is the energy dissipation and σ_r is the angle between the roller slope and the horizontal, approximately $5^o - 10^o$. The energy dissipation D_n is computed following Equation (14) with a modified total fraction of wave breaking given as

$$Q_{b,tot}^{mod} = Q_{b,tot} + Q_{b,lag} \tag{19}$$

where $Q_{b,lag}$ is the fraction of breaking wave due to roller lag, also described in Cambazoglu and Haas (2011). The inclusion of this term aims to account for the fact that a wave breaking roller would require a "roller-lag" transitional distance before it reaches a fully developed stage (e.g. Nairn et al. 1990; Nairn and Southgate 1993).

4.1.2 Circulation model: SHORECIRC

SHORECIRC is a quasi-3D model that solves the depth-integrated, wave-averaged governing equations coupled with a set of analytical solutions to describe depth-varying nearshore currents. The total instantaneous fluid velocity in the model is defined to consist of three components, written in the cross-shore (x) direction only as

$$u_x = u'_x + u_{wx} + V_x \tag{20}$$

where the terms on the right hand side define contribution from turbulence, short wave motion, and mean flow, respectively. A definition sketch of parameters utilized in the

model is given in Figure 27. Accordingly, the total volume flux Q_x and the volume flux due to the wave motion Q_{wx} are defined following

$$Q_x = \overline{\int_{-h_o}^{\zeta} u_x \, dz} \tag{21}$$

$$Q_{wx} = \overline{\int_{-h_o}^{\zeta} u_{wx} \, dz} = \overline{\int_{\zeta_t}^{\zeta} u_{wx} \, dz} \tag{22}$$

where h_o and ζ are the local still water depth and the instantaneous water surface elevation, with ζ_t indicates the level at the wave trough.

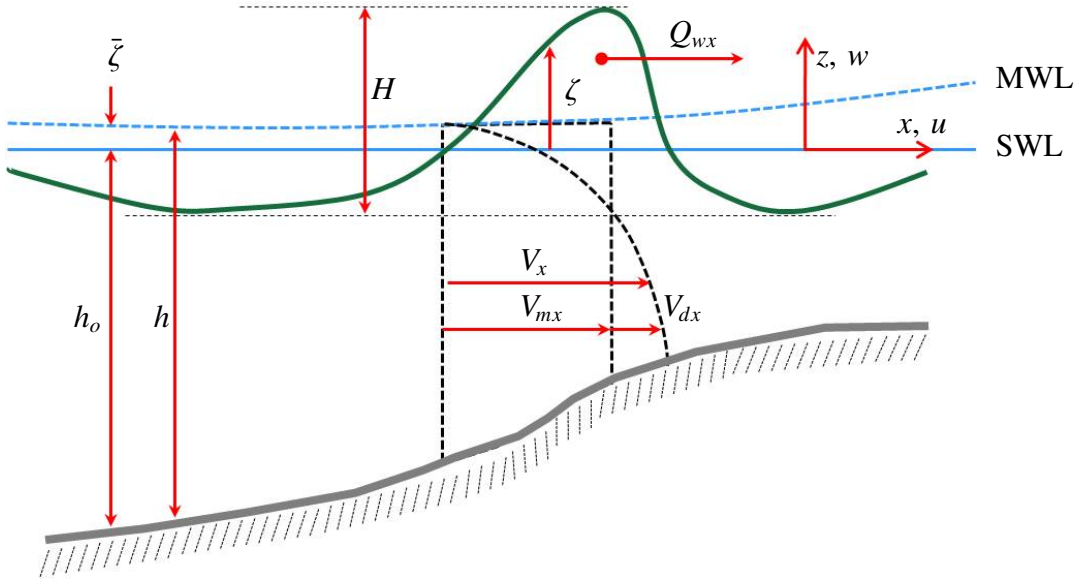

Figure 27: Definition sketch of the variables in the circulation model SHORECIRC.

The current velocity V_x in Equation (20) is again split into a depth uniform part V_{mx} and a depth-varying part V_{dx} as shown in Figure 27. For the cross-shore problem of interest in this study, the depth-integrated, wave-averaged continuity and momentum equations in the model can be written respectively as follows

$$\frac{\partial \bar{\zeta}}{\partial t} + \frac{\partial Q_x}{\partial x} = 0 \tag{23}$$

$$\frac{\partial Q_x}{\partial t} + \frac{\partial}{\partial x}\left[\frac{Q_x^2}{h}\right] + \frac{\partial}{\partial x}\overline{\left[\int_{-h_o}^{\zeta} V_{dx}^2\, dz\right]} + \frac{\partial}{\partial x}\overline{\left[\int_{\zeta_t}^{\zeta} 2(u_{wx}V_{dx})\, dz\right]}$$

$$+g(h_o+\bar{\zeta})\frac{\partial \bar{\zeta}}{\partial x} + \frac{1}{\rho}\frac{\partial}{\partial x}\left[S_{xx} - \overline{\int_{-h_o}^{\zeta} \tau_{xx}\, dz}\right] - \frac{\tau_x^B}{\rho} = 0 \tag{24}$$

where τ_{xx} is the turbulent stress in the water column, and τ_x^B is the bottom shear stress. The radiation stress S_{xx} is defined following

$$S_{xx} = \overline{\int_{-h_o}^{\zeta} (p + \rho u_{wx}^2)\, dz} - \frac{1}{2}\rho g h^2 - \rho\frac{Q_{wx}^2}{h} \tag{25}$$

where p is the total fluid pressure, including both hydrostatic and wave-induced components. The turbulent shear stress τ_{xx} is computed using a depth-uniform eddy viscosity formula

$$\tau_{xx} = 2\rho\nu_t\left(\frac{\partial V_{mx}}{\partial x}\right) \tag{26}$$

with the depth-uniform eddy viscosity parameter ν_t that accounts for both bottom friction and wave breaking effects, given as

$$\nu_t = C_\nu \kappa\sqrt{\frac{f_w}{2}}u_{o,b}h + Mh\left(\frac{D}{\rho}\right)^{1/3} + \nu_{t,0} + \nu_s \tag{27}$$

where C_ν and M are adjustable constants; κ is the von Karmann number; f_w is the wave-related friction coefficient; $u_{o,b}$ is the near-bed orbital velocity amplitude; D is the energy dissipation in Equation (9); and $\nu_{t,0}$ represents a constant background eddy viscosity. Turbulence with a scale smaller than the grid resolution is included in the Smagorinsky eddy viscosity

$$\nu_s = (C_s\Delta x)^2\sqrt{\frac{\partial V_x}{\partial x}} \tag{28}$$

where C_s is the Smagorinsky coefficient typically around 0.05 to 0.25. The cross-shore

bottom shear stress τ_x^B is estimated by time averaging of the combined wave and current contributions following

$$\tau_x^B = \frac{1}{2}\rho f_{cw}\overline{(u_{wx,b}(t) + V_{x,b})\left|u_{wx,b}(t) + V_{x,b}\right|} \tag{29}$$

where the subscript b denotes the near-bed values and f_{cw} is the wave- and current-related friction coefficient. In this equation, the instantaneous shear stress is phase-averaged to represent the mean quantity. The bottom shear stress due to steady streaming is also included in the model using the approximation by Longuet-Higgins (1956)

$$\tau_x^{B,str} = 0.1\rho f_{cw}\frac{H}{h}u_{o,b}^2 \tag{30}$$

The above governing equations are solved on a uniform grid using the Predictor-Corrector method by Wei and Kirby (1995). This particular technique is a central finite difference scheme that utilizes an explicit Adams-Bashford predictor and an Adams-Moulton corrector over the time steps. The method provides third-order accuracy in time and forth-order accuracy in space, except for the diffusion terms that are second-order accurate in space. Detailed information about the numerical scheme and its implementation in SHORECIRC can be found in Sancho and Svendsen (2000).

The solutions of the depth-averaged governing equations yield the depth-uniform mean flow (V_{mx}) and the mean water level ($\bar{\zeta}$). The depth-varying component of the velocity (V_{dx}) is subsequently obtained by solving the local wave-averaged, "depth-varying" horizontal momentum equation

$$\frac{\partial V_x}{\partial t} + V_x\frac{\partial V_x}{\partial x} + W\frac{\partial V_x}{\partial Z} + \frac{\partial}{\partial x}(\overline{u_{wx}^2}) + \frac{\partial}{\partial z}(\overline{u_{wx}w_w})$$

$$= -g\frac{\partial\bar{\zeta}}{\partial x} + \frac{1}{\rho}\left[\frac{\partial\overline{\tau_{xx}}}{\partial x} + \frac{\partial\overline{\tau_{xz}}}{\partial z}\right] \tag{31}$$

where W is the mean vertical current and w_w is the vertical part of wave orbital velocity. The last term indicates the viscous stresses. The solution for this equation is found by

assuming a quasi-steady flow and expressing Equation (31) in an eddy-viscosity formula (Putrevu and Svendsen, 1999). The solution is constrained by two boundary conditions; one for matching the bottom shear stress and the other for the condition of the depth-varying part of the current, which follow

$$1) \quad \nu_t \frac{\partial V_{dx}}{\partial z}\bigg|_{z=-h_o} = \frac{\tau_x^B + \tau_x^{B,str}}{\rho} \quad ; \text{ and } \quad 2) \quad \int_{-h_o}^{\bar{\zeta}} V_{dx}\, dz = 0 \tag{32}$$

where $\tau_x^{B,str}$ is the steady-streaming stress shown in Equation (30). A perturbation method is then introduced to allow analytical derivation of the depth-varying velocity, divided into two solution orders

$$V_{dx} = V_{dx}^{(0)} + V_{dx}^{(1)} \tag{33}$$

A number of lengthy steps are involved with the solutions of these velocity terms and their use in solving the eddy-viscosity equation. These steps are explained in detail in Haas and Svendsen (2000). A simplified version of the eddy-viscosity formula is shown in Equation (37) in the next section as the physical implication of each momentum term is explained.

4.2 Laboratory wave and current modeling

Under the laboratory conditions described in Chapter 3, REF/DIF S and SHORECIRC were utilized to model wave and current parameters that are required for the sediment transport model. A uniform numerical grid of 5-cm resolution was utilized in both models, spanning from the offshore wave gauge (WG1 @ x=12 m) to the flume wall (x=30 m). Wave data collected at the offshore gauge were specified as the input wave spectra with predicted wave reflection filtered out (see Section 3.3.3). An absorbing-generating offshore boundary condition was specified with a no-flux condition at the shoreline, defined at a minimum depth $h_{min} = {}^1\!/_3\, H_{mo}^{\text{incident}}$. The swash zone model that is employed shoreward from this location is illustrated later in this chapter.

Calibration of the adjustable parameters in the models was performed for each of the three wave conditions to optimize the modeling results. Some of these important parameters and their values are shown in Table 9. Mostly, values of these parameters

close to recommended in the models yielded optimal simulation results, except for the friction factors that needed to be greater than the suggested values by around five times in REF/DIF S (f_w) and up to nine times in SHORECIRC (f_{cw}).

Table 9: Values of semi-empirical parameters in wave and current models (REF/DIF S and SHORECIRC) for the simulation under the present laboratory conditions.

Parameter	Typical value	Value used for each wave condition			Description
		(A)	(B)	(C)	
B (Eq. 12)	≈ 1	0.9	0.8	1	Breaking intensity
B_o (Eq. 36)	0.04-0.125	0.11			Surface shape parameter
σ_r (Eq. 18)	5^o-10^o	5			Wave roller angle
f_w (Eq. 10)	0.2-0.4	2.0			Friction factor (wave)
f_{cw} (Eq. 29)	0.005-0.03	0.27		0.17	Friction factor (wave+current)
M (Eq. 27)	0.05-0.1	0.05	0.025		Viscosity coefficient (1)
C_v (Eq. 27)	0.08	0.16	0.08	0.16	Viscosity coefficient (2)

The above requirement for the friction factors is believed to be an effect of extensive frictional damping on the waves due to a narrow width, with the side walls not included in the simulation, and a considerably rough, concrete bottom of the flume. As evidence, measured waves heights were found to decrease as much as 20% after propagating around 12 m from the incident wave gauge to the first wave measurement location on a profile. Figure 28 shows general comparisons between the modeled and the measured wave heights and current velocities for Exp. 2A, 2B and 3C. Similar comparisons are illustrated in this section based on nine of the ten experiments as Exp. 1A was excluded due to its lack of experimental data. The wave condition in each experiment is recapitulated in Table 10 below for convenience; full experimental description may be found in Table 6, Chapter 3.

4.2.1 Wave parameters

Water level time series recorded in all experiments were analyzed for spectral wave heights (H_{mo}) via a frequency-domain analysis and significant wave heights (H_s) via a time-domain analysis and the average difference between the two parameters was found to be only around 3%. An excellent agreement between the modeled and the measured wave heights

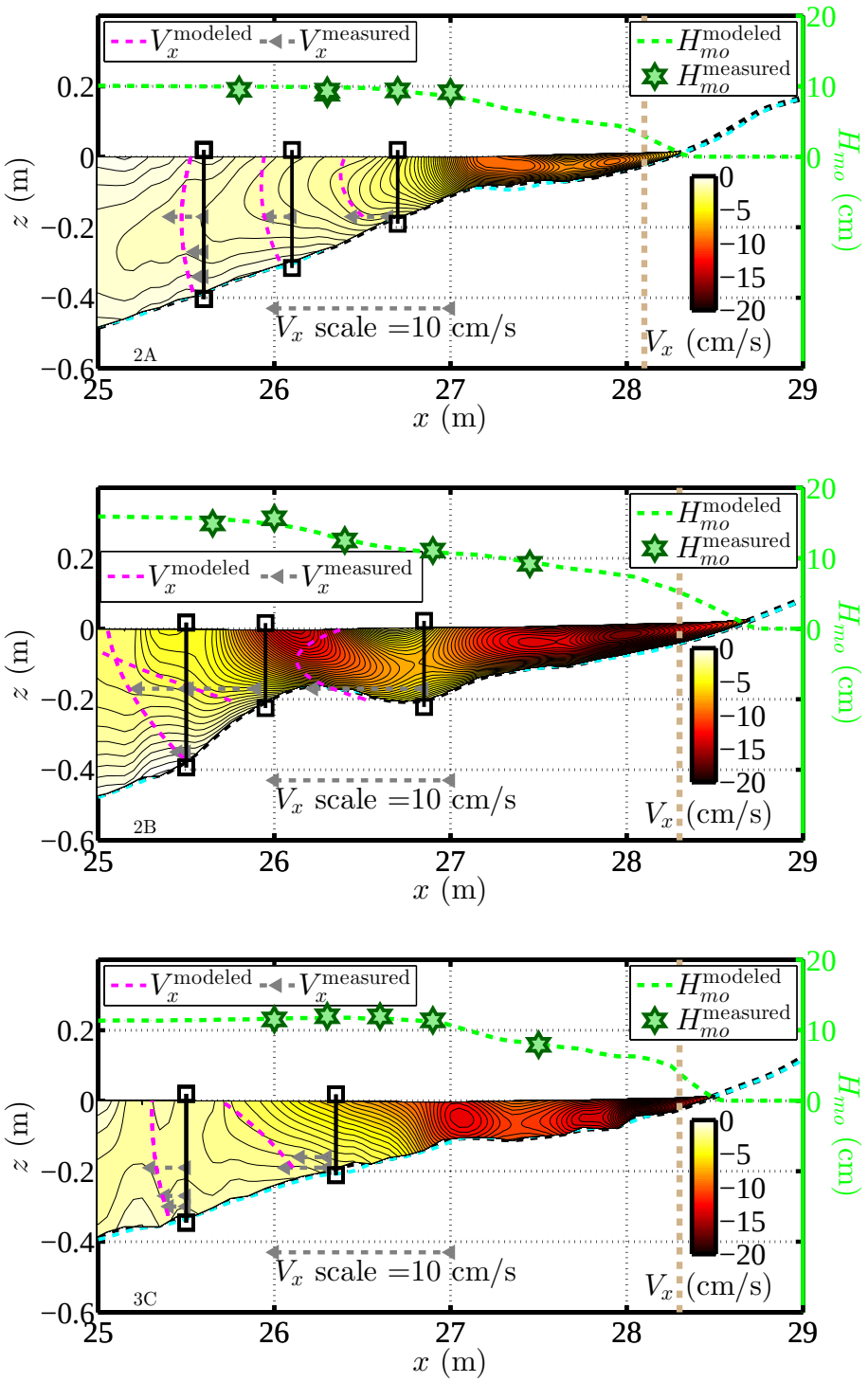

(a) Exp. 2A: H_{mo} = 10.5 cm, T_p = 1.21 s.

(b) Exp. 2B: H_{mo} = 16.8 cm, T_p = 1.21 s.

(c) Exp. 3C: H_{mo} = 11.5 cm, T_p = 1.93 s.

Figure 28: Modeled and measured wave heights and mean currents in Exp. 2A, 2B and 3C. Wave heights are plotted against the right axis. Contours show the modeled currents. Measured currents velocities shown in gray arrows are compared to modeled currents shown in magenta lines extracted from the contours. Velocity scale is shown in the bottom of each panel and vertical brown lines show the last grid points defined in the surf zone models (REF/DIF S and SHORECIRC). Cyan lines show bathymetric profiles from the repeated surveys after data collection.

Table 10: Wave conditions in the physical model tests that are considered in the validation of the wave and hydrodynamic models.

Experiments ↓	Wave condition	H_{mo}†(cm)	T_p†(s)
2A, 3A	Erosive	10	1.5
1B, 2B, 2B2, 3B	Storm	20	
1C, 2C, 3C	Accretive	10	2

† Nominal values; measured values will be shown with the result in each illustration.

can be observed in Figure 28. Figure 29 shows a comparison between these two types of data based on all of the available experiments. The mean absolute difference in the comparison was found to be only around 6.5%. A straight line fit through the data features a slope of 0.98, i.e. H_{mo}^{modeled}=0.98H_{mo}^{measured}, which implies a negligible underprediction trend of the wave heights in the model. The model also tended to show better accuracy for smaller wave heights that were likely obtained from the cases with smaller cross-shore variation of the waves in the flume.

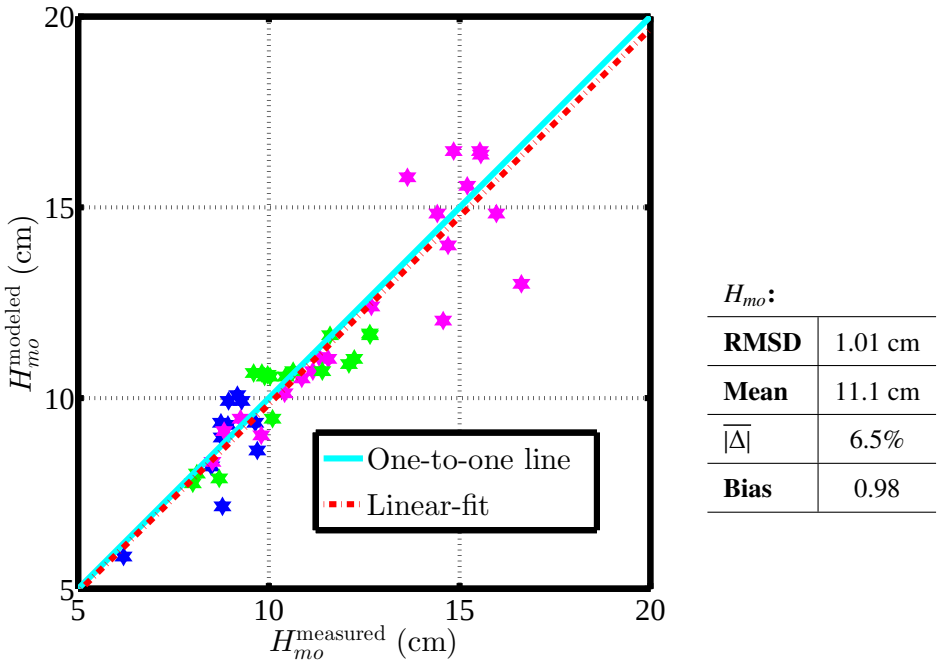

H_{mo}:	
RMSD	1.01 cm
Mean	11.1 cm
$\overline{\lvert\Delta\rvert}$	6.5%
Bias	0.98

Figure 29: Comparison between measured and modeled wave heights based on all available experiments. Blue markers: erosive waves; Magenta markers: storm waves; Green markers: accretive waves. **RMSD** is the root-mean-square difference; **Mean** is computed from the measured data; $\overline{|\Delta|}$ is the mean absolute difference. **Bias** is the slope of a straight line fit through the data being compared; a value less than unity indicates underestimation in the model.

Besides the wave heights, three of the most important parameters obtained in the wave model include the wave radiation stress (S_{xx}), volume flux (Q_{wx}), and energy flux (E_{fw}). Each of these parameters consists of non-broken wave and wave-breaking roller components as shown earlier. Based on measured wave spectra, the non-broken wave parts can be estimated using the following equations that express the parameters in terms of wave spectral energy

$$S_{xx}^{\text{estimated}} = \rho g B_o \int_{f_L}^{f_H} S_\eta(f) \left(\frac{2C_g(f)}{C(f)} - \frac{1}{2} \right) df \tag{34}$$

$$Q_{wx}^{\text{estimated}} = g B_o \int_{f_L}^{f_H} \frac{S_\eta(f)}{C(f)} df \tag{35}$$

$$E_{fx}^{\text{estimated}} = \rho g B_o \int_{f_L}^{f_H} S_\eta(f) C_g(f) df \tag{36}$$

where $S_\eta(f)$ is the surface wave energy (m^2/Hz); f_L and f_H are the low and the high frequency cut-off limits to eliminate noise. The surface shape parameter (B_o) equal to 0.115 in the model is also applied in these equations, compared to the values of 0.125 and 0.083 for linear and saw-tooth waves, respectively. Figure 30 shows the parameters estimated from the measured wave spectra by the use of these equations, compared to the modeled results.

For all of the three parameters, S_{xx}, Q_{wx} and E_{fx}, the modeled results of the non-broken wave parts and the spectral estimate values only show about 10% differences in terms of the mean absolute errors. The model shows a tendency in slightly underpredicting the parameters, around 6% according to the computed biases. Figure 30 also shows that the roller components of the parameters could be up to twice greater than the non-broken wave components under the storm wave condition. This intensive roller contribution originated mainly from the energy dissipation factor (D_n) used in the computation of the roller area. Basically this factor is proportional to a power of the relative wave height (e.g. H_{rms}/h in Equation (13)) which is generally much greater under the storm wave condition compared

to the other two smaller wave conditions. This roller contribution cannot be validated with the available wave energy spectra that were derived from the heave time series of random waves.

4.2.2 Depth-varying currents

As mentioned earlier, SHORECIRC utilizes a simplified eddy viscosity formula for resolving depth-varying velocities analytically. This eddy viscosity formula consists of momentum balance terms that can be quantified for investigating their influences on the velocity profiles in the model (e.g. Haas and Warner 2009), given as

$$\underbrace{\frac{\partial}{\partial z}\left(\nu_t \frac{\partial V_{dx}}{\partial z}\right)}_{\text{vvisc}} = \underbrace{g\frac{\partial \bar{\zeta}}{\partial x}}_{\text{prsgrd}} + \underbrace{V_x \frac{\partial V_x}{\partial x}}_{\text{hadv}} + \underbrace{W\frac{\partial V_x}{\partial z}}_{\text{vadv}} + \underbrace{\left(\frac{\partial \overline{u_{wx}^2}}{\partial x} + \frac{\partial \overline{u_{wx} w_w}}{\partial z}\right)}_{\text{wforc}} \tag{37}$$

The terms in this equation represent viscosity (vvisc), pressure gradient (prsgrd), horizontal advection (hadv), vertical advection (vadv) and wave forcing (wforc). All of these momentum terms are depth-uniform but the depth-varying velocity (V_{dx}) insides the second-order derivative term is parabolic. Figure 31 shows the values of these terms that vary along the profile in Exp. 1B, which result in different curvatures of the local currents.

In Figure 31, the surf zone can be roughly identified as the region shoreward from the bar crest. Along most of the profile, the two dominant momentum terms are the pressure gradient (prsgrd) and the wave forcing (wforc). Outside the surf zone, the wave setdown leads to a negative pressure gradient but the wave forcing is positive since the shoaling wave initiates an increase in the radiation stress. Inside the surf zone, the variations of these two terms are opposite. The pressure gradient for wave setup is positive and the wave forcing term is negative due to wave breaking. Due to the shoaling of some smaller waves, the magnitudes of both terms decrease significantly around the onshore side of the bar trough as observed in Figure 31.

A negative pressure gradient results in a quadratic mean flow curvature (concave) in the offshore direction with a larger flow at the surface; positive pressure gradients leads to an opposite curvature with a stronger offshore current at the bottom. For the wave forcing

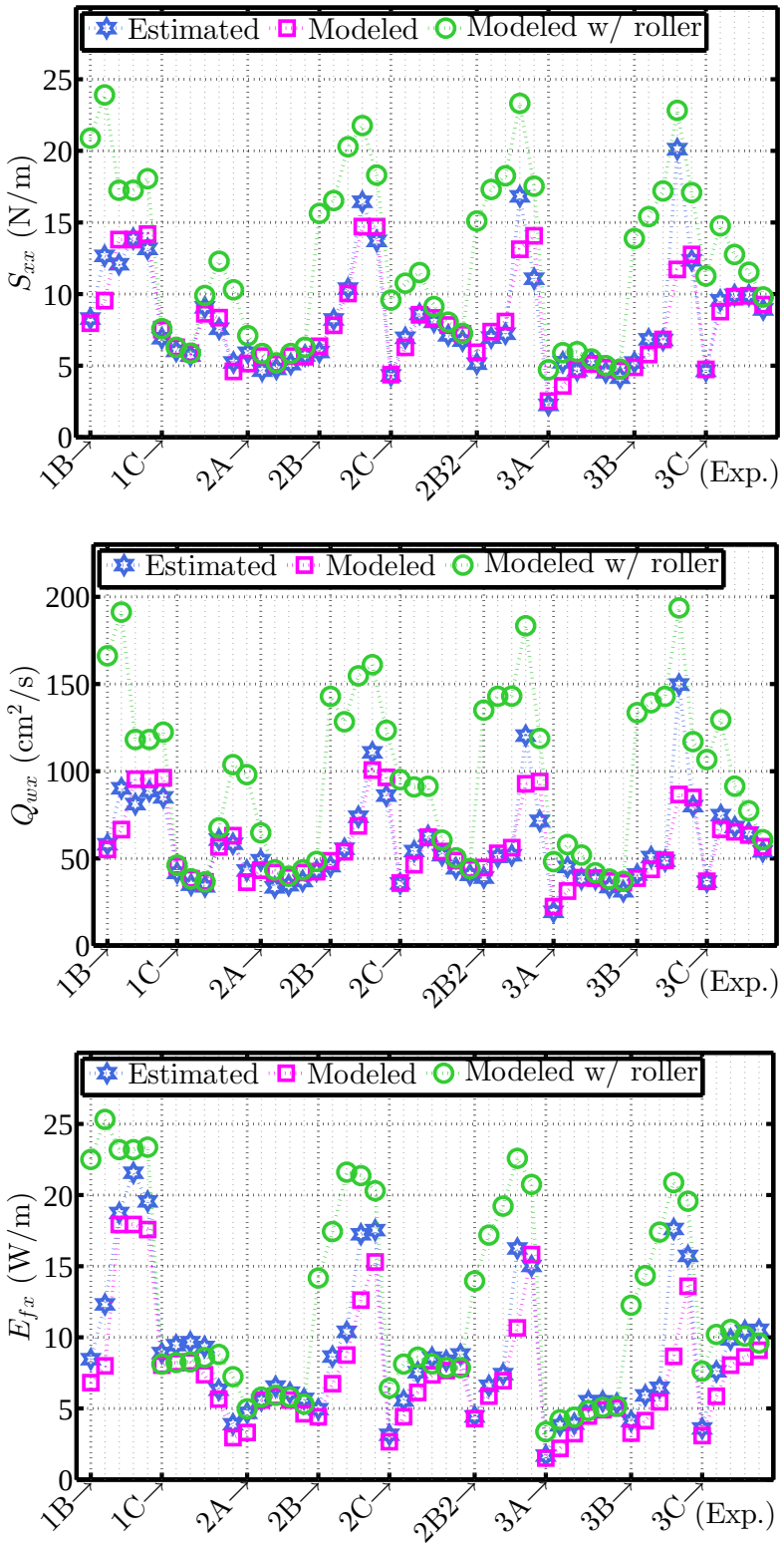

(a) S_{xx}

r^2	0.84
Mean	8.15 N/m
$\overline{\lvert\Delta\rvert}$	8.6%
Bias	0.95

(b) Q_{wx}

r^2	0.79
Mean	57.1 cm^2/s
$\overline{\lvert\Delta\rvert}$	9.8%
Bias	0.94

(c) E_{fx}

r^2	0.91
Mean	8.85 W/m
$\overline{\lvert\Delta\rvert}$	9.1%
Bias	0.97

Figure 30: Cross-shore wave radiation stresses (S_{xx}), volume fluxes (Q_{wx}), and energy fluxes (E_{fx}) yielded by the model and estimated from measured wave spectra in all experiments. The modeled results without the roller components (magenta squares) are compared to the spectral estimate values (blue hexagons) for statistical information. r^2 is the coefficient of determination indicating the model performance. See Figure 29 for definitions of the other parameters.

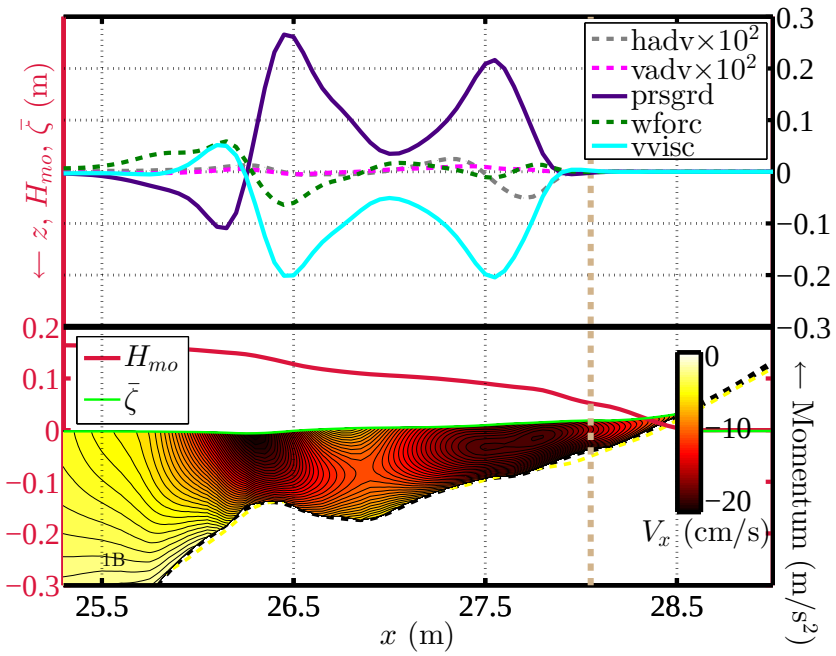

Exp. 1B:
H_{mo} = 17.5 cm,
T_p = 1.21 s.

Figure 31: Momentum terms in the eddy viscosity formula computed for Exp. 1B. The momentum terms are plotted on the top against the right axis. Modeled wave height and mean water level are shown in the bottom with the mean flow contours. Vertical brown line shows the last grid point of the surf zone models.

term, these curvatures are opposite. The pressure gradient term is slightly greater than the wave forcing in the surf zone and this should lead to an onshore-concave profile with a stronger offshore flow at the bottom. However, the flow curvature also depends on the bottom shear stress as a boundary condition which leads to a linear variation of the current with a bottom onshore flow and a surface offshore flow. This latter reason helps explain why the surf zone flow at the surface in Figure 31 appears to be as strong as the flow at the bottom.

In Figure 32, modeled current velocities are compared to the measured data analyzed from all of the experiments. The comparison yields a mean absolute error of 8.6 mm/s compared to the mean measured value of 2.1 cm/s. A linear line fit through the comparison features a slope of 0.64 which implies that the model substantially underpredicted the velocities. The agreement in this comparison is clearly not as excellent as found for the wave parameters. One primary reason behind this inaccuracy lies on the fact that most of the measured data were in the offshore zone where the velocities were small. Despite the measurement uncertainty of only about 1 mm/s, hydrodynamic uncertainties such as those

due to nonlinearity and turbulence are believed to become a significant portion in such small wave-induced mean flows. For instance, had stronger velocities in the surf zone been recorded, the mean absolute error of 8.6 mm/s found in the comparison here would not increase proportionally to such velocity magnitudes.

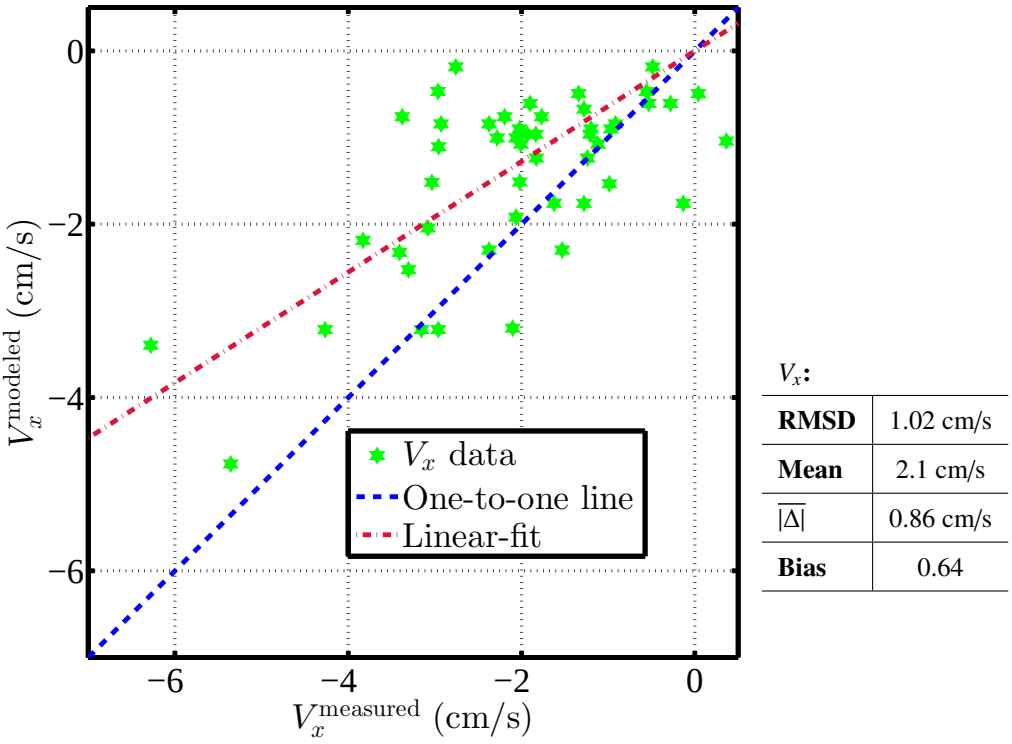

V_x:	
RMSD	1.02 cm/s
Mean	2.1 cm/s
$\overline{\lvert\Delta\rvert}$	0.86 cm/s
Bias	0.64

Figure 32: Comparison between measured and modeled current velocities based on all available experimental data. See Figure 29 for definitions of statistical parameters.

4.3 Supplemental models

Wave orbital velocities are required for a complete description of sediment transport in this study. Hydrodynamics in the swash zone also must be described due to significant local profile changes that affect the process in the surf zone. The existing wave and circulation models, REF/DIF S and SHORECIRC, do not feature capabilities in modeling these two components since they only resolve wave-averaged parameters in the surf zone. Thus, an orbital velocity model and a swash zone model are integrated into the modeling system. These two additional models are described in this section, beginning with necessary extension of mean water level and prediction of maximum wave runup in the simulation domain.

4.3.1 Mean water level extension and maximum wave runup prediction

The swash zone is defined here as the area between the starting point of a bore uprush and the maximum wave run-up location. The former was roughly taken at a depth of one third of the incident wave height where most of the larger broken waves would already behave like breaking bores. This location is also the last grid point where the surf zone models were configured in the simulation. The mean water level ($\bar{\zeta}$) therefore needs to be extended beyond this location to the shoreline. This extension is achieved following the nonlinear time-averaged model by Johnson and Kobayashi (1998), in which the cross-shore momentum balance is written following

$$(2P+1)\frac{dh}{dx} = -h\frac{dP}{dx} - \frac{dz_b}{dx} \tag{38}$$

in which,

$$P = \sigma_*^2\left[\left(2n-\frac{1}{2}\right) + \sigma_* f(H_*) - \sigma_*^2\right] \;\; ; \text{ and } \;\; n = \frac{1}{2}\left[1 + \frac{2k_p h}{\sinh 2k_p h}\right] \tag{39}$$

where σ_* is the dimensionless standard deviation of the water level $\eta(t)$ expressed as $H_*/\sqrt{8}$ with $H_* = H_{rms}/h$; k_p is the wave number at the peak frequency; and z_b is the bed elevation, measured from the still water level. It is worth noting that Equation (38) is actually a modified version of the cross-shore momentum balance between the radiation stress and the mean water level, i.e. $\dfrac{dS_{xx}}{dx} = -\rho g h \dfrac{d\bar{\zeta}}{dx}$.

Since both h and H_* are unknown in Equation (38), a semi-empirical formula to estimate H_* is utilized. The derivation and expression for this parameter as well as those for $f(H_*)$ can be found in Johnson and Kobayashi (1998). Estimated values of H_* then allow Equation (38) to be solved numerically by taking the initial parameters at the last grid point of the surf zone models and marching forward until the local depth is close to zero. Figure 33 shows the mean water levels extended to the shorelines for two experiments with different wave conditions.

Based on the bathymetric data, the maximum wave run-up location was defined as the most shoreward position with an observable profile change. This location is imperative

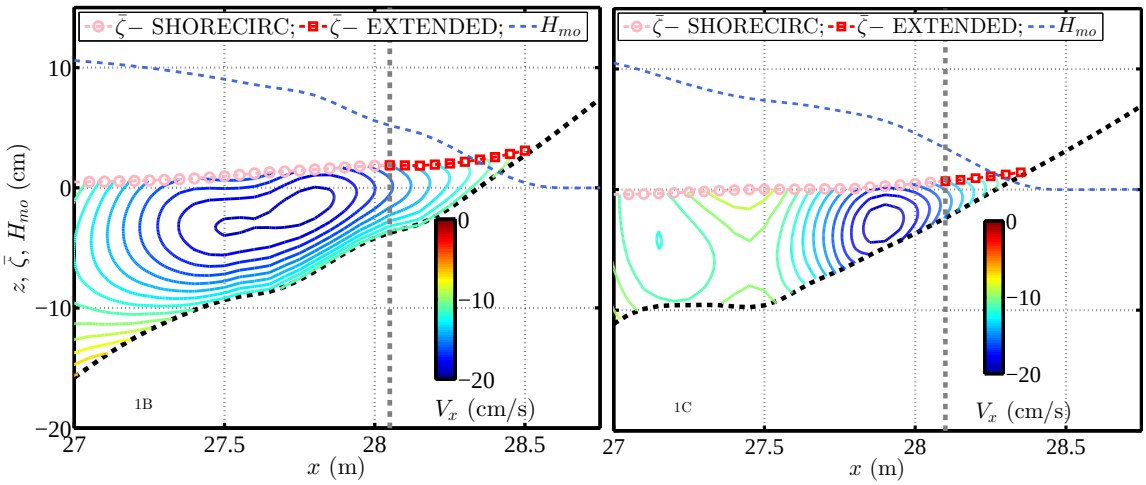

Figure 33: Mean water levels (MWL) extended to the shorelines in Exp. 1B (left) and in Exp. 1C (right). Vertical gray lines indicate the last grid points in the surf zone models where the MWL resolved by SHORECIRC (pink circles) are connected with the extended MWL (red squares).

in the numerical model since it defines the shoreward boundary of the active part of the domain. It is also utilized in the calibration of the swash-zone hydrodynamic model described in the next section. For a predictive purpose, a formula suggested by Nielsen and Hanslow (1991) is utilized to relate this wave run-up location to the wave parameters and the cross-shore slope. Assuming that the maximum wave runup is mainly initiated by the biggest 2% of the waves ($\overline{H_{2\%}}$), this predictive formula is written following

$$z_{wm} = \text{SWL} + 1.98 L_{zwm} \tag{40}$$

in which

$$L_{zwm} = 0.6 \sqrt{H_{orms} L_o} \tan\beta \tag{41}$$

where SWL is the still water level; H_{orms} is the root-mean-square offshore wave height; L_o is the offshore wave length; and β is the beach slope. For the random wave experiment here, H_{orms} is taken as $H_{mo}/\sqrt{2}$ and L_o is computed based on the peak wave frequency. The beach slope is estimated as plane from the still water shoreline to the previously-identified run-up location, starting from a known initially plane slope. Figure 34 shows the prediction results for six experiments where the maximum wave run-up locations could

clearly be identified at their equilibrium states.

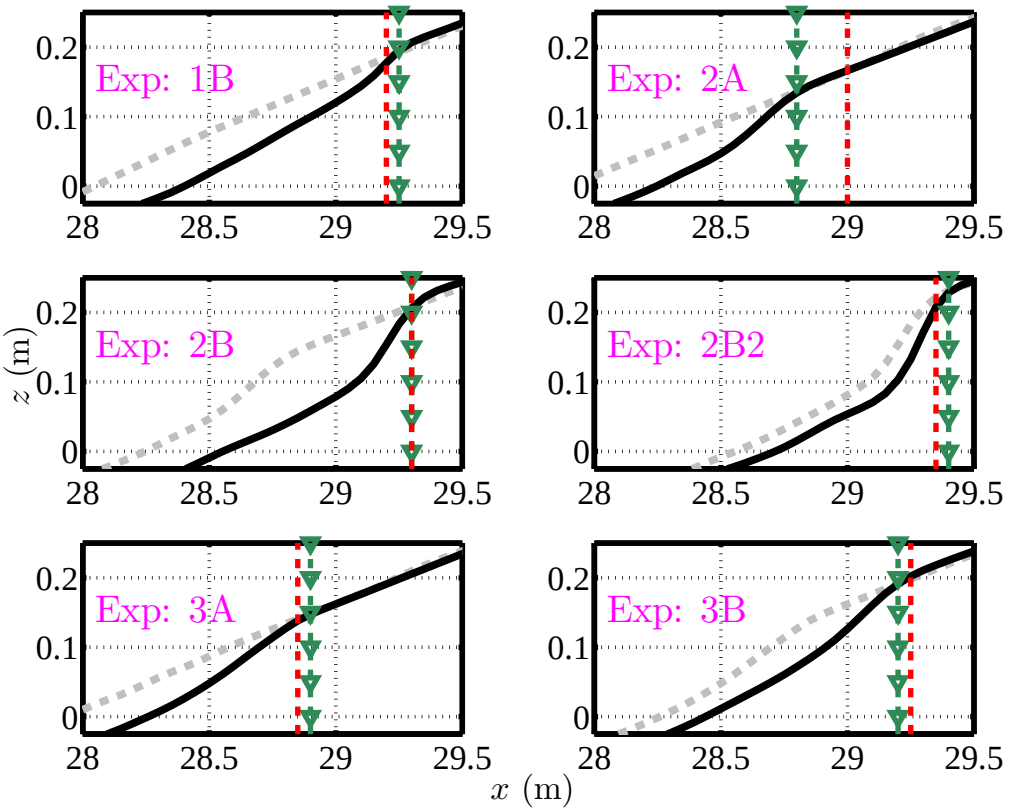

Figure 34: Maximum wave run-up locations observed in the experiments (green triangles) compared to the predicted locations (red dashed lines) on the equilibrium profiles (black solid lines). Gray dashed lines show the initial profiles.

4.3.2 Swash zone model

The swash zone hydrodynamic model here is developed based on a classical problem of waves climbing the beach slope analogous to a ballistic motion (e.g. Shen and Meyer 1963a,b). For clarity, the description of the model is given here starting first from the estimation of the target parameter which is the fluid velocity under a swash motion u_{sw} determined according to continuity as (e.g. Hughes and Baldock 2004)

$$u_{sw}(x,t) = \frac{1}{h_{sw}(x,t)} \frac{\partial \mathbb{V}(x,t)}{\partial t} \tag{42}$$

in which h_{sw} is the instantaneous depth, i.e. equal to the thickness of the swash lens; and $\mathbb{V}$ is the volume of water shoreward from the location of interest (x), computed following

$$\mathbb{V}(x,t) = \int_x^X h_{sw}(x,t)\,dx \tag{43}$$

where X is the time-dependent waterline position (wave front). This velocity estimation under the continuity constraint assumes depth-uniform flow and neglects possible infiltration on the beach profile. The depth h_{sw} is approximated following the semi-empirical formula, based on experimental observation, introduced by Baldock and Holmes (1997)

$$h_{sw}(x,t) = H_b \left(\frac{X-x}{X}\right)^C \left(\frac{T_s - t}{T_s}\right)^D \tag{44}$$

where H_b is the terminal bore height taken here as the wave height at the swash zone seaward boundary; C and D are adjustable parameters given as 0.75 and 2, respectively; and T_s is the total swash period. Despite neglecting infiltration and swash-swash interaction, this type of swash zone model has been proved to produce reasonably accurate swash lens and swash velocities (e.g. Puleo and Holland 2001). Possible swash-swash interaction may, in fact, be accounted for by considering momentum conservation but such effect is usually found to be small for steep beach profiles where swash periods are typically shorter than wave periods (Erikson et al., 2005).

Still, the performance of this type of model depends largely on the accuracy in determining the swash motion described by its instantaneous position X and period T_s. These two parameters can be computed based on the waterline velocity U_s given in the form of ballistic model

$$\frac{dU_s}{dt} + g\sin\beta + \frac{f_{sw}}{2\delta_{sw}} U_s\,|U_s| = 0 \tag{45}$$

where β is the profile slope; f_{sw} is the swash friction factor; and δ_{sw} is the total depth of the fluid column at the bore edge. This equation represents the acceleration of the waterline in the first term relative to the gravity and the friction effects. To solve for U_s, the initial shoreline speed is given as the celerity of the terminal bore. The depth δ is approximated

as the summation of the mean water depth and the terminal bore height ($h + H_b$).

In this study, the above set of equations are solved for breaking bores of multiple heights that would be generated from random waves. A wave-by-wave approach is applied considering four statistical wave heights, $\overline{H_{33\%}}$, $\overline{H_{20\%}}$, $\overline{H_{10\%}}$, and $\overline{H_{2\%}}$, according to the Rayleigh distribution function. All smaller waves are neglected since they were found to feature very small swash motions mainly due to relatively steep slopes in the experiment. Equation (45) is then solved numerically for each statistical wave. The friction factor (f_{sw}) is treated as a calibration parameter matching the most shoreward waterline position (X) of $\overline{H_{2\%}}$ with the predicted maximum wave run-up location (Equation (41)). Figure 35 shows the instantaneous shoreline positions $X(t)$ associated with each of the four statistical waves in Exp. 1B, obtained by integrating Equation (45) with time.

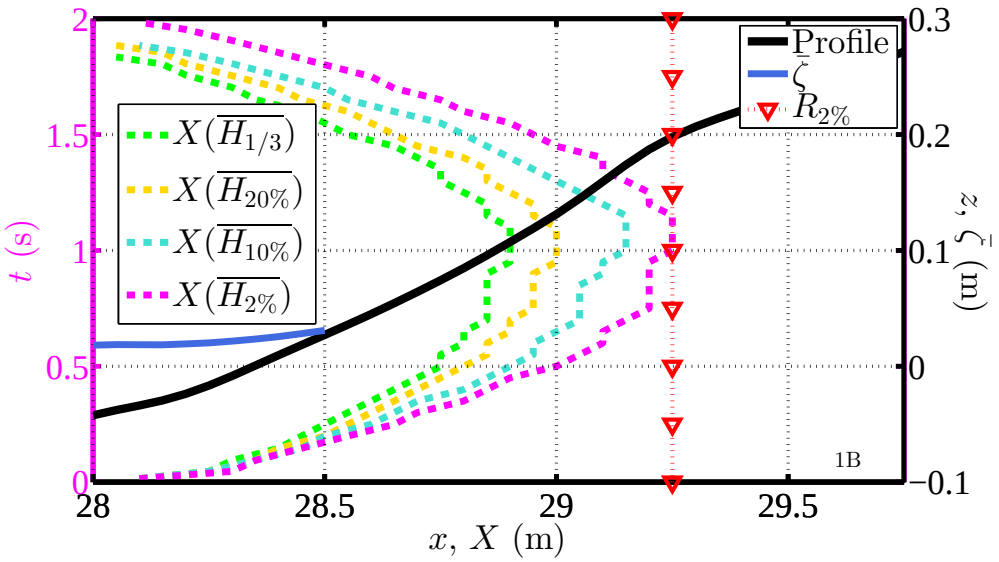

Figure 35: Instantaneous positions of the moving waterline induced by each of the four statistical waves in Exp. 1B. The positions are plotted against the time on the left axis; the profile and the mean water level are plotted against the right axis. Vertical red line indicates the maximum wave run-up location.

The swash-lens depth h_{sw} is then estimated by the use of Equation (44) for each bore height given its position ($X(t)$) and period (T_s). Figure 36 shows the swash lens induced by $\overline{H_{2\%}}$ that leads to the swash velocities shown in Figure 37, for multiple cross-shore locations on the same case. These velocities were computed following the mass conservation constraint shown in Equations (42) and (43). The results show that the

reversing flow velocity at each local position occurs before the bore edge reaches its maximum displacement. Consequently, the backwash is generally associated with a longer period than that of the uprush. This asymmetric swash velocity is also commonly found in actual swash events due to, among other factors, deceleration and acceleration involved with the uprush and the backwash, respectively (e.g. Hughes et al. 1997; Holland and Puleo 2001).

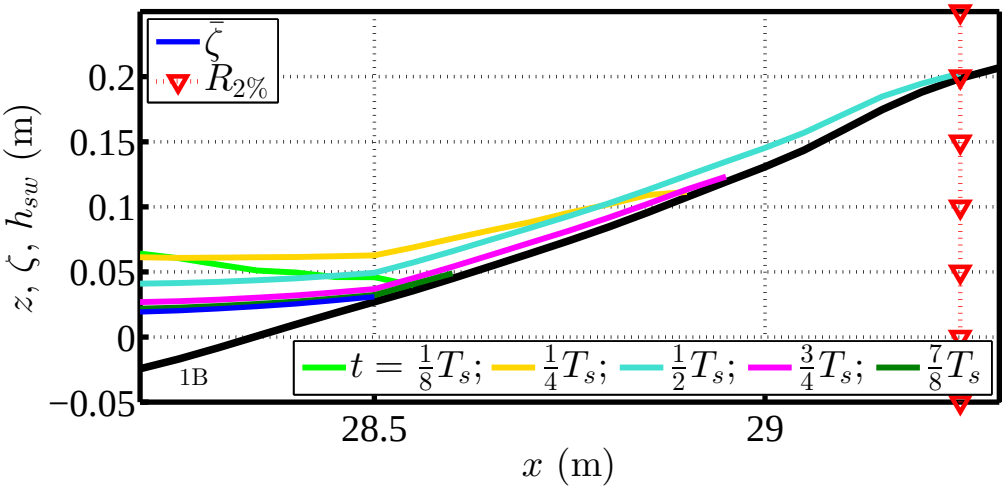

Figure 36: Swash lens (h_{sw}) resolved using Equation (44) under a swash period for the bore associated with $\overline{H_{2\%}}$ in Exp. 1B. Black solid line shows the beach profile. Vertical red line indicates the maximum wave run-up location.

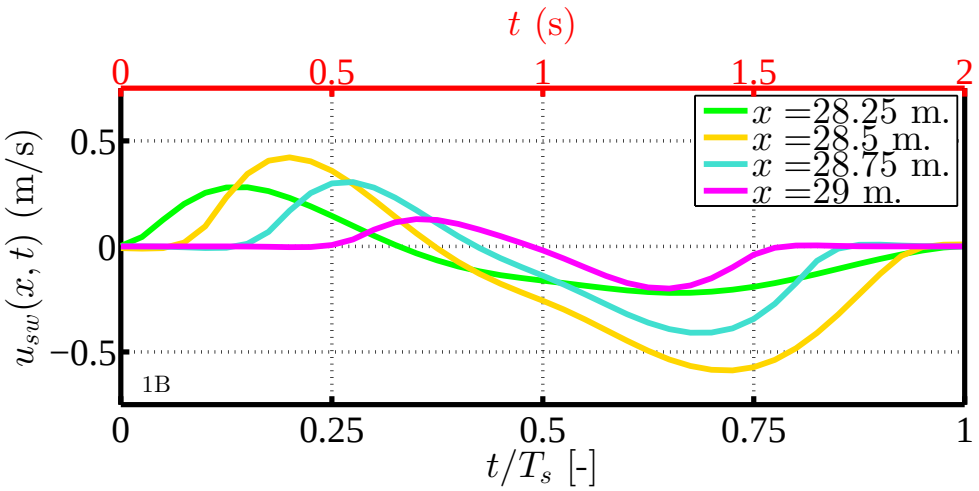

Figure 37: Instantaneous swash velocities resolved using Equation (42) under the swash lens in Figure 36. Actual and normalized times are shown on the top and the bottom axes, respectively.

Swash lens and swash velocities induced by the other given waves are estimated like

shown for $\overline{H_{2\%}}$ in the above figures. Mean velocity under the swash motion (V_{sw}) is then computed by summing the time-averaged swash velocities weighted by the percent occurrences (p_n) of the waves, following

$$V_{sw}(x) = \sum_{n=1}^{N} \frac{\overline{u_{sw}^n(x,t)\, p_n}}{\sum_{n=1}^{N} p_n} \tag{46}$$

where the superscript n denotes each given wave. The weighted average here implies that all of the waves smaller than the $H_{33\%}$ are neglected. In this study, this mean swash velocity is employed to facilitate an estimation of sediment transport in the swash zone. For matching the surf zone and the swash velocities, it is assumed that the depth-varying velocity profile at the last grid point in the surf zone model slowly decays shoreward and becomes depth-uniform at the shoreline. Over the same transitional distance, the magnitude of the depth-averaged velocity is assumed to vary so that it matches the mean swash velocity (V_{sw}).

Figure 38 illustrates two cases of matching the mean surf zone velocities and the mean swash zone velocities computed using Equation (46). In both cases, the connections show smooth transitions of the velocities which would be expected in an actual scenario. The surf zone depth-averaged velocities (V_x) and near-bed velocities (V_b) are identical to the mean swash velocities (V_{sw}) at the shoreline according to the assumption. The near-bed velocities only vary slightly due to fact that they decrease as the depth-averaged velocities decrease but also tend to increase as the onshore-concave velocity profiles transition to be depth-uniform. It might be worth noting that, on a milder slope prior to an equilibrium state, a mean swash velocity usually features a slower decrease towards the shoreward boundary at the maximum wave run-up location.

4.3.3 Wave orbital velocity model

Sediment transport in the nearshore zone is known to be sensitive to intra-wave velocities and their nonlinearity. In this study, wave orbital velocities are simulated via another modeling component extended from the time-averaged, linear wave model REF/DIF S. It may be noted that several existing methods for a similar purpose are available but they

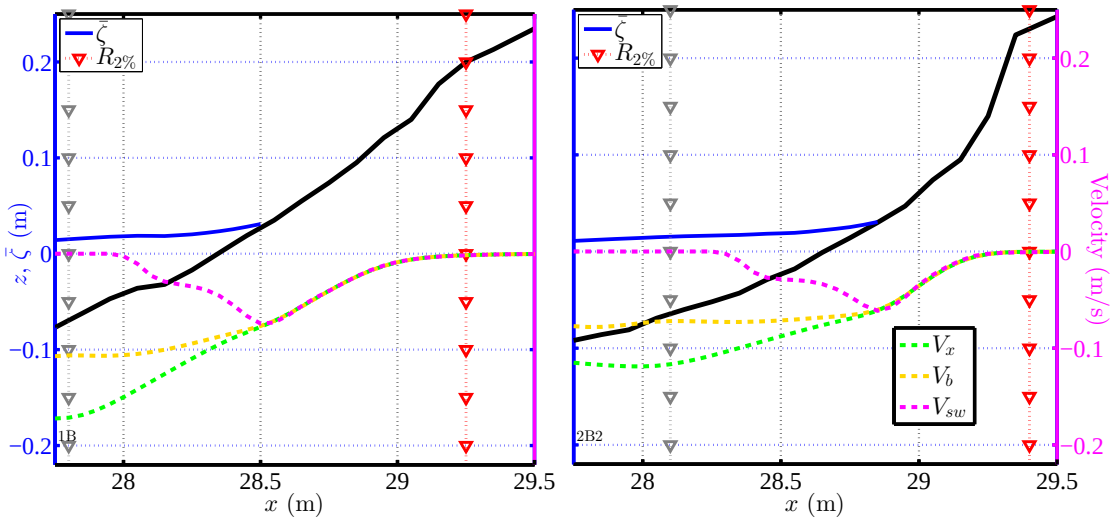

Figure 38: Depth-averaged (V_x) and near-bed velocities (V_b) in the surf zone that are adjusted and connected with the mean swash velocities (V_{sw}) yielded by Equation (46). The results are shown for Exp. 1B (Left) and Exp. 2B2 (Right). Gray triangles show the last grid points in the surf zone models (REF/DIF S and SHORECIRC). Vertical red lines indicate the maximum wave run-up locations.

are mostly for near-bed velocity only and also limited with an applicable range of wave conditions (e.g. Isobe and Horikawa 1982; Elfrink et al. 2006).

In the model here, a predictive formula for specifying wave nonlinearity is developed together with analytical solutions for generating both the horizontal and vertical components of the orbital velocity of a representative wave, based on the spectral wave height (H_{mo}). The nonlinear parameter of interest is the velocity skewness S_k which is particularly influential to energetics-type sediment transport models, defined as

$$S_k = \frac{\overline{u_w(t)^3}}{u_{w,rms}^3} \tag{47}$$

where u_w is the horizontal orbital velocity. Various arguments could be made regarding vertical variation of the skewness over the water column (e.g. Greenwood and Osborne 1990; Doering and Baryla 2002). Theoretically, if the horizontal velocities over the depth can be described using the same linear phase function, they are associated with an identical skewness regardless of any differences in their magnitudes. Similarly, the skewness of the wave surface displacement that is governed by such phase function would also match the

velocity skewness.

Given the above facts, the skewness parameter considered here is assumed to be depth-uniform and follow the surface displacement skewness. Using Equation (47) with u_w replaced by η, this parameter can be obtained from the heave time series recorded in the experiment. A new predictive formula was developed based on dimensional analysis and calibrated with the measured skewness parameters. For the best prediction, the relationship between the skewness parameter and the chosen nondimensional terms is found to follow

$$S_k = 0.3\overline{(\tan\beta)}^{0.25} + 0.15\overline{\left(\frac{h}{L}\right)}^{-0.6} - 0.5\left(\frac{C_{sp}}{T_m}\right)^{0.35} + 0.2\overline{\left(\frac{\partial H_{mo}}{\partial x}\right)}^{0.4} \tag{48}$$

where $\tan\beta$ is the local bed slope; L is the local wave length; and T_m is the mean wave period. The variable C_{sp} represents the wave spectral width computed as the difference between the two wave periods above which the wave spectrum contains 25% and 75% of the energy. The overbar denotes averaging of the parameters over one-wavelength distance seaward from the location of interest in order to account for historical effects of the parameters. All of the constants in Equation (48) are empirical calibration parameters. Since they could be negative on a profile, the first and the last terms are computed using their absolute values with the signs applied later.

Figure 39 shows the skewness parameters predicted for Exp. 3C using Equation (48), compared to those obtained in the measurement and yielded by Elfrink's formula. Generally, the values obtained from the new formula and the measured skewness parameters show an agreement in their substantial onshore increases in the measurement area. Based on all of the available experiments, Figure 40 shows that the skewness parameters can be predicted with less than 30% error in terms of the mean absolute difference. The deviation between the prediction and measurement is primarily contributed by higher skewness values. In both Figures 39 and 40, Elfrink's formula shows severe inaccuracies in the predictions primarily because it was applied beyond its applicable range. It should be noted that the new formula here is derived empirically and will require a recalibration when applied to different data sets.

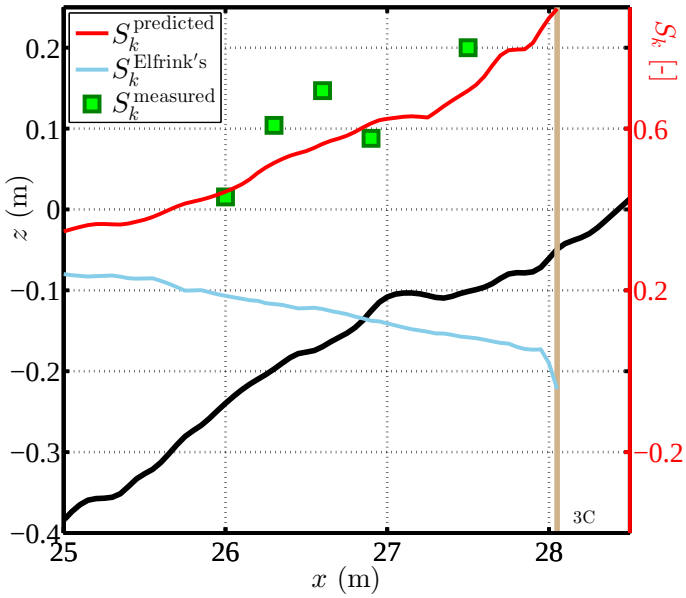

Figure 39: Estimation of wave skewness by the use of the predictive formula for Exp. 3C. Black solid line shows the beach profile plotted against the left axis. The skewness parameters are plotted against the right axis. Vertical brown line shows the last grid point in the surf zone.

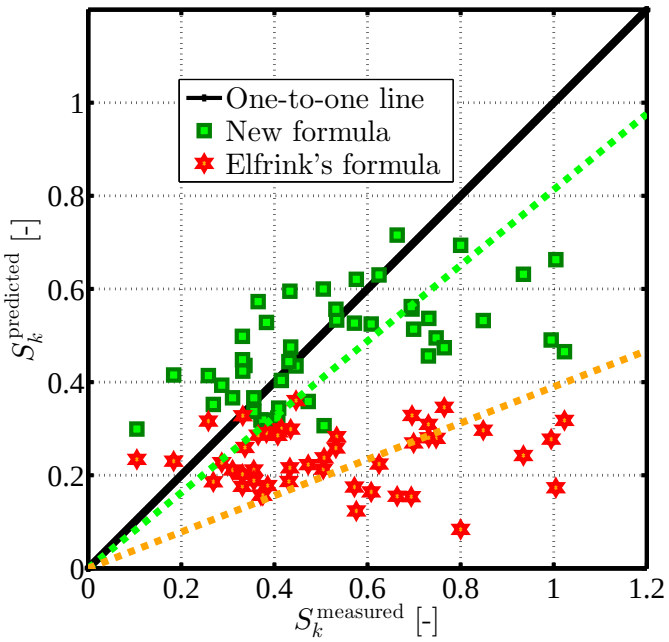

S_k:

Method	Eq. (48)	Elfrink's
Mean	0.52 (measured)	
RMSD	0.19	0.36
$\overline{\lvert\Delta\rvert}$	29%	51%
Bias	0.81	0.39

Figure 40: Comparison between the skewness parameters measured in the experiments and the results obtained from Equation (48) and Elfrink's method. **RMSD** is the root-mean-square difference; $\overline{|\Delta|}$ is the mean absolute difference. **Bias** is the slope of a straight line fit through the compared data; less than unity indicates underestimation in the model.

Wave orbital velocities with the skewness parameters specified from the predictive formula are generated for the use in the sediment transport model in this study. The horizontal velocity component (u_w) is obtained based on the analytical equation for near-bed velocity introduced by Abreu et al. (2010). This equation is extended for the velocities over the entire water column assuming a depth variation of the velocity magnitudes according to linear wave theory. Subsequently, the cross-shore continuity equation, $\frac{\partial u_w}{\partial x} + \frac{\partial w_w}{\partial z} = 0$, is applied to obtain the vertical components (u_w) of the orbital velocities. The expressions for these horizontal and vertical orbital velocities at a local cross-shore position are finally written as

$$u_w(z,t) = A_u(z)\sqrt{1-r^2}\left[\frac{\sin(\sigma t) + \frac{r\sin\phi}{1+\sqrt{1-r^2}}}{1 - r\cos(\sigma t + \phi)}\right] \tag{49}$$

$$w_w(z,t) = A_w(z)\frac{\sqrt{1-r^2}\cos(\sigma t)}{(1 - r\cos(\sigma t + \phi))}\left[1 - \frac{r\sin(\sigma t + \phi)\left(\sin(\sigma t) + \frac{r\sin\phi}{1+\sqrt{1-r^2}}\right)}{\cos(\sigma t)(1 - r\cos(\sigma t + \phi))}\right] \tag{50}$$

where $A_u(z)$ and $A_w(z)$ are the horizontal and the vertical velocity amplitudes that follow linear wave theory. The factor r represents a skewed waveform with $0 \leq r < 1$ for sinusoidal to cnoidal-like wave profiles. The factor ϕ represents an asymmetric waveform with $-\pi/2 \leq \phi \leq 0$ for symmetric to saw-tooth waves. The wave skewness parameter S_k defined in Equation (47) depends on both r and ϕ and their relationship is shown in Figure 41. It can be seen that both sawtooth (ϕ=0) and sinusoidal (r=0) wave profiles are associated with zero skewness regardless of the value of the other factor.

The relationship shown in Figure 41 means that the wave asymmetry factor ϕ also needs to be specified for obtaining a velocity profile with a given skewness S_k. As they are becoming skewed, waves propagating towards the shoreline would also tend to pitch forward and approach a sawtooth shape. Likewise, both the skewness and the asymmetry of the waves and their velocities should increase. This fact implies that the factor ϕ may approach zero which will, however, lead to a contrary waveform that is asymmetric but non-skewed. Because of this constraint, the value of ϕ at the most shoreward location in the experiment here is assumed to be the maximum value that still allows the target skewness parameter S_k. A constant value of $\phi = -\pi/2$ is given in the offshore part of

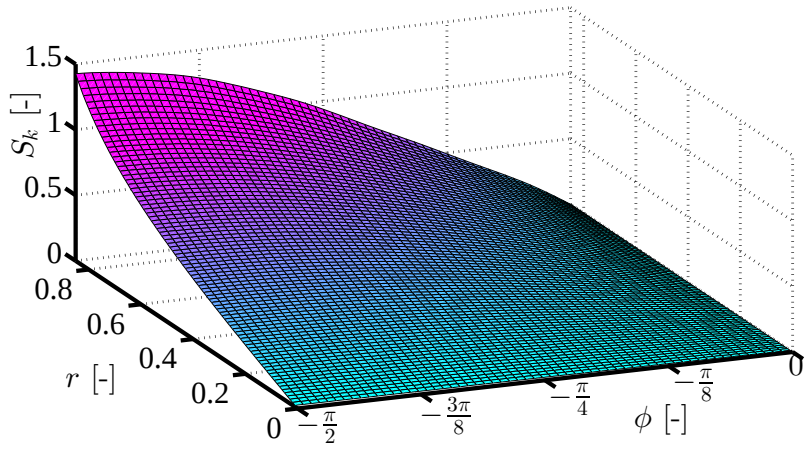

Figure 41: Relationship between the factors r and ϕ in Equation (49) and the skewness parameter S_k in Equation (47).

the domain and a linear variation of the factor is assumed between the profile toe and the shoreward boundary. For a given value of ϕ, the factor r is then selected so that the simulation yields the orbital velocity with the specified skewness S_k.

Figure 42 shows the values of r and ϕ along the profile for the simulation of the orbital velocities in Exp. 1B. The values of r and S_k almost match since these two parameters are nearly equal for small ϕ in this case. Figure 43 shows the near-bed velocities simulated at four locations on the beach profile in Figure 42. At the furthest offshore location (x = 25 m), the velocity appears to be slightly skewed with a crest amplitude larger than that of the trough. Both skewness and asymmetry in the velocity profiles increase towards the shoreline according to the values of r and ϕ specified in the simulation. The velocity at the most shoreward location features a skewed waveform with a crest pitching forward similar to a sawtooth wave.

Figure 44 shows instantaneous horizontal velocities under a wave period, $u_w(x, z, t)$, at six locations on the same beach profile. The depth variations of the velocities typically follow a horizontal velocity decay that would be expected from linear wave theory. The variations decrease closer to the shoreline because of shallower water depths. Due to the assumption of depth-uniform skewness, the ratios between the maximum velocities and the minimum velocities at any given depths would be a constant, i.e. $U_{max}(z)/U_{min}(z) = C$.

Figure 45 shows instantaneous vertical velocities, $w_w(x, z, t)$, at the same locations. To satisfy continuity, the vertical velocities vanish at the maximum vertical excursions of the

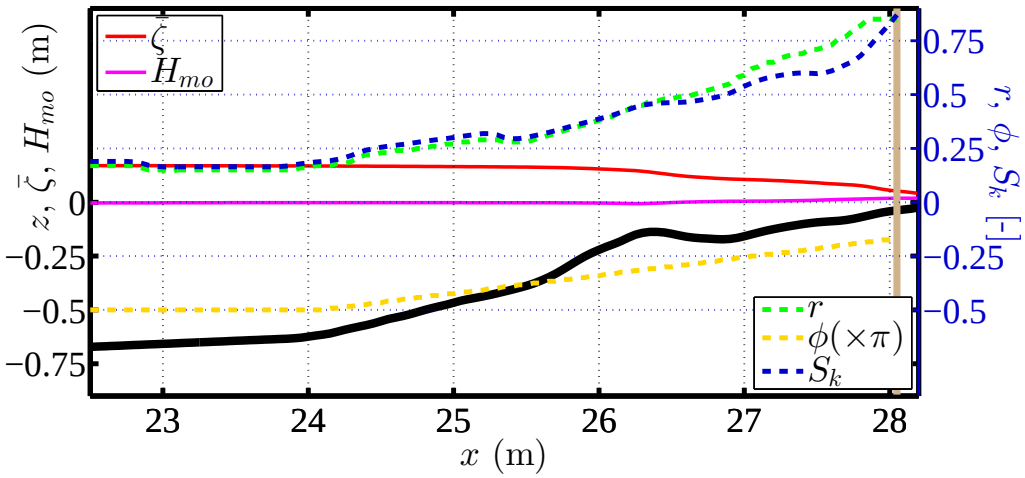

Figure 42: Values of r and ϕ factors in Exp. 1B that yield the orbital velocities with the skewness S_k predicted by Equation (48). Vertical brown line shows the last grid point in the surf zone models (REF/DIF S and SHORECIRC) that are connected with the swash zone model.

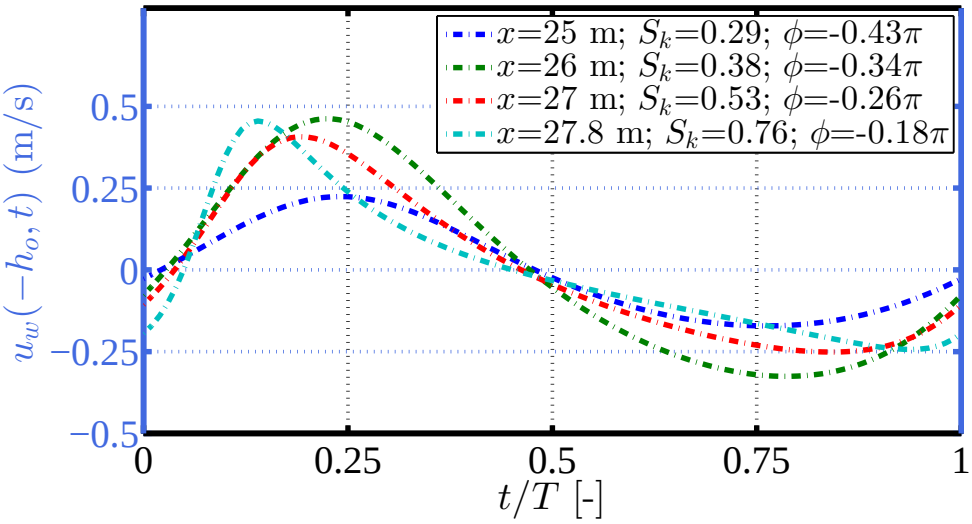

Figure 43: Near-bed horizontal velocities simulated at four locations along the beach profile in Exp. 1B with wave skewness and asymmetry parameters shown in Figure 42.

wave and peak when the slope of the water surface reaches a maximum or a minimum. The depth variation of the velocities at a particular location is also qualitatively similar to that expected for linear waves. However, a major difference is found in the cross-shore variations of the velocity profiles. Despite shallower water closer to the shoreline, the maximum velocities tend to increase slightly and the depth variations of the velocities tend to decrease significantly. These variations occur as a result of the increasing wave skewness and asymmetry which lead to a narrower waveform with a peaky wave crest. Under such profile, the wave features a steeper surface slope and likewise exhibits an orbital velocity with a higher vertical component. All of the major wave and hydrodynamic parameters illustrated in this chapter are recapitulated in Table 11 with statistical information that summarizes the model performance.

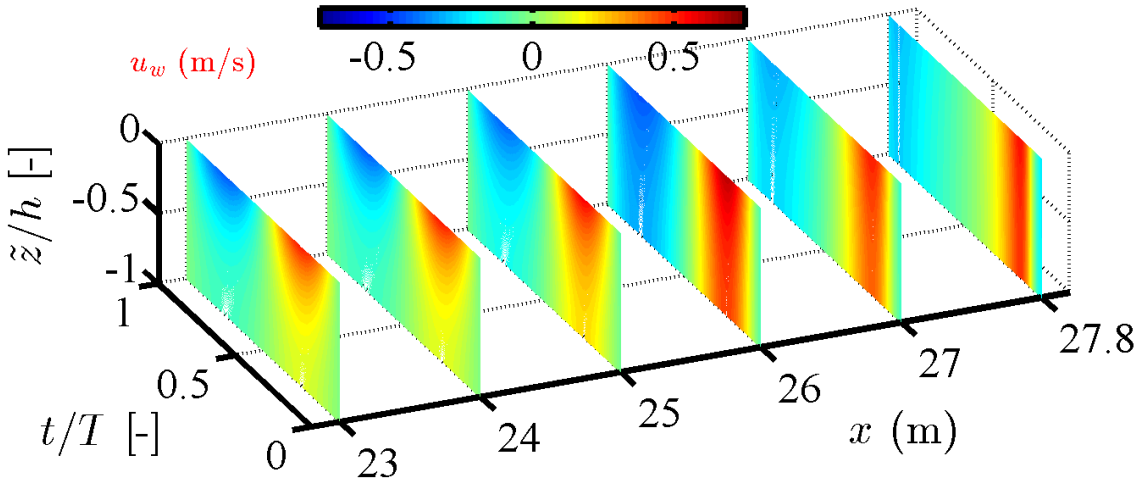

Figure 44: Instantaneous horizontal velocities $u_w(x, z, t)$ at six locations along the beach profile shown in Figure 42. Contours show the velocity magnitudes over normalized depth and wave period. On the vertical axis, $\tilde{z}$ is equal to $z - \bar{\zeta}$ in which $\bar{\zeta}$ is the mean surface water level; h is the mean water depth.

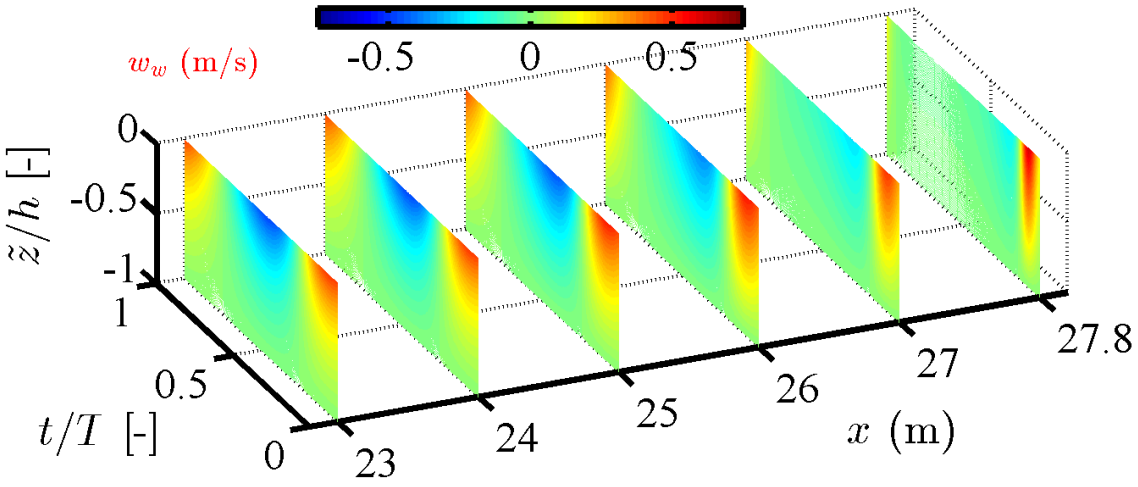

Figure 45: Instantaneous vertical velocities $w_w(x,z,t)$ at six locations along the beach profile shown in Figure 42. See Figure 44 for more details.

Table 11: Summary of hydrodynamic parameters that were modeled and validated against the laboratory data sets.

Parameter	**Mean measured**	$\overline{\lvert\Delta\rvert}^{\dagger}$	**Prediction bias** ††
Wave reflection K_r **(%)**	16.0%	6.2%	0.86
Wave height H_{mo} **(cm)**	11.1	1.01	0.98
Radiation stress††† S_{xx} **(N/m)**	8.15	0.79	0.95
Mass flux††† Q_{wx} **(cm^2/s)**	57.10	6.58	0.93
Energy flux††† E_{fx} **(W/m)**	8.85	0.84	0.94
Mean current V_x **(cm/s)**	2.10	0.86	0.64
Wave runup $R_{2\%}$ **(m) (for swash zone velocity)**	0.74	0.07	1.00
Wave skewness S_k **[-] (for wave orbital velocity)**	0.52	0.14	0.81

$^{\dagger}\overline{|\Delta|}$ is the mean absolute error between the measured and the modeled values.
††Bias is the slope of a linear line fitted through the two types of results, lower than one if the model tends to underpredict the parameter.
†††These parameters are based on spectral estimates rather than direct measurement in the flume.

CHAPTER V

NUMERICAL MODELING OF SIZE-SELECTIVE SEDIMENT TRANSPORT AND SEDIMENT GRAIN SORTING

This chapter describes the size-selective sediment transport and grain sorting models that were developed in this study. Figure 46 shows an overview of these models including the major processes that are considered in each of them. Utility of the models for a comprehensive morphodynamic simulation are illustrated in the next chapter under the laboratory conditions described earlier in Chapter 3.

In the sections that follow, general aspects in the size-selective modeling approach are discussed, focusing on its superiority over a traditional single-size approach. The transport models for bedload and suspended loads are separately explained in detail. The morphology model that is coupled with the transport models to resolve both bathymetry and sediment grain sorting is then described. Sensitivity analyses of the models are covered in the last section.

5.1 Size-selective sediment transport

Modeling of size-selective sediment transport may be achieved using two broad approaches. One is to consider the transport rates of multiple size fractions independently, regardless of the mixture composition; the other is similar but also accounting for interdependent effects among the size fractions. These two approaches are illustrated here briefly for a better comprehension in the dependency between sediment size characteristics and their multi-fractional transport rates.

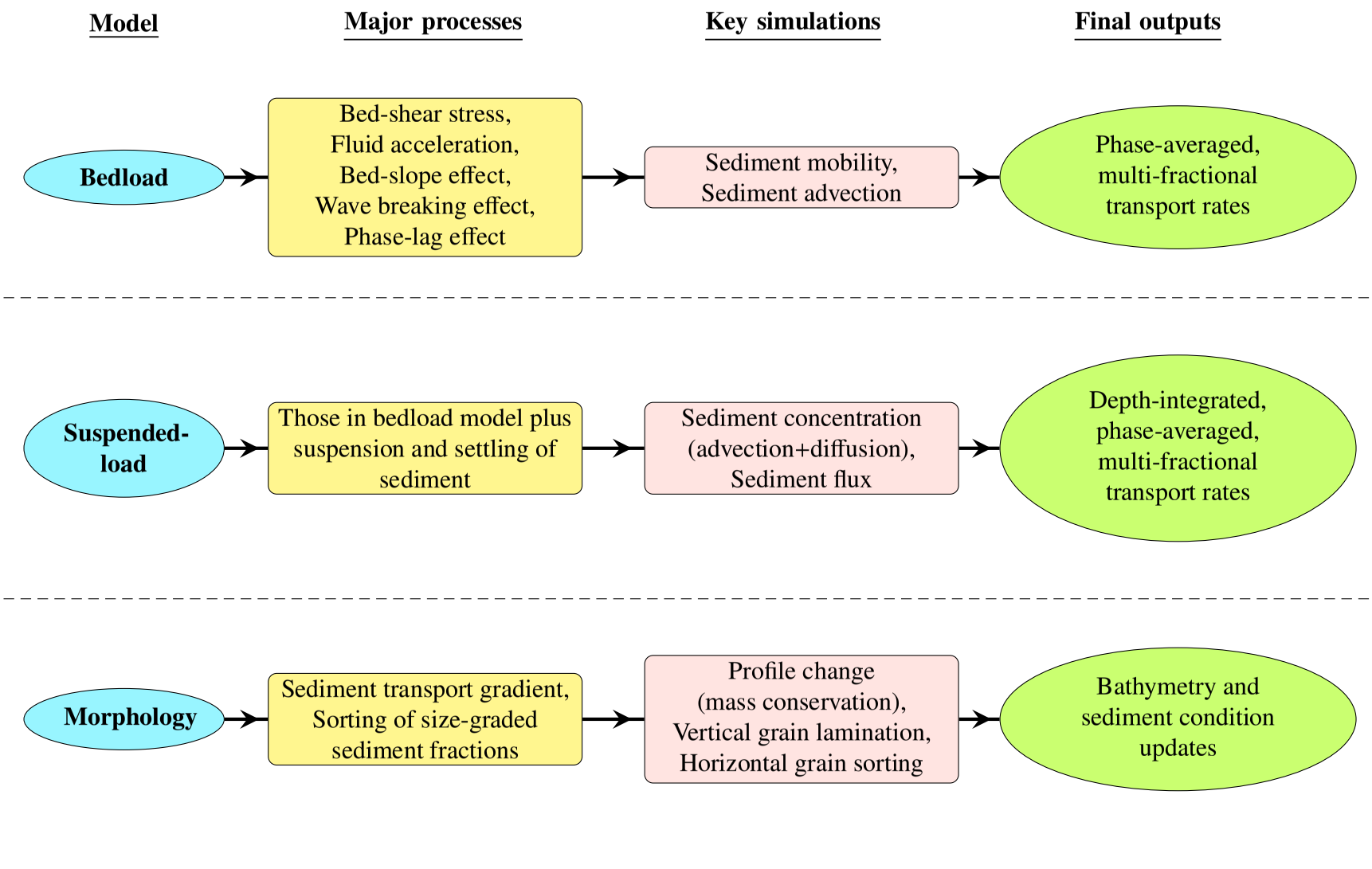

Figure 46: Overview of the numerical models for size-selective sediment transport and sediment grain sorting and their major roles in the process simulations. Note that both of the transport models simulate the listed processes for each individual sediment size fraction.

For the first approach, a traditional single-size transport formula may easily be modified by applying it for individual size fractions. An example can be given for a transport formula in a simple form (e.g. Van Rijn et al. 2003), following

$$\text{(a)}\ q_t \propto d_{rep}^{\lambda} u^3 \ \rightarrow\ \text{(b)}\ q_{d_i} \propto d_i^{\lambda} u^3 \ \rightarrow\ \text{(c)}\ q_t = \sum_{i=1}^{N} p_i\, q_{d_i} \tag{51}$$

in which q_t is the total sediment transport rate; d_i is the diameter of an individual size fraction with percent of occurrence p_i; u is the fluid velocity; and λ is a constant representing the dependency of the transport rate on the particle size. The representative diameter d_{rep} is the mean (d_m) or the median diameter (d_{50}) of the mixture. After obtaining the multi-fractional rates (q_{d_i}), the net transport rate is subsequently computed following the weighted summation in the last term.

Figure 47 illustrates the changes in total sediment transport rates and associated grain-size compositions computed using the simple formulas in Equation (51). A Gaussian distribution was assumed for the initial size composition with d_{50} as the representative diameter. Compared to the single-size formula, the modified formula is found to always yield greater transport rates that are also increasing for wider grain-size distributions and higher magnitudes of the nonlinear dependency parameter λ. For an inverse grain-size dependency (λ<0), the median grain sizes d_{50} in the transport mixtures decrease since the transport rates of the finer size fractions (d_i<d_{50}) are greater than those of the coarser fractions. This bias towards the finer fractions also results in a narrower size distribution according to the changing standard deviations μ shown in Figure 47. Both of these changes are opposite in the case of dominating transport rates in the coarser fractions (λ>0).

The above modification allows for some consideration of basic dependencies of transport rates on the grain sizes. However, size-graded sediment in nature does not always follow such description since interactive effects among different size fractions are also influential both in bedload (e.g. Dibajnia and Watanabe 1996; Hassan and Ribberink 2005a,b) and in suspended load (e.g. Sistermans 2002; Van Rijn 2007a). Such effects can be attributed to physical characteristics of nonuniform sediment that lead to unique patterns of protrusion, sheltering, and pivoting angles among the size-graded fractions. All

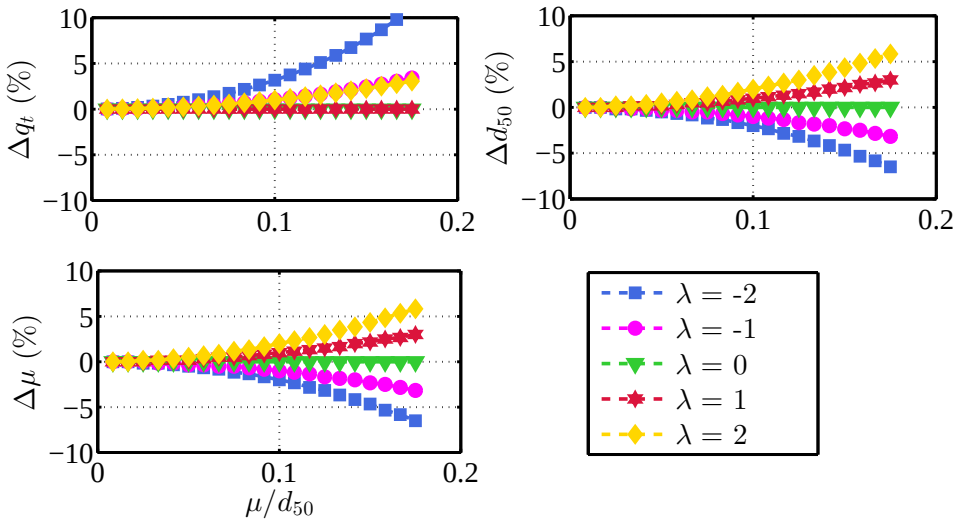

Figure 47: Changes in the net sediment transport rates and associated grain size compositions yielded by the multi-fractional transport formula modified in Equation (51). All of the changes were computed as percent differences to the corresponding results yielded by the original single-size formula in which d_{50} and μ do not change.

of these related mechanisms are hypothesized to affect the size selectivity in the transport process and often described collectively as a "hiding and exposure" effect.

For energetics-type sediment transport models, an attempt to account for the hiding/exposure effect has been to correct for related shear stress terms of individual size fractions. Egiazaroff (1965) suggested an adjustment for the critical shear stress that follows

$$\xi_i^E = \left(\frac{\tau_{b,cr,d_i}}{\tau_{b,cr,d_m}}\right)\left(\frac{d_m}{d_i}\right) \tag{52}$$

where ξ_i^E is the hiding/exposure factor of the i^{th} size fraction; $\tau_{b,cr,i}$ and τ_{b,cr,d_m} are the critical bed shear stresses of each size class and that of the mean size, respectively. On a theoretical basis, concerning forces acting on size-graded grains, Egiazaroff showed that the relationship in Equation (52) can be rewritten in terms of the relative diameter d_i/d_m as

$$\xi_i^E = [\log(19)/\log(19 d_i/d_m)]^2 \tag{53}$$

Van Rijn (2007b) demonstrated that this equation, while having d_m replaced by d_{50}, allowed a fairly accurate prediction of threshold shear stresses based on numerous experimental data (e.g. Wilcock 1993; Petit 1994; Kuhnle 1993). For the same purpose, Van Rijn (2007b) also suggested an alternative adjusting factor given as

$$\xi_i^V = \left(\frac{\tau_{b,cr,d_i}}{\tau_{b,cr,d_i^{\text{Uniform}}}} \right) \tag{54}$$

where $\tau_{b,cr,d_i^{\text{Uniform}}}$ is the critical shear stress of a uniform sediment with a diameter equal to the i^{th} size class, obtained from Shields diagram. The critical stress term τ_{b,cr,d_i} are the same in both Egiazaroff's and Van Rijn's factors, and Equation (54) may thus be expressed in terms of the relative diameter d_i/d_m, or d_i/d_{50}.

The above hiding/exposure factors are only determined for adjusting the critical bed shear stress. For the instantaneous bed shear stress, another hiding/exposure factor may also be considered using a simple formula that follows

$$\lambda_i = \left(\frac{\tau_{b,d_i}}{\tau_{b,d_{rep}}} \right) = \left(\frac{d_i}{d_{rep}} \right)^n \tag{55}$$

Day (1980) showed that the exponent "n" in this expression may vary for different transport regimes. An optimal value of 0.25 was given when d_{rep} is taken as d_{50}. Figure 48 compares the hiding/exposure factors given in Equations (53), (54) and (55). For the finer fractions (d_i<d_{rep}), the factors λ_i are found to be lower than unity while the factors ξ_i are greater than unity. These resulting numbers imply that their instantaneous bed shear stresses would decrease while their critical shear stresses increase. These implications are opposite for the coarser fractions (d_i>d_{rep}) due to the reversing trends in both of the factors. Compared to ξ_i^V, the factor ξ_i^E features a larger deviation from unity which also exceedingly increases for very fine and very coarse size fractions.

The hiding/exposure factors in Figure 48 appear to lead to the transport rates that are reduced for the finer size fractions and increased for the coarser fractions, i.e. compared to what would be expected from their availabilities. These potentials, however, depend also on the use of the factors in a particular formula and the nonlinear dependency between

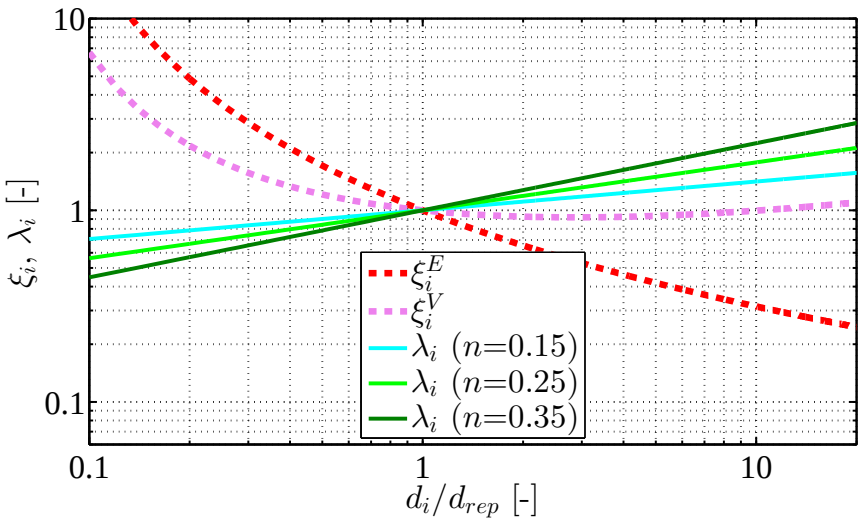

Figure 48: Adjusting factors on the instantaneous and the critical shear stress terms estimated using the hiding/exposure parameters. See Equations (53), (54), and (55) for their expressions.

grain sizes and the sediment transport rates. For instance, the factors would affect a transport prediction differently whether the transport rate is described to be directly or inversely proportional to the grain diameter (e.g. Figure 47). Selection and application of these hiding/exposure factors in this study are illustrated next, together with their fundamental consequences as the transport models are developed.

5.2 Bedload transport model

Both bedload and suspended-load sediment transports are considered in this study since their occurrences are simultaneous and significant in the nearshore zone. Each transport mode is defined according to its distinct mechanisms rather than a spatial reference. Bedload refers to the transport that is advected by near-bed velocity with at least intermittent contact with the bed surface. Suspended load accounts for the transport over the water column in the form of sediment flux. These mobilizing sediments may be induced by either or both bed shear stress and wave-breaking turbulence.

5.2.1 General formula

The bedload model introduced here is developed on the basis of conventional energetics-type, single-size sediment transport models (e.g. Watanabe 1987, 1992; Ribberink 1998;

Haas and Hanes 2004). The local volumetric transport rate $q_b(t)$ is related to the sediment mobility and the sediment advection velocity following

$$q_b(t) = \frac{C_b}{\rho g} \left[\tau_b(t) - \tau_{b,cr}\right] u_{b,sed}(t) \tag{56}$$

in which C_b is a calibration constant; τ_b is the instantaneous bottom shear stress; $\tau_{b,cr}$ is the critical shear stress; and $u_{b,sed}$ is the particle velocity at the bed level. The total near-bed fluid velocity which is utilized to determine τ_b is computed following

$$u_{b,tot}(t) = u_{w,b}(t) + V_b \tag{57}$$

where $u_{w,b}$ and V_b are the orbital velocity and the mean flow, both of which are considered on the bed level right above the wave boundary layer. Usually the particle velocity (u_{sed}) is assumed identical to this total fluid velocity, not only at this bed level but also higher up in the water column. Since this assumption is not always the case, a dedicated formula for a better description of the particle velocity was developed in this study and shown later in this chapter (Section 5.4).

The modification of Equation (56) for computing multi-size sediment transport rates was achieved by adopting the hiding/exposure concept discussed previously. The hiding factor on the critical shear stress ξ_i^E introduced by Egiazaroff (1965) is utilized as opposed to ξ_i^V suggested by Van Rijn (2007b). This decision was made since the latter factor is only defined relative to the basis critical stresses of nominally uniform sediment (see Equation (54)). Hence, the factor will never change from its initial value even if the sediment size composition changes as the size-selective sediment transport and grain sorting occur. The correction factor λ_i on the instantaneous shear stress term is also considered in the modification. Both of the factors ξ_i^E, henceforth ξ_i, and λ_i are related to the mean diameter (d_m) of the mixture.

With the consideration on the two hiding/exposure effects, the formulation of the new size-selective bedload transport model starts from estimating the effective bed-shear stress for each individual sediment size fraction following

$$\tau_{b,\text{eff},d_i}(t) = \left[\lambda_i \tau_{b,ins,d_m}(t) - \xi_i \tau_{b,cr,d_m}\left(\frac{d_i}{d_m}\right)\right] \tag{58}$$

in which the terms highlighted in red indicate the modifications by the hiding/exposure factors. If this effective shear stress is negative, it is taken as zero since this implies that the instantaneous shear stress is not strong enough for a sediment initiation of motion. The formula for estimating the potential transport rate of the i^{th} size fraction is then given as

$$q_{b,i}(t) = \frac{C_b}{\rho g}\left[\tau_{b,\text{eff},d_i}(t)\,(1 + F_{ecg})\right] u_{b,sed,d_i}(t) \tag{59}$$

where F_{ecg} is a wave breaking factor that accounts for turbulence-induced sediment pickup, approximated to be proportional to the effective shear stress. The derivation of this factor and related physical implication are illustrated later in Section 5.2.3. It may be noted that the advection velocity u_{b,sed,d_i} is now specified for each sediment fraction due to its dependency on the particle size. The total transport rate $q_{b,t}$ is subsequently computed by summing the potential transport rates in Equation (59), weighted by their percent occurrences in the mixture following

$$q_{b,t} = \sum_{i=1}^{N} p_i \overline{q_{b,i}} \tag{60}$$

where the overbar indicates a wave-averaged quantity, and N is the total number of sediment size fractions being considered with p_i as their percent of occurrences. The instantaneous shear stress term based on the mean diameter (τ_{b,ins,d_m}) in Equation (58) is described to consist of two important parts as follows

$$\tau_{b,ins,d_m}(t) = C_\tau \rho f'_{cw}\left[\frac{u^2_{b,tot}(t)}{2} + \kappa_s\left(\frac{d\,(u_{b,tot})}{dt}\right)_{RMS}\right] \tag{61}$$

where C_τ is a bed-shear adjustable coefficient; f'_{cw} is a friction factor; and κ_s is a local grain

roughness parameter. The first term in Equation (61) represents the shear stress induced by drag determined under a quadratic law. The second term represents an inertial effect under a wave motion, estimated based on the root-mean-square value of the local fluid acceleration. This latter influence is often neglected despite many proven effects of the acceleration on sediment transport and beach profile evolution (e.g. Elgar et al. 2001; Hoefel and Elgar 2003; Henderson et al. 2004). The friction factor f'_{cw} is calculated as a linear combination of the local wave and mean flow effects (e.g. Swart 1974; Ribberink 1998)

$$f'_{cw} = \alpha \cdot \underbrace{\left[0.8/\log\left(\frac{\delta}{\kappa_s/30}\right)\right]}_{f'_c} + (1-\alpha) \cdot \underbrace{\exp\left[5.2\left(\frac{\kappa_s}{\langle u_{w,b}\rangle}\right)^{0.194} - 5.98\right]}_{f'_w} \tag{62}$$

in which δ is a reference elevation approximated to be 1 cm, and α represents the relative influence between the wave and the current determined according to their magnitudes following

$$\alpha = \frac{\langle u_{w,b}\rangle}{[\langle u_{w,b}\rangle + V_b]} \tag{63}$$

where $\langle u_{w,b}\rangle$ is defined here as the velocity under the crest of a skewed/asymmetric wave; and V_b is the near-bed mean flow. Typically, the grain roughness κ_s is estimated to be proportional to a characteristic grain size such as d_m or d_{50} (e.g. Wilson 1989; Nielsen 1992). In the present model, it is approximated to be equal to "$50d_m$". An important criterion in describing this factor is to maintain reasonable proportions between the velocity and the acceleration contributions to the total shear stress in Equation (61). When the value of κ_s increases, the velocity term generally rises more slowly than the acceleration term that is directly proportional to κ_s.

5.2.2 Critical shear stress and bed-slope effect

The critical bed-shear stress τ_{b,cr,d_m} in Equation (58) is estimated on the basis of Shields diagram. The estimation is achieved by means of the following set of equations (Van Rijn, 1993) that relate the shear stress magnitude to a nondimensional grain size D_*:

$$D_* = d_m \left[\frac{g(\gamma_s - 1)}{\nu^2} \right]^{1/3} \tag{64}$$

$$\theta_{cr,d_m} = C_1 D_*^{C_2} \tag{65}$$

$$\tau_{b,cr,d_m} = \theta_{cr,d_m} \left[(\gamma_s - 1) \rho g d_m \right] \tag{66}$$

with C_1 and C_2 given as

D_* **range**	C_1	C_2
$1 < D_* \leq 4$	0.24	-1
$4 < D_* \leq 10$	0.14	-0.64
$10 < D_* \leq 20$	0.04	-0.1

where ν is the water kinematic viscosity; θ_{cr,d_m} is the Shields parameter; and γ_s is sediment specific gravity. The constants C_1 and C_2 depend on the ranges of D_* as shown on the right. Using this set of equations, Figure 49 shows estimated critical shear stresses for sand-size mixture of $0.065 \leq d_m \leq 0.8$ mm. In this given range, the resulting Shields parameters decrease for larger particles but the critical shear stresses increase due to a strong grain-diameter dependency.

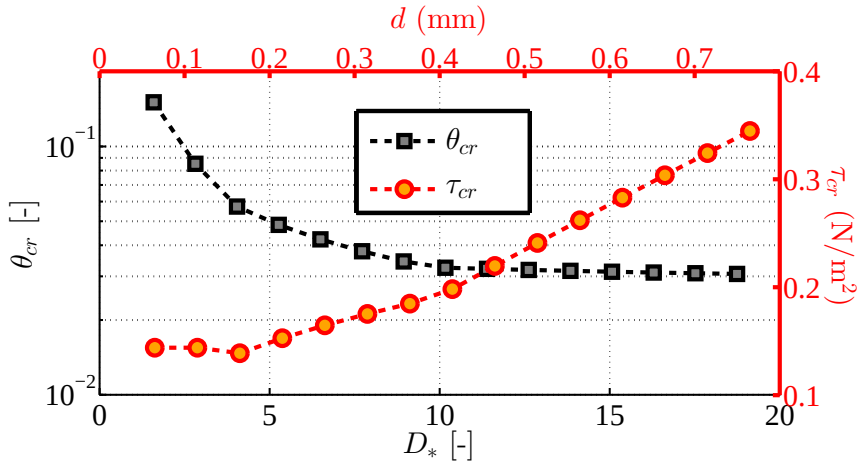

Figure 49: Shields parameters and critical bed-shear stresses estimated for sand-size mixture of $0.065 \leq d_m \leq 0.8$ mm. Top axis shows actual grain sizes and bottom axis shows non-dimensional grain sizes.

Bed-slope effect can be influential on sediment transport especially for steep and bar-type beach profiles. A bed-slope term is included in the present transport model to consider such effects through possible alteration of the local critical bed-shear stress. This term was obtained on the basis of a force balance equation of a sand grain resting on a longitudinal

slope (e.g. Fredsoe and Deigaard 1992), which follows

$$\tau_{b,cr,d_m} A + W_g \sin\beta = W_g \tan(\phi_s) \cos\beta \tag{67}$$

in which W_g is the grain weight; A is the grain surface area; and ϕ_s is the sediment angle of repose. The bed slope β is positive for decreasing depths towards the shoreline. By comparing between the cases of a flat bottom and a sloping bed, and considering the flow directions, the bed-slope term B_{st} that allows an alteration in the critical shear stress is given as

$$B_{st} = \left(\frac{\tau^{\beta}_{b,cr,d_m}}{\tau^{\beta=0}_{b,cr,d_m}} \right) = \cos\beta \left[1 - \frac{\tan\beta}{\tan\phi_s} \left(\frac{u_{b,tot}}{|u_{b,tot}|} \right) \right] \tag{68}$$

where $u_{b,tot}$ is the total near-bed fluid velocity. Ideally the angle of repose ϕ_s could also be a function of sediment characteristics but for a sandy mixture it may reasonably be approximated as 30^o constant (Dean and Dalrymple, 2002). Figure 50 shows the degrees of alteration on the critical bed shear stress up to this angle of repose. In overall, the resulting factors imply that a downslope transport will be enhanced and an upslope transport will be reduced due to the given bed-slope effect. At the angle of repose, the downslope transport will occur without any resistance and the upslope transport will feature the critical shear stress that is increased by approximately 70%.

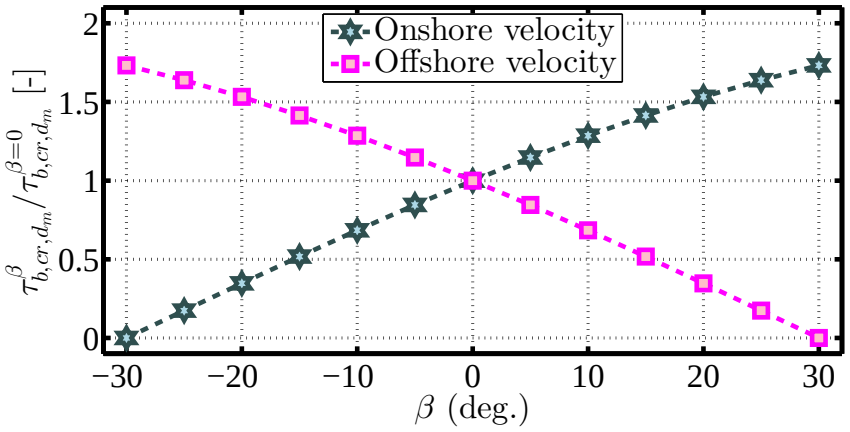

Figure 50: Alteration of the critical shear stress due to bed-slope effect estimated using the bed-slope term. Note that the alteration for a particular slope is considered separately for the two different flow directions.

5.2.3 Wave breaking effect on sediment mobility

Many field studies have confirmed a significant effect of wave-breaking turbulence on a profile evolution in the surf zone (e.g. Thornton et al. 1996; Voulgaris and Collins 2000; Aagaard and Hughes 2010). This effect is often claimed to be accounted for by resolving the velocity field under a breaking-wave condition. Besides that partial consideration, an attempt is made here to include a more direct wave-breaking impact on the sediment mobility as a breaking wave crest tumbles down on the profile. This mechanism can be observed extensively in many field studies and physical models as well as in the laboratory experiment conducted in this research.

Very limited knowledge is available for modeling the given wave-breaking effect. Dally and Dean (1984) attempted to include an extra shear stress term which was based on breaking wave energy dissipation, uncorrelated to the fluid velocity. The attempt resulted in an overemphasized impact of the breaking process attributed to the lack of attention on the cushioning mechanism in the water column. Morfett (1992) suggested that velocity- and turbulence-induced effects on the sediment motion occur simultaneously and were not usually separable for most surf zone data.

An alternative to account for the wave-breaking effect was attempted here to introduce a consistent and robust method in spite of the above limitations. The method involves an inclusion of a new wave-breaking factor with a role to predict additional sediment mobility. By representing the wave breaking turbulence via the gradient of the cross-shore energy flux, this wave-breaking factor is determined following

$$F_{ecg} = A_{br} \underbrace{\left(\frac{1}{\rho}\frac{\partial E_{fx}}{\partial x}\right)^{2/3}}_{TKE} \underbrace{\left(\frac{\overline{\tan\beta}^{(L/2)} + \gamma_h}{g\, H_{rmso}}\right)}_{PEN} \tag{69}$$

where A_{br} is the coefficient representing the intensity of the breaking effect; $\overline{\tan\beta}^{(L/2)}$ is the bed slope averaged over a distance of half of the local wave length; γ_h is the local relative wave height parameter (H_{mo}/h); H_{rmso} is the offshore RMS wave height; and E_{fx} is the cross-shore energy flux, a phase-averaged quantity.

The first term in the bracket in Equation (69) represents the turbulent kinetic energy

dissipation (TKE). The second term is described as a penetration factor (PEN) that indicates the degree at which the sediment is to be mobilized due to the breaking waves. This term accounts for the type of wave breaking via a surf-similarity-like parameter, and the effect of water cushioning via the relative wave height parameter. The formulation of these terms is achieved based partly on Church and Thornton (1993) who suggested a similar parameter for vertical mixing effect in a longshore current problem.

In the bedload model, this wave-breaking factor is applied directly in the determination of the sediment transport rate as shown in Equation (59). One noteworthy assumption here is the fact that the extra sediment mobility is predicted proportional to the mobility due to the effective shear stress. Therefore, the wave breaking effect may not be presented solely where the bottom shear stress is lower than the threshold level (Equation (75)). This limitation, however, is unlikely to be the case since the fluid velocity is usually strong enough for an active bed condition over the wave-breaking zone.

5.3 Suspended-load transport model

5.3.1 Advection-diffusion model

The suspended sediment transport is modeled here based on the horizontal sediment flux, computed for an individual size fraction as functions of the sediment concentration "c_i" and the advection velocity "$u_{sed,i}$". The determination of the concentration (c_i) is achieved following an advection-diffusion model that treats the sediment suspension as a diffusive process. A full governing equation for this type of model consists of convective and diffusive terms in both the vertical and the horizontal. For a nearshore application, a simplification is typically made by considering only the vertical terms since the horizontal concentration gradient is usually very small (e.g. Fredsoe and Deigaard 1992). Under this simplified condition, the first-order governing equation in the model can be written as

$$\frac{\partial c_i}{\partial t} - (W_{f,i})\frac{\partial c_i}{\partial z} = \epsilon_s \frac{\partial}{\partial z}\left(\frac{\partial c_i}{\partial z}\right) \tag{70}$$

in which $W_{f,i}$ is the sediment fall velocity for each size fraction and ϵ_s is the sediment diffusivity coefficient. Multiple fall velocities in this equation are expected to lead to varying

degrees of the grain size dependency in the sediment suspension. The vertical convection term due to vertical orbital velocity, i.e. $w_w \frac{\partial c_i}{\partial z}$, is neglected in this equation. Demir (2007) concluded that this term, actually second-order, would modify the concentration only where the concentration is very low. It is excluded here, however, also because of an instability issue in cases of very fine size fractions under highly skewed/asymmetric waves with very strong upward velocities. The vertical orbital velocity prediction may have to be revised for the robustness of the model with this convection term included.

The diffusivity factor ϵ_s in Equation (70) may ideally be described for individual size fractions, i.e. written otherwise as $\epsilon_{s,i}$. However, no information regarding these fractional dependencies in a sediment mixture is available. The factor here is therefore treated as a size-invariant factor, related to the eddy viscosity in the flow ν_t via a proportional factor following

$$\epsilon_s = \beta_\epsilon \nu_t \tag{71}$$

where ν_t is taken as estimated in the hydrodynamic model (e.g. Equation (27), Chapter 4). Even though poorly understood and often taken as one, the proportionality factor β_ϵ is certainly a function of a "representative" sediment size and the intensity of the flow (e.g. Davies 1995). For this reason, the factor is given here following the semi-empirical formula suggested by Van Rijn (1984) that follows

$$\beta_\epsilon = 1 + 2\left[\frac{W_{f,d_m}}{\sqrt{\tau_{b,d_m}^{\max}/\rho}}\right]^2 \tag{72}$$

where $\tau_{b,d_m}^{\max}$ is taken as the maximum bottom shear stress over a wave period; in the original formula, the bottom shear stress under a steady flow was utilized. In the zone where sediment transport occurs, the varying term in this equation is usually less than one which yields the values of β_ϵ between 1.0 to 3.0. This range of the factor is comparable to suggested in other investigations between 0.5 to 4.0 (e.g. Dohmen-Janssen et al. 2001; Malarkey et al. 2003; Davies and Thorne 2005). Note that this parameter only varies along the cross-shore direction, not over the vertical nor the wave period.

Equation (70) is solved numerically using a Crank-Nicolson scheme to obtain the sediment concentration over the water column. Two boundary conditions that are involved in the solution include a zero-flux condition at the water surface and a reference concentration given at the bottom. The surface condition is written as

$$\epsilon_s \frac{\partial c_i}{\partial z} + (W_{f,i}) c_i = 0 \Big|_{z=\bar{\zeta}} \tag{73}$$

in which a steady water surface under a wave is assumed at the mean water level ($\bar{\zeta}$) to facilitate the numerical solution. This simplification is often justified by arguing that the concentration near the surface is negligible which, in fact, is not always the case. Suspended sediment fluxes in the wave crest region are also considered in this study using a simplified formula illustrated later (Equation (79)).

5.3.2 Reference concentration

Bottom shear stress and wave-breaking turbulence are the most significant processes that entrain nearshore sediment into suspension (Dally and Dean, 1984). Both of these mechanisms are considered here in the determination of the reference concentration which essentially controls both magnitude and variation of a resulting sediment concentration field.

The entrainment of sediment induced by shear stress is analogous to the process considered in the bedload model. The bed-shear stress would also act to pick up the sediment into suspension besides initiating the bedload transport. This part of the concentration is thus related to the effective shear stress term following

$$c_{b,sh,d_i} = \frac{d_i}{\delta D_{*,i}^{0.3}} \Theta_i'^{,1.5} \tag{74}$$

where c_{b,sh,d_i} is the volumetric shear-based concentration of the i^{th} size fraction; δ is the reference elevation measured from the bottom; and $D_{*,i}$ is the non-dimensional grain size

(Equation (64)). The normalized shear parameter Θ'_i is given as a function of the size-dependent effective shear stress following

$$\Theta'_i = \underbrace{\left[\lambda_i \tau_{b,ins,d_m}(t) - \xi_i \tau_{b,cr,d_m}\left(\frac{d_i}{d_m}\right)\right]}_{=\tau_{b,\mathrm{eff},d_i}(t)} \Big/ \left[\tau_{b,cr,d_m}\left(\frac{d_i}{d_m}\right)\right] \tag{75}$$

in which all of the shear stress terms are as described in the bedload model. Again, the terms highlighted in red indicate the modifications by the hiding/exposure factors. For a single-size consideration, all of these highlighted terms are equal to one and may thus be dropped to yield a total concentration based on the mean grain size c_{b,sh,d_m}. Equation (74) was developed based on a general formula suggested by Van Rijn (1993, 2007b) which had been validated with many steady and oscillatory-flow data sets. The formula here, however, features a different size-selective consideration and does not include an empirical constant.

A dedicated reference concentration term is introduced here in order to account for the wave-breaking effect on the sediment suspension. With the use of the wave-breaking factor (Equation (69)), this turbulence-induced reference concentration is described to be proportional to the shear-based reference concentration following

$$c_{b,br} = \left[\frac{d_m}{\delta D_{*,d_m}^{0.3}} \Theta'^{,1.5}_{d_m}\right] . F_{ecg} \tag{76}$$

in which the term in the bracket is essentially Equation (74) computed for the mean size of the mixture (c_{b,sh,d_m}). The major assumption in this formula was made regarding the size-selectivity consideration. It is assumed that the turbulence acts equally to pick up all size-graded fractions in the sediment mixture. The net reference concentration for each size fraction can thus be computed as a combination of the two concentration terms as follows

$$c_{b,net,d_i} = (c_{b,sh,d_i} + c_{b,br})\, p_i \tag{77}$$

where p_i is the percent occurrence of the i^{th} size fraction. This net reference concentration

is the bottom boundary condition in the advection-diffusion model that is solved for the concentration field of each size fraction in the sediment mixture.

5.3.3 Sediment flux and transport rate

The total sediment flux here is described to consist of two portions. One is the major flux in the water column covering up to the mean water level, and the other is the flux found in the wave crest region. The first portion is computed based on the concentration obtained from the advection-diffusion equation following

$$f_{s,i} = \frac{1}{T} \int_{-h_o}^{\bar{\zeta}} \int_{0}^{T} u_{sed,i}(z,t)\, c_i(z,t)\, dt\, dz \tag{78}$$

where T is the wave period; $f_{s,i}$ is the phase-averaged net sediment flux; $u_{sed,i}$ is the horizontal particle velocity; and c_i is the volumetric sediment concentration. All of these parameters are described for the i^{th} size fraction.

A negligence of sediment flux above a mean water surface may not be realistic in the surf zone where a substantial amount of sediment can be suspended in part of the wave crest and promptly advected onshore. This fact is the main reason that the sediment flux in the wave crest region is also included in the present model. The formula for the estimation of this portion of sediment flux is given as

$$f_{s,\mathrm{crest},i} = Q_{wx}\, \overline{c_{\mathrm{crest},i}} \tag{79}$$

in which $f_{s,\mathrm{crest},i}$ is the phase-averaged, wave-crest sediment flux; Q_{wx} is the wave mass flux; and $\overline{c_{\mathrm{crest},i}}$ is an approximated, wave-averaged concentration that is carried onshore with the wave. This concentration is determined by weight averaging the surface concentration over the wave crest passage following

$$\overline{c_{\mathrm{crest},i}} = \frac{\int_{\xi}^{\xi+T_c} c_i(\bar{\zeta},t)\, \eta(t)\, dt}{\int_{\xi}^{\xi+T_c} \eta(t)\, dt} \tag{80}$$

where $c_i(\bar{\zeta},t)$ is the instantaneous concentration modeled at the mean water level ($\bar{\zeta}$); $\eta(t)$

is the instantaneous water surface measured from the mean water level ($\bar{\zeta}$); ξ is the starting time that the wave crest arrives ($\eta(t)>0$); and T_c is the period of the wave crest passage. The use of this equation assumes that the instantaneous sediment concentration is constant between the mean water level to the actual water surface. For an individual sediment size fraction, the local net suspended transport rate $q_{s,i}$ is finally computed based on the combined sediment fluxes following

$$q_{s,i} = C_s \left[f_{s,i} + f_{s,\text{crest},i} \right] \tag{81}$$

in which the suspended-load transport efficacy factor C_s is treated as a calibration constant. Similar to that of the bedload, the total suspended sediment transport rate $q_{s,t}$ is subsequently computed as a summation of the contributions from all available sediment size fractions

$$q_{s,t} = \sum_{i=1}^{N} q_{s,i} \tag{82}$$

where it should be noted that the percent of occurrences (p_i) of the fractions in the mixture are already accounted for in the computation of their concentrations.

5.4 Determination of sediment particle velocity

For a steady or long-period oscillatory flow, the sediment velocity u_{sed} and the total fluid velocity u_{tot} may reasonably be assumed identical since any difference between them would eventually vanish. This aspect is, however, not the case under a short wave motion where the sediment may not even reach the flow velocity before it reverses. For this reason, a separate instantaneous particle velocity $u_{sed}(t)$ is clearly preferred for the present sediment transport models. An expression for this new velocity was developed on the basis of the laws of motion. Drawing a free body diagram of a sand grain freely suspended in the water, the force balance between the drag and the inertia on the particle can be expressed

in terms of the two velocities as

$$\frac{1}{2}\rho\, C_d \mathbb{A}\,[u_{tot}(t) - u_{sed}(t)]^2 = \mathbb{M}\,\frac{\partial(u_{sed}(t))}{\partial t} \tag{83}$$

where C_d is the drag coefficient; $\mathbb{A}$ is the projected area on the sediment particle; and $\mathbb{M}$ is the mass of the particle. The instantaneous fluid velocity u_{tot} is provided from the hydrodynamic model (wave+current) leaving the sediment velocity u_{sed} as the only unknown to be solved readily. An important assumption made here is that the horizontal advection of the suspended particle is either occurring much faster than its vertical settling, or featuring very small variation over the water column. This latter condition is generally the case in the nearshore zone where the horizontal orbital velocity is fairly depth uniform. The mean current may feature more depth variation but its magnitude is usually considerably smaller than that of the orbital velocity.

To obtain a time series of u_{sed}, Equation (83) was solved using a simple finite-difference scheme. The equation is rewritten in a discretized form as

$$u_{sed}^{n+1} = \frac{\Delta t}{2\mathbb{M}}\rho\, C_d \mathbb{A}\,(\Delta u^n)^2\,\frac{\Delta u^n}{|\Delta u^n|} + (u_{sed}^n) \tag{84}$$

in which the superscript n denotes the time step and Δu^n is the instantaneous difference between the two velocities equal to $u_{tot}^n - u_{sed}^n$. Figure 51 shows a comparison between the flow velocity under a skewed wave and the sediment velocities estimated for three different particle diameters. The particles are assumed spherical and the drag coefficients (C_d) are obtained as a function of time-dependent Reynolds numbers. In general, both phase lags and magnitude differences between the two velocities are found to increase for larger particles that feature higher masses. Due to the interdependencies among the drag coefficient and the two velocities, the differences shown in Figure 51 may also change as the flow condition changes.

Figure 52 shows estimated phase lags and magnitude differences between the two velocities as a function of the relative water depth kh. The results are computed per their peak magnitudes and cover up to intermediate-water waves ($kh<\pi$). It is around this upper limit that the maximum magnitude difference of 20% and the maximum phase

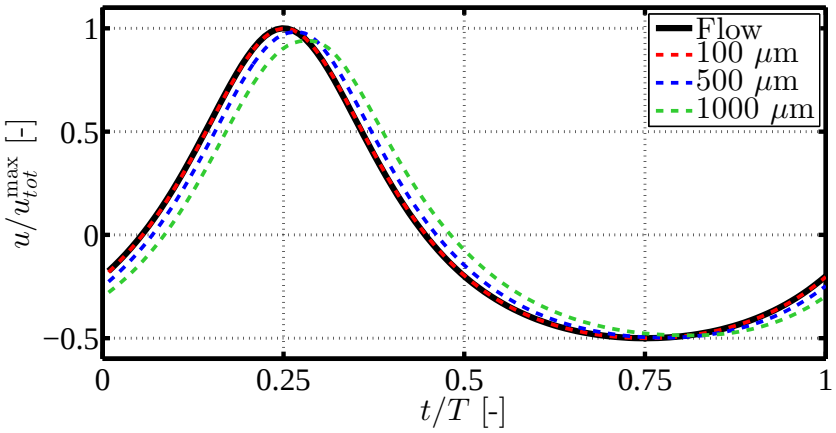

Figure 51: Comparison between the fluid and sediment velocities estimated for three different grain sizes. Assumed H/h and kh are equal to 0.25 and 1.5 respectively (intermediate water depth), with a wave skewness of 0.6. The time series were computed at half of the water depth.

lag of 17^o are observed. These differences are lower for longer waves that are associated with reduced acceleration. The magnitude of the orbital velocity itself (i.e. constant kh) would also have a substantial influence on the results. Smaller waves would be associated with larger values of the two differences, primarily due to the fact that the increases in the drag coefficients are not as acute as the reduced advection velocities.

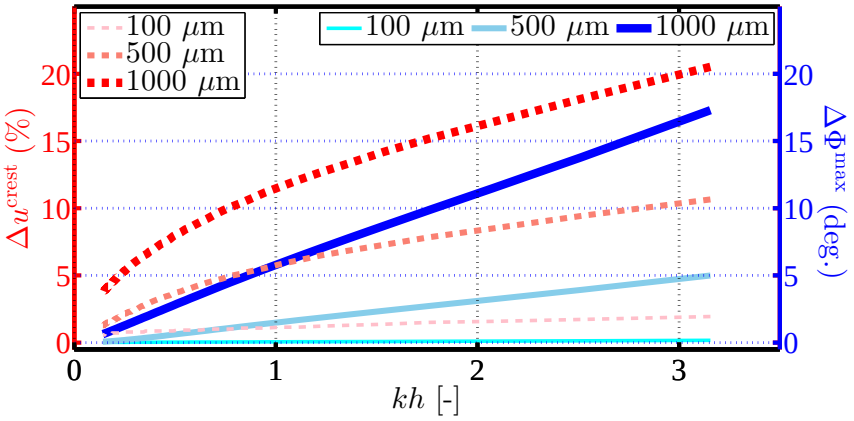

Figure 52: Phase lags and magnitude differences between the flow and sediment velocities evaluated at their peak magnitudes. Assumed H/h of 0.25 and varying wave periods are used with a wave skewness of 0.6. The results are based on the computation at half of the water depth.

5.5 *Morphology model*

The major role of the morphology model here is to resolve evolving bathymetry and changing sediment-bed condition. The former task is achieved by the use of the Euler-WENO (Weighted Essentially Non-Oscillatory) numerical model that is built in to the NearCOM modeling system. The determination of the time-dependent bed condition is performed using a newly developed grain sorting model. Details of these two interactive models are provided in this and the next sections.

The Euler-WENO numerical scheme (Long et al., 2006) solves for a bathymetric evolution following a sediment conservation equation, written in a cross-shore domain as

$$\frac{\partial h_o(x,t)}{\partial t} = \frac{1}{(1-\varrho)}\frac{\partial (q_{tot})}{\partial x} \tag{85}$$

where h_o is the depth from the still water level; ϱ is the sediment porosity; and q_{tot} is the time-averaged, depth-integrated, total sediment transport rate combining bedload and suspended load ($q_{b,t}$+$q_{s,t}$). The WENO scheme aims to resolve Equation (85) while preventing oscillation of the bathymetry that may occur due to large sediment transport gradients. The oscillation is prevented by first redefining a local sediment transport gradient following

$$\frac{\partial (q_{tot})}{\partial x} = \frac{\hat{q}_{t,k+1/2} - \hat{q}_{t,k-1/2}}{\Delta x} \tag{86}$$

in which the subscript k denotes a grid point at a cross-shore location. Each of the $\hat{q}_t$ terms indicates an estimated transport rate at half of the distance between a pair of computational cells. In this estimation, the term is split again into a left-bias(-) and a right-bias flux(+); for instance

$$\hat{q}_{t,k+1/2} = \hat{q}^{(-)}_{t,k+1/2} + \hat{q}^{(+)}_{t,k+1/2} \tag{87}$$

This "bias flux" term is defined since the transport rates at three adjacent points in the given side are weight-averaged, while only two points in the other direction are considered. It is recommended to refer to Long et al. (2006) for the derivation of these bias terms. At a

particular location, only one bias term is utilized depending on the celerity of the changing bedform $C_{x,k}$ that follows

$$C_{x,k} = -\frac{1}{(1-\varrho)} \frac{\partial q_{tot}}{\partial x} \Big/ \frac{\partial h_o}{\partial x} \tag{88}$$

The left-bias term is considered for a positive bedform celerity indicating a profile accretion ($0<C_{x,k}$), and the right-bias term is used for the opposite condition ($0>C_{x,k}$). Once these terms are determined, the transport gradient in Equation (86) can be computed and inserted into the mass conservation equation which is subsequently solved by means of an Euler-explicit method. This WENO numerical scheme provides fifth-order accuracy in space and first-order accuracy in time.

5.6 Grain sorting model

The principle of sediment size composition tracking under mass conservation is utilized in the new grain sorting model developed in this research. The model is configured to function at a chosen time interval over which the bed profile evolution is significant. Once determined, a new sediment-bed condition is superimposed onto the bathymetry updated using the WENO scheme described above.

For clarity, the model is illustrated here consecutively for its initial setup and two major steps associated with erosion and deposition of size-graded sediment fractions in the grain-sorting processes.

5.6.1 Initial setup

A dedicated two-dimensional numerical grid is established for the model to facilitate the tracking of size composition changes inside the sediment bed. The horizontal resolution of the grid is taken as that of the sediment transport model to avoid additional interpolation. An appropriate vertical resolution of the grid, which is crucial for resolving the vertical grain lamination, can be chosen based on the scale of the domain and the intensity of the sediment transport process.

An example is given in Figure 53 for a multi-layer grid that was created for an application under the laboratory condition in this study. The grid was created so that it covered the

zone with potential profile evolution and still allowed sufficient vertical space for keeping track of the mobilizing sediment fractions. This entire zone, i.e. for this particular example only, was anticipated to be within 30 cm above and below the initial profile spanning from the profile toe to the maximum wave run-up location.

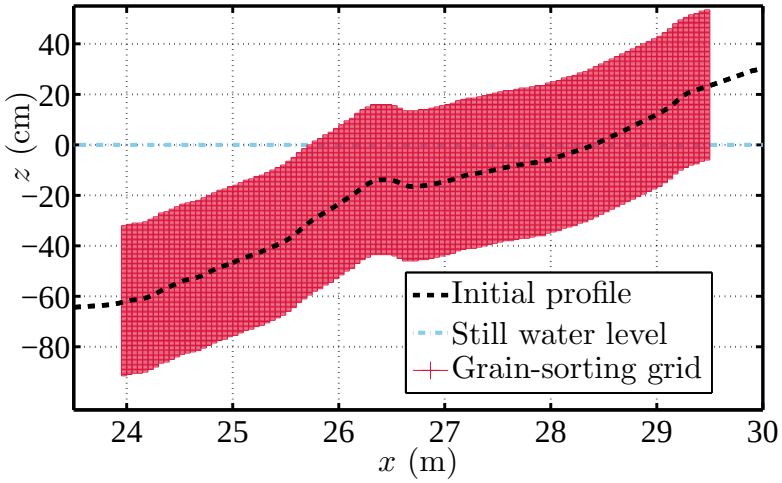

Figure 53: Example of a multi-layer numerical grid utilized in the grain sorting model. Horizontal and vertical resolutions are 5 cm and 0.25 cm, respectively.

At the initial condition, a user-defined number of sediment size classes and their percent occurrences are assigned for the cells beneath the bed surface. The profile and the sediment properties are updated by resolving the grain sorting based on inputs from the sediment transport model. These inputs are the multi-fractional sediment transport rates that are rearranged as

$$q^{L}_{k,i} = \overline{q_{b,k,i}(-)} + \overline{q_{s,k,i}(-)} \tag{89}$$

and

$$q^{R}_{k,i} = \overline{q_{b,k,i}(+)} + \overline{q_{s,k,i}(+)} \tag{90}$$

where the subscript k and i denote a cross-shore grid point and a sediment size fraction, respectively. Equation (89) represents the multi-fractional sediment transport rates that are directed offshore (left direction). These rates are obtained by summing time-averaged values of both bedload ($\overline{q_{b,k,i}(-)}$) and suspended load ($\overline{q_{s,k,i}(-)}$) that are negative. Similarly,

the corresponding rates that are directed onshore are computed as shown in Equation (90). Given a horizontally uniform grid spacing ($\Delta x'$), the volumes of these two eroded sediments can be represented through their thicknesses $G_k^{q_L}$ and $G_k^{q_R}$ computed as

$$G_k^{q_L} = \frac{T_{gm}}{\Delta x'} \sum_{i=1}^{N} q_{k,i}^{L} \;\; ; \text{ and } \;\; G_k^{q_R} = \frac{T_{gm}}{\Delta x'} \sum_{i=1}^{N} q_{k,i}^{R} \tag{91}$$

where N is the total number of size fractions; and T_{gm} is the duration after the previous call to the grain sorting model, equal to the period over which the input multi-fractional rates in Equations (89) and (90) are time-averaged.

The total erosion depth G_k^{ero} at a local position is given as a combination of the thicknesses given in the above equations ($G_k^{q_L} + G_k^{q_R}$). The size composition of the sediment in this eroded sediment $D_{k,i}^{ero}$ can be thus obtained following

$$D_{k,i}^{ero} = \frac{D_{k,i}^{q_L} G^{q_L} + D_{k,i}^{q_R} G^{q_R}}{(G_k^{ero})} \tag{92}$$

in which $D_{k,i}^{q_L}$ and $D_{k,i}^{q_R}$ are obtained straightforwardly based on the multi-fractional sediment transport rates $q_{k,i}^{L}$ and $q_{k,i}^{R}$.

5.6.2 Erosion stage

The size selectivity in the sediment transport is assumed to lead to three distinctive sediment portions, referred to as an eroded portion, a mixing portion, and a remaining portion. Figure 54 shows a definition sketch of these three portions and related parameters that are determined in this erosion stage. Two associated properties required to be known for these sediment portions includes their size compositions ($D_{k,i}$) and their volumes, i.e. represented via the thickness (G_k). These quantities in the eroded portion obtained readily from the size-selective transport rates are utilized for an estimation for the other two portions.

The mixing depth in the sediment bed (G_k^{mix}) is estimated considering the availability of each sediment size fraction, neglecting the armoring effect that is expected to be minimal for a sand-size mixture. For example, if the abundance of a size fraction in the predicted

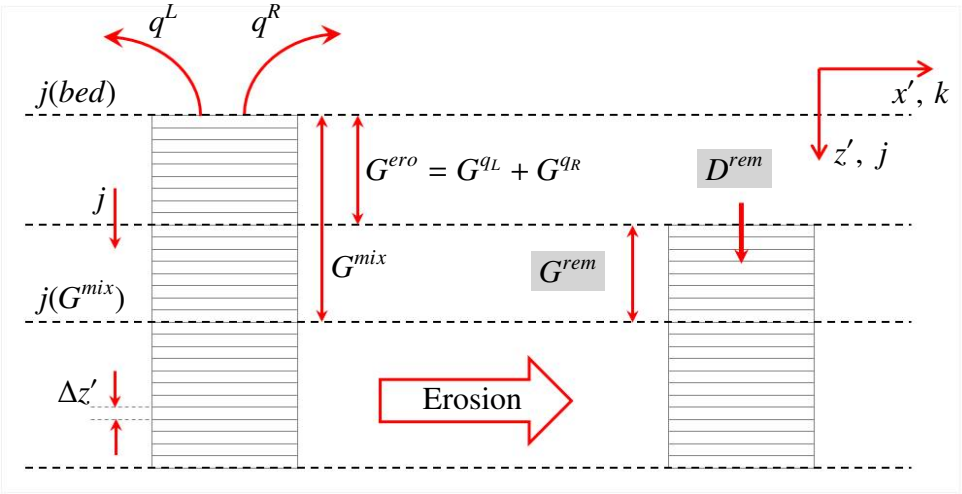

Figure 54: Overview of three sediment portions and associated parameters in the erosion stage of grain sorting computation. Sediment outflow at an individual cell is considered at this stage. Coordinate $x' - z'$ has its origin at the top of the numerical grid at the furthest offshore location.

transport rate is twice as much as that of the initial mixture, the mixing depth will need to be twice the thickness of the erosion depth so that the amount of this particular size fraction can be satisfied. The mixing depth is then estimated so that the most critical fraction can be fulfilled. Assuming a complete mixing process, the size composition within this mixing depth is thus computed following

$$D_{k,i}^{mix} = \frac{1}{G_k^{mix}} \sum_{j(bed)}^{j(G^{mix})} D_{k,i,j}^{ini} \Delta z' \tag{93}$$

where $D_{k,i}^{mix}$ is the percent occurrence of the i^{th} size fraction in the mixing portion at the k^{th} cross-shore grid point; the other notations are as defined in Figure 54. The starting values of the size distributions $D_{k,i,j}^{ini}$ are known from the initial sediment condition or provided from the previous computation step.

The remaining portion represents the sediment that is left behind in the mixing layer as a consequence of the erosion. The size composition in this portion can be computed by weighted averaging of the different amounts of the mixing and the eroded portions and the

percent occurrences of their individual size fractions, following

$$D_{k,i}^{rem} = \frac{D_{k,i}^{mix} G^{mix} - D_{k,i}^{ero} G^{ero}}{G_k^{rem}} \tag{94}$$

At the end of this stage, an eroded sediment bed and the size composition beneath its surface are prepared at every cross-shore grid point on the profile. This information is utilized in the next computation stage that considers the deposition of sediment into each eroded cell.

5.6.3 Deposition stage

The deposition of sediment into an eroded cell is determined based on the sediment fluxes from its adjacent cells. For a particular cell at the k^{th} grid point on the profile, the net sediment deposition $q_{k,i}^{dep}$ can be determined as

$$q_{k,i}^{dep} = q_{k-1,i}^{R} + q_{k+1,i}^{L} \tag{95}$$

where $q_{k-1,i}^{R}$ is the onshore sediment flux of the adjacent "seaward" cell, and $q_{k+1,i}^{L}$ is the offshore sediment flux of the adjacent "shoreward" cell. Note that this expression is specified for each individual i^{th} sediment size fraction. Figure 54 shows an overview of this deposition stage and a definition sketch of related parameters.

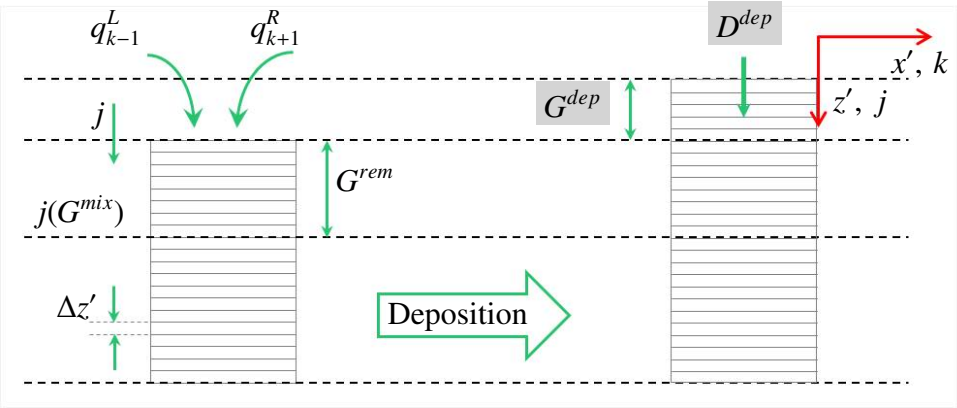

Figure 55: Overview of three sediment portions and associated parameters in the deposition stage of grain sorting computation. Sediment influx at an individual cell is considered at this stage. See Figure 54 for more details.

Based on the incoming sediment fluxes, the grain size composition of the sediment deposited into a cell is determined for updating the sediment bed condition. This size distribution is computed by weighted averaging of the availabilities of individual size fractions in the fluxes from the seaward and the shoreward cells, following

$$D_k^{dep} = \frac{q_{k-1,i}^R G_{k-1}^{q_R} + q_{k+1,i}^L G_{k+1}^{q_L}}{G_k^{dep}} \tag{96}$$

where G_k^{dep} is the total deposition depth, equal to $G_{k-1}^{q_R} + G_{k+1}^{q_L}$ (see Equation (91)). All of the other associated terms are as computed earlier in the erosion stage. Once this deposition-stage computation is completed, sediment size characteristics beneath the bed profile are stored for the next time step. The size composition in the surface layer averaged over 2 cm is utilized in the sediment transport model to compute for the representative diameter (d_m). This grain sorting computation is then continued for the erosion stage with new sediment fluxes from the sediment transport model.

5.7 Model tests and sensitivity analyses

The sediment transport and grain sorting models described above are tested in this section. The primary goal is to investigate behaviors of the models under the size-selective approach, compared to the single-size approach, including their sensitivities to various hydrodynamic and sediment size characteristics.

5.7.1 Bedload model

It is worthwhile to first illustrate the size-selectivity trend predicted by the bedload model. Figure 58 provides this information based on the ratios between the potential fractional transport rates and that of the mean grain size d_m, for three types of sand utilized in this study. Note that "potential" transport rates are computed "excluding" percent occurrences of sediment size fractions in a mixture. Regardless of the mixtures, these ratios are less than one for the finer fractions ($d_i/d_m<1$), which imply reduced transport rates influenced mainly by the hiding and exposure factors λ_i and ξ_i. The resulting ratios here generally indicate that the coarser fractions would be transported more than what would be expected

based only on their abundances. This transport tendency is in agreement with general findings of size-graded sediment transport classified as bedload (e.g. Dibajnia and Watanabe 1996; Dohmen-Janssen 1999; Ahmed and Sato 2003).

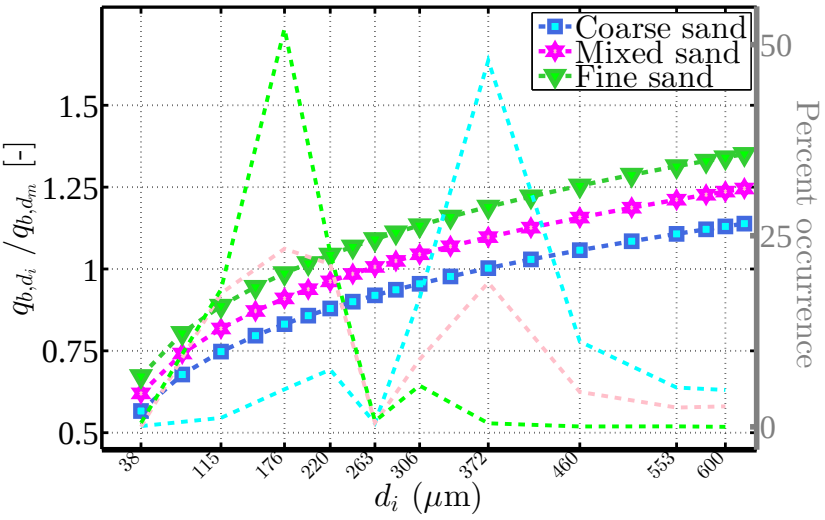

Figure 56: Size-selectivity trend in the potential multi-fractional transport rates predicted by the bedload model. Percent occurrences (p_i) are shown in dashed lines against the right axis; they are not considered in computing the potential transport rates q_{b,d_i}.

Figure 58 shows instantaneous multi-fractional transport rates computed for three size fractions from the mixed sand, under four cases, each with skewed-only or skewed-asymmetric wave, and offshore(-) or onshore(+) mean flow (Figure 57). The coarsest fraction (460 μm) is found to feature the highest potential transport rates ($q_{b,i}$) in every case but its actual transport rates $q_{b,i}p_i$ are the lowest due to its limited abundance. The skewed-asymmetric wave with an offshore mean flow in Figure 58(a) is a typical condition in the surf zone and the predicted transport rates are dominating under the wave trough because of a stronger combined wave and current velocity ($u_{b,tot}$). The skewed-only wave with a small onshore mean flow is a common scenario just outside the surf zone, which leads to dominant transport rates under the wave crest. These two different transport patterns result in opposite directions of the net sediment transport rates that are hypothesized as a mechanism for a sandbar formation. A subsequently onshore or offshore sandbar migration will also be influenced by potential variations in these sediment transport patterns.

In general, the single-size and the multi-fractional approaches will yield increasingly different results as the sediment size distribution becomes broader. This difference will

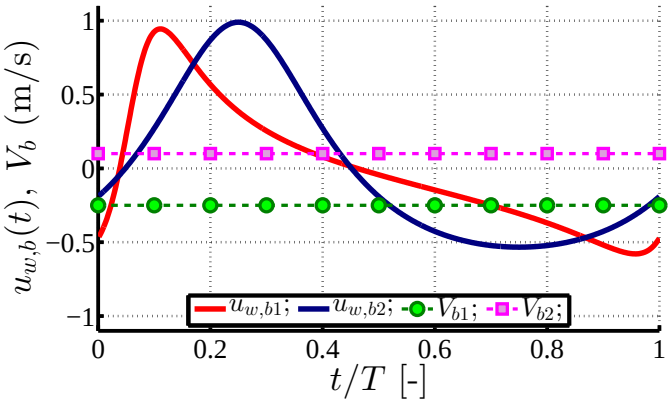

Figure 57: Near-bed orbital velocities and mean flows assumed for the bedload transport demonstration in Figure 58. Four combinations of wave and mean flow are generated from these given velocities.

also be much more prominent as the size distribution becomes more asymmetric against the representative diameter d_m. Figure 59 illustrates percent differences between the net sediment transport rates computed using the two approaches ($\Delta q_{b,t}$) based on three types of sand. Sensitivities in the transport rates due to coarsening and fining in the mixtures, as a result of grain sorting, are also illustrated in this example. Here it is assumed that the coarsening is the condition where the mixture is sorted to approach the coarse-sand size composition. This assumption is reversed for the fining and these assumed changes are shown in Figure 60.

At an initial condition (Δp_i=0), the computed percent differences of the net transport rates between the two approaches are negligibly small for all types of sand since their size distributions are rather symmetric against d_m. Coarsening of the mixtures is found to be associated with a decrease of the percent differences as a result of a reduction in the net sediment transport rate predicted by the multi-size model. This reduction is simply due to an increase of critical shear stress because of a larger mean diameter. The instantaneous shear stress may also increase, i.e. due to a larger grain roughness κ_s, but not more than the increment in the critical shear stress term. Due to opposite reasons, a positive change of the percent differences is found to be the case for grain fining in the sediment mixtures.

While either transport model may always be changed or recalibrated on a case-to-case basis, only the size-selective model accounts for the time-dependent grain sorting and changing sediment size characteristics. This aspect may be regarded as one of the most promising utilities of the size-selective approach over a traditional single-size approach. It may be remarked that the linear sensitivities against the grain sorting found here are a

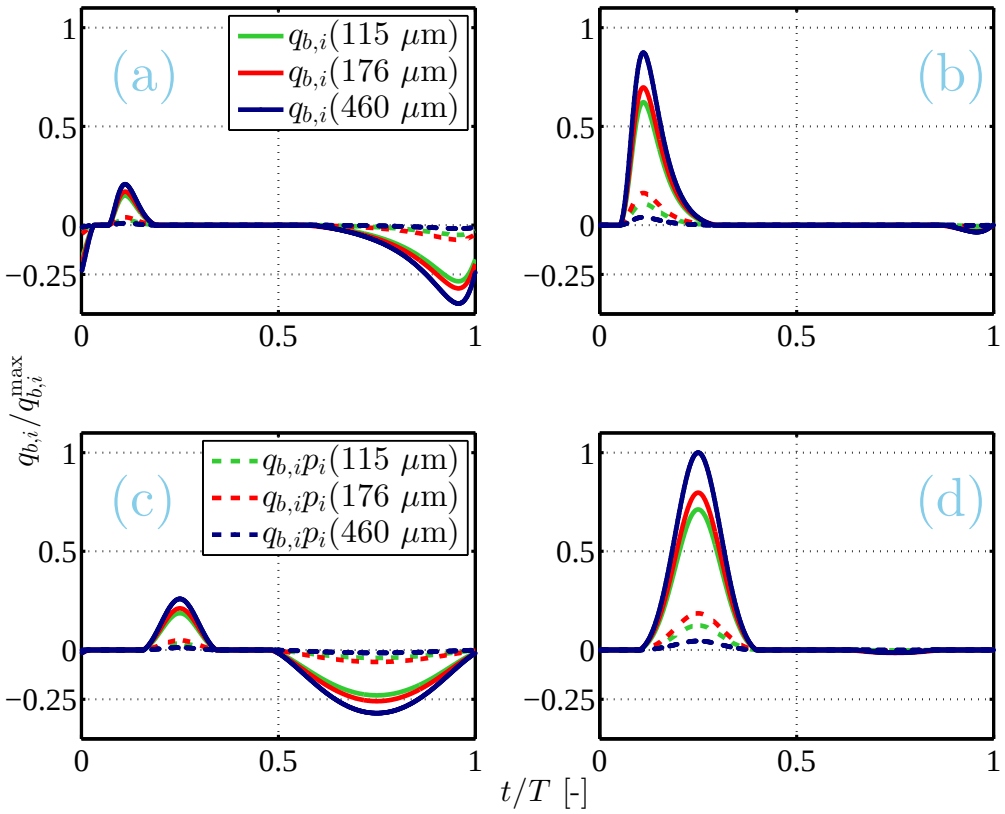

Figure 58: Examples of instantaneous bedload transport rates computed under a wave period based on four assumed scenarios in Figure 57: (a) $u_{w,b1} + V_{b1}$; (b) $u_{w,b1} + V_{b2}$; (c) $u_{w,b2} + V_{b1}$; (d) $u_{w,b2} + V_{b2}$. The resulting transport rates were normalized against the maximum value. Solid lines indicate potential transport rates; dashed lines indicate actual transport rates.

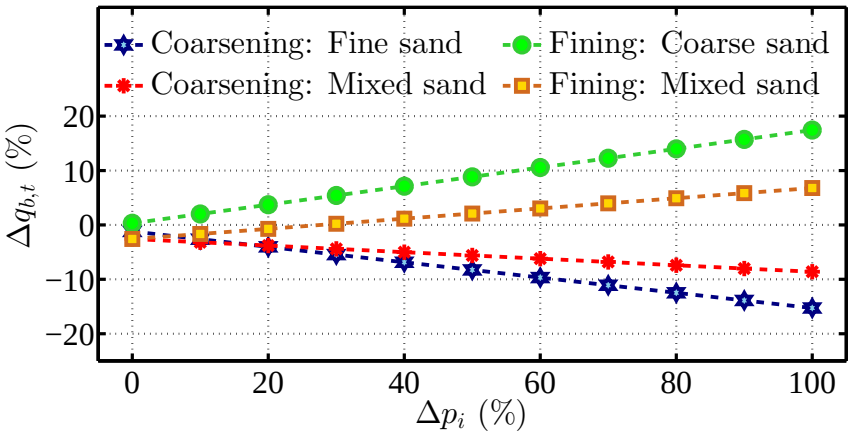

Figure 59: Percent differences between the total transport rates predicted by the size-selective and the single-size approaches. The percentages $\Delta q_{b,t}$ are defined based on the size-selective results. The sorting degree Δp_i is defined as shown in Figure 60.

possible consequence from the systematic size-composition changes assumed in the test (e.g. Figure 60). Grain sorting in nature will occur randomly which may not lead to a linear sensitivity in the model.

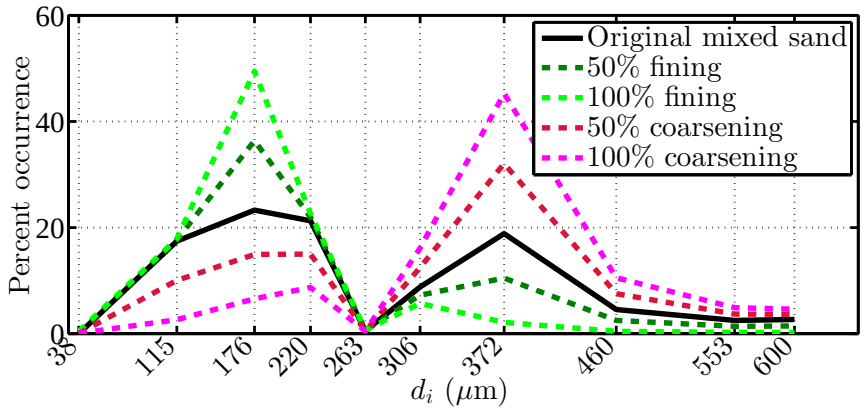

Figure 60: Assumed conditions of grain fining and coarsening of the mixed-sand mixture. The mixture is assumed to become identical to fine sand and coarse sand at 100% fining and coarsening, respectively.

5.7.2 Suspended-load model

Several computational steps in the suspended-load model are illustrated here based on the surf zone wave condition assumed previously (see Figure 58(a)). Reference concentrations computed for three size classes in the mixed sand are illustrated in Figure 61. These concentrations consist of bottom shear and wave-breaking-induced portions with only the former described to be size-selective. The wave-breaking influence is roughly taken here as three times of the shear-stress influence; this magnitude is to be computed via an energy dissipation term for actual breaking waves on a beach profile (Equation (76)).

Despite the shear stress reduction due to a hiding/exposure effect, the finer size fractions (d_i/d_m<1) are predicted to feature higher potential reference concentrations because of the grain-diameter dependency in the concentration formula. In the net concentrations, the wave-breaking concentration and the percent occurrences are included and the size selectivities among the fractions become slightly less significant. Still, the net concentrations of the finer fractions will be greater than what would be expected from their abundances in the mixture. This particular tendency agrees with a common finding that finer particles in a mixture are usually entrained more into the water column than coarser particles (e.g.

Tomkins et al. 2003; Van Rijn 2007b; Sistermans 2002).

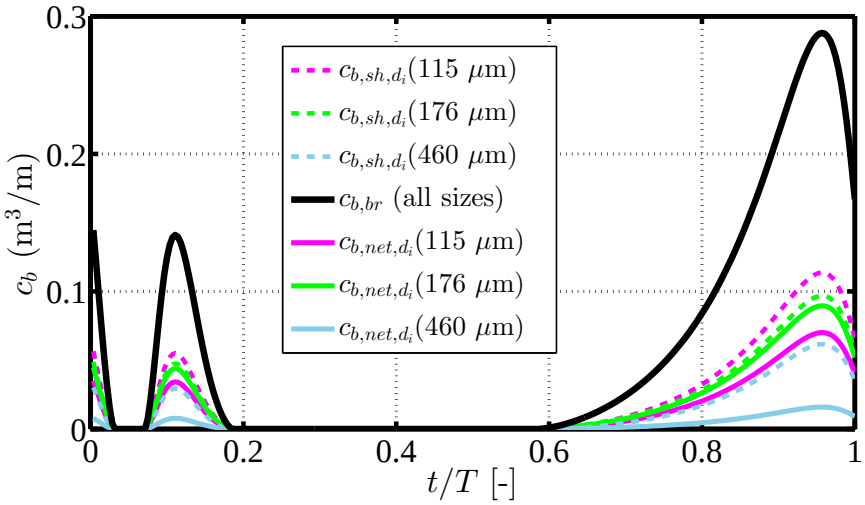

Figure 61: Reference concentrations determined for three size fractions in the mixed-sand mixture. The net concentrations are composed of the shear-based and the wave-breaking portions considering their percent occurrences in the mixture $(c_{b,sh,d_i} + c_{b,br})p_i$.

Figure 62 shows instantaneous sediment concentrations in the water column based on the net reference concentrations resolved in Figure 61. When the reference concentration is available, a diffusion process causes the sediment to disperse into suspension. The suspension decreases after the wave crest passage since a portion of the sediment would start settling to the bottom before being picked up again under the wave trough. The largest concentration is found for the 176-μm fraction which is the modal grain size of the mixture. Apart from the reference concentration, two major influential factors in the advection-diffusion model include the sediment diffusivity and the fall velocity. Only the latter is described to vary for individual sediment size classes, which allows finer size fractions to feature higher concentrations spreading over the wave period.

Figure 63 shows instantaneous sediment fluxes in the horizontal computed based on the concentrations in Figure 62. The sediment velocity here is assumed to be the same as the fluid velocity; hence, any difference among the fluxes are due to differing concentrations. An effect from these possibly different velocities will be shown later. In this case, the velocity under the wave trough is very strong because of the undertow which results in substantial offshore sediment fluxes (negative). The vertical variation of the sediment

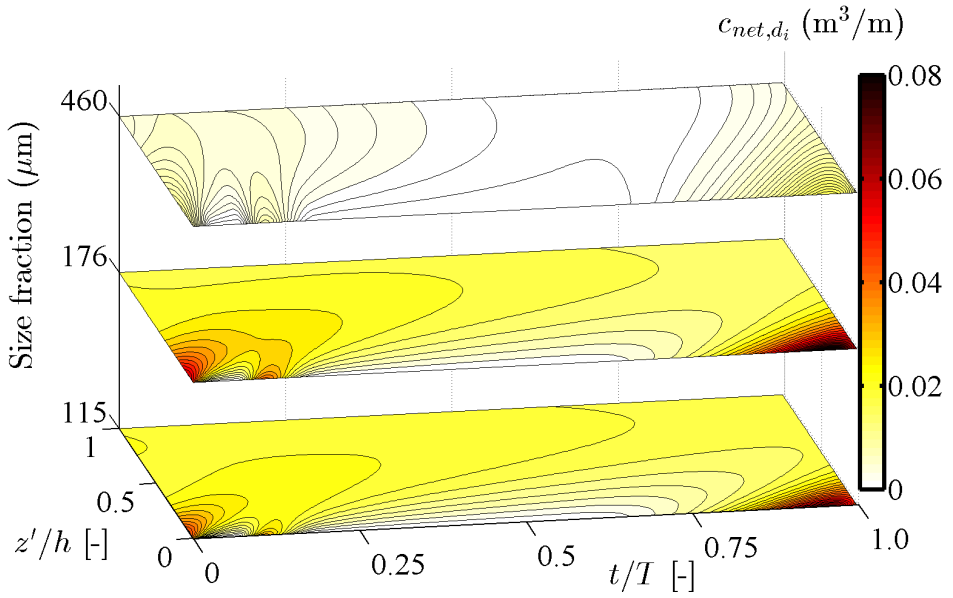

Figure 62: Instantaneous sediment concentrations resolved for three size fractions in the mixed-sand mixture. The net reference concentrations in Figure 61 are imposed as the bottom boundary conditions. The vertical coordinate z' has its origin at the bottom.

fluxes depends on the intensities between the concentration and the velocity. In general, the total flow velocity increases towards the water surface while the concentrations decrease.

The vertical gradients of the concentrations under the wave trough in Figure 62 are very significant and lead to similar gradients for the resulting sediment fluxes in Figure 63. Under the wave crest, the onshore sediment fluxes may feature two different peaks as can be observed from the contours. One is found at the bottom due to a very high concentration, and the other is found around the middle part of the water column due to a stronger velocity despite the decreasing concentrations.

The total sediment concentrations computed from the multi-size and the single-size approaches are compared in Figure 64. The major difference between the two approaches is found for the concentrations in the higher part of the water column as a result of the sensitivity in the advection-diffusion model. Because of the delayed settlings in fine fractions, the multi-fractional approach results in a net concentration that disperses more widely, which leads to up to 12% increment in the net sediment flux. As emphasized earlier, the most significant difference between the two approaches is usually found when the sediment characteristics change which is only accounted for in the size-selective model. Figure 65

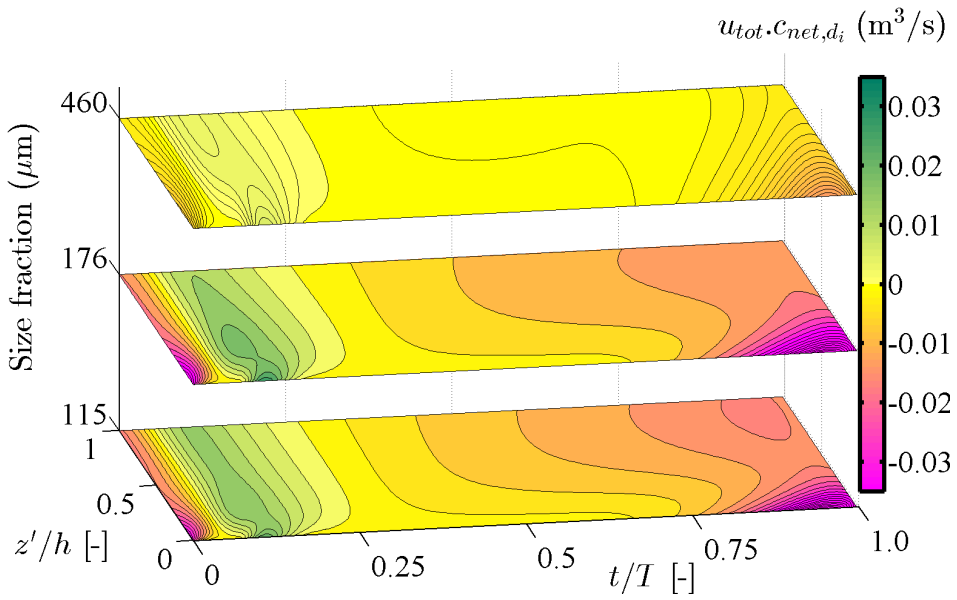

Figure 63: Instantaneous sediment fluxes computed for the three sediment size fractions following the concentrations in Figure 62. Negative fluxes are directed offshore.

shows an example for this situation based on the grain fining and coarsening conditions assumed previously in the bedload analysis (Figure 60).

In the case of grain fining in Figure 65(a), the size-selective approach results in sediment suspension higher up in the water column which leads to an increase in the percent differences between the two approaches in most part under the wave. For the grain-coarsening test in Figure 65(b), the resulting differences are almost entirely opposite because of the decreasing suspensions of the coarser fractions. Based on the concentrations in Figure 65, estimated differences in terms of the total sediment transport rates computed from each approach are shown in Figure 66.

The resulting percent differences can be represented via two linear lines that feature slopes of 0.12 and -0.25 for the fining and the coarsening scenarios, respectively. While similar to the results in the bedload model, these linear sensitivities may be found more surprising due to possible influences from several extra factors such as sediment diffusivity, sediment fall speed, and wave orbital velocity. These linear tendencies are believed to still occur primarily due to the assumption of systematic changes in the size composition; grain sorting in nature that is more complex will certainly lead a nonlinear sensitivity in the model.

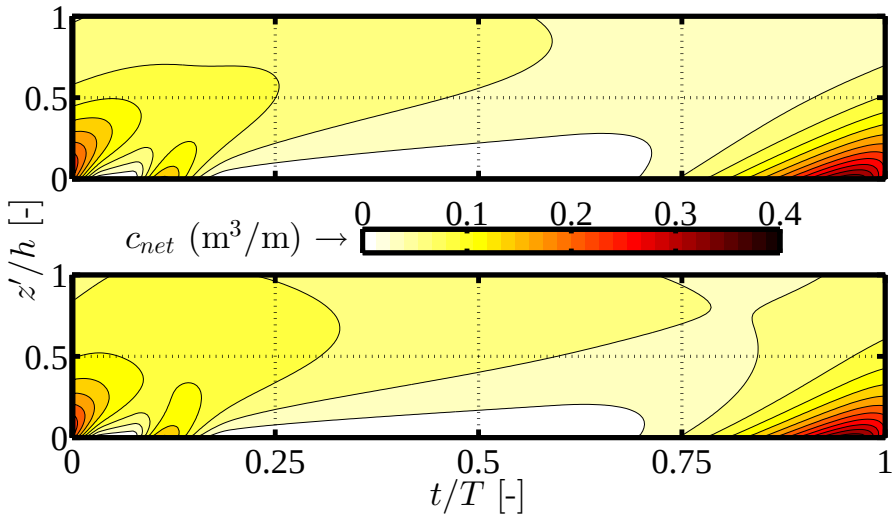

Figure 64: Total sediment concentrations determined using the single-size (upper) and the size-selective (lower) approaches. The mean diameter was utilized in the single-size computation. Ten size-dependent concentrations were considered in the size-selective model.

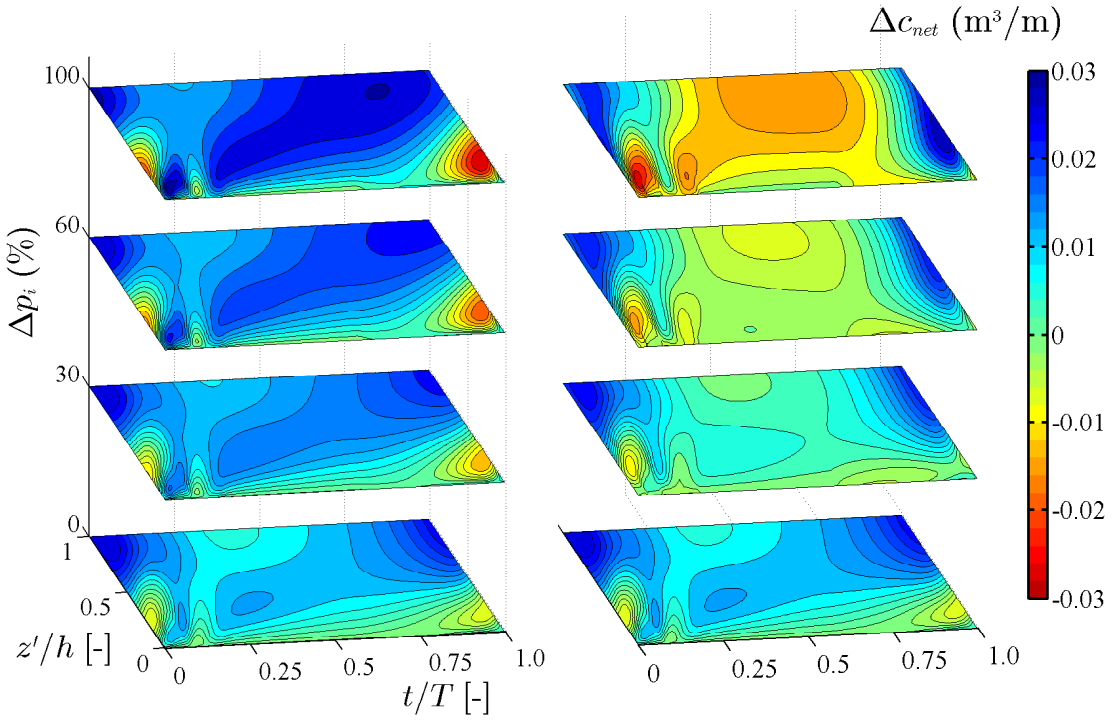

(a) Fining scenario.

(b) Coarsening scenario.

Figure 65: Percent differences in the instantaneous concentrations computed using the size-selective and the single-size approaches. The differences Δc_{net} with positive values imply higher concentration in the size-selective approach. The sorting degree Δp_i is defined as shown earlier in Figure 60.

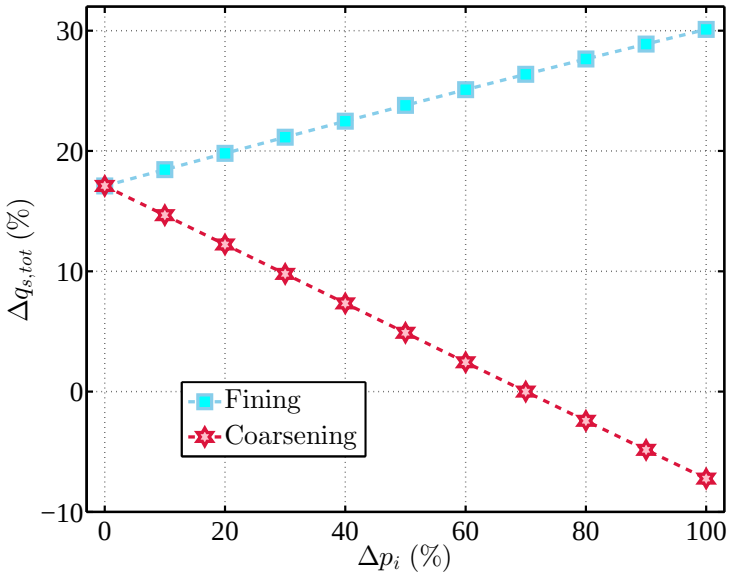

Figure 66: Percent differences between the total suspended transport rates predicted by the size-selective and the single size approaches. The total transport rates were computed based on the total concentrations resolved for Figure 65.

5.7.3 Grain sorting model

The grain sorting model is tested here to demonstrate general model behavior based on a simplified scenario of a symmetrical coarse-sand sandbar on a flat fine-sand bed (Figure 67). A depth-uniform steady flow of 0.5 m^3/s was specified in the problem and the local velocity is assumed to be inversely proportional to the depth so that this volume flux is conserved. The test was run for 3½ hours with the grain sorting model connected to either the bedload or the suspended-load transport model.

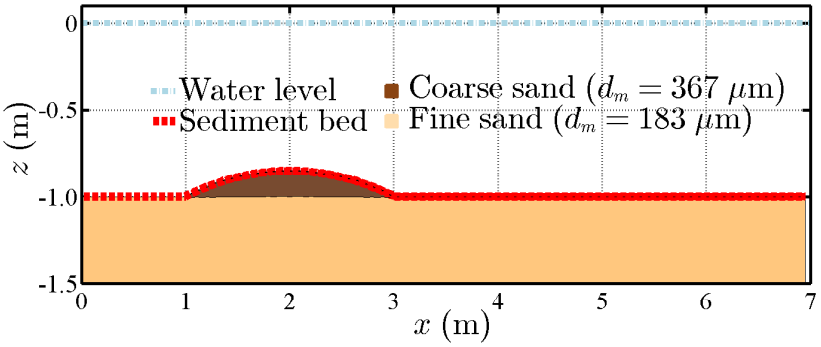

Figure 67: Symmetrical sandbar assumed in the test of the grain sorting model. Size compositions of the two sand mixtures may be found in Figure 56.

The resulting profile evolution and associated grain sorting under the bedload simulation are shown in Figure 68. Once the sediment transport begins, surface material starts to shift downflow since the active transport condition leads to sediment fluxes everywhere in the domain. As the bar migrates, the coarse material is mixed with the native fine material, leading to sediment mixtures of different size compositions noticeable from their

mean diameters in the figure. A similar mixing effect also occurs at the upflow part of the domain due to the transport of the fine material onto the migrating sandbar.

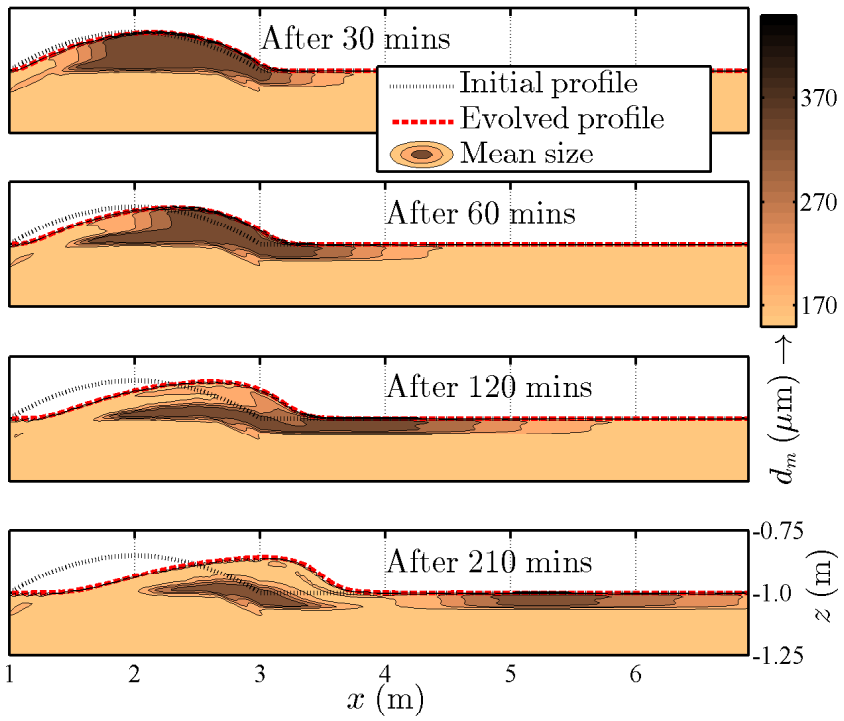

Figure 68: Profile evolution and associated grain sorting found during the test scenario with the bedload sediment transport model. The initial condition is shown in Figure 67. An open lateral boundary condition is applied at both ends of the domain.

A significant vertical lamination over the sandbar starts to appear after 60 mins of the test as the fine material is deposited above the coarse-material layers that are deeper than the mixing depth. After 120 mins, the entire sandbar features a surface layer that is composed of the majority of fine sand. These bed composition changes do not occur due to the mixing only but also the fact that the bedload model predicts greater transport rates of the coarser fractions in a mixture.

The continuous sediment transport and grain sorting after 210 mins result in a separation of the coarse material that was removed from the sandbar and the other portion that remains under the initial bar location. Upper layers of this latter portion would also be removed if the bar continued to migrate, allowing the erosion and the mixing depths to reach the layers. Meanwhile, the downflow portion of the coarse material would still be shifting and spreading over a larger horizontal extent. This occurrence appears as if it is

an advection-diffusion process of the coarse-sand mixture on the bed surface.

Figures 69 shows the surface sediment characteristics that are changing during the sequential grain-sorting processes. The coarse mixture transporting away from the bar features the mean diameters that are decreasing over the time as it is mixed with the native fine sand. Figures 69(b) illustrates the changing grain size compositions of the surface mixture at the initial bar crest location (x = 2 m). The arrival of the fine sand after 60 mins leads the mixture to start approaching the fine-sand composition which is eventually reached after around 120 mins. The surface mean diameters around this location after 210 mins are even smaller than that of the initial fine sand. This result occurs since the bedload model predicts greater transport rates of the coarser fractions and some of the finer fractions are remained behind.

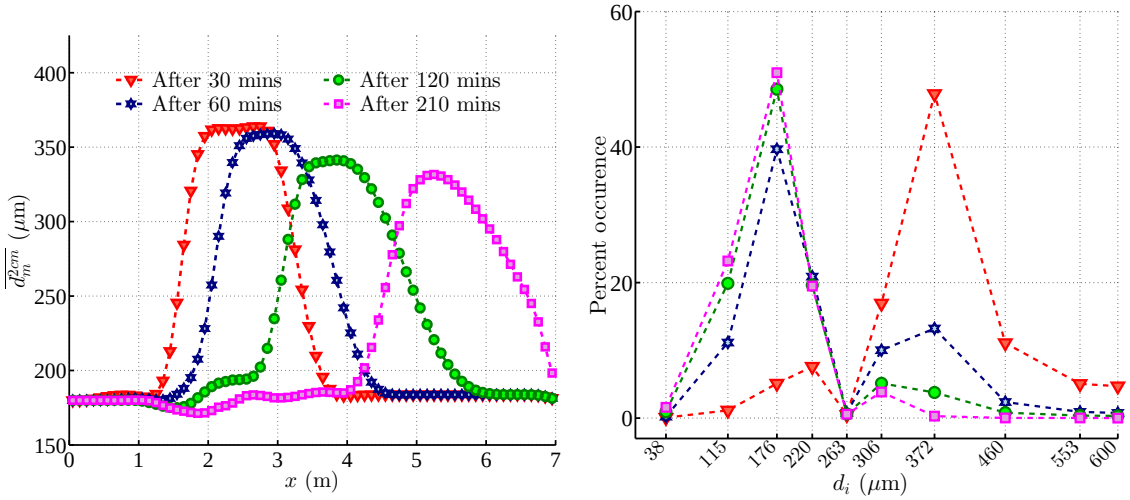

(a) Mean diameters. **(b)** Grain size compositions.

Figure 69: Grain size characteristics of the surface mixture in the grain-sorting test case. The size compositions (b) are evaluated at the initial bar crest location (x=2 m). Both results are based on averaging over a 2-cm layer beneath the bed surface.

On the same test case, Figure 70 shows the resulting grain sorting by the use the suspended transport model. The size selectivities in two transport modes may be different but the grain sorting in this test is mostly contributed by the mixing of the two different mixtures. Nevertheless, the prediction of greater transport rates of the finer fractions in the suspended mode results in a higher amount of the coarser fractions that are left behind. An evidence for this occurrence may be found by comparing the grain size changes over

the initial sandbar in Figure 70 to those found under the bedload test in Figure 68. It may be noted that the final sandbars in the two examples are almost identical since the two transport models were calibrated for matching net sediment transport rates.

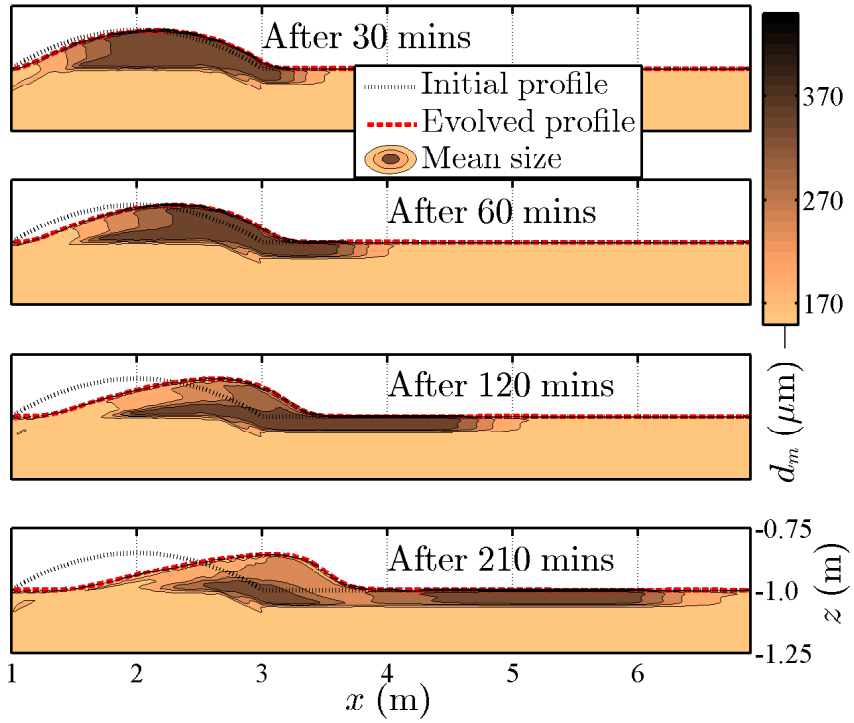

Figure 70: Profile evolution and associated grain sorting found during the test scenario with the suspended-load sediment transport model. See Figure 68 for more details.

In the simplified scenario here, the entire differences among the fractional sediment transport rates are assumed to contribute to the size composition changes. This consideration leads to very substantial and organized variations in the resulting grain sorting on most part of the domain. A grain-sorting process in nature may involve a certain degree of randomness that may lessen such strong changes in the sediment bed. This randomness will be accounted for by incorporating a grain sorting efficacy in an actual application of the model. This consideration is described in Section 6.2.2 in the next chapter.

CHAPTER VI

NUMERICAL MODELING OF CROSS-SHORE MORPHODYNAMICS

This chapter describes a validation and application of the numerical models that were developed in this study. The multi-size sediment transport and grain sorting models (Chapter 5) are coupled with the hydrodynamic models (Chapter 4) to function as a comprehensive morphodynamic modeling unit. This integrated system is then tested by simulating beach profile evolution under the laboratory conditions given in Chapter 3.

The first two sections provide important information regarding model configuration. Simulation results for each experiment set are illustrated next, together with selected sensitivity analyses of related processes (see Table 12). Single-size and bimodal-size settings as alternative model applications are illustrated in the last section, including a model performance evaluation and a discussion of the potential for modeling an equilibrium beach profile.

Table 12: List of experiments simulated and illustrated for the morphodynamics together with selected sensitivity analyses for each experiment set.

Exp.		**Sand type**	**Wave spectrum**†		**Sensitivity analyses illustrated in the chapter**
			T_p	H_{mo}	
1	B	Coarse	1.5 s	20 cm	1) Significance of bedload and suspended load 2) Wave hydrodynamic effects
	C		2.0 s	10 cm	
2	A	Mixed	1.5 s	10 cm	1) Sediment concentration and sediment flux 2) Grain sorting and mixing effects
	B			20 cm	
	C		2.0 s	10 cm	
	B2		1.5 s	20 cm	
3	B	Coarse on fine	1.5 s	20 cm	1) Differences in sediment/fluid velocities 2) Bed-slope influences
	C		2.0 s	10 cm	

† Nominal conditions; actual values are slightly different as shown in Figure 11, Chapter 3.

6.1 Model configuration

6.1.1 General settings

An overview of the implementation of the morphodynamic modeling system is illustrated in Figure 71. The spatial and temporal intervals were chosen to be constant for every test at 5 cm and 15 s, respectively. This setup means the profile evolution timescale is equal to the mean-flow timescale. Ten sediment size classes were assigned for both the multi-size transport model and the grain sorting model, following the number of sieves utilized in the laboratory experiment.

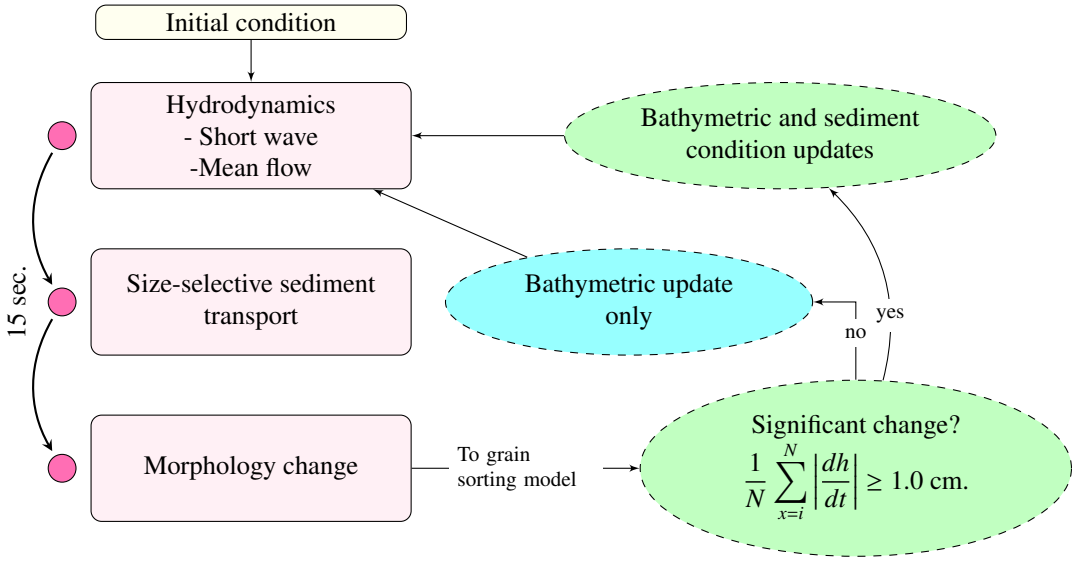

Figure 71: Flowchart of the implementation of the comprehensive morphodynamic model. Target modeling time is defined on the basis of the profile-equilibrium time observed in the physical model.

The grain sorting model was called every time step but configured to update once the mean cumulative profile change was greater than 1.0 cm. This necessity arose as bathymetric change during a 15-s interval was usually smaller than the vertical resolution in the grain-sorting grid (0.25 cm). All of these numbers were proven to provide numerical stability in the model and were also sufficient for resolving important structure on a beach profile.

In the simulation of each experiment, both initial conditions for bathymetry and grain-size distribution were required. To avoid cumulative error, a measured profile was specified for the initial bathymetry. Due to limited numbers of sediment samples collected

along the profile, the initial sediment condition was based on the modeled grain sorting superimposed on the measured bathymetry. It is important to note that this modeled grain size information was already validated with available sediment samples collected on the final beach profile of the preceding test, i.e. the initial profile of the present test.

6.1.2 Treatment of the swash zone

It was evident in the physical model that sediment transport from the swash zone played a major role in the cross-shore profile evolution problem. A simplified swash zone sediment transport formula, coupled with the surf zone model, is introduced in this numerical study. This formula approximates the sediment transport rate proportional to the wave-averaged cross-shore velocity following

$$q(x > X_{sw}) = q(X_{sw}) \left(\frac{\overline{V}_b(x)}{\overline{V}_b(X_{sw})} \right)^n \tag{97}$$

where q is the net transport rate; $\overline{V_b}$ is the mean near-bed velocity, also equal to the depth-averaged velocity in the swash zone; and X_{sw} denotes the connection location between the surf zone and the swash zone models. A positive exponent n allows the trend of the transport rate to be adjusted. In general, the value is inversely proportional to the cross-shore gradient of the sediment transport. Albeit, numerous tests showed that n equal to one provides the most optimal result of the transport rate.

Figure 72 illustrates the approximation for a case of bedload in Exp. 2B. The connection of the two models is selected to be at half of the distance between the still water shoreline and the last grid point of the surf zone models (REF/DIF S and SHORECIRC). The transitional zone is treated such that the continuity of the hydrodynamics is satisfied and the vertical variation of the mean velocity vanishes (see Section 4.3.2, Chapter 4).

6.2 Model calibration

6.2.1 Sediment transport model

While primarily process-based, the new sediment transport model includes several adjustable, semi-empirical parameters. Table 13 illustrates the values of these parameters

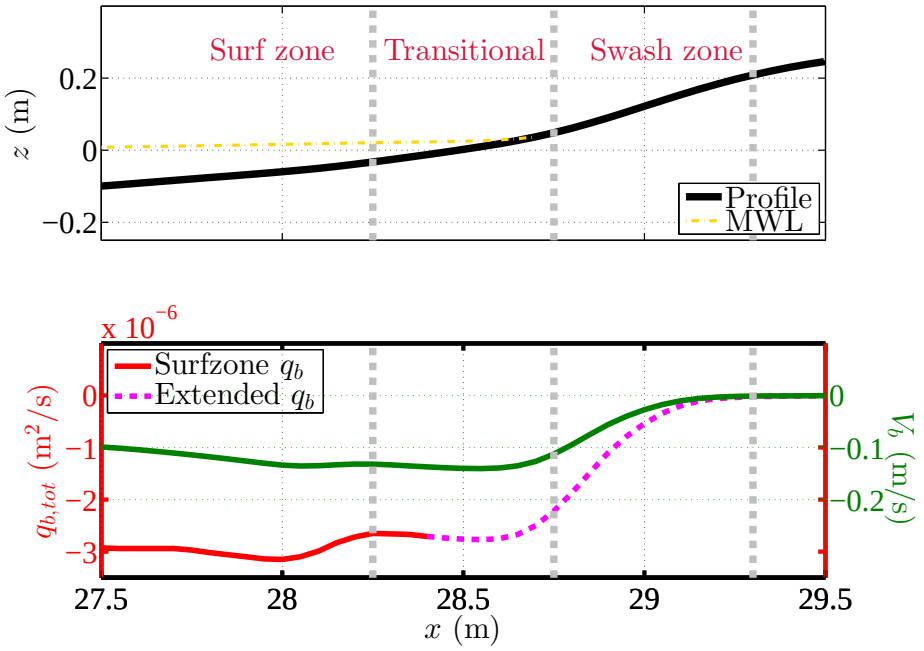

Figure 72: Example for the approximation of swash zone sediment transport rates. The predicted values (q_b) are shown against the left axis in the bottom panel, where the green line is the near-bed velocity against the right axis.

that were optimized for the model application here. It was found that the transport efficacy factors (C_b and C_s) needed to be different between the small and the large wave conditions. This requirement is believed to be the case since the sediment transport predicted in the model is proportional to the shear stress that increases with the square of the velocity, which is, again, a function of the wave height squared.

The optimization for the parameters in Table 13 was achieved through calibrating the models based on two agreement numbers. One is referred to as the "performance" index which quantifies the capability of the model to resolve the beach profile evolution, given as a function of the simulation time as

$$ppf(t) = 1 - \left[\frac{\sum |\Delta h_{mod} - \Delta h_{mea}|}{\sum (|\Delta h_{mod}| + |\Delta h_{mea}|)} \right] \tag{98}$$

where Δh_{mod} and Δh_{mea} are the local changes of the profile predicted by the model and obtained from the measurement, respectively. The summation notations indicate a cross-shore integration; without them, a local performance index can also be computed for evaluating a model performance at a particular location along the cross-shore profile. In

either case, an index equal to one indicates a perfect agreement between the measurement and the model results.

The performance index can be evaluated over any interval in the simulation but mostly it is utilized here for comparing between the resulting profile after the equilibrium time and the initial condition, i.e. in the determination of Δh_{mod} and Δh_{mea}. A simple test to evaluate the performance index itself showed a value of the index equal to 0.8 when 70% of profile change was predicted by the model at every local position. In an actual use, the index may need to be interpreted more carefully since this type of percentage is certain to vary along a profile. It is recommended that the illustration of resulting profiles being compared be also considered for a more qualitative perception of the model performance.

Table 13: Values of semi-empirical parameters that are optimal for the multi-size sediment transport model. These numbers are obtained from the model calibration for the present application.

Parameter	Wave condition			Description
	A) 10 cm/1.5 s	C) 10 cm/2.0 s	B) 20 cm/1.5 s	
C_τ (Eq. 61)	0.135			Friction coefficient
C_b (Eq. 59)	1.65		0.8	Bedload efficiency
C_s (Eq. 81)	0.175		0.03	Suspended-load efficiency
A (Eq. 76)	275			Breaking intensity

The other agreement number is defined as the "equilibrium" index which helps evaluate the model's ability to predict the equilibrium state on a beach profile, given as

$$eef(t) = \frac{\sum(dhdt)^2}{\overline{\sum(dhdt)^2}^{(5\text{ mins})}} \tag{99}$$

where *dhdt* is the instantaneous rate of bathymetric change on the profile. The denominator term represents the initial value averaged over the first 5 mins of the simulation. The index would be equal to zero under a perfect profile equilibrium condition.

6.2.2 Grain sorting model

An effort to optimize the grain sorting model is described here briefly for clarity in the following sections. A more detailed sensitivity analysis in the grain sorting model is shown

later in Section 6.4.3.

Without any adjustment, the grain sorting model was consistently found to overestimate the resulting grain size change, hypothetically due to two aspects that are not described perfectly in the model. One is the lack of description for the randomness involved in the natural grain mixing process. The other is the fact that the grain-sorting process under an oscillatory flow is not fully captured since the model relies upon the net sediment transport rates computed over many wave periods.

The efficacy in the grain-sorting process should decrease as the randomness increases. The actual grain sorting would thus be less significant than what would be expected based on the individual transport rates of size-graded sediment fractions. This possible reduction is accounted for by assuming separate fractional occurrences p_i^{eff} that would be effective in the grain mixing process, approximated following

$$p_i^{\text{eff}} = p_i^{\text{pre}} - (1 - SF)\,[p_i^{\text{pre}} - p_i^{\text{ini}}] \tag{100}$$

where p_i^{pre} is the percent occurrence based on the predicted sediment transport rates and p_i^{ini} represents those of the local sediment bed. Ranging between zero to one, the sorting efficacy factor SF is applied to reduce the fractional deviations between the two mixtures. The value of SF equal to 0.5 was found to produce the most accurate magnitude of the grain sorting change. Figure 73 illustrates an example for the use of Equation (100) for a case of the mixed-sand mixture.

Another improvement in the grain sorting model was also performed by calibrating the hiding exposure factor λ_i, i.e. equal to $(d_i/d_m)^n$. This factor acts to control the relative magnitudes of instantaneous shear stresses on individual size fractions in the sediment mixture. Essentially, the higher the exponent n, the greater the transport rates of the coarser size fractions ($d_i/d_m > 1$). It was found that the value of n of "1/3" provided the most optimal result for the grain sorting trend. This number is marginally higher than suggested in some other steady-flow studies of 0.2-0.3 (Day, 1980; Komar, 1996).

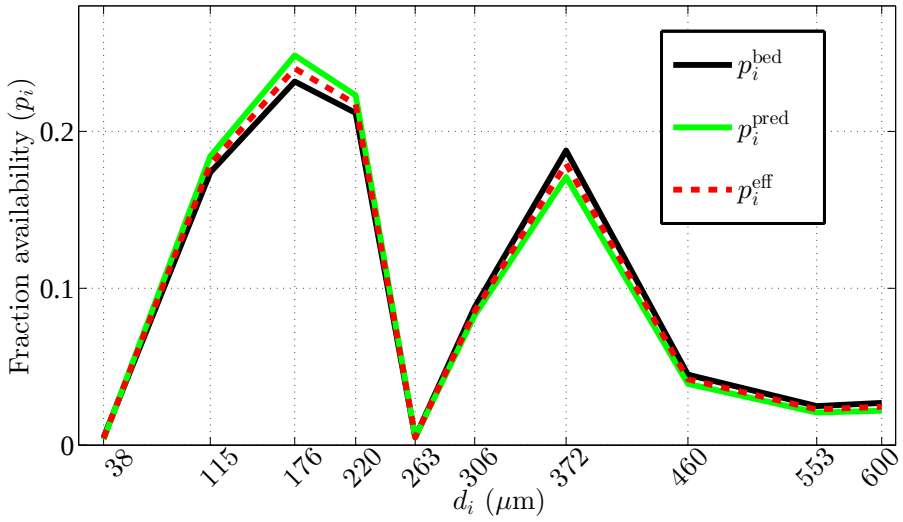

Figure 73: Example for the consideration of grain sorting efficacy and adjustment on the percent occurrences of size-graded fractions. The three percent occurrence terms, p_i^{bed}, p_i^{pre}, and p_i^{eff}, are defined after Equation (100).

6.3 Experiment 1: Coarse sand on initially plane profile

6.3.1 Simulation results

Beach profile evolution results for Exp. 1B and 1C are illustrated in Figures 74 and 75, respectively. Evolving profiles found at intermediate times are also shown besides the resulting profiles at the equilibrium times since they are important for overall accuracy in the model. The storm wave condition in Exp. 1B led to severe erosive profile evolution which could be simulated accurately by the model as shown in Figure 74. The overall performance indices (ppf) computed at the two intervals (40 and 85 mins) are 0.89 and 0.91, respectively. The model appears to simulate a slightly faster profile evolution, compared to the measurements. The local performance indices drop significantly around a trough region right onshore from the bar crest, as well as the maximum wave-runup and the offshore zones. The reductions at the two onshore/offshore boundaries, however, occur mainly due to very small profile changes observed in the physical model.

Figure 75 illustrates the accretive profile test started from the final storm profile in Exp. 1B. Mainly, the accretion was found to lead to an onshore sandbar migration (x<27.3 m) and a foreshore profile recovery (x≥27.3 m). Both of these features were contributed by the erosion of the initial sandbar structure. The model was found to be capable of

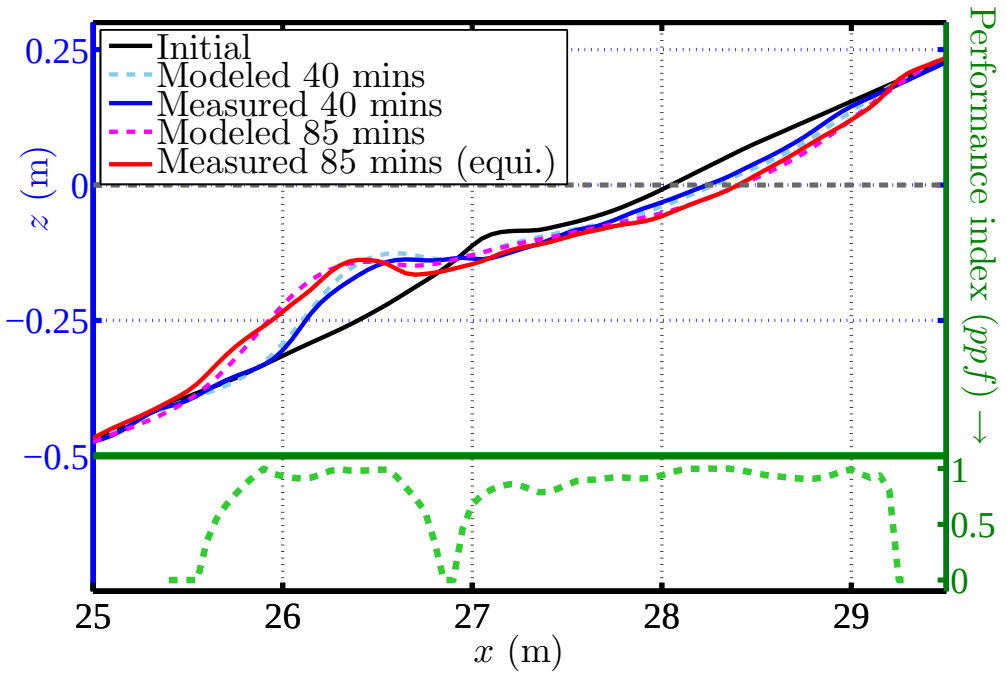

Figure 74: Profile evolution resolved by the model compared to the measurement in Exp. 1B. The test was performed on the coarse-sand profile under the storm-wave condition. Profile changes at the top are against the left axis; performance index in the bottom is against the right axis.

simulating this erosion and the sandbar migration successfully. The predicted amount and the shoreward extent of the onshore transport, however, did not satisfy the deposition that contributed to the foreshore recovery. The local performance indices in Figure 75 clearly illustrate this deficiency as their computed values drop to zero onshore from the bar trough zone.

The modeling inaccuracy in the bar trough area in the storm test (Exp. 1B) is believed to occur following an underestimation of the wave breaking intensity just onshore of the sandbar. The accretion in the foreshore zone in Exp. 1C could not be simulated since the model simply did not predict the correct transport direction in the adjacent area. Explanation of these modeling issues is given in the next sections where many of the associated processes involved in the model simulation are investigated.

6.3.2 Significance of bedload and suspended load

The sediment transport model in this study computes both bedload and suspended load that coexist in nature. The resulting grain sorting and their variation on a profile was

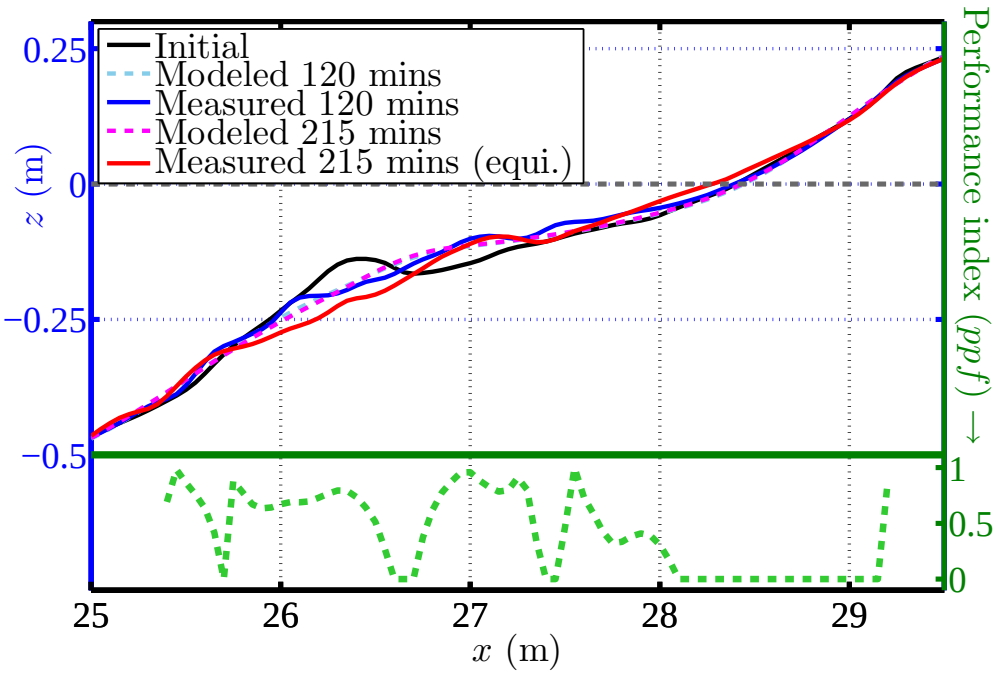

Figure 75: Profile evolution resolved by the model compared to the measurement in Exp. 1C. This accretive test was performed after the storm-wave test (1B). See Figure 74 for details.

also locally contributed by each transport mode and this aspect will be shown in details later when Exp. Set 2 is investigated. The major interest here is the significance of each transport mode on the final profile evolution.

Figure 76 illustrates the ratios between the transport rates in bedload and suspended load computed at several intervals and as time-averaged values in Exp. 1B. The ratios range from 0.25 to 4.5, meaning that one mode is always within about four times of the other. These relative magnitudes are influenced substantially by the efficacy factor C_b or C_s in either transport formula.

Suspended load is typically dominant further offshore where the undertow, the orbital velocity, and the wave skewness are weak thus limiting the transport by bedload. The deeper water column also allows a greater amount of the sediment suspension. The decline of the suspended load at the furthest offshore zone in Figure 76 occurs since the sediment only starts to mobilize and the local transport rates are very small.

As discussed earlier, the size selectivity in the transport process depends on the particle-size dependency and the interaction among the size-graded fractions referred to as the "hiding/exposure" effect. In the suspended load, the size dependency is more significant

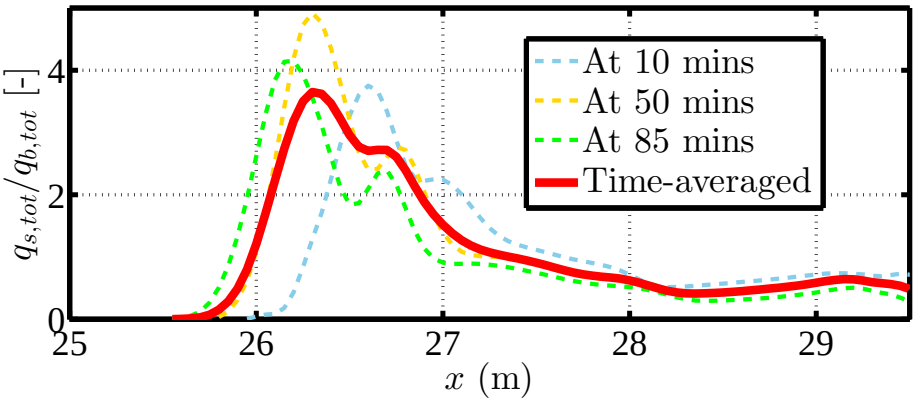

Figure 76: Ratios between bedload and suspended load in the profile simulation of Exp. 1B. The values are computed based on wave-averaged, depth-integrated, net transport rates in either transport mode, contributed from all available size fractions.

which enhances the mobilities of the finer fractions in the mixture (d_i<d_m). This trend is opposite for the bedload where the hiding effect promotes the transport of the coarser fractions.

Figure 77 illustrates these size-selectivity occurrences based on the simulation results in Exp. 1B, represented as the ratios between the fractional transport rates and that of the coarsest size class (d_i = 600 μm). The ratios are, as expected, lower than one for bedload and decrease as the sediment sizes decrease. Note that, for clarity, these ratios are computed based on the potential transport rates excluding their percent occurrences in the mixture.

The result of a profile simulation is largely subject to the proportion of the net bedload and the suspended load. Figure 78 shows an example for the simulation considering either transport mode alone. The bedload-only scenario seems to result in an underestimation of the offshore sediment transport which leads to an offshore profile slope that is too steep. The sole inclusion of the suspended load, despite a surprisingly accurate result in this example, typically leads to a flatter beach profile with an obscure sandbar structure. The potential for a better simulation result using a single-mode configuration is very unlikely and this option can also be eliminated completely when considering the consequent grain sorting on a beach profile (Section 6.4.3).

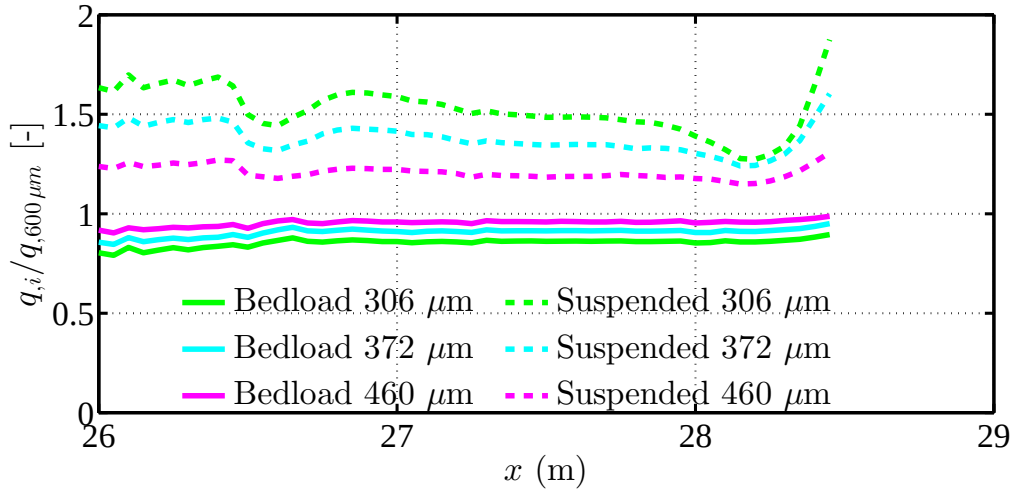

Figure 77: Fractional sediment transport rates in each transport mode in Exp. 1B compared to that of the coarsest size fraction. The ratios are computed from the simulation at half of the equilibrium time, based on wave-averaged, depth-integrated, potential fractional transport rates (percent occurrences not considered).

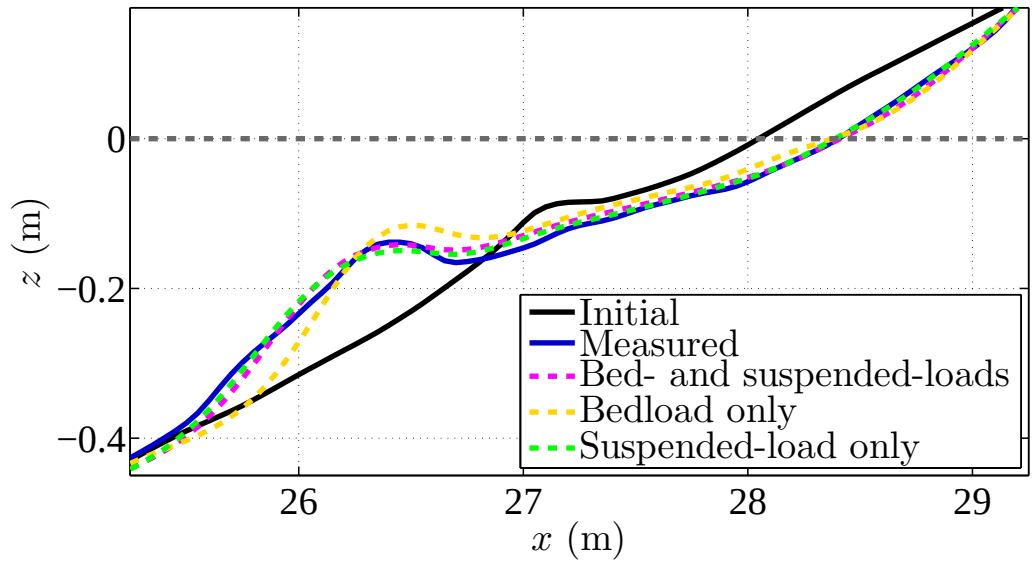

Figure 78: Example of profile simulation with bedload or suspended load only in Exp. 1B. The transport efficacy factor (C_b or C_s) is doubled from its default value when only one transport mode is simulated in order to approach the target profile.

6.3.3 Wave hydrodynamic effects

The major objective here is to illustrate the key mechanisms that lead to various sediment transport patterns in the simulation of the erosive or accretive profile change. The parameter that is most influential on these transport patterns is the "effective" shear stress term. Figure 79 shows an example of how this effective shear stress can be determined over a wave period. The intra-wave transport rates are computed based on this shear stress term and later phase-averaged to yield a local net sediment transport rate.

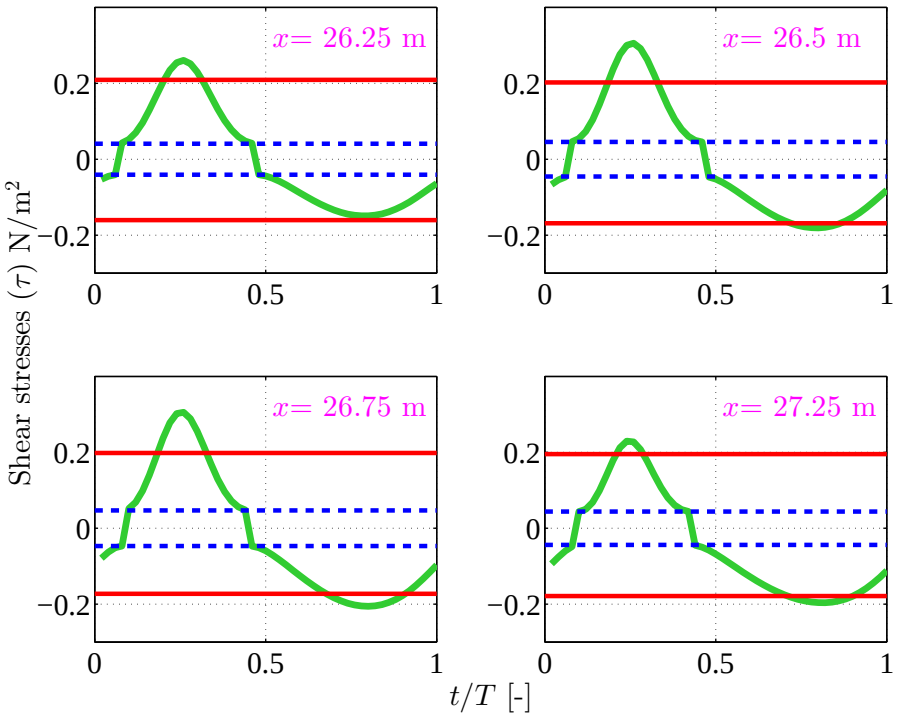

Figure 79: Bed shear stress terms involved in the determination of the effective shear stresses at four cross-shore locations in Exp. 1C. Solid red lines indicate the local critical shear stresses; solid green lines show instantaneous shear stresses computed as a function of the total fluid velocities plus acceleration-induced shear stresses that are locally constant (dashed blue lines).

The direction of the net sediment transport depends mainly on the wave orbital velocity and undertow magnitudes. Having a higher velocity under the wave crest, a skewed orbital velocity tends to result in an onshore transport in the offshore region. As the orbital velocity increases towards the shoreline, the offshore sediment transport under the wave trough becomes non-zero. Due to a broader trough velocity and the influence of undertow, this offshore transport portion rises more rapidly than the onshore portion and eventually

the net sediment transport is reversed to be offshore-directed.

The transport directions at the four locations in Figure 79 may roughly be speculated by considering that the net transport rate is proportional to the phase-averaged quantities of the effective shear stresses. They would thus clearly be directed onshore for the first three locations but possibly offshore-directed at the most shoreward location. These transport patterns allowed a successful simulation of the sandbar migration but a deficiency for the foreshore material recovery in the accretive profile test in Exp. 1C shown earlier.

Besides the wave skewness, the inclusion of the fluid acceleration is also one of the keys to the successful simulation. The acceleration is represented in the model as a phase-averaged, root-mean-square value, resembling a "destabilization" term that lowers the critical shear stress of local sediment. Typically, the acceleration term tends to increase shoreward proportional to the skewness and the asymmetry of the wave.

Figure 80 illustrates profile simulations for Exp. 1C without considering the skewness or the acceleration. The first case reveals a clear incompetency to resolve the accretion due to the lack of onshore sediment transport prediction. The negligence of the acceleration results in a slightly smaller extent of the onshore bar migration. Even though this change is very minimal, the acceleration is mandatory in the model because it represents an influence of the wave period. For this reason, the model was able to simulate either the erosive or accretive profile changes under wave condition "A" or "C" using an identical set of the calibration parameters.

Wave breaking is clearly an important mechanism that affects a beach profile change, especially under erosive profile evolution. Aiming at its direct impact on the transport rate, this mechanism is accounted for via the newly-developed wave breaking factor (F_{ecg}) in the model (Equation (76), Chapter 5). Figure 81 illustrates the values of this factor found in the simulation of Exp. 1B. The factor is a product of two terms that represent the wave-breaking energy dissipation and the potential penetration of such turbulence on the profile (PEN)- also shown in the figure. Both bedload and suspended-load sediment transport rates are described to increase proportionally to the value of this wave breaking factor.

It may be roughly estimated from Figure 81 that the transport rates are enhanced up to 3.5 times after considering the wave breaking effect. The breaking factors reach their

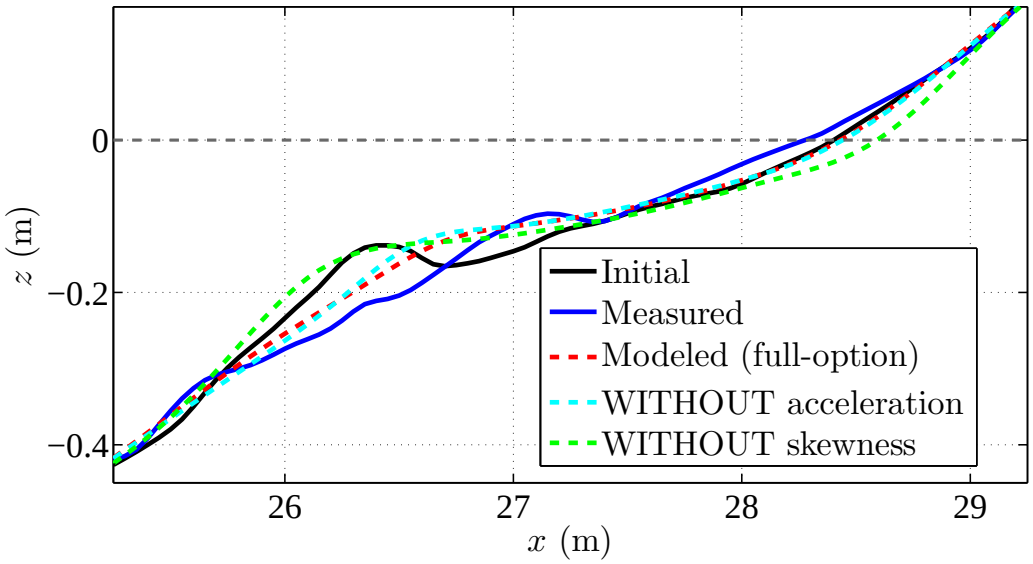

Figure 80: Simulation results for Exp. 1C without considering the wave skewness or the fluid acceleration. To approach the target profile, the calibration parameters were reduced by 50% for the skewness test, and increased by 25% for the acceleration test.

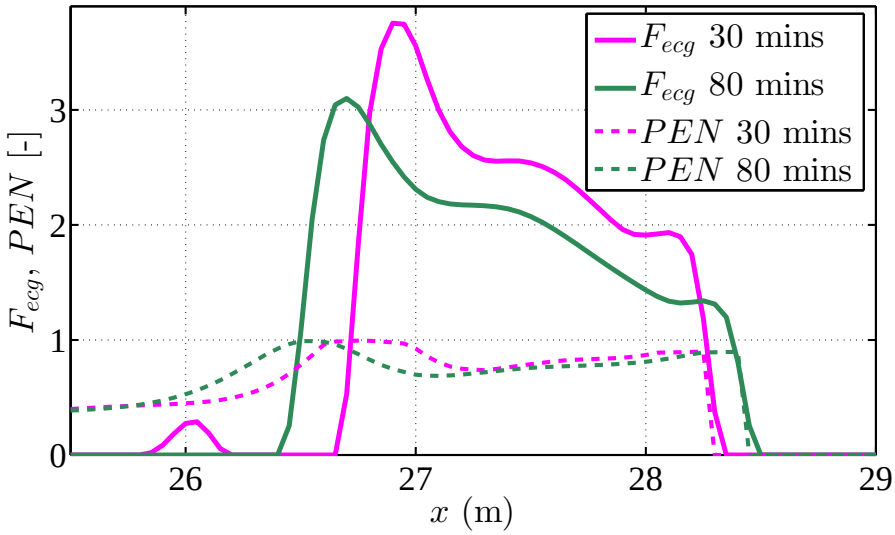

Figure 81: Values of wave breaking factor (F_{ecg}) computed at two intervals in Exp. 1B. The components in each of the terms (F_{ecg} and PEN) may be found in Equation (76), Chapter 5.

maxima where the energy dissipation and the penetration terms are both large, occurring around the bar crest with the coincidence of steep slope, shallow water, and large gradient of wave energy flux. The factors decrease as the profile evolves primarily because of an increasing water depth and a reduction of the energy dissipation.

Figure 82 shows a simulation result for Exp. 1B without considering the wave-breaking effect. It is clear that the final beach profile is flatter and associated with an unclear sandbar feature compared to the resulting profile from the full-option model. This distinction originated mainly from the difference in the cross-shore sediment transport gradients. With the breaking effect, the gradients changed more rapidly around the area where the sandbar is formed, particularly in the bar-trough zone.

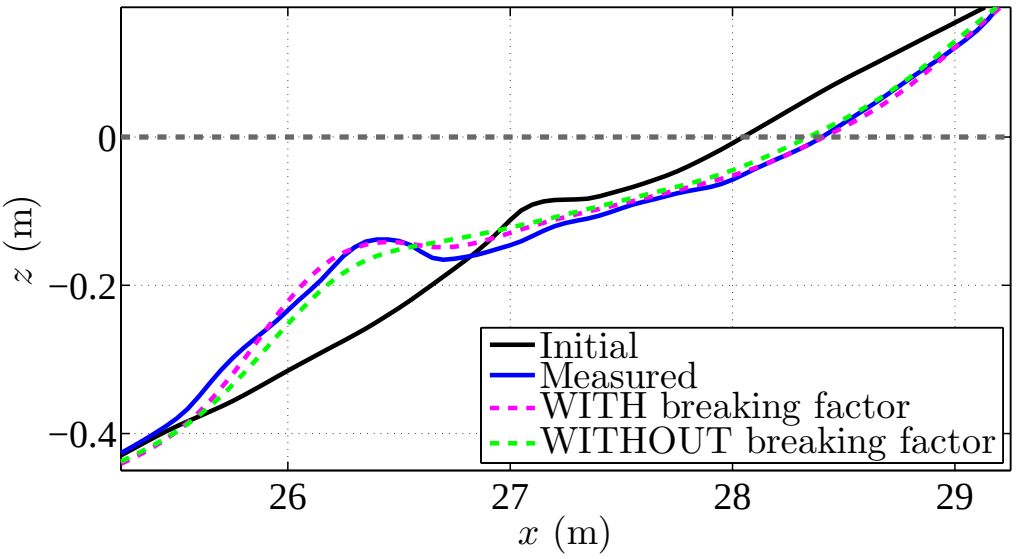

Figure 82: Profile simulation in Exp. 1B without considering the wave breaking factor in the sediment transport model. The transport efficacy factors (C_b and C_s) were both multiplied by three which is a typical value of the wave-breaking factor.

Even with the given wave-breaking effect, it is observed in Exp. 1B that the erosion in the bar trough was still underpredicted. Much effort had been attempted for an improvement but it seemed that this deficiency may not be completely solved with the existing components in the present formula. Other important mechanisms such as vortex shedding or influence of pressure gradient under breaking waves may also need to be described for a better modeling accuracy in such a complex zone on a cross-shore profile.

6.4 Experiment 2: Mixed sand on initially plane profile

6.4.1 Simulation results

This set of experiments featured the most comprehensive tests and measurements for both beach profile evolution and grain sorting. Starting from an initially plane slope, consecutive tests were performed for the erosive (2A), storm (2B), accretive (2C), and then repeated again for the storm (2B2) wave conditions.

Modeled results for profile evolution and grain sorting in Exp. 2A and 2B are illustrated consecutively in Figures 83 and 84. In both cases, the clear foreshore erosions and formations of the sandbar were resolved accurately by the model, yielding the performance indices of 0.86 and 0.90, respectively. These profile changes were mainly influenced by the undertow current that initiated strong offshore net sediment transport fluxes in both bedload and suspended load. The only zone where the model seems to underestimate the change is again the bar-trough region right onshore from the bar crest, where the erosion and the deposition are switching on the profile. This modeling deficiency is still believed to occur as a result of lacking of sufficient wave-breaking effect incorporated in the model.

The capability of the new grain sorting model can be noticed based on the resulting mean surface diameters compared to the measurement in the lower panels in Figures 83 and 84. The trends of the grain sorting are identical between the two tests since they are both erosive-type profiles. Coarsening of the mixture is mostly found in the foreshore zone through the bar crest, and grain fining is found further offshore. The model achieves in representing these changes mainly via the opposite trends in the bedload and the suspended load transports that are dominating closer to the shore and around the sandbar, respectively.

Higher fractional transport rates of the coarser size classes ($d_i > d_m$) in the bedload lead to their increased percent occurrences on the surface near the shoreline. This increment also becomes more significant towards the sandbar as the suspended load becomes more influential and the finer fractions are also removed offshore simultaneously. For this reason, the zone where the model yields the coarsest mixture should be found where the relative magnitude of the two transport modes are most comparable. This location will, however, move as the profile evolves.

Grain fining on the offshore part of the profile is clearly contributed by the removal

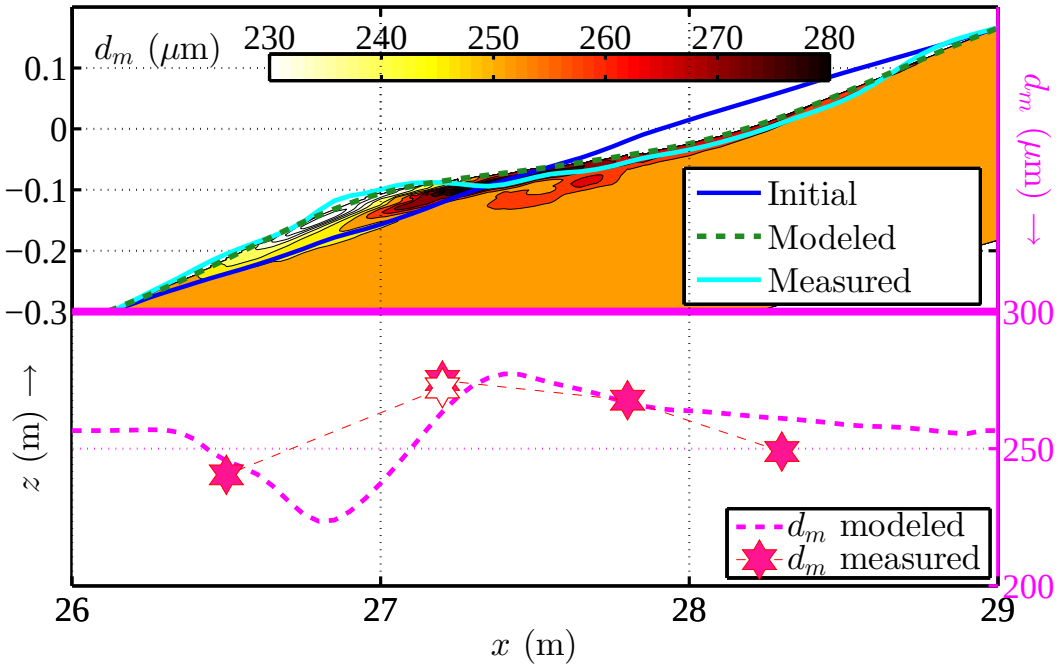

Figure 83: Simulation results for profile evolution and grain sorting in the erosive wave test Exp. 2A. Profile results in the top are shown with contours of the sediment mean grain sizes modeled at the equilibrium time. Mean grain sizes computed on the surface layer (2 cm) are compared to the measurement in the lower panel. Hollow marker indicates the subsurface sample. Uncertainty in the grain size analysis is ±5 μm.

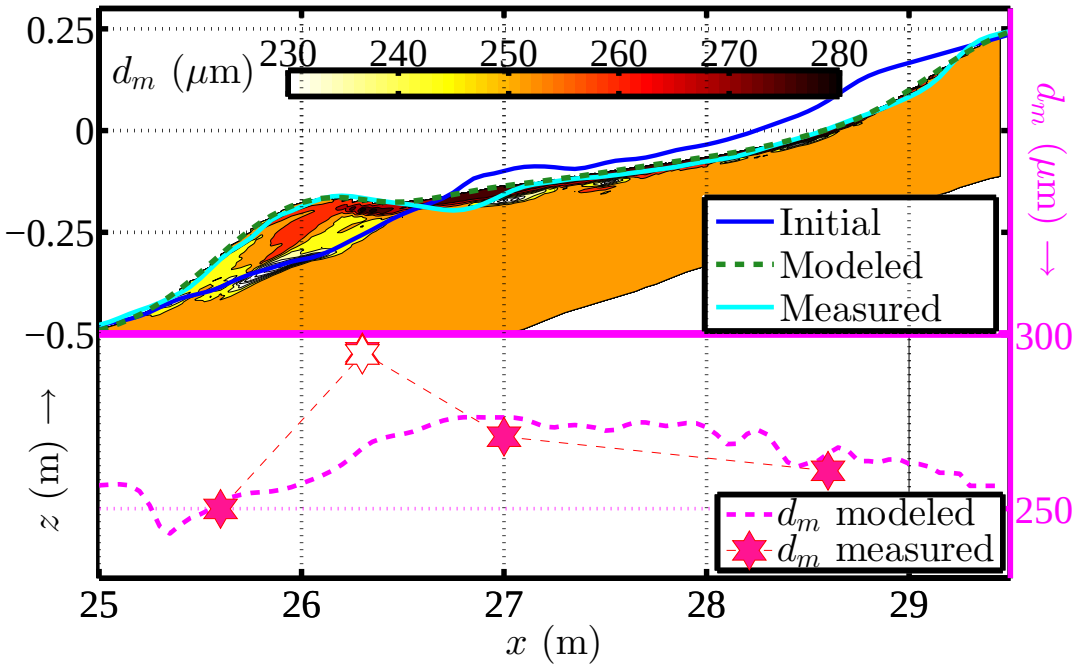

Figure 84: Simulation results for profile evolution and grain sorting in the storm wave test Exp. 2B. Uncertainty in the grain size analysis is ±5 μm. See Figure 83 for more details.

of fine material from the sandbar area via the suspended load. This fine material removal generally also results in grain fining on the surface of the sandbar itself, as well as coarsening in the deeper bed layers where the coarser fractions were remained. The clear vertical grain lamination observed in Figure 84 was, however, created primarily by consequent material depositions over the sandbar structure. From Exp. 2A, the fine material was first disposed offshore, and was later over-topped by the coarser sediment that was eventually supplied from the foreshore zone. When the bar continued to grow, the surface of the offshore part of the bar was predicted to become finer once again due to the dominance of the suspended sediment transport mentioned earlier.

Figure 85 shows the sediment size compositions modeled at five locations in Exp. 2B where measured data are also available. The model was found to yield correct trends of the grain size changes for all of the locations including those in the swash zone (A) and the sandbar subsurface (D). The results at the bar crest, however, involve considerable underestimation of the maximum grain coarsening found on the profiles. Even though the model indeed predicted the coarsest mixture around that zone, it is found in a deeper layer due to a more recent surface deposition of the finer fractions initiated by the suspended load.

Simulation results for the accretive beach profile evolution and grain sorting in Exp. 2C are shown in Figure 86. The onshore sandbar migration in this test was very significant with the new bar crest located on the initial bar-trough region. The accretion around the foreshore zone was almost negligible, unlike the accretive test of the coarse-sand profile in Exp. 1C (Figure 75). An overall performance index of 0.82 was found for this profile simulation. The sandbar migration and a slight erosion in the offshore part were resolved very accurately but a small foreshore erosion that was not observed in the experiment was also predicted.

Based on Figure 86, the coarsening at the initial bar-crest surface (x=26.5 m) suggests that fine material was removed shoreward as the new sandbar was formed. This important process was captured in the grain sorting model as noticeable from the prediction of the coarsening itself as well as the finest material on the new sandbar area. The magnitude of the modeled surface mean diameter in this zone matches the number found in the available

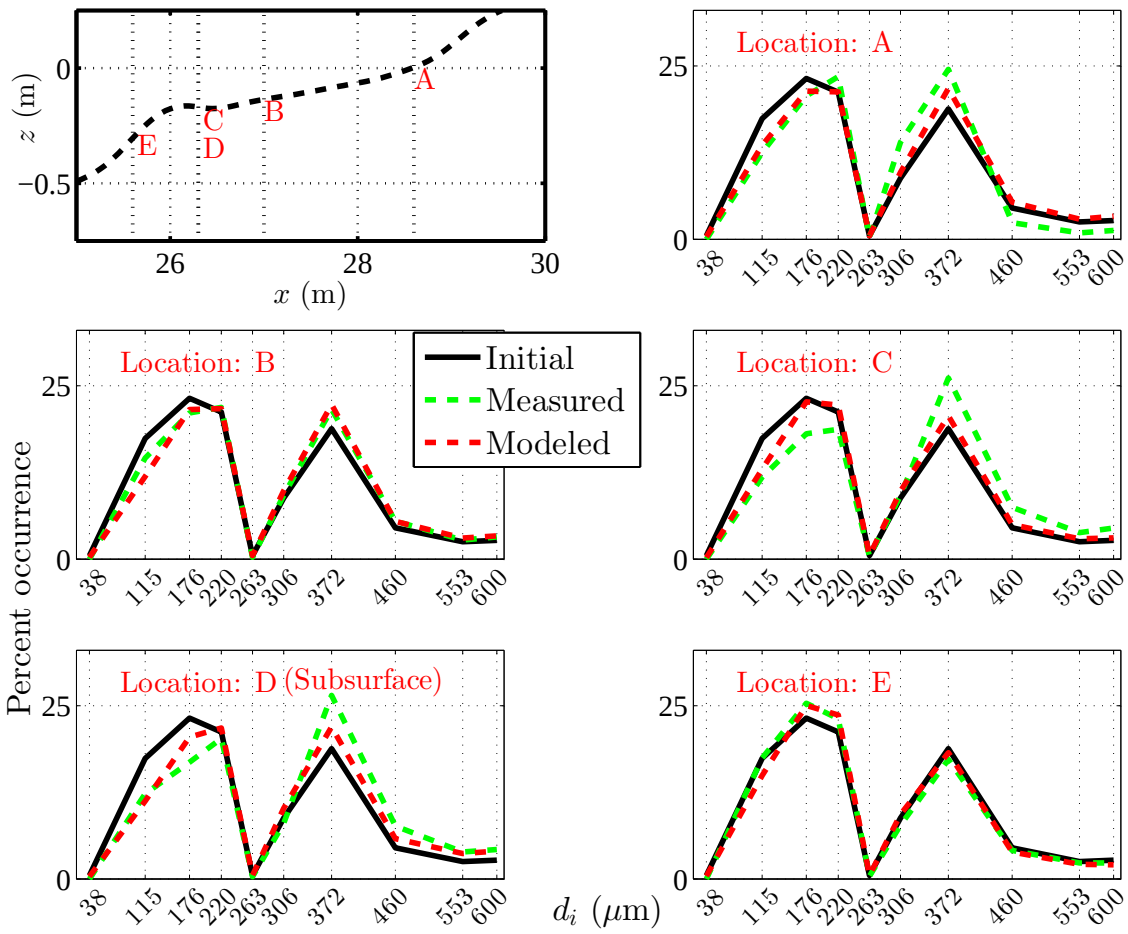

Figure 85: Modeled sediment size compositions of the surface mixtures at five locations where measured data are available in Exp. 2B. Top-left panel shows the locations. The initial mixtures are uniformly-distributed mixed sand on the starting profile (Exp. 2A).

sediment sample collected at x = 27.6 m.

One of the keys to the successful simulation of the profile evolution in this accretive test is the consideration of the sediment size change. Compared to Exp. 1C, the grain size effect arises more significantly here due to the characteristics of the bimodal mixed sand utilized in the experiment. The mixture was also sorted previously in Exp. 2A and 2B which thus increased the variation of the grain size composition on the beach profile. Detailed investigation of this effect is given shortly by explaining related hydrodynamic and sediment transport processes (Figures 89 - 94).

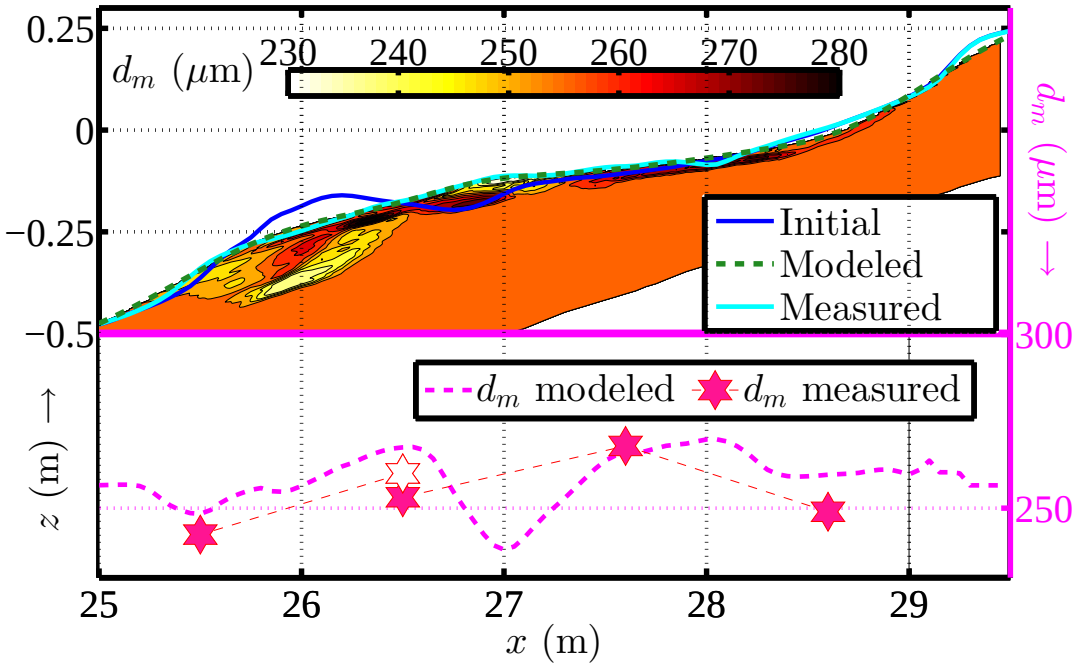

Figure 86: Simulation results for profile evolution and grain sorting in the accretive wave test Exp. 2C. Uncertainty in the grain size analysis is ±5 μm. See Figure 83 for more details.

Figure 87 illustrates the simulation results for Exp. 2B2, the repeated storm wave condition conducted after the accretive test (2C). Of the greatest interest in this test was the reformation of the beach profile and the grain sorting pattern compared to the earlier observation in Exp. 2B with the same wave condition. Ultimately, these aspects between the two tests were found to be very similar and this consistency was also simulated successfully by the numerical model. The only noticeable difference is that the earlier sandbar structure in Exp. 2B appears to be more peaky with a deeper bar trough and a steeper offshore slope.

The initial fine material on the accretive profile was predicted to return to the offshore

side of the new sandbar in Exp. 2B2 and, as a consequence, the foreshore zone became the coarser part once again. Regarding grain sorting, the only difference between Exp. 2B and 2B2 is found for the vertical laminations over the bar structure due to their different erosion and deposition histories. These findings suggest that a wave condition would probably lead to a certain beach profile type and grain sorting pattern. Other details such as curvature of the sandbar and cross-shore sediment size variation would, however, also be dependent on both the initial bathymetry and associated sediment grain sorting.

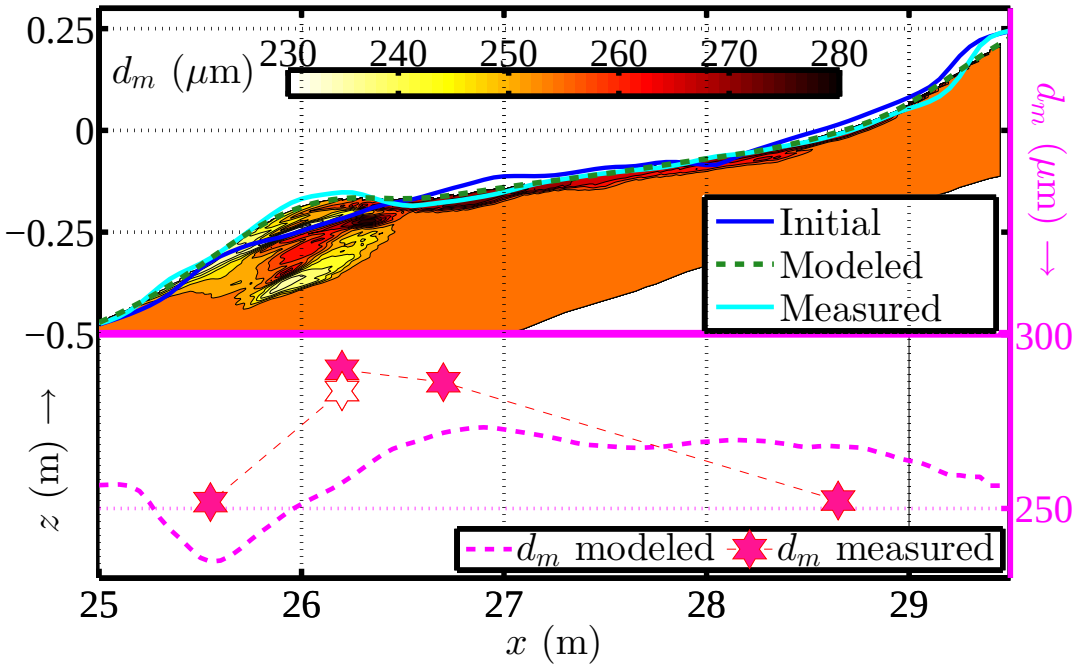

Figure 87: Simulation results for profile evolution and grain sorting in the repeated storm-wave test Exp. 2B2. Uncertainty in the grain size analysis is ±5 μm. See Figure 83 for more details.

6.4.2 Sediment concentration and sediment flux

The simulation of sediment suspension involves a few sophisticated processes which, under various hydrodynamic regimes, result in different erosive and accretive transport patterns. Figure 88 illustrates the fractional sediment concentrations computed per the storm test in Exp. 2B, compared to those per the accretive test (Exp. 2C) in Figure 89. The major difference between the two cases, for every sediment size class, is clearly observed on the crest and trough concentrations.

In the storm test, the concentration under the trough is slightly more intensive which

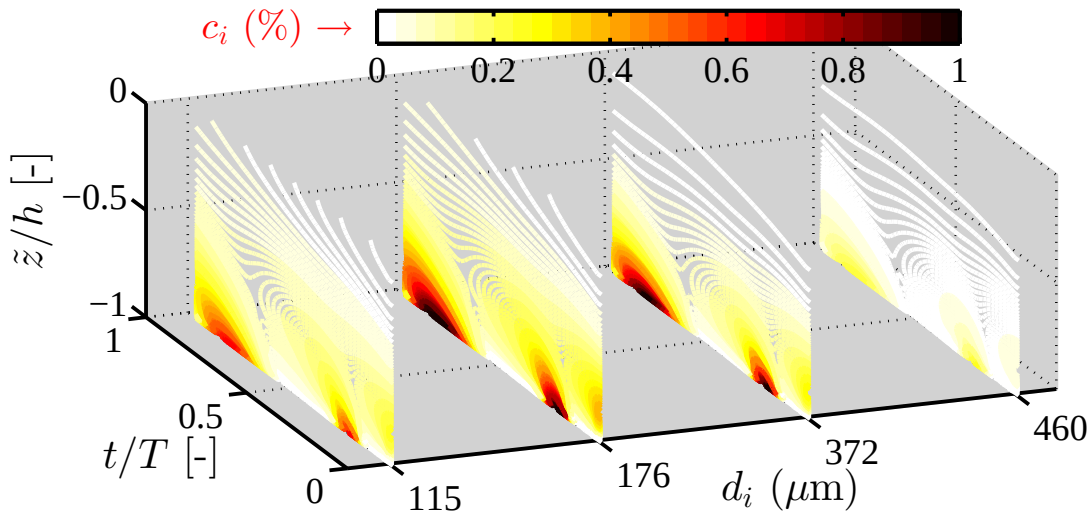

Figure 88: Example of instantaneous concentrations of four sediment size classes simulated under the storm wave condition in Exp. 2B. The computation was performed at half of the equilibrium time at the most energetic location (x=27.0 m). Percent occurrences of the size classes are considered. On the vertical axis, $\tilde{z}$ is equal to $z - \bar{\zeta}$ in which $\bar{\zeta}$ is the mean surface water level; h is the mean water depth.

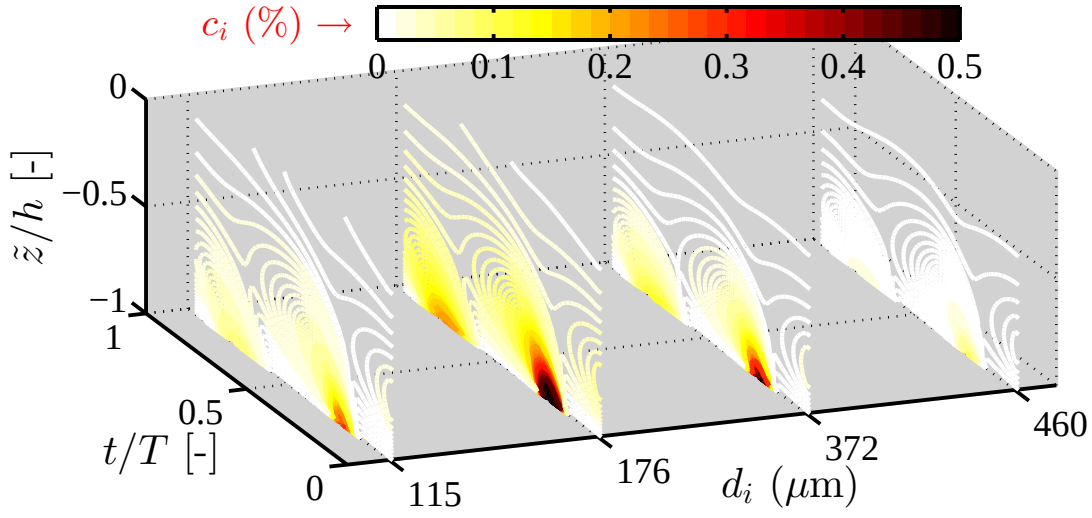

Figure 89: Example of instantaneous concentrations of four sediment size classes simulated under the accretive wave condition in Exp. 2C. The computation was performed at the most energetic location (x=26.75 m). See Figure 88 for details.

initiates an erosive sediment transport pattern due to an offshore sediment advection during the corresponding wave phase. On the contrary, the larger concentration under the crest in the accretive test leads to a resulting onshore sediment transport. The cross-shore variation of these concentrations, however, can be very significant depending on the hydrodynamics. For example, the crest concentration close to the shoreline is almost always smaller than the trough's due to a strong undertow. This typical occurrence can be observed in Figure 90 where the computed potential sediment transport rates for two size classes are shown for both suspended load and bedload along the profile in Exp. 2C.

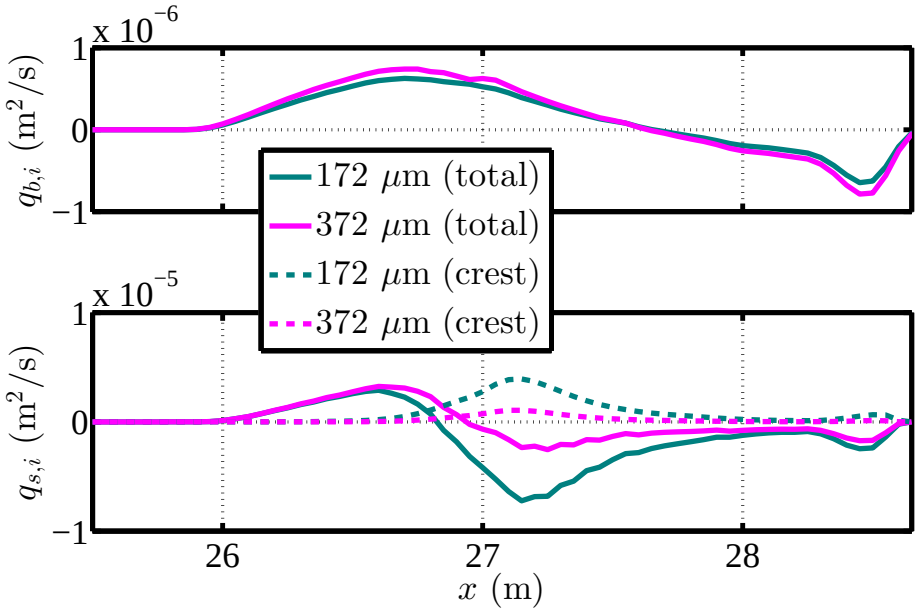

Figure 90: Time-averaged potential sediment transport rates of two size fractions computed at half of the equilibrium time in Exp. 2C. Top panel shows the bedload transport rates. Bottom panel shows the suspended-transport rates including the total depth-averaged values and the portions estimated in the wave crest. Percent occurrences of sediment fractions are not considered in potential transport rates.

One important mechanism considered in the model here is the suspended sediment portion in the wave crest region that would be conveyed onshore with the wave mass flux. The concentration of this sediment is determined as a time-averaged value based on the concentration at the still water level (Equation (82), Chapter 5). This wave-crest concentration thus becomes more significant as the suspension near the surface increases. In the most intensive transport region in Figure 90, the onshore transport via this portion is modeled to account for up to 50% of the total quantity.

The inclusion of sediment fluxes in the wave crest allows a better prediction of the cross-shore evolution in the accretive profile tests. The simulation result of Exp. 2C without this extra term is illustrated in Figure 91 where both of the initial bar erosion and the consequent deposition on the new sandbar are underestimated. When the crest concentration is considered, these inaccuracies were simply eliminated through the addition of onshore transport rates as shown in Figure 90. Note that this improvement does not interfere with any erosive profile test where the offshore transport is so strong that it always prevails the additional onshore sediment transport portion.

Calibration parameters may be readjusted for a better simulation result without the wave crest flux but such adjustment would indicate a compensation rather than a representation of the process. Fractional sediment transport rates will also differ after the adjustment, leading to a new grain sorting result which would not be as optimal as the original one when the wave crest sediment flux is considered.

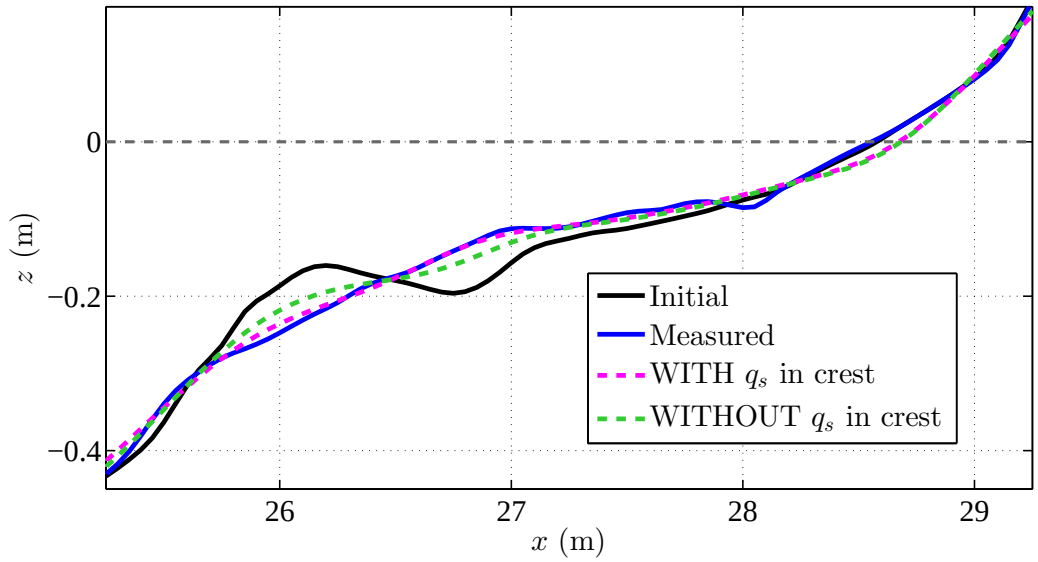

Figure 91: Simulation results of Exp. 2C with and without the inclusion of sediment fluxes in the wave crest. The transport efficacy factors (C_b and C_s) were both kept at their default values shown in Table 13.

6.4.3 Grain sorting and grain mixing effects

It is first worthwhile to discuss two major factors that influence the sensitivity of the grain sorting model. One is the sorting efficacy (*SF* in Equation (100)). For various values

of this factor, grain sorting results were tested in Exp. 2A and illustrated in Figure 92. The grain size changes in the test were found to increase for larger values of the factor, straightforwardly following the fact that the resulting grain sorting intensity is described to be proportional to the grain sorting efficacy.

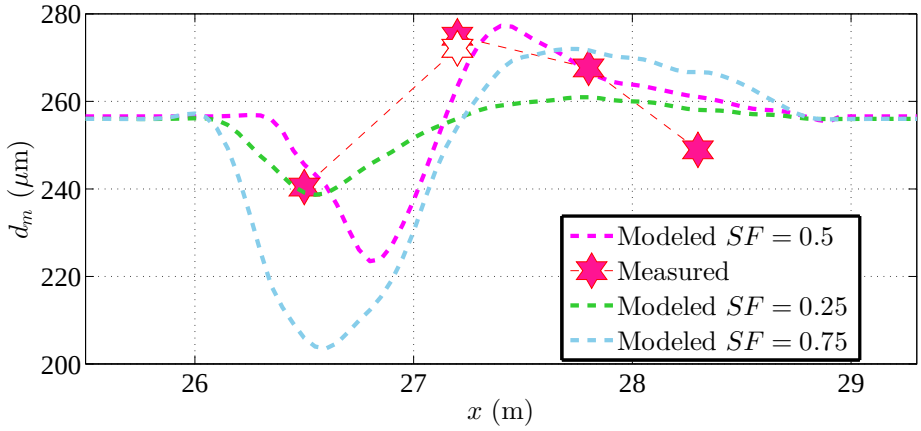

Figure 92: Influence of the sorting efficacy factor (*SF*) on the grain sorting results in Exp. 2A. The comparison is made based on the surface mean diameters. The value of *SF* of 0.5 is used as default in the model.

The other influential factor is the sediment size selectivity that is different in bedload and suspended load. Figure 93 shows the resulting grain sorting when either transport mode was solely configured in the simulation for Exp. 2B. It is clear that the sandbars are formed by coarser and finer materials in the cases of the bedload and the suspended load, respectively. All of the available fractions are conserved in each case which implies that the mean sediment size change near the shoreline is opposite to observed on the sandbar. The resulting cross-shore profile changes in Figure 93 also confirm that a configuration for each transport mode alone would not yield an accurate beach profile evolution. The sediment size composition change also would not be resolved considering the typical variation of the grain sorting observed over the sandbar area.

The multi-size sediment transport model might be operated without resolving the cross-shore grain size change, i.e. the initial size composition is repeatedly employed in the computation. An example for the consequence of this possible setup is shown in Figure 94 based on the simulation results for Exp. 2B2. The better accuracy is found for the case when the grain sorting was resolved essentially due to the presence of the finer

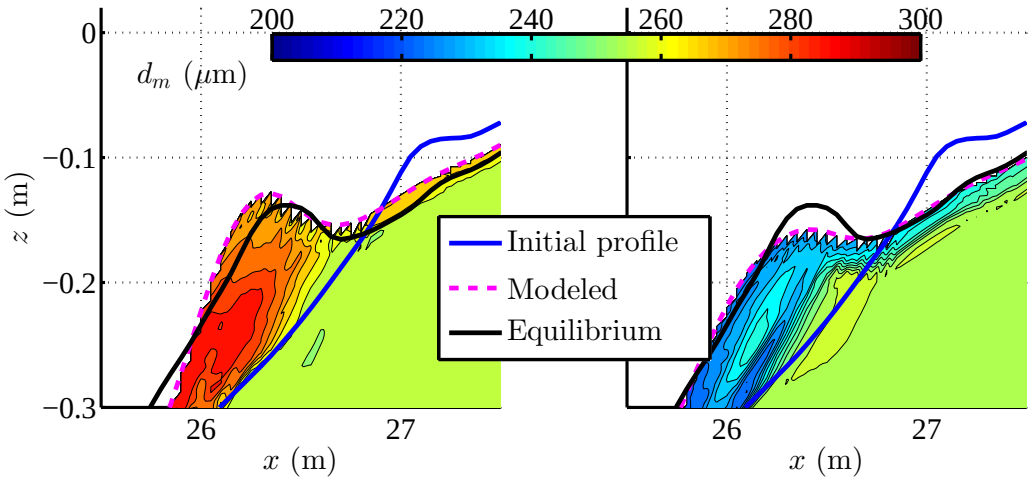

Figure 93: Profile evolution and grain sorting results modeled in Exp. 2B using bedload only (left) or suspended load only (right). The transport efficacy factor (C_b or C_s) is doubled from its default value in order to approach the target profile.

sediment fractions on the initial bar region. The greater mobility in this fine material allowed sufficient amount of the sediment transport that led to the formation of the new sandbar.

The model without grain sorting may be recalibrated for a better result; yet one of the greatest potentials in the multi-size transport model would still be omitted in such application. This potential is the modeling capability to account for the dependency between the beach profile evolution and the time-varying, cross-shore sediment size composition change. In fact, without the grain sorting, the multi-size model would behave similarly to a single-size model that is only relied on a representative diameter of the mixture. A comparison between the performances of the full-option, multi-size model and that of a single-size version is given later in this chapter in Section 6.6.

6.5 Experiment 3: Beach nourishment scenario

6.5.1 Simulation results

Profile evolution and grain sorting results for the beach nourishment scenario are illustrated in Figure 95 for the storm test (Exp. 3B) and in Figure 96 for the accretive test (Exp. 3C). This scenario featured two unique characteristics that were hypothesized to influence the cross-shore morphodynamics. One was the initial profile that consisted of

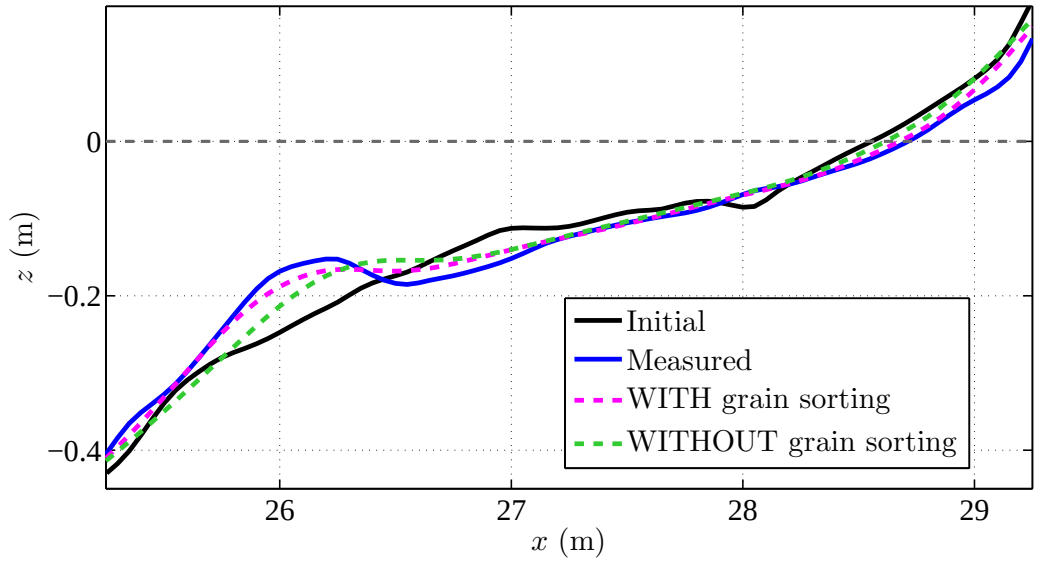

Figure 94: Profile evolution simulated for the repeated storm test (Exp. 2B2) with or without incorporating the grain sorting model. All of the adjustable parameters are default and consistent between the two cases.

two intersecting slopes, and the other was the potential mixing of the two different mixtures on the profile.

The presence of the milder native slope in Exp. 3B seems to influence the final profile, i.e. compared to Exp. 1B with an identical upper coarse-sand slope. The sandbar structure in this case appears to be broader, having a shallower trough and a less peaked crest. This feature is believed to occur primarily as the waves transformed earlier and some of the largest waves broke thus becoming less energetic once approaching the upper profile. The hydrodynamic model was able to capture this process and allowed for an accurate prediction of the mean, time-averaged sediment transport and, consequently, the resulting profile evolution with a computed performance index of 0.88.

The grain sorting trends in this experiment were observed to be very similar to those in the earlier tests. Two exceptions, however, include the fact that the native fine sand led to more comparable mean grain sizes between the bar-crest and the bar-trough sediment samples, as well as grain fining on the entire upper slope despite the obvious grain sorting trends. Both of these occurrences are believed to be a result of the mixing of the two different types of sand. Since the lower profile did not change, this additional mixing must have occurred as the materials on the two slopes were exchanging, most likely due to a

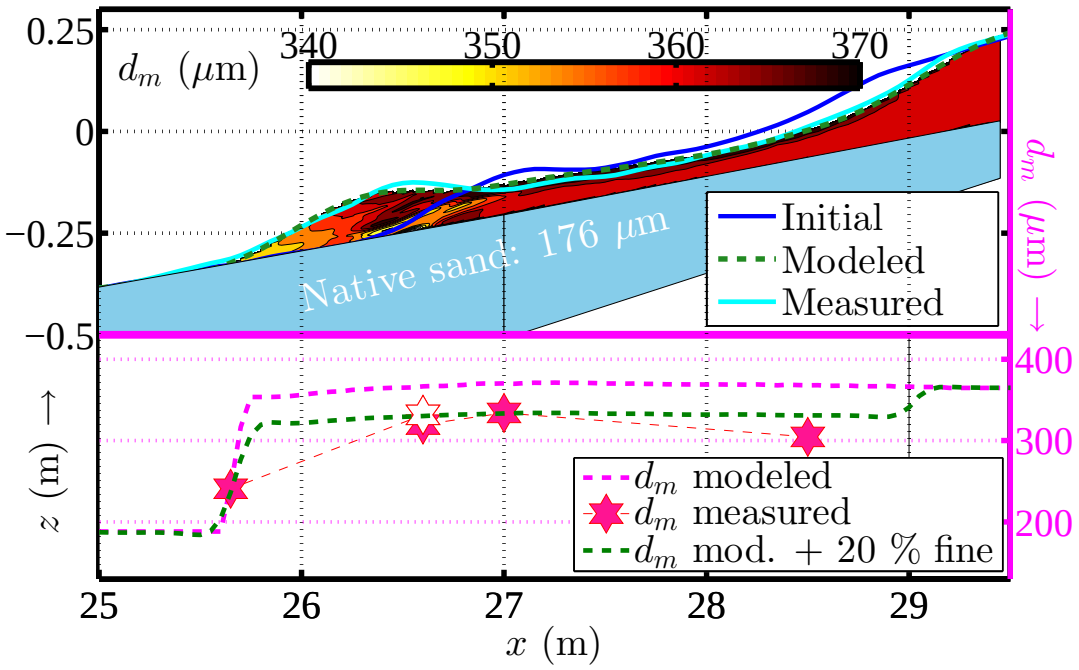

Figure 95: Simulation results for profile evolution and grain sorting in the erosive wave test Exp. 3B. Profile results in the top are shown with contours of the mean sediment sizes modeled at the equilibrium time. Mean grain sizes computed on the surface layer (2 cm) are compared to the measurement in the lower panel. Hollow marker indicates the subsurface sample. Uncertainty in the grain size analysis is ±5 μm.

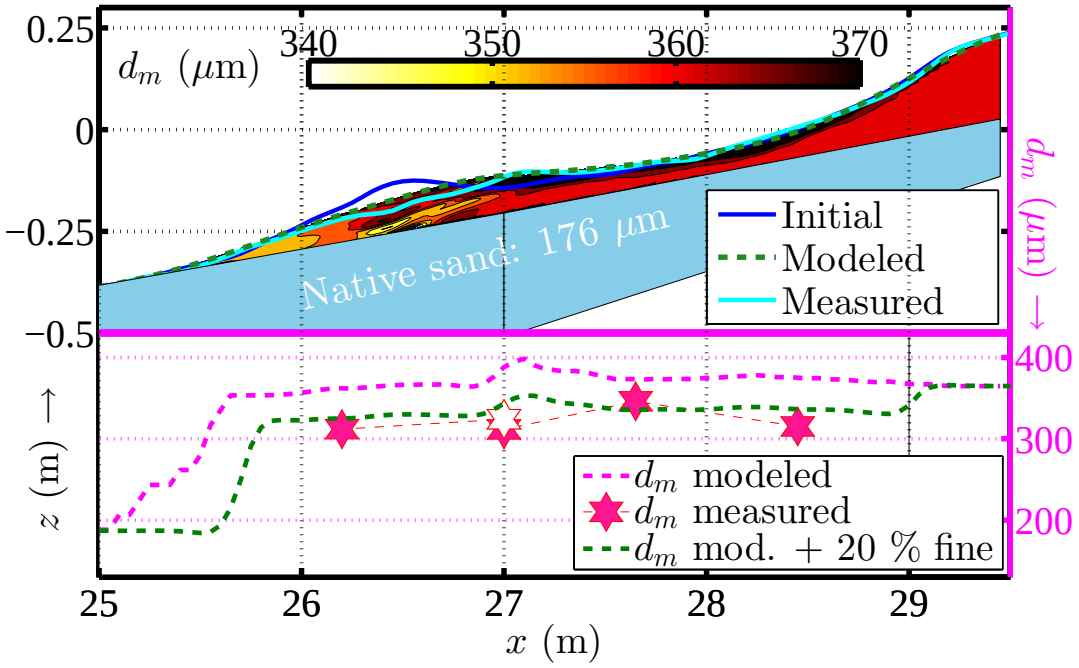

Figure 96: Simulation results for profile evolution and grain sorting in the accretive test of the beach nourishment scenario (Exp. 3C). Uncertainty in the grain size analysis is ±5 μm. See Figure 95 for more details.

longer-scale delayed settling in the suspended sediment transport. Unfortunately, these occurrences could not be simulated in the numerical model with the default configuration that predicted no or very minimal transport on the lower profile. A particle-tracking-based model would be an option as it would be able to capture a "leapfrogging" transport of sediment between any two distant locations.

Alternatively, the extra grain mixing may be estimated by assuming a certain percentage of the fine sand that was mixed with the coarse sand on the upper profile surface. Recomputed mean grain sizes under this assumption are shown together with the originals in Figures 95 and 96. In both cases, the percentage of mixing of 20% seems to yield the most comparable resulting mean grain sizes compared to those of the available sediment samples. It may be noted that this additional fine material was not accounted for in the prediction of the sediment transport rates, i.e. the sorting of the coarse sand considered and the mixing assumed later. The net transport rates should not be different by much due to the additional mixing, and neither should the profile evolution since this artificial mixing was assumed to be cross-shore uniform.

6.5.2 Effects of magnitude and phase differences between fluid and sediment velocities

An attempt is performed here to investigate potential influence of phase lag and magnitude difference between the sediment velocity and the fluid velocity as discussed earlier (Section 5.4). Figure 97 shows the ratios between the maximum magnitudes of these two velocities under the wave crest computed for three different sediment size fractions in Exp. 3B. All of the values are below unity since the sediment velocities are always the smaller term. The ratios decrease for larger sediments that are more resistant to the acceleration and drag.

Despite increasing drag coefficients, the difference between the two velocities becomes more significant towards the shoreline since the smaller flow velocities cause a nonlinear reduction on the particle advection process. Phase lags between the two velocities were found to be around 10^o-20^o, proportional to the sediment diameters. Unlike the velocities, these phase lags feature very minimal cross-shore variation of around 2^o-3^o which is

reasonably negligible.

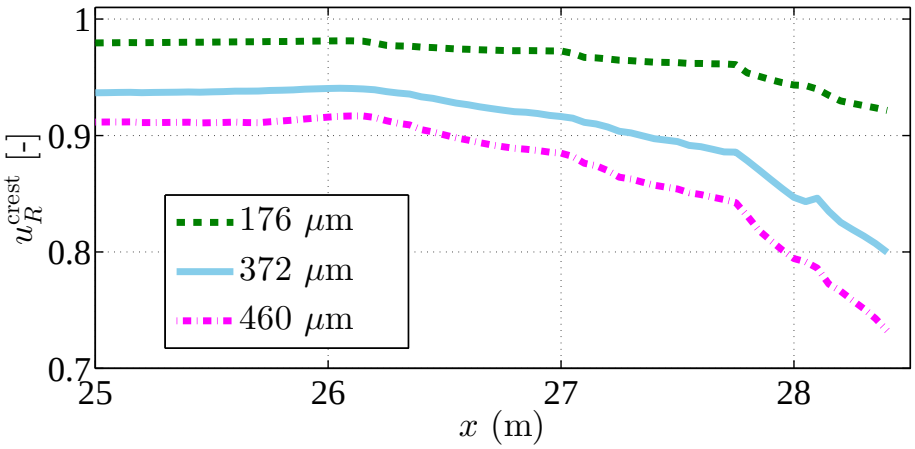

Figure 97: Ratios between the maximum sediment velocities and fluid velocities along the beach profile in Exp. 3B. The values are based on the velocities around the middle of the water column ($z = -h_o/2$), computed under the wave crest.

Effects of the velocity reduction and phase lag in the numerical modeling results are shown in Figure 98 for Exp. 3B and 3C. Despite the substantial magnitude reduction shown in Figure 97, the effects were predicted to result in a very small impact on the two final beach profiles. The main reason behind this surprising outcome lies in the fact that a profile change is determined from the gradient of the local "net" sediment transport rates computed in a phase-averaged fashion. The velocity magnitude reductions in both onshore and offshore velocity phases are present which, consequently, tend to be canceled out and result in a minimal change after the time averaging.

A similar scenario is also the case for the phase lag since a shift in the oscillatory velocity would lead to a comparable alteration of the transport fluxes under the crest and the trough of a wave. Generally, the magnitude reduction and the phase lag lead to a small decrease of the net sediment transport in the predetermined directions, i.e. offshore and onshore for the erosive and the accretive conditions, respectively. Such decrease occurs since the sediment mobility under that given onshore/offshore flow is dominant and its transport rate, therefore, is affected more by the reduction in the velocity magnitude.

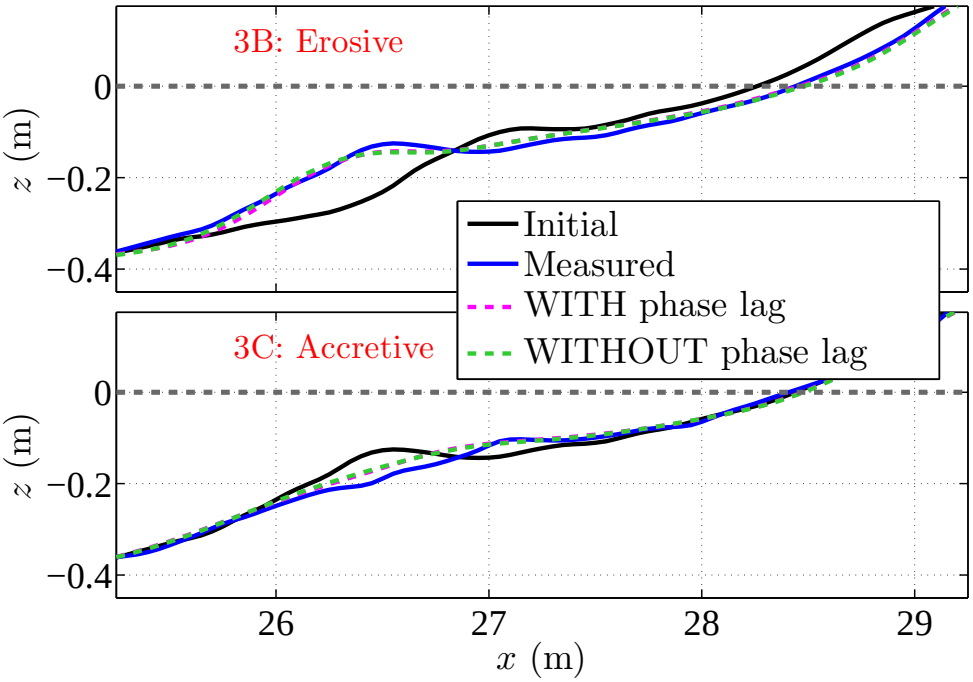

Figure 98: Example of profile simulations with and without the consideration on the magnitude reduction and phase lag in the sediment velocity. Top panel compares the results for Exp. 3B; bottom panel for Exp. 3C. The transport efficacy factors (C_b and C_s) were kept at their default values in both cases.

6.5.3 Bed-slope effects

The bed-slope term in the model was included for a more realistic determination of the critical shear stress along a beach profile (Equation (68), Chapter 5). Figure 99 shows an example of the influence of this slope term in Exp. 3C. Two different values of critical shear stress are given locally for upslope or downslope transport scenarios depending on the instantaneous oscillatory flow direction. Since the upslope transport is associated with decreased sediment mobility, the critical stress under the wave crest is usually greater than that under the wave trough on most of the profile.

Figure 99 also illustrates the instantaneous bed shear stresses found under the crest and the trough of the wave. These shear stress magnitudes exceeding the critical values lead to effective shear stresses that drive the sediment transport. In this case, the more dominant effective shear stress under the wave crest would clearly result in a predominant net onshore sediment transport and consequently an accretive profile evolution. The bed-slope term is designed to be optimal for any beach profile evolution conditions.

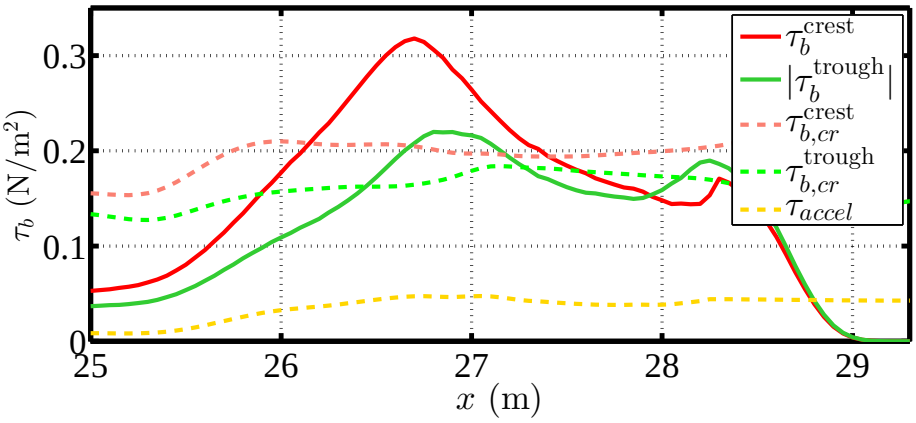

Figure 99: Instantaneous and critical shear stresses determined on the bed profile in Exp. 3C. The values are computed separately for the crest and the trough velocities which differ due to the effect of bed slope, except for the acceleration-induced shear (τ_{accel}) that is a locally-constant *RMS* quantity.

Figure 100 illustrates the bed-slope effects on the cross-shore profile changes in the erosive (3B) and accretive (3C) tests. Without the bed-slope term in Exp. 3B, the offshore transport rates were slightly over-predicted over the bar trough but under-predicted over the bar crest, consequently leading to a peaky new sandbar that does not match the observation. The effect is less apparent in Exp. 3C. With the bed-slope term, the model shows a slightly better performance around the new sandbar structure since the accretion was enhanced by the down-sloping surface shoreward from the initial bar crest.

6.6 Grain-size configuration and model performance evaluation

A user-defined number of sediment size classes is required in both the multi-size sediment transport model and the grain sorting model. Thus far, this number has been selected to be ten matching the resolution of the sieve analysis of sediment samples in the experiment. Generally, the model is found to be robust under a sufficient number of size classes, with "seven" as a recommended minimum. The significance of this number arises when the mean diameter of the mixture is computed and the "finer" and the "coarser" size groups are assigned. For seven size classes, three or four size fractions will be given in each of the two groups.

If the number of size fractions in each group are fewer, an issue may arise as the different particle sizes between the two groups could be too extreme and cause nonuniformity in

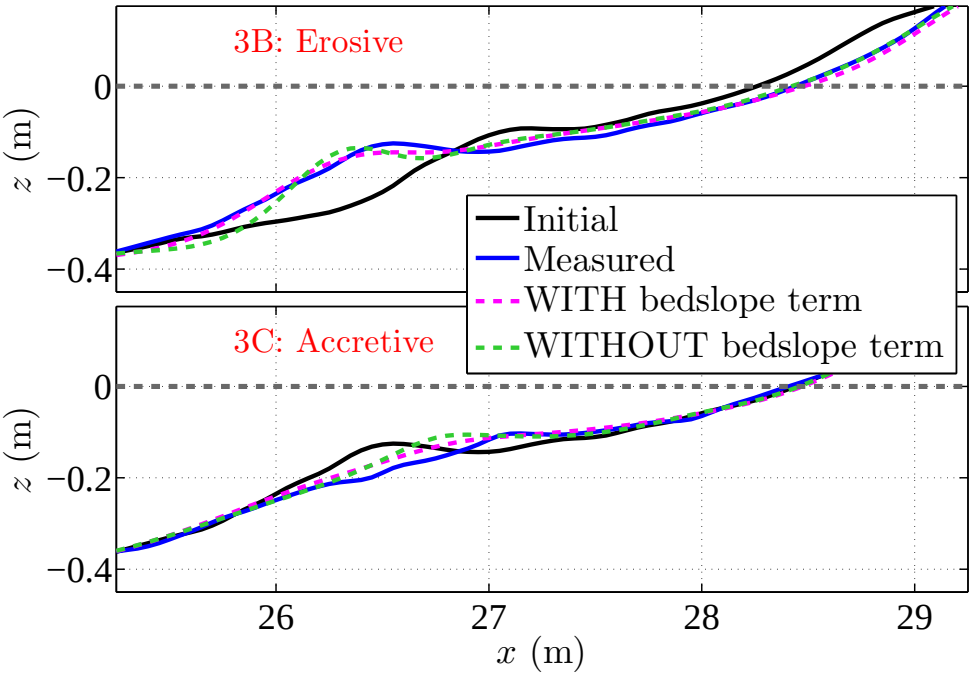

Figure 100: Example of simulation results with and without the bed-slope term for the beach nourishment scenario. Top panel compares the results for Exp. 3B; bottom panel for Exp. 3C. The transport efficacy factors (C_b and C_s) were kept at their default values in both cases.

the transport rates and consequently in the resulting grain sorting. This particular problem is discussed next in an analogous model test of a two-size mixture based on the sediment bimodality. The operation of the multi-size model as a single-size model is also another case of interest that is described in this section. Necessary modifications on the models under these two special applications are first illustrated. The simulation results are then presented and compared to those obtained earlier from the full-option, ten-size-fraction model.

6.6.1 Bimodal sediment distribution

An example for a two-size-class configuration in the model is shown and investigated here for the case of the bimodal mixed-sand experiments in this study. The given two-fraction mixture comprises of 62% of 176 μm and of 38% 372 μm sands, with the initial mean diameter of 250 μm. One advantage for this setting is a more straightforward interpretation of any fractional-dependent results since only two size classes are involved.

Under this special setting, Figure 101 illustrates the cross-shore profile evolution and

grain sorting results for Exp. 2A. The model tends to slightly overpredict both types of the results, i.e. compared to the measurement and the full-size simulation (Figure 83). The overestimated erosion around the shoreline as well as the excessive deposition around the offshore part of the bar are evident for the case of the profile evolution. Figure 102 shows the two-fractional percent occurrences modeled for the mixture on the profile surface.

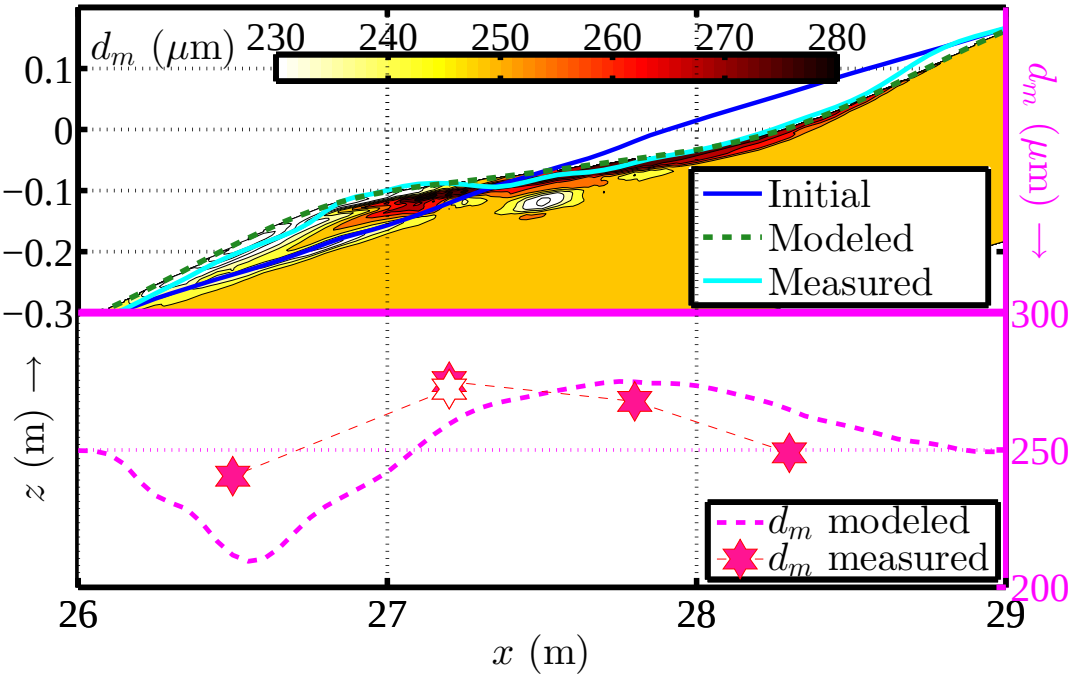

Figure 101: Two-fractional simulation results for profile evolution and grain sorting in the erosive wave test on the mixed-sand profile (Exp. 2A). Uncertainty in the grain size analysis is ±5 μm. See Figure 96 for more details.

The trends of the modeled size distributions in Figure 102 are in agreement with the observation for all locations but the waterline position. The magnitudes of these grain size changes, however, were overpredicted for both the coarsening and the fining at either end of the profile. This particular result implies that an overestimation of the finer fraction was repeatedly computed in the model. It is also this finer portion that led to the overprediction of the net sediment transport rates, and consequently the excessive erosion and deposition on the cross-shore profile observed in Figure 101.

The overestimation of this finer fraction occurred mainly due to an increased suspended-load transport rate led by some extreme values of the parameters that describe the size selectivity bias the smaller size class (176 μm). For example, having a very small fall

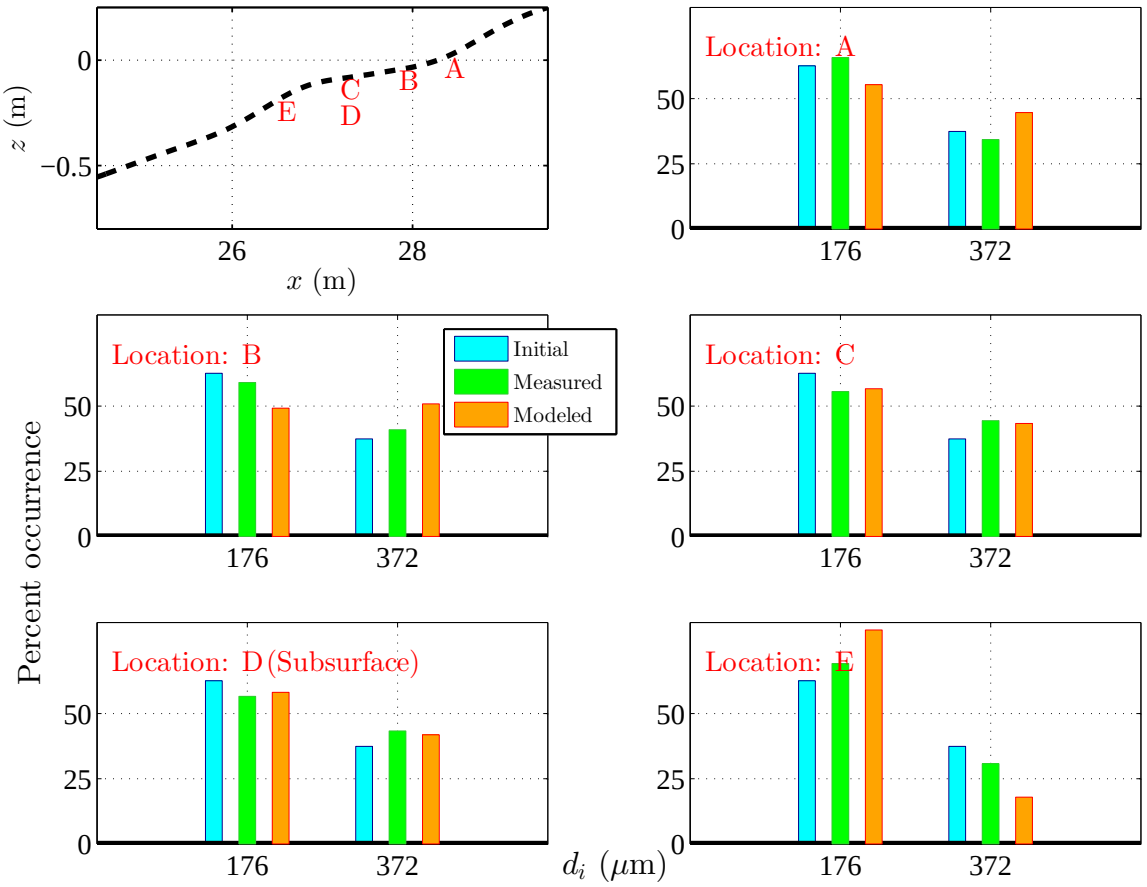

Figure 102: Modeled two-fractional size compositions of the surface mixtures at five locations where measured data are available in Exp. 2A. Top-left panel shows the locations. The initial mixtures are the mixed-sand on the starting profile treated as a two-size mixture.

velocity, this size class was involved with a drastic grain-size dependency that is very significant in the concentration estimation. The bedload of this finer fraction may be reduced at the same time but this reduction would be trivial compared to its increment in the suspended load.

The two-fraction application was also attempted for the other consecutive mixed-sand tests (2B, 2C, and 2B2) where another crucial issue arose as the two fractions on the profile tended to be completely sorted out from each other. This occurrence is clearly not the case found in the measurement in this study, or realistically anywhere in the nature since it implies that all of the fractions in one size group are either completely removed or remained at a cross-shore location.

The extreme fractional transport rates between the two fractions were the main reason for the size-class separation, which also led to the recommended minimum number of size classes for the multi-size model. The profile simulation might be improved by recalibrating the adjustable parameters but this grain-size separation issue would still occur eventually. The bimodal setting may be improved but the use of this modeling option is not deemed advantageous, except for a shorter computational time which could always be improved by other means in the numerical model execution.

6.6.2 Single-size modeling

The multi-size model can be operated as a single-size model by simply assigning the mean, or another representative grain size, as the only size class in the sediment mixture. In this setting, the grain sorting model will become inactive and the chosen initial grain size will be both uniform and permanent in the simulation domain. For a fair comparison between the two different types of model, a recalibration effort to optimize the single-size model was performed. The most optimal results for the single-size model could be obtained by adjusting the transport efficacy factors (C_b and C_s) in the multi-size model by certain percentages shown in Table 14.

It is very important to note that the new coefficients for the single-size model do not follow the criteria applied for the multi-size model (Table 13). Their suspended/bedload proportions are not controlled, and the factors for the two 10-cm wave conditions (A

Table 14: Adjustment in sediment transport efficacy factors for the single-size model application. Values are given as percent changes compared to the default numbers for the multi-size model (Table 13).

Parameter	Percent adjusted for each wave condition			Description
	A) 10 cm/1.5 s	B) 20 cm/1.5 s	C) 10 cm/2.0 s	
C_b (Eq. 59)	+10%	-42.5%	+22.5%	Bedload efficiency
C_s (Eq. 81)	+7.5%	-10%	+37.5%	Suspended-load efficiency

and C) are arbitrary. These freely-selected values are possible due to an absence of the requirement for monitoring relative fractional sediment transport rates and the consequent sediment grain sorting.

6.6.3 Comparison of model performance

The single-size model was utilized to simulate all of the experiments and their results were compared to those obtained earlier from the multi-fraction model (Table 15). The differences between these two types of results can be evaluated to reveal several distinguishable capabilities in the multi-size and the single-size models.

It is worthwhile to begin the evaluation by imagining a case of perfectly uniform sand where the resulting profiles from the two models would be identical. This ideal scenario is somewhat analogous to Exp. Set 1 with the coarse sand that featured a narrow unimodal sediment size distribution. Even though it was observed and also resolved by the model, the grain size change on the profile was not significant enough to be a dominating factor in the process. Several other influential mechanisms and their uncertainties could possibly overwhelm any effect from this small grain size change.

The conditions designed for Exp. Set 2 are clearly more encouraging for the study of grain size effects. The significant grain size change of up to 20% was essentially promoted by both the mixed sand characteristics and the consecutive profile evolution tests in Exp. 2A to 2B2. Once it continuously amplified, the grain sorting on the profile led to noticeable differences between the performances of the two models as observed for Exp. 2B, 2C and 2B2 in Table 15.

The resulting accretive profiles yielded by the two models for Exp. 2C are compared

Table 15: Summary on the capabilities of the multi-size and single-size models to predict cross-shore evolution and equilibrium profiles. The performance index (ppf, Equation (98)) and the equilibrium index (eef, Equation (99)) were computed for both models with highlighted numbers indicate the better capabilities.

Exp.		Sand Type	Test Condition	Perf. index (ppf)		Equi. index (eef)	
				Single-size	Multi-size	Single-size	Multi-size
1	B	Coarse	Storm	0.89	0.91	0.066	0.052
	C		Accretive	0.61	0.59	0.002	0.003
2	A	Mixed	Erosive	0.86	0.85	0.002	0.001
	B		Storm	0.86	0.90	0.028	0.023
	C		Accretive	0.68	0.82	0.011	0.010
	B2		Storm	0.74	0.81	0.061	0.041
3	A	Coarse on fine	Erosive	0.87	0.86	0.002	0.003
	B		Storm	0.85	0.87	0.051	0.031
	C		Accretive	0.74	0.75	0.006	0.013

in Figure 103(a). A comparison of the local performance indices based on the results is shown in Figure 104. The most obvious distinction between the two sets of simulation results is found in this case with the multi-size model clearly outperforms the single-size model at the most crucial part of the profile. This particular part is the zone around the new sandbar structure observed at the given equilibrium time ($26 \leq x \leq 27.5$ m).

The inaccuracy in the single-size simulation arose primarily as a result of overestimated onshore sediment transport rates over the initial bar trough zone. This local overestimation prevented a sufficient net deposition for the formation of the new sandbar structure, even though the initial bar crest was simulated to migrate onshore into the bar-trough zone. Besides, the erosion around the offshore part of the initial sandbar was also slightly underestimated, which also led to a reduction in the onshore sediment flux into the new sandbar area.

The consideration in the temporal and spatial variations of sediment grain sizes is the key to the superiority of the multi-size model. In Exp. 2C, the initial condition was associated with previous grain sorting that featured coarser material around the trough and

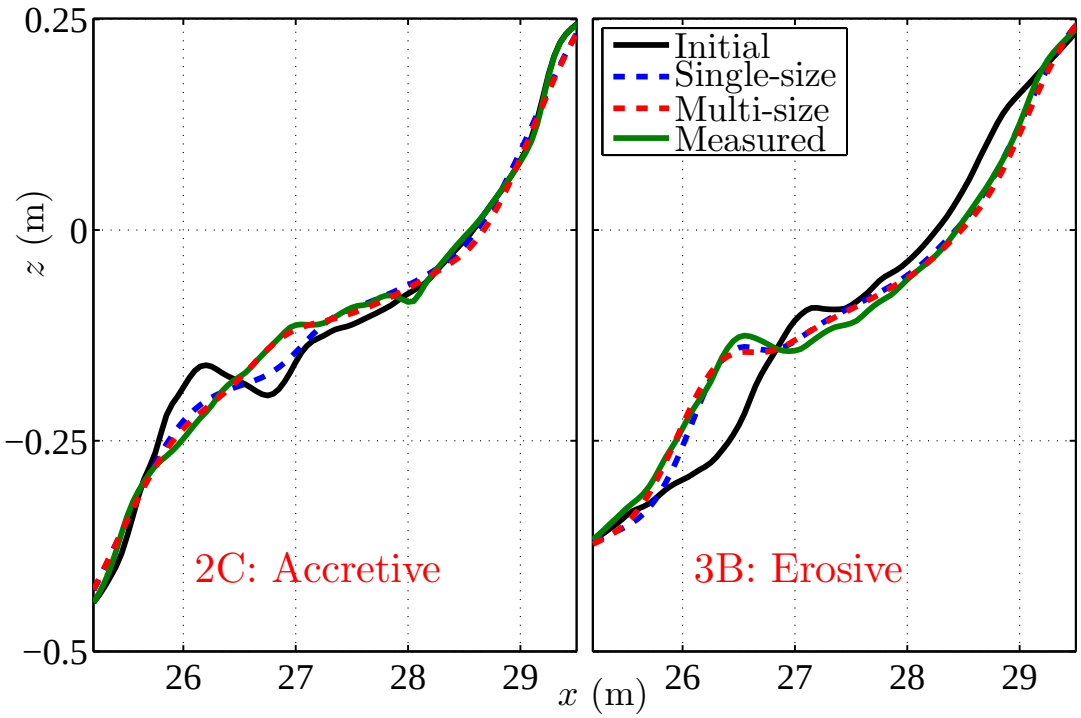

Figure 103: Example of cross-shore profile evolution results simulated by the multi-size model and the single-size model. Both sets of results are determined at the given equilibrium times in the experiments.

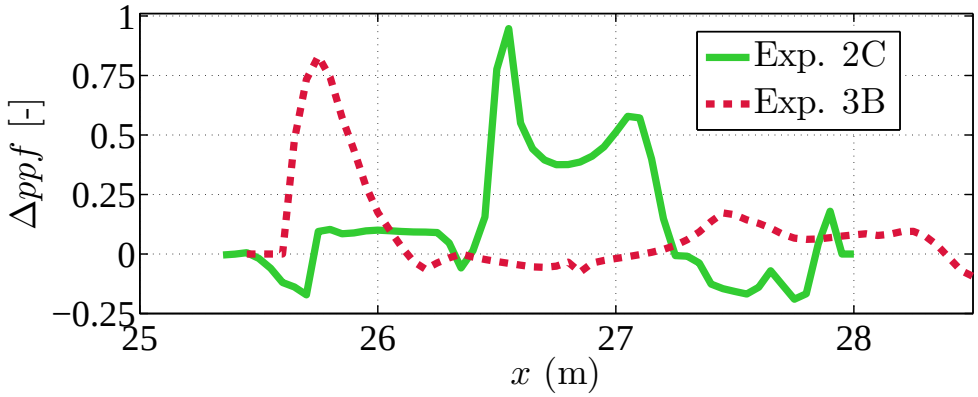

Figure 104: Differences in local performance indices based on the results between the multi-size and the single-size models in Figure 103. The deviation Δppf is simply defined as the index from the multi-size model minus the index from the single-size model at the same location.

finer material around the offshore part of the bar (Figure 84). Compared to the case of a uniform mixture, the coarser sand led to a reduction while the finer sand led to an increase in the local sediment transport rates. These mechanisms counteracted and eliminated the overestimation in the bar trough and the underestimation on the bar crest found in the use of the single-size model.

In Figure 103(b), the cross-shore evolution results from the two models are compared for the storm-wave beach nourishment test (Exp. 3B). The performance indices corresponding to the results are also compared in Figure 104. This case shows a clear example of the better prediction by the multi-size model around the offshore part of the sandbar of an erosive-type beach profile. The slope of this part predicted in the single-size model is typically steeper than observed. This inaccuracy is led by the negligence in the fining of the local material, of which the consequences are the underpredicting sediment transport rates and offshore bar migration, respectively.

Besides its superior accuracy to the single-size model, it should be emphasized again that the multi-size model also featured more consistent descriptions in the application. The model always resulted in reasonable proportions between bedload and suspended load that were indirectly verified based on the available grain sorting information. The configuration in the model was also identical for the two smaller wave conditions in the erosive and accretive profile tests.

Ultimately, there might only be two aspects in which the single-size model could be more advantageous. One is the simplicity for its usage, certainly as a trade off for the modeling accuracy and the grain sorting information. The other is the computational time. In the present parallel computation, the multi-size model required a duration about 3 times longer than the single-size model. This duration, however, depends greatly on programing and computers that are certain to be improved drastically in the near future.

6.6.4 Equilibrium beach profile simulation

Besides the simulation accuracy, the capability to resolve an equilibrium beach profile is another desired aspect in the numerical model. Under such condition, a profile may not evolve further with time or may feature minimal periodic changes with the mean that

approaches zero. In the laboratory experiment, an equilibrium state was evident in every test (see Chapter 3). The capability to approach this equilibrium state can also assure that the numerical model is stable for a long-term simulation. This capability is evaluated based on the equilibrium index (eef), i.e Equation (98), which would eventually be equal to zero if the model truly reaches an equilibrium state.

Figure 105 shows the equilibrium indices computed during the four profile simulations in Exp. Set 2. These values are also shown separately for the single-size and multi-size models for a comparison purpose. In every case, the equilibrium indices are found to decay exponentially but do not drop to zero within the given equilibrium times. Exp. 2A with the smaller-erosive wave results in the final index that is closest to zero, as opposed to the storm-wave tests in Exp. 2B and 2B2. The use of the multi-size model seems to be associated with lower values of the indices. As per these findings, two aspects to be discussed next include a comparison between these two types of model and the potential for a long-term model simulation.

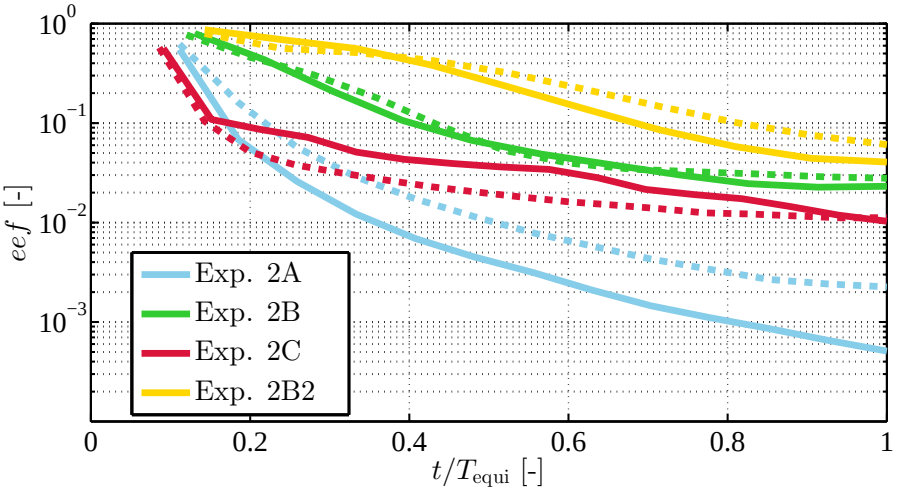

Figure 105: Equilibrium indices computed during the simulations of the mixed-sand experiments. Solid lines are multi-size modeled; dashed lines are single-size modeled. Exp. 2A: Erosive wave. 2B: Storm wave. 2C: Accretive wave. 2B2: Repeated storm wave.

The equilibrium indices computed for all of the experiments at their equilibrium times are also shown in Table 15 (page 170). Although non-zero, the indices are rather small with the largest value in a storm test that roughly implies 5% of the profile change at the equilibrium still, compared to the initial change. This implication should however be

considered carefully since the index is based on a cross-shore summation of the rate of change on the profile. The local rates of change at the equilibrium time could be very minimal but covered a wider part on the profile. The equilibrium index may thus seem rather substantial as a result of the summation.

For several cases in Table 15, the multi-size model tends to yield the resulting profiles that better approach an equilibrium state. This favorable result originates following the surface sediment coarsening process around the most energetic zone which leads to a local sediment mixture that is less mobile. Fining on the surface may also occur but mainly in a less energetic zone. By comparing the hydrodynamics and the resulting grain sorting, these two zones can be separated roughly at a location right onshore from the bar crest. The shoreward part is the more energetic area with the coarser material.

All of the experiments were simulated for periods three times longer than the given equilibrium times to investigate model behavior and potential to reach equilibrium states. These special tests are shown for the accretive test 2C in Figure 106, and for the repeated storm test 2B2 in Figure 107. The existing onshore transport in the case of Exp. 2C would still lead to additional accretion, at an expense of the overpredicted erosion around the offshore part of the profile. Nevertheless, it is clear that these ongoing processes are exceedingly small and almost completely discontinued after twice the equilibrium time.

The additional changes found in Exp. 2B2 are similar to those in Exp. 2C, except for that the continuing sediment transports were in the opposite directions. In this erosive test, the offshore part of the bar was still receiving additional deposition as a result of the material loss around the foreshore area. Although these changes are considerably larger, mainly due to the more energetic wave condition, they also tend to decrease very quickly during the last two equilibrium times. Surface mean grain diameters that changed during the two extended simulations are also shown in the lower panels in Figures 106 and 107.

The additional grain sorting in Exp. 2C is very small since the grain sorting model is only activated if the cross-shore profile evolution is significant. The grain-sorting changes in Exp. 2B2 are substantially larger with very intensive grain coarsening near the shoreline. These latter results appear to be questionable and could not be investigated using available data sets. Except for this overestimated part, however, the trends of the grain sorting results

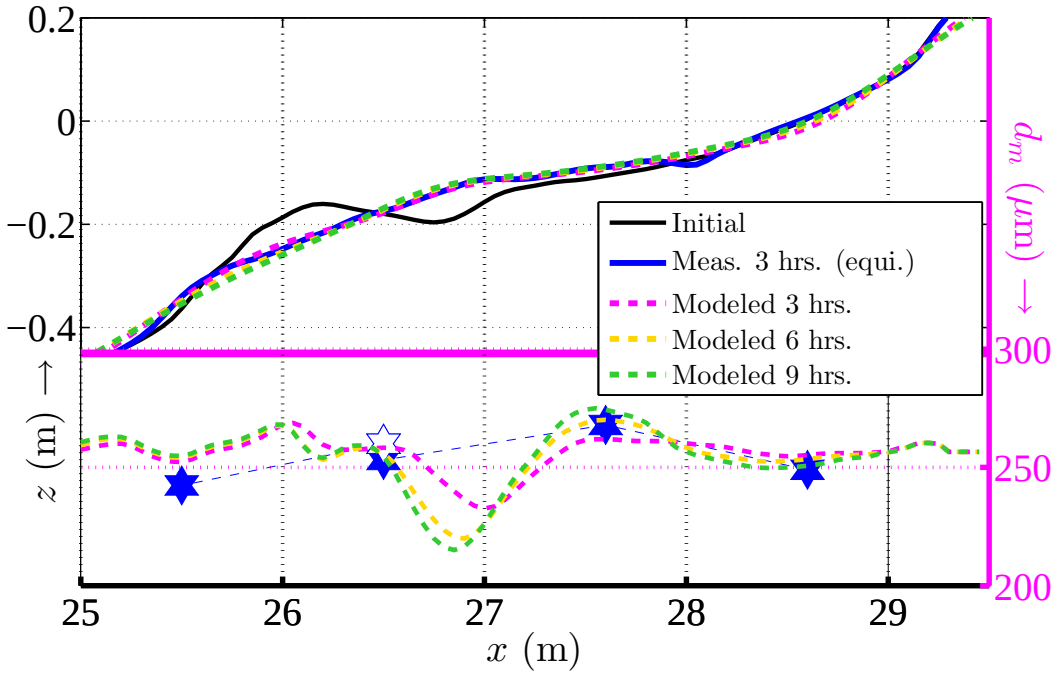

Figure 106: Long-term simulation of the accretive test on the mixed-sand profile (Exp. 2C). The legends are shared between the profiles and the mean surface (2 cm) grain sizes in the bottom. Hollow marker indicates the subsurface sample. Uncertainty in the grain size analysis is ±5 μm.

are consistent with the measurement, which is arguably more important. The accuracy in the sorting magnitude may always be improved if desired, for example, via the adjustable sorting efficacy or the configuration between the sediment transport and the grain sorting models.

In order to make a conclusion, it is preferable that the typical modeling result be compared with possible theoretical explanation for an equilibrium beach profile. In a closed-environment, cross-shore domain, a cross-shore bathymetric evolution will discontinue if only the gradient of sediment transport rates vanishes which is possible in two different scenarios. One is that the net transport rates in both transport loads are zero everywhere due to the lack of initiation of sediment motion. This scenario may seem skeptical as sediment may still be picked up to some extent even on an equilibrium profile.

The second scenario is that the bedload and the suspended load are nearly identical in magnitude but opposite in directions, thus adding up to the net sediment transport rate of about zero. This scenario may be regarded as being more feasible than the first possibility. A weak dependency between the two transport modes might exist on a beach profile but it

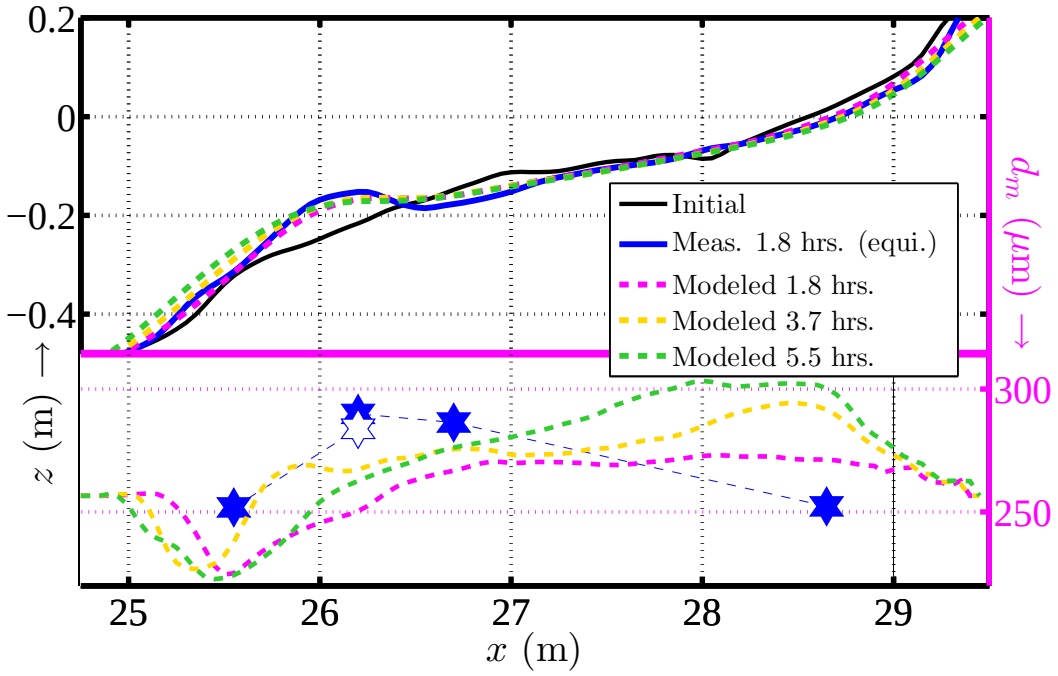

Figure 107: Long-term simulation of the repeated storm test on mixed-sand profile (Exp. 2B2). Uncertainty in the grain size analysis is ±5 μm. See Figure 106 for more details.

should not be able to prevent the opposite transport directions to occur. Given this scenario, the grain sorting on the profile would also be expected to continue during the equilibrium state.

As per the results and the above explanation, it has to be admitted that the present numerical model does not predict a perfect profile equilibrium condition. The equilibrium times and the final profiles in the simulation were found to be somewhat different from the physical modeling results. The model also tended to approach an equilibrium via the reduction of the bedload and suspended load that is less likely than the case where the two transport modes are balanced. Despite these few shortcomings, the model was shown for its capability to approach a profile equilibrium to a satisfactory degree as shown in Figures 105 and 106.

6.7 Model application at prototype scale

Developed under a process-based principle, the present numerical modeling system will be capable of resolving related processes and resulting profile evolution in a field scale. Such

application will, however, need to be performed with a special consideration on two major aspects. One is the fact that the model does not describe every process that could be found at field scale; the other is the scaling effect arising from some dimensionless parameters that were not preserved between the physical model and the prototype. A separate attempt in the configuration and calibration of the model will likely be required for re-optimizing the comprehensive modeling system.

The model is designed to describe the cross-shore morphodynamics only. For this reason, a sole use of the model will be appropriate for a duration over which longshore processes can reasonably be assumed negligible, or where such processes are less significant. This latter condition includes the scenario where the incident wave angles are predominantly close to shore-normal, or for a relatively straight coast with very small variation of the longshore processes along the shoreline. For a more extensive use, it is advised that the new cross-shore model here be coupled with a longshore morphodynamic model. Tidal variation can also be influential in a field simulation. This factor may be accounted for by adjusting the effective water depth along the profile according to the changing still water level.

Scaling effects in the model simulation are mainly originated from the fact that the numerical model was configured and tested on the basis of the small scale, distorted physical model. Regarding wave and hydrodynamics, the parameters that are involved with wave breaking may need to be recalibrated, primarily due to an influences of steeper profile slopes in the wave flume. These may include the wave breaking intensity and surface shape parameters (B and B_o). The bottom friction factors f_w and f_{cw} will likely need to be lower since previously they were also treated to account for the side wall friction that was present in the flume but not in the numerical models. For a recalibration of the wave and the current models, it is advised that the suggested default values be utilized for a starting attempt (see Table 9, Chapter 4).

Scaling effects are also expected to be the case for sediment transport primarily due to the fact that the sediment sizes were not scaled down for the physical model profiles. A primary difference between the processes in the two scales would be the magnitudes of the bedload and suspended load and the ratio between them. In general, the suspended

sediment transport might be underemphasized in the physical model due to the relative sediment fall times that were not proportional to those in the prototype. These possible changes in the two transport modes may be revised by recalibrating the transport efficacy parameters C_b and C_s. The wave breaking factor (F_{ecg}) that estimates a direct sediment pickup due to tumbling wave front is also expected to feature a less substantial effect due to a deeper water column which would act as a cushioning medium.

The grain sorting result is dependent on the bedload and suspended load ratio. As such, a typical magnitude of the sediment grain size change is expected to be different between the two scales, most likely larger in the field. The sediment transport models after recalibrating should be able to resolve this scaling effect in the grain sorting. If further recalibration is needed, the grain sorting efficacy factor (SF, Equation (100)) may be re-tested for its sensitivity and a value for the most optimal result. Another important consideration for a model setup in the field scale is the vertical resolution of the grain sorting model, due to the significance of vertical grain lamination in the problem. It is recommended that a chosen resolution allows for at least 4-5 layers per a total thickness of the profile change over a model update (user-defined, see Figure 71). For example, if a typical change is 10 cm over a model call, the resolution should not be less than 2 cm.

In this chapter, the new morphodynamic modeling system is extensively tested by simulating the physical model conditions. The multi-size sediment transport and grain sorting models were shown to enhance the capability to resolve beach profile evolution, while also providing information on the sediment grain size change. The superiority of the new model over a traditional single-size modeling approach was found to be increasingly evident as the grain sorting on a beach profile became intensive. The multi-size model also tends to approach a profile equilibrium state better since the sediment bed is stabilized as a consequence of the grain sorting. A discussion is also given for the application of the model at prototype scale. Recommendations for future model development are provided in the next chapter.

CHAPTER VII

CONCLUSION

Highly complex flows driven by ocean waves, currents, and their interactions lead to many threatening phenomena in the nearshore zone. Beach profile erosion, shoreline change, and loss of valuable land are one common series of fearsome consequences that concern the coastal community. In this study, physical and numerical models were developed to investigate related processes in such phenomena and to describe them in a morphodynamic model. With the use of new multi-size sediment transport and grain sorting models, the ultimate goal is to introduce a new comprehensive modeling system that features a superior predictive capability.

The specific domain of interest is the 2-D cross-shore profile, spanning from the maximum wave run-up location to the depth of closure, within which sediment transport is active. The study focused on a beach profile equilibrium timescale. The current state of the art in modeling this problem shows a lack of sufficient description for the influence of sediment size characteristics. Most available models assume a single grain size at a given cross-shore location; actual sediment size composition, as well as its spatial and temporal changes, is rarely considered during the beach evolution process. The new sediment transport and grain sorting models developed here fully account for these aspects by the use of a size-selective sediment transport approach and a grain-size composition tracking algorithm.

The effects of grain size characteristics on sediment transport have long been studied but mostly for steady flow in open channels, or oscillatory flow in water tunnels without a free surface, a bottom slope, or breaking waves. Some field data are available but also associated with unknown or uncertain hydrodynamic conditions. These facts clearly indicated the need for new data from a physical model that focused on cross-shore grain sorting and equilibrium beach profiles. The random-wave flume at Karadeniz Technical University, Turkey, featuring dimensions of $30 \times 1.4 \times 1.2$ m, was utilized for this purpose.

A small-scale experiment was conducted in the flume, with uniquely designed features that encouraged the study of sediment grain size effects, including

- Three types of beach profiles: coarse or bimodal sand on an initially-plane slope; coarse on top of fine sands for a beach nourishment scenario.
- Three wave conditions consecutively applied on each profile: small, short-period wave for erosive condition; large, short-period wave for storm event; and small, longer-period wave for accretive condition;
- Collection and analysis of sediment samples for the investigation of time-dependent grain size characteristics on the profile.

Each experiment continued until the measurable profile evolution ceased. Waves and currents were measured and utilized for data interpretation and validation purposes in the numerical study. Regarding the beach profile evolution and grain sorting problems, the major findings in the laboratory experiment include

- Existence of an equilibrium state in every profile evolution test;
- Distinct and consistent resulting beach profile under each wave condition;
- Influence of sediment size characteristics that led to different features on the beach profiles of different materials;
- Consistent sediment size composition changes at certain cross-shore locations with two major dependencies on wave condition and sediment transport history;
- Exchange and mixing of fine and coarse sands from the native and fill slopes in the beach nourishment scenario.

The distinctive final beach profiles among the tests clearly showed that beach equilibrium profiles differ by wave and sediment conditions. Erosive-, storm-, and accretive-type beach profiles may be speculated based only on the wave conditions. Other miscellaneous features such as sandbar structure and beach profile gradient were also dependent on the sediment size characteristics. The relationships found among these observations have led to an acknowledgment for the priority of the influences in the problem. The waves and hydrodynamics are the primary driver of the beach profile evolution. The sediment condition shows a secondary influence which, however, can be increasingly important when

larger ranges of sediments are considered. Note that this conclusion should specifically be applied to sandy materials with diameters ranging from 62.5 to 1,000 μm.

It is clear that the occurrence of "grain sorting" and its influence on the cross-shore profile evolution depend mainly on the grain size characteristics. For the well-sorted coarse sand in the study, the grain sorting was found to be very small over the profile equilibrium timescale, i.e within ±5% in terms of the mean diameter (d_m) changes. No consensus exists for a threshold at which this grain sorting effect should be considered. Van Rijn (2007b) suggested a grain sorting index (d_{90}/d_{10}) greater than 4.0 as an indicator. It was clear, however, that the effect was also very significant for the mixed-sand experiment here with the initial sorting index of 3.5, compared to 2.3 for the coarse sand.

The grain sorting trend was consistent for a certain type of beach profile in the experiment. For an erosive-type profile, coarsening of the bed surface was generally found from the waterline to the bar crest while fining was found on the offshore part of the bar structure. In the subsequent accretive test, both the coarser and finer materials around the bar structure moved onshore with the sandbar. These observations suggest that both hydrodynamics and sediment condition are influential on the resulting grain sorting on a beach profile. Basically, coarsening of the mixture can be expected in a more energetic, erosive zone where finer material is removed. The magnitude of this process is subject to the characteristics of the local mixture which largely depend on the grain sorting history.

The new morphodynamic model developed in this study is a comprehensive, predictive tool for the simulation of wave-driven hydrodynamics, cross-shore profile evolution, and associated sediment grain sorting. The model was validated using the new laboratory data. The hydrodynamic modeling component, consisting of existing REF/DIF S and SHORECIRC models, simulated wave-related parameters and depth-varying currents with mean absolute differences less than 10% and 41% based on available data from the measurement, respectively. Besides these major components, supplemental modules were also developed for describing other essential hydrodynamic parameters or processes, including

- Semi-empirical formula for skewness and asymmetry of velocity time series of transforming waves;
- Parametric equations for modeling 2-D wave orbital velocities;

- Ballistic model for swash zone velocity, including prediction of wave runup.

The components for the velocity skewness, asymmetry and orbital velocities allow the simulation of a nonlinear wave form that is the case in nature. This simulation is crucial for the model performance especially for an accretive-type profile with dominant onshore sediment transport. The ballistic model for the swash zone velocity treats the breaking bore as a moving object with momentum, affected by gravity and friction. In the model test here, the inclusion of this component in the morphodynamic model proved more important than expected. Erosion in the swash zone clearly controlled the magnitude of the beach profile change in the surf zone, including the sandbar formation.

Important parameters from the hydrodynamic modeling components are utilized in the new size-selective sediment transport and grain sorting models developed as a major goal in this study. The novel features in these two models include

- Determination of the concentration field of each sediment size class;
- Computation of intra-wave, fractional sediment transport rates in both bedload and suspended load;
- Velocity skewness and fluid acceleration included in the estimation of instantaneous bed shear stress;
- Wave-breaking turbulence in addition to shear-based prediction of sediment pickup;
- Inclusion of onshore suspended sediment transport within the wave crest;
- Influence of bed slope on critical shear stress and sediment mobility;
- Effect of phase and magnitude differences between fluid and particle velocities;
- Prediction of horizontal grain sorting changes along the beach profile;
- Multi-layer, bookkeeping of sediment size compositions for vertical sediment grain lamination;
- Time-dependent sediment size and composition in the computation of size-selective sediment transport rates.

The bedload transport is modeled using an energetic approach, considering size selectivity that is dominated by the interaction of different grain sizes, referred to as a "hiding/exposure" effect. This interaction leads to an enhancement in the transport rates of the

coarser size fractions in the mixture (d_i/d_m>1). The suspended load transport is modeled based on the sediment concentration solved using an advection-diffusion equation. The nonlinear grain-size dependency is dominating in the determination of this concentration so that the finer size fractions are the favorable group in the transport process.

The bed-slope effect was included using a generic force balance equation that predicts a sediment mobility decreasing for an upslope transport and increasing for a downslope transport. The fluid acceleration is also treated as a "destabilizing" term regarding sediment mobility, which helps to distinguish the effect of wave period on the sediment transport process. The effect of wave breaking is accounted for via a factor that acts to enhance both bedload and suspended load, representing a direct impact due to turbulence-induced sediment pickup under breaking waves.

The model was tested under the laboratory conditions and evaluated based on a profile evolution "performance" index ranging from 0 to 1 (best). The results in the erosive-type profile tests were associated with indices greater than 0.8. A major key to these successful simulations was the prediction of dominant offshore sediment transport due to strong undertow and intensive wave breaking. The bed-slope term was also particularly important for resolving the sandbar curvature. The only region with a fairly weak simulation accuracy was the part of the bar trough right onshore from the bar crest, where the erosion was underpredicted in the zone that wave plunging would be most pronounced. The use of the wave breaking factor has clearly helped to reduce this insufficiency, but not to the extent where the highly-concave bar trough could be fully simulated.

The performance indices were found to be greater than 0.75 for the accretive tests in the mixed-sand and beach nourishment experiments. The model was generally able to predict the event of onshore sandbar migration but failed to represent the profile recovery closer to the shoreline. Because of this reason, the model performance index dropped to 0.59 in the test of the coarse-sand slope, which was the least accurate result among all of the model tests. This inaccuracy was clearly due to an overestimated sediment transport under the wave trough, associated with a large offshore-directed mean flow. The simplified swash zone transport formula also contributed as its prediction was dependent on the sediment transport rate in the inner surf zone.

The consistent sediment grain sorting trends observed in the experiment were simulated successfully in the model. In the erosive-type profiles, coarsening of the bed mixture was predicted from the shoreline through the bar crest region where the bedload was more abundant, rather than the suspended load that led to the grain fining further offshore. In the accretive tests, the material on the bar crest was predicted to be the first to relocate into the bar-trough zone. The finer material in the offshore part was then estimated to transport more slowly as the new sandbar was being formed. A multi-layer deposition of various mixtures was typically found in the sandbar structure due to the dependency of vertical grain lamination on the grain sorting history.

The size-selective model can also be run in a single-size mode which makes it more similar to several previous beach profile models. When the grain sorting was intensive, the superiority of the multi-size model was clearly evident. It allowed a better prediction of the offshore slope on a profile under the storm-wave condition. In the accretive tests, it improved results near the sandbar versus the single-size model. These modeling capabilities were achieved through the consideration on the local sediment characteristics that allowed the model to predict the sediment transport rates more accurately.

The capability of the morphodynamic model to simulate a profile equilibrium was also evaluated based on an "equilibrium" index, ranging from 0 (best) to 1. In most cases, these indices were found to be very small which indicated minimal profile changes at large simulation times, typically $O(10^{-2})$ and $O(10^{-3})$ for the large and the smaller wave conditions, respectively. The multi-size model also showed a tendency to approach an equilibrium state better than the single-size model. This favorable result occurred due to the coarsening mechanism of the surface mixture around the most energetic zone on the profile. This particular process initiated a "stabilizing" condition as a consequence from an overall reduction in the sediment transport rates.

The model serves as a comprehensive simulation tool, requiring only two types of inputs: 1) the wave spectrum at the offshore boundary and 2) the initial beach condition. The use of the new multi-size sediment transport and grain sorting models proved to be one of the key components that improve the modeling accuracy for the cross-shore bathymetric evolution. Grain sorting information on the profile is also obtained from the model.

The superiority of the new model over a commonly-used, existing, single-size model depends on the intensity of grain sorting on the beach profile. Since this grain sorting phenomenon is always the case in nature, either under present or future condition, the model is suitable for an application on any sandy beach. In the most unlikely case that no grain sorting occurs, the multi-size model will asymptotically behave like a single-size model and their simulation results will be similar. Some of the scenarios that the multi-size model will prove most beneficial include

- Beach profiles with non-uniform sediment size characteristics, e.g. $d_{90}/d_{10} \gtrsim 3.0$;
- Nearshore projects that involve potential mixing of multiple types of sediment, e.g. nearshore dredging and land reclamation such as beach nourishment;
- Scenarios where grain sorting information is required, e.g. for recreational, geological, or biological purposes.

Future effort for improving the model may include an upgrade to a fully-2D, wave-resolving model for a more accurate description of wave orbital velocities. The effect of wave breaking could be revised especially for the bar trough region, possibly by also including vortex shedding and pressure gradient effects under breaking waves. The swash zone model may still be utilized while also accounting for swash-swash interaction and infiltration through the sediment bed. The grain sorting model may be improved in order to capture the actual grain sorting process that is instantaneous under an oscillatory flow.

A validation of the model against field data would be mandatory before a practical model application. At field scale, the model may require recalibration of some of the factors that were influenced by scaling effects in the laboratory experiment. These may include wave-breaking related parameters and, more importantly, the magnitudes of and the ratio between the bedload and suspended load. Appropriate data sets for this purpose should be collected from a straight coast with relatively non-uniform sand mixtures. The present sediment bed condition at the site must also be made available as a mandatory initial condition in the model. An ultimate development of the model will include a major task to incorporate longshore morphodynamics, including grain sorting, into the model for a complete simulation of the actual 3-D processes in nature.

References

Aagaard, T., Hughes, M. G., 2010. Breaker turbulence and sediment suspension in the surf zone. Marine Geology 271 (34), 250–259.

Abreu, T., Silva, P. A., Sancho, F., Temperville, A., 2010. Analytical approximate wave form for asymmetric waves. Coastal Eng. 57 (7), 656–667.

Ahmed, A. S. M., Sato, S., 2003. A sheetflow transport model for asymmetric oscillatory flows - Part I: Uniform grain size sediments. Coastal Eng. J. 45 (3), 321–337.

Bagnold, R., 1940. Beach formation by waves: Some model experiments in a wave tank. J. of the Institute of Civil Eng. 15, 27–52.

Bagnold, R., 1966. An approach to the sediment transport problem from general physics. United States Geological Survey Professional Papers 422-1, 1–37.

Bagnold, R. A., 1937. The size-grading of sand by wind. Proc. of Royal Society of London Series A, Mathematical and Physical Sciences 163 (A913), 250–264.

Bagnold, R. A., 1956. The flow of cohesionless grains in fluids. Philosophical Transactions of the Royal Society of London Series A: Mathematical and Physical Sciences 249 (964), 235–297.

Bagnold, R. A., 1963. Mechanics of Marine Sedimentation. Vol. 3. M. N. Hill, Interscience, New York.

Bailard, J., 1981. An energetics total load sediment transport model for a plane sloping beach. J. Geophys. Res. 86 (C11), 10938–10955.

Bailard, J., Inman, D., 1981. An energetics bedload model for a plane sloping beach: Local transport. J. Geophys. Res. 86 (C3), 2035–2043.

Bakhtyar, R., Barry, D. A., Li, L., Jeng, D. S., Yeganeh-Bakhtiary, A., 2009a. Modeling sediment transport in the swash zone: A review. Ocean Eng. 36 (9-10), 767–783.

Bakhtyar, R., Yeganeh-Bakhtiary, A., Barry, D. A., Ghaheri, A., 2009b. Two-phase hydrodynamic and sediment transport modeling of wave-generated sheet flow. Adv. in Water Resources 32 (8), 1267–1283.

Baldock, T., Holmes, P., 1997. Swash hydrodynamics on a steep beach. In: Proc. of Coastal Dynamics. ASCE, 784–793.

Baldock, T. E., Holmes, P., 1999. Simulation and prediction of swash oscillations on a steep beach. Coastal Eng. 36 (3), 219–242.

Battjes, J., Janssen, J., 1978. Energy loss and set-up due to breaking of random waves. In: Proc. of 16th Int. Conf. on Coastal Eng. Vol. 1. ASCE, 569–587.

Battjes, J. A., Stive, M. J. F., 1985. Calibration and verification of a dissipation model for random breaking waves. J. Geophys. Res. 90 (C5), 9159–9167.

Berkhoff, J. C. W., 1972. Computation of combined refraction-diffraction. Proc. of 13th Int. Conf. on Coastal Eng. 2, 471–490.

Bowen, A., 1980. Simple models of nearshore sedimentation; beach profiles and longshore bars. The coastline of Canada (Special Paper: 80-100), 1–11.

Bridge, J. S., Bennett, S. J., 1992. A model for the entrainment and transport of sediment grains of mixed sizes, shapes, and densities. Water Resour. Res. 28 (2), 337–363.

Bruun, P., 1954. Coast erosion and the development of beach profiles. Tech. rep., Beach erosion board technical memorandum. No. 44. U.S. Army Engineer Waterways Experiment Station. Vicksburg, MS.

Butt, T., Russell, P., 2000. Hydrodynamics and cross-shore sediment transport in the swash-zone of natural beaches: A review. J. of Coastal Res. 16 (2), 255–268.

Cambazoglu, M., Haas, K., Hanes, D., 2006. Numerical investigations on the effect of wave skewness on sandbar migration. In: Proc. of 30th Int. Conf. on Coastal Eng., 2286–2298.

Cambazoglu, M. K., 2009. Numerical modeling of cross-shore sediment transport and sandbar migration. Ph.D. thesis, Georgia Institute of Technology.

Cambazoglu, M. K., Haas, K. A., 2011. Numerical modeling of breaking waves and cross-shore currents on barred beaches. J. of the Waterway Port Coastal and Ocean Eng. 137 (6), 310–323.

Camenen, B., Larson, M., 2005. A general formula for non-cohesive bed load sediment transport. Estuarine, Coastal and Shelf Science 63 (1-2), 249–260.

Camenen, B., Larson, M., 2006. Phase-lag effects in sheet flow transport. Coastal Eng. 53 (5-6), 531–542.

Cazenave, A., Lombard, A., Llovel, W., 2008. Present-day sea level rise: A synthesis. Comptes Rendus Geosciences 340 (11), 761–770.

Cea, L., Ferreiro, A., Vazquez-Cendon, M. E., Puertas, J., 2004. Experimental and numerical analysis of solitary waves generated by bed and boundary movements. Int. J. for Numerical Methods in Fluids 46 (8), 793–813.

Celikoglu, Y., Yuksel, Y., Kabdasli, M. S., 2006. Cross-shore sorting on a beach under wave action. J. Coastal Res. 22 (3), 487–501.

CEM, 2006. Coastal engineering manual. Tech. rep., U.S. Army Corps of Engineers. Washington, D.C.

Church, J. C., Thornton, E. B., 1993. Effects of breaking wave induced turbulence within a longshore current model. Coastal Eng. 20 (12), 1–28.

Cimaglia, C. A., Thosteson, E. D., 2002. Design and testing of an economical wave generation facility. Oceans 2002 MTS/IEEE Conference and Exhibition, Vols 1-4, Conference Proceedings, 2482–2487.

Dally, W., 1980. A numerical model for beach profile evolution. Ph.D. thesis, Univ. of Delaware.

Dally, W., 1987. Longshore bar formation: Surf beat or undertow? In: Proc. of Coastal Sediments. Vol. 1. ASCE, 71–86.

Dally, W. R., Dean, R. G., 1984. Suspended sediment transport and beach profile evolution. J. of the Waterway Port Coastal and Ocean Eng. 110 (1), 15–33.

Dalrymple, R., 1992. Prediction of storm/normal beach profiles. J. of the Waterway Port Coastal and Ocean Eng. 118 (2), 193–200.

Davies, A. G., 1995. Effects of unsteadiness on the suspended sediment flux in co-linear wave-current flow. Continental Shelf Research 15 (8), 949–979.

Davies, A. G., Ribberink, J. S., Temperville, A., Zyserman, J. A., 1997. Comparisons between sediment transport models and observations made in wave and current flows above plane beds. Coastal Eng. 31 (1-4), 163–198.

Davies, A. G., Thorne, P. D., 2005. Modeling and measurement of sediment transport by waves in the vortex ripple regime. J. Geophys. Res. 110 (C5), C05017.

Davies, A. G., Villaret, C., 1999. Eulerian drift induced by progressive waves above rippled and very rough beds. J. Geophys. Res. 104 (C1), 1465–1488.

Day, T., 1980. A study of the transport of graded sediments. Tech. rep., Report No. IT 190. Hydraulics Research Station. Wallingford, England.

De Vriend, H. J., Stive, M. J. F., 1987. Quasi-3D modelling of nearshore currents. Coastal Eng. 11 (5-6), 565–601.

De Vriend, H. J., Zyserman, J., Nicholson, J., Roelvink, J. A., Pechon, P., Southgate, H. N., 1993. Medium-term 2DH coastal area modelling. Coastal Eng. 21 (1-3), 193–224.

Dean, R., 1977. Equilibrium beach profiles: US Atlantic and Gulf coasts. Tech. rep., Ocean Engineering Report NO. 12. Dept. of Civil Engineering and College of Marine Studies, Univ. of Delaware.

Dean, R., 1987. Coastal sediment processes: Toward engineering solutions. In: Proc. of Coastal Sediments. ASCE, 1–24.

Dean, R. G., 2002. Beach Nourishment : Theory and Practice. Adv. Series on Ocean Eng. World Scientific, River Edge, NJ.

Dean, R. G., Dalrymple, R. A., 2002. Coastal Processes with Engineering Applications. Cambridge Univ. Press, Cambridge, UK.

Deigaard, R., Jakobsen, J. B., Fredsoe, J., 1999. Net sediment transport under wave groups and bound long waves. J. Geophys. Res. 104 (C6), 13559–13575.

Demir, H., 2007. A process-based model for beach profile evolution. Ph.D. thesis, Georgia Institute of Technology.

Dibajnia, M., Watanabe, A., 1992. Sheet flow under nonlinear waves and currents. In: Proc. of 23rd Int. Conf. on Coastal Eng. ASCE, 2015–2028.

Dibajnia, M., Watanabe, A., 1996. A transport rate formula for mixed-size sands. In: Proc. of 25th Int. Conf. on Coastal Eng. ASCE, 3791–3804.

Ding, Y., Wang, S. S. Y., Jia, Y. F., 2006. Development and validation of a quasi-three-dimensional coastal area morphological model. J. of the Waterway Port Coastal and Ocean Eng. 132 (6), 462–476.

Doering, J. C., Baryla, A. J., 2002. An investigation of the velocity field under regular and irregular waves over a sand beach. Coastal Eng. 44 (4), 275–300.

Dohmen-Janssen, C., 1999. Grain size influence on sediment transport in oscillatory sheet flow; phase lags and mobile-bed effects. Ph.D. thesis, Delft Univ. of Technology.

Dohmen-Janssen, C. M., Hassan, W. N., Ribberink, J. S., 2001. Mobile-bed effects in oscillatory sheet flow. J. Geophys. Res. 106 (C11), 27103–27115.

Dohmen-Janssen, C. M., Kroekenstoel, D. F., Hassan, W. N., Ribberink, J. S., 2002. Phase lags in oscillatory sheet flow: Experiments and bed load modelling. Coastal Eng. 46 (1), 61–87.

Dong, P., Zhang, K., 1999. Two-phase flow modelling of sediment motions in oscillatory sheet flow. Coastal Eng. 36 (2), 87–109.

Edwards, A. C., 2001. Grain size and sorting in modern beach sands. J. Coastal Res. 17 (1), 38–52.

Egiazaroff, I., 1965. Calculation of nonuniform sediment concentrations. J. Hydraul. Div. Am. Soc. Civ. Eng 91 (4), 225–247.

Einstein, H. A., 1950. The bed-load function for sediment transportation in open channel flows. Tech. rep., Technical bulletin no. 1026. U.S. Dept. of Agriculture Washington DC.

Elfrink, B., Baldock, T., 2002. Hydrodynamics and sediment transport in the swash zone: A review and perspectives. Coastal Eng. 45 (3-4), 149–167.

Elfrink, B., Hanes, D. M., Ruessink, B. G., 2006. Parameterization and simulation of near bed orbital velocities under irregular waves in shallow water. Coastal Eng. 53 (11), 915–927.

Elgar, S., Gallagher, E. L., Guza, R. T., 2001. Nearshore sandbar migration. J. Geophys. Res. 106 (C6), 11623–11627.

Erikson, L., Larson, M., Hanson, H., 2005. Prediction of swash motion and run-up including the effects of swash interaction. Coastal Eng. 52 (3), 285–302.

Fenton, J., Abbott, J., 1977. Initial movement of grains on a stream bed: The effect of relative protrusion. Proc. of The Royal Society of London. Series A, Mathematical and Physical Sciences 352 (1671), 523–537.

Fox, W., Ladd, J., Martin, M., 1966. A profile of the four moment measures perpendicular to a shoreline, South Haven, Michigan. J. Sedimentary Res. 36 (4), 1126–1130.

Fredsoe, J., Deigaard, R., 1992. Mechanics of Coastal Sediment Transport. Adv. Series on Ocean Eng. World Scientific, Singapore ; New Jersey.

Greenwood, B., Osborne, P. D., 1990. Vertical and horizontal structure in cross-shore flows: An example of undertow and wave set-up on a barred beach. Coastal Eng. 14 (6), 543–580.

Haas, A. K., Svendsen, I., 2000. Three-dimensional modeling of rip current systems. Tech. rep., (Ph.D. Dissertation) Res. CACR-00-06. Center for Applied Coastal Research, Univ. of Delaware.

Haas, K. A., Hanes, D. M., 2004. Process based modeling of total longshore sediment transport. J. Coastal Res. 20 (3), 853–861.

Haas, K. A., Svendsen, I. A., Haller, M. C., Zhao, Q., 2003. Quasi-three-dimensional modeling of rip current systems. J. Geophys. Res. 108 (C7), 3217–3238.

Haas, K. A., Warner, J. C., 2009. Comparing a quasi-3D to a full 3D nearshore circulation model: SHORECIRC and ROMS. Ocean Modelling 26 (1-2), 91–103.

Hassan, W., 2001. Sand transport processes in oscillatory sheet flows with different wave periods- CCM measurements in the large oscillating water tunnel. Tech. rep., MICS Report 2001W-002. Civil Eng. and Management, Univ. of Twente, The Netherlands.

Hassan, W., Kroekenstoel, D., Ribberink, J., Van Rijn, L., 1999. Gradation effects on sand transport under oscillatory sheet-flow conditions. Tech. rep., Research report. WL/Delft Hydraulics and Univ. of Twente, The Netherlands.

Hassan, W., Ribberink, J., 2005a. Modelling of sand transport with graded sands under oscillatory sheet flows. In: Proc. of Coastal Dynamics. ASCE.

Hassan, W. N., Ribberink, J. S., 2005b. Transport processes of uniform and mixed sands in oscillatory sheet flow. Coastal Eng. 52 (9), 745–770.

Haus, B. K., Shay, L. K., Work, P. A., Voulgaris, G., Ramos, R. J., Martinez-Pedraja, J., 2010. Wind speed dependence of single-site wave-height retrievals from high-frequency radars. J. of Atmos. and Oceanic Tech. 27 (8), 1381–1394.

Hayashi, T., Ozaki, S., Ichibashi, T., 1980. Study of bedload transport of sediment mixture. In: 24th Japanese Conf. on Hydraulics.

Hecht, J., 2007. Frequency of atlantic hurricanes doubled during last century. The New Scientist 195 (2615), 15.

Hedges, T., 1976. An empirical modification to linear wave theory. In: Proc. Inst. Civ Eng. Vol. 61, 575–579.

Henderson, S. M., Allen, J. S., Newberger, P. A., 2004. Nearshore sandbar migration predicted by an eddy-diffusive boundary layer model. J. Geophys. Res. 109 (C6), C06024.

Hoefel, F., Elgar, S., 2003. Wave-induced sediment transport and sandbar migration. Science 299 (5614), 1885–1887.

Holland, K. T., Puleo, J. A., 2001. Variable swash motions associated with foreshore profile change. J. Geophys. Res. 106 (C3), 4613–4623.

Hsu, T. J., Elgar, S., Guza, R. T., 2006. Wave-induced sediment transport and onshore sandbar migration. Coastal Eng. 53 (10), 817–824.

Hsu, T. J., Hanes, D. M., 2004. Effects of wave shape on sheet flow sediment transport. J. Geophys. Res. 109 (C5), C05025.

Hughes, M. G., Baldock, T. E., 2004. Eulerian flow velocities in the swash zone: Field data and model predictions. J. Geophys. Res. 109 (C8).

Hughes, M. G., Masselink, G., Brander, R. W., 1997. Flow velocity and sediment transport in the swash zone of a steep beach. Marine Geology 138 (1-2), 91–103.

Hughes, S. A., 1993. Laboratory wave reflection analysis using co-located gages. Coastal Eng. 20 (3-4), 223–247.

Ingle, J. C., 1966. The Movement of Beach Sand: An Analysis Using Fluorescent Grains. Developments in sedimentology. Elsevier Pub. Co., Amsterdam, New York.

Inman, D., 1953. Areal and seasonal variations in beach and nearshore sediments at La Jolla, California. Tech. rep., U.S. Army Corps Eng. Beach Erosion Board Tech. Mem., Scripps Institution of Oceanography, La Jolla CA.

Inman, D. L., Chamberlain, T. K., 1959. Tracing beach sand movement with irradiated quartz. J. Geophys. Res. 64 (1), 41–47.

Ippen, A., Eagleson, P., 1955. A study of sediment sorting by waves shoaling on a plane beach. Tech. rep., Tech Memo 63. US Army Corps of Eng. Beach Erosion Board.

Isobe, M., Horikawa, K., 1982. Study on water particle velocities of shoaling and breaking waves. Coastal Eng. in Japan 25, 109–123.

Johnson, B., Kobayashi, N., 1998. Nonlinear time-averaged model in surf and swash zones. In: Proc. of 26th Int. Conf. on Coastal Eng. ASCE, 27852798.

Kaczmarek, L. M., Biegowski, J., Ostrowski, R., 2004. Modelling cross-shore intensive sand transport and changes of bed grain size distribution versus field data. Coastal Eng. 51 (5-6), 501–529.

Kaczmarek, L. M., Ostrowski, R., 2002. Modelling intensive near-bed sand transport under wave-current flow versus laboratory and field data. Coastal Eng. 45 (1), 1–18.

Kamphuis, J., 2009. Introduction to Coastal Engineering and Management. World Scientific Publishing Company.

Katoh, K., Yanagishima, S., 1995. Changes of sand grain distribution in the surf zone. In: Proc. of Coastal Dynamics. ASCE, 639–650.

Kirby, J., Dalrymple, R., 1983. A parabolic equation for the combined refraction-diffraction of Stokes waves by mildly varying topography. J. Fluid Mech. 136, 543–566.

Kirby, J. T., Dalrymple, R., Shi, F., 2005. REF/DIF S version 1.3: Documentation and users manual. Tech. rep., Research Report NO. CACR-04-01. Center for Applied Coastal Research, Univ. of Delaware.

Kleinhans, M., van Rijn, L., 2002. Stochastic prediction of sediment transport in sand-gravel bed rivers. J. of Hydraulic Eng. 128, 412–425.

Kobayashi, N., De Silva, G. S., Watson, K. D., 1989. Wave transformation and swash oscillation on gentle and steep slopes. J. Geophys. Res. 94 (C1), 951–966.

Komar, P., 1996. Entrainment of Sediments from Deposits of Mixed Grain Sizes and Densities. Wiley and Sons, pp. 127–181.

Komar, P. D., 1987. Selective gravel entrainment and the empirical evaluation of flow competence. Sedimentology 34 (6), 1165–1176.

Kraus, N., 1994. SUPERTANK laboratory data collection project. Tech. rep., Volume I: Main text. Technical Report CERC-94-3, Coastal Engineering Research Center, Vicksburg MS.

Kraus, N., Mason, J., 1993. Discussion of "Prediction of Storm/Normal Beach Profiles". J. of the Waterway Port Coastal and Ocean Eng. 119 (4), 466–473.

Kriebel, D., Kraus, N., Larson, M., 1991. Engineering methods for predicting beach profile response. In: Proc. of Coastal Sediments. ASCE, 557–571.

Kriebel, D. L., Dean, R. G., 1985. Numerical simulation of time-dependent beach and dune erosion. Coastal Eng. 9 (3), 221–245.

Kuhnle, R., 1993. Incipient motion of sand gravel sediment mixtures. J. of Hydraulic Eng. 119, 1400–1415.

Lawrance, J., Karunarathna, H., Chadwick, A. J., Fleming, C., 2002. Cross-shore sediment transport on mixed coarse grain sized beaches: Modeling and measurements. In: Proc. of 28th Int. Conf. on Coastal Eng. Vol. 3. ASCE, 2565–2577.

Li, M., Fernando, P. T., Pan, S., O'Connor, B. A., Chen, D., 2007. Development of a quasi-3D numerical model for sediment transport prediction in the coastal region. J.of Hydro-Environment Res. 1 (2), 143–156.

Li, M., Pan, S., O'Connor, B. A., 2008. A two-phase numerical model for sediment transport prediction under oscillatory sheet flows. Coastal Eng. 55 (12), 1159–1173.

Lippmann, T. C., Brookins, A. H., Thornton, E. B., 1996. Wave energy transformation on natural profiles. Coastal Eng. 27 (1-2), 1–20.

Liu, H., Sato, S., 2006. A two-phase flow model for asymmetric sheetflow conditions. Coastal Eng. 53 (10), 825–843.

Liu, J. T., Zarillo, G. A., 1993. Simulation of grain-size abundances on a barred upper shoreface. Marine Geology 109 (3-4), 237–251.

Long, W., Kirby, J. T., Shao, Z., 2006. Numerical schemes for bed level updating in sediment transport. Tech. rep., Res. Report CACR-06-01, Center for Applied Coastal Research, Univ. of Delaware.

Longuet-Higgins, M., 1956. The mechanics of the boundary layer near the bottom in a progressive wave. In: Proc. of 22th Int. Conf. on Coastal Eng. Vol. 1. ASCE, 184–193.

Longuet-Higgins, M., Stewart, R. W., 1964. Radiation stress in water waves, a physical discussion with applications. Deep Sea Research 11, 529–563.

Lopez de San Roman-Blanco, B., Coates, T. T., Holmes, P., Chadwick, A. J., Bradbury, A., Baldock, T. E., Pedrozo-Acuna, A., Lawrence, J., Grune, J., 2006. Large scale experiments on gravel and mixed beaches: Experimental procedure, data documentation and initial results. Coastal Eng. 53 (4), 349–362.

Luijendijk, A., Henrotte, J., Walstra, D., van Ormondt, M., 2010. Quasi-3D modelling of surf zone dynamics. In: Proc. of Coastal Eng. Vol. 32.

Malarkey, J., Davies, A. G., Li, Z., 2003. A simple model of unsteady sheet-flow sediment transport. Coastal Eng. 48 (3), 171–188.

Martinez, M. L., Intralawan, A., Vazquez, G., Perez-Maqueo, O., Sutton, P., Landgrave, R., 2007. The coasts of our world: Ecological, economic and social importance. Ecological Economics 63 (2-3), 254–272.

Massel, S. R., 1996. Ocean Surface Waves : Their Physics and Prediction. Adv. Series on Ocean Eng. World Scientific, Singapore; River Edge NJ.

Masselink, G., 2004. Formation and evolution of multiple intertidal bars on macrotidal beaches: Application of a morphodynamic model. Coastal Eng. 51 (8-9), 713–730.

Medina, R., Losada, M. A., Losada, I. J., Vidal, C., 1994. Temporal and spatial relationship between sediment grain size and beach profile. Marine Geology 118 (3-4), 195–206.

Meyer-Peter, E., Muller, P., 1948. Formulas for bed-load transport. In: Proc. of 2nd Meeting of Int. Assoc. of Hydraulic Structure Research, 39–64.

Miskovic, I., Eskinja, Z., Horvat, K., 2008. Wavemaker control system for irregular developed sea waves generation. 2008 Mediterranean Conf. on Control Automation, Vols 1-4, 1426–1429.

Misri, R., Raju, K., 1984. Bed load transport of coarse nonuniform sediment. J. of Hydraulic Eng. 110, 312–328.

Morfett, J. C., 1992. Threshold of motion of coarse-grained sediment under waves in shallow water. Coastal Eng. 18 (34), 283–295.

Moutzouris, C., 1988. Longshore sediment transport rate versus cross-shore distribution of sediment grain size. In: Proc. of 21th Int. Conf. on Coastal Eng. ASCE, 1959–1973.

Nairn, R., Roelvink, J., Southgate, H., 1990. Transition zone width and implications for modeling surfzone hydrodynamics. In: Proc. of 22nd Int. Conf. on Coastal Eng. Vol. 22. ASCE, 68–81.

Nairn, R. B., Southgate, H. N., 1993. Deterministic profile modelling of nearshore processes. Part 2. sediment transport and beach profile development. Coastal Eng. 19 (1-2), 57–96.

Nielsen, P., 1986. Suspended sediment concentrations under waves. Coastal Eng. 10 (1), 23–31.

Nielsen, P., 1992. Coastal Bottom Boundary Layers and Sediment Transport. Adv. Series on Ocean Eng. World Scientific, Singapore ; River Edge, N.J.

Nielsen, P., Hanslow, D. J., 1991. Wave runup distributions on natural beaches. J. Coastal. Res. 7 (4), 1139–1152.

Nortek, 2004. Vectrino: Acoustic Doppler velocimeter user guide.

O'Donoghue, T., Wright, S., 2004a. Concentrations in oscillatory sheet flow for well sorted and graded sands. Coastal Eng. 50 (3), 117–138.

O'Donoghue, T., Wright, S., 2004b. Flow tunnel measurements of velocities and sand flux in oscillatory sheet flow for well-sorted and graded sands. Coastal Eng. 51 (11-12), 1163–1184.

Parker, G., Klingeman, P., McLean, D., 1982. Bedload and size distribution in paved gravel-bed streams. J. of the Hydraulics Division 108 (4), 544–571.

Pawka, S. S., 1983. Island shadows in wave directional spectra. J. Geophys. Res. 88 (Nc4), 2579–2591.

Peters, K., Newe, J., Dette, H., 1996. Development of underwater beach profile by monochromatic and random waves. In: Proc. of 25th Int. Conf. on Coastal Eng. ASCE, 3442–3452.

Petit, F., 1994. Dimensionless critical shear stress evaluation from flume experiments using different gravel beds. Earth Surface Processes and Landforms 19 (6), 565–576.

Pope, L. R., Ward, C. W., 1998. Manual on Test Sieving Methods: Guidelines for Establishing Sieve Analysis Procedures, 1998th Edition. ASTM manual series. American Society for Testing and Materials, West Conshochocken, PA.

Puleo, J. A., Holland, K. T., 2001. Estimating swash zone friction coefficients on a sandy beach. Coastal Eng. 43 (1), 25–40.

Putrevu, U., Svendsen, I. A., 1993. Vertical structure of the undertow outside the surf zone. J. Geophys. Res. 98 (C12), 22707–22716.

Putrevu, U., Svendsen, I. A., 1999. Three-dimensional dispersion of momentum in wave-induced nearshore currents. European Journal of Mechanics - B/Fluids 18 (3), 409–427.

Rakha, K. A., 1998. A quasi-3D phase-resolving hydrodynamic and sediment transport model. Coastal Eng. 34 (3-4), 277–311.

Ribberink, J. S., 1998. Bed-load transport for steady flows and unsteady oscillatory flows. Coastal Eng. 34 (1-2), 59–82.

Ribberink, J. S., Al Salem, A. A., 1995. Sheet flow and suspension of sand in oscillatory boundary layers. Coastal Eng. 25 (3-4), 205–225.

Richmond, B., Sallenger, A., 1984. Cross-shore transport of bimodal sands. Proc. of 19th Int. Conf. on Coastal Eng., 1997–2008.

Roelvink, J., Stive, M., 1989. Bar-generating cross-shore flow mechanisms on a beach. J. Geophys. Res. 94 (C4), 4785–4800.

Rouse, H., 1937. Modern conceptions of the mechanics of fluid turbulence. Transactions of ASCE 102 (1), 463–543.

Ruessink, B. G., Walstra, D. J. R., Southgate, H. N., 2003. Calibration and verification of a parametric wave model on barred beaches. Coastal Eng. 48 (3), 139–149.

Russell, P., Huntley, D., 1999. A cross-shore transport “shape function” for high energy beaches. J. Coastal Res. 15 (1), 198–205.

Sancho, F. E., Svendsen, I., 2000. Unsteady nearshore currents on longshore varying topographies. Tech. rep., Res. Report CACR-97-10. Center for Applied Coastal Research, Univ. of Delaware.

Schoonees, J. S., Theron, A. K., 1995. Evaluation of 10 cross-shore sediment transport morphological models. Coastal Eng. 25 (1-2), 1–41.

Shen, M. C., Meyer, R. E., 1963a. Climb of a bore on a beach: 2. Non-uniform beach slope. J. of Fluid Mech. 16 (1), 108–112.

Shen, M. C., Meyer, R. E., 1963b. Climb of a bore on a beach: 3. Run-up. J. of Fluid Mech. 16 (1), 113–125.

Sistermans, P. J. G., 2002. Graded sediment transport by non-breaking waves and a current. Ph.D. thesis, Delft Univ. of Technology, Delft, The Netherlands.

Sonu, C. J., 1972. Bimodal composition and cyclic characteristics of beach sediment in continuously changing profiles. J. Sedimentary Res. 42 (4), 852–857.

Sorensen, O. R., Schaffer, H. A., Sorensen, L. S., 2004. Boussinesq-type modelling using an unstructured finite element technique. Coastal Eng. 50 (4), 181–198.

Soulsby, R. L., 2001. Sediment transport and morphodynamics on complex coastlines- the COAST3D project. In: Proc. of Coastal Dynamics. ASCE.

Srisuwan, C., Work, P. A., in review. Directional surface wave spectra from acoustic doppler current profiler data in sheared and stratified flows, Contact authors for a copy.

Stauble, D., Cialone, M., 1996. Sediment dynamics and profile interactions: Duck94. In: 25th ICCE. Vol. 4. ASCE, 3921–3934.

Steetzel, H. J., 1987. A model for beach and dune profile changes near dune revetments. In: Proc. of Coastal Sediments. ASCE, 87–97.

Steetzel, H. J., 1990. Cross-shore transport during storm surges. In: Proc. of 22nd Int. Conf. on Coastal Eng. ASCE, 1922–1934.

Stive, M., 1988. A model for cross-shore sediment transport. In: Proc. of 20th Int. Conf. on Coastal Eng. Vol. 2. ASCE, 1550–1564.

Sunamura, T., Okazaki, S., 1996. Breaker types and wave reflection coefficient: Laboratory relationships. J. Coastal. Res. 12 (1), 240–245.

Svendsen, I. A., 2006. Introduction to Nearshore Hydrodynamics. Adv. Series on Ocean Eng. World Scientific, Hackensack, NJ.

Svendsen, I. A., Haas, K. A., Zhao, Q., 2002. Quasi-3D nearshore circulation model (SHORECIRC). Tech. rep., CACR-02-01. Center for Applied Coastal Research, Univ. of Delaware.

Swart, D., 1974. Offshore sediment transport and equilibrium beach profiles. Tech. rep., Delft Hydr. Lab. Publ., No. 131. Delft Hydraulics, The Netherlands.

Swart, D., 1976. Predictive equations regarding coastal transports. In: Proc. of 15th Int. Conf. on Coastal Eng. ASCE.

Terray, E. A., Brumley, B. H., Strong, B., 1999. Measuring waves and currents with an upward-looking ADCP. In: Proc. of IEEE 6th Working Conf. on Current Meas., 1999, 66–71.

Terwindt, J. J., 1962. Study of grain size variations at the coast of Katwijk. Tech. rep., The Netherlands, Note K-324, Rijkswaterstaat, Deltadienst, Den Haag, Netherlands.

Thornton, E., Guza, R., 1983. Transformation of wave height distribution. J. Geophys. Res. 88 (10), 5925–5938.

Thornton, E., Humiston, R., Birkemeier, W., 1996. Bar/trough generation on a natural beach. J. Geophys. Res 101 (C5), 12,097–12,110.

Tomkins, M. R., Nielsen, P., Hughes, M. G., 2003. Selective entrainment of sediment graded by size and density under waves. J. Sedimentary Res. 73 (6), 906–911.

Trowbridge, J., Madsen, O. S., 1984. Turbulent wave boundary layers: 1. Model formulation and first-order solution. J. Geophys. Res. 89 (C5), 7989–7997.

Van Rijn, L., 1984. Sediment pick-up functions. J. of Hydraulic Eng. 110 (10), 1494–1502.

Van Rijn, L., 1993. Principles of Sediment Transport in Rivers, Estuaries and Coastal Seas. Aqua Publications, Amsterdam.

Van Rijn, L., 1997a. Cross-shore modelling of graded sediments. Tech. rep., Basic Research. Delft Hydraulics, The Netherlands.

Van Rijn, L., 1997b. Sand transport and bed composition along cross-shore profile. In: Proc. of Coastal Dynamics, 88–98.

Van Rijn, L., 2007a. Unified view of sediment transport by currents and waves. II: Suspended transport. J. of Hydraulic Eng. 133 (6), 668–689.

Van Rijn, L., 2007b. Unified view of sediment transport by currents and waves. III: Graded beds. J. of Hydraulic Eng. 133 (7), 761–775.

Van Rijn, L., Tonnon, P. K., Walstra, D. J. R., 2011. Numerical modelling of erosion and accretion of plane sloping beaches at different scales. Coastal Eng. 58 (7), 637–655.

Van Rijn, L., Walstra, D. J. R., Grasmeijer, B., Sutherland, J., Pan, S., Sierra, J. P., 2003. The predictability of cross-shore bed evolution of sandy beaches at the time scale of storms and seasons using process-based profile models. Coastal Eng. 47 (3), 295–327.

Van Rijn, L. C., 2000. General view on sand transport by currents and waves: Data analysis and engineering modelling for uniform and graded sand (TRANSPOR 2000 and CROSMOR 2000 models). WL/Delft Hydraulics, Delft Cluster.

Van Wellen, E., Chadwick, A. J., Mason, T., 2000. A review and assessment of longshore sediment transport equations for coarse-grained beaches. Coastal Eng. 40 (3), 243–275.

Voulgaris, G., Collins, M. B., 2000. Sediment resuspension on beaches: Response to breaking waves. Marine Geology 167 (12), 167–187.

Warner, J. C., Sherwood, C. R., Signell, R. P., Harris, C. K., Arango, H. G., 2008. Development of a three-dimensional, regional, coupled wave, current, and sediment-transport model. Computers and Geosciences 34 (10), 1284–1306.

Watanabe, A., 1987. 3-Dimensional numerical model of beach evolution. In: Proc. of Coastal Sediments, 801–817.

Watanabe, A., 1992. Total rate and distribution of longshore sand transport. In: Proc. of 23rd Int. Conf. on Coastal Eng. ASCE, 2528–2541.

Wei, G., Kirby, J. T., 1995. Time-dependent numerical code for extended Boussinesq Equations. J. of the Waterway Port Coastal and Ocean Eng. 121 (5), 251–261.

Wilcock, P. R., 1993. Critical shear-stress of natural sediments. J. of Hydraulic Eng. 119 (4), 491–505.

Wilson, K. C., 1989. Friction of wave-induced sheet flow. Coastal Eng. 12 (4), 371–379.

Work, P. A., 2008. Nearshore directional wave measurements by surface-following buoy and acoustic Doppler current profiler. Ocean Eng. 35 (8-9), 727–737.

Work, P. A., Karasu, S., Cambazoglu, M., Srisuwan, C., 2010. Sediment size influence on beach nourishment evolution. In: Proc. of 9th Int. Congress on Adv. in Civil Eng., Contact authors for a copy.

Work, P. A., Rogers, W. E., 1998. Laboratory study of beach nourishment behavior. J. of the Waterway Port Coastal and Ocean Eng. 124 (5), 229–237.

Wu, B., Molinas, A., Shu, A., 2003. Fractional transport of sediment mixtures. Int. J. of Sed. Research 18 (3), 232–247.

Zeigler, J., Hayes, C., Tuttle, S., 1959. Beach changes during storms on outer Cape Cod, Massachusetts. J. of Geology 67 (3), 318–336.

Zheng, J., Dean, R. G., 1997. Numerical models and intercomparisons of beach profile evolution. Coastal Eng. 30 (3-4), 169–201.

Zyserman, J., Fredsoe, J., 1994. Data analysis of bed concentration of suspended sediment. J. of Hydraulic Eng. 120 (9), 1021–1042.

VITA

Chatchawin Srisuwan or "Ouddy" was born on September 11, 1983 in Hatyai, Thailand. He received his BEng in Civil Engineering from Prince of Songkla University in his hometown in 2006. In 2007, he obtained an MSc (Eng) in Environmental Engineering and Project Management from the University of Leeds in the UK. He came to the USA in 2008 to pursue a PhD in Civil Engineering at Georgia Institute of Technology, with a specialization in Coastal and Ocean Engineering. In 2010, he received another MSc in Civil Engineering from the Institute on his pathway to the PhD. He successfully defended his PhD thesis on October 29, 2012. He enjoys watching and practicing any kind of sports except for baseball and cricket. He would like to pursue another degree in Economics or Nuclear Technology in a near future.